Weight Estimation of Gas Turbine Engines

Development of a Component-Based Preliminary Engine Design Tool

Isaac H. Boersma

Technische Universiteit Delft

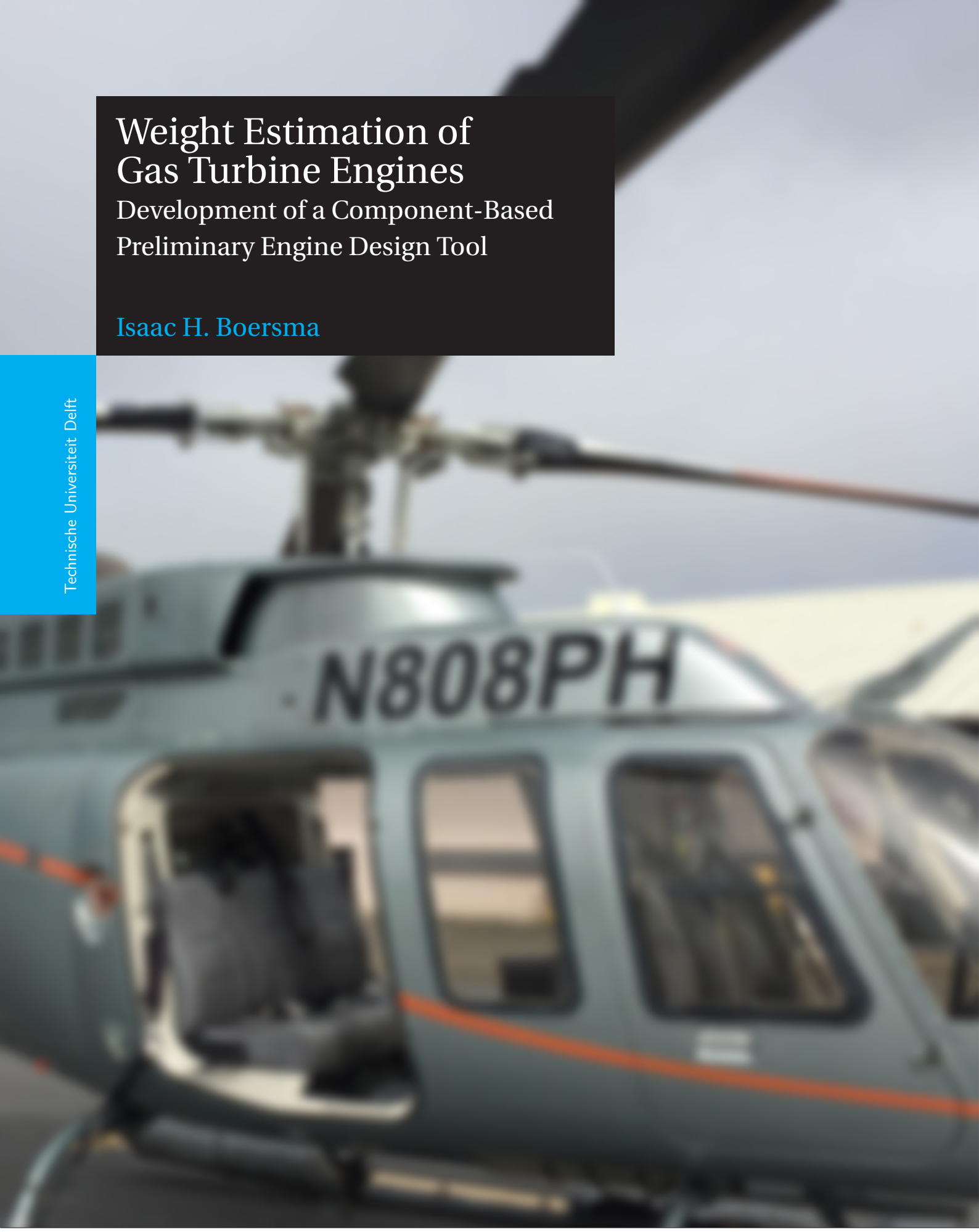

TU Delft Delft University of Technology

Challenge the future

Weight Estimation of Gas Turbine Engines

Development of a Component-Based Preliminary Engine Design Tool

by

Isaac H. Boersma

in partial fulfillment of the requirements for the degree of

Master of Science
in Aerospace Engineering

at the Delft University of Technology,
to be defended publicly on Friday August 26, 2022 at 1:30 PM.

Supervisor:	Dr. ir. Carlo De Servi	TU Delft
Thesis committee:	Prof. dr. ir. Piero Colonna,	TU Delft
	Prof. dr. ir. Sikke Klein,	TU Delft
	Dr. ir. Matteo Pini,	TU Delft

An electronic version of this thesis is available at http://repository.tudelft.nl/.

TU Delft Delft University of Technology

PREFACE

This journey began in the fall of 2016, when I felt God leading me to do a master's degree, but knowing not why or where. Things became clear when, in August 2017, I travelled to the Netherlands, the birthplace of all four of my grandparents, and thus the nation of my heritage. Ever since I was young, I had wanted to live here, and so as soon as I had come for the first time, all I wanted to do was stay. A few days into the trip, I googled 'top university in the Netherlands', for which TU Delft was the top result. The first result within that was 'Aerospace Engineering' since, of course, that comes first alphabetically. As soon as I read the program description, I knew it was for me – it was everything I was looking for in a master's degree and none of the things I wasn't. It was only three years later before I finally ventured here, but it was well worth the wait.

Isaac H. Boersma
Delft, August 2022

ACKNOWLEDGEMENTS

I would like to acknowledge the help of my supervisor, Dr. Carlo De Servi. He provided me with the initial thesis topic, the updated thesis topic, as well as continued support throughout the duration of this project. I appreciate him giving me so much access to both his time and expertise.

I would also like to especially acknowledge the help of Dabo Krempus, a PhD-candidate who followed my progress closely and offered feedback and assistance all along the way. Several key literature sources used in the development of the program described in this report were provided to me by Dabo, so a share of the initial quality of the methodology can be attributed to him.

I would like to thank my thesis committee for agreeing to participate and for giving me the chance to defend the work that I have put so much effort into.

I would like to thank many of the professors of the Aerospace Engineering faculty at Delft University of Technology for modernizing my education, for teaching me so much about aero engine technology, and for preparing me so well for this thesis. Most notably are Dr. Gianfranco La Rocca, Dr. Matteo Pini, and Dr. Carlo De Servi.

I would like to thank the Mechanical Engineering department of the University of Waterloo and all the professors who taught me along the way for providing me with the foundation by which I was able to complete this master's degree. My grueling bachelor's degree meant that the infamous 'TU Delft Aerospace Engineering' program was simply par for the course.

I would like to thank the TU Delft and the Justus & Louise van Effen Excellence Scholarship for making this opportunity possible, as well as my parents for providing additional financial and emotional support throughout both of my degrees.

I would like to thank my grandparents, who led me to the Netherlands due simply to the fact that they were Dutch.

And finally, I would like to thank God, who has fathered me for many years, training me in the way I should go and continually providing for all of my needs. I am who I am because of who HE IS.

ABSTRACT

The need for more efficient aircraft has spawned the conception of a variety of novel engine and aircraft architectures, such as the combined-cycle engine proposed by researchers at Delft University of Technology. To evaluate the potential benefits of these concepts comprehensively, in-depth performance simulations are required. Furthermore, penalties with regard to weight and drag are critical considerations, thus new engine technologies must be evaluated within their full airframe-level integration and mission profile. Accurate weight estimations of a variety of design alternatives are therefore necessary in order to properly assess the validity of such technologies and to reach an optimal design with respect to the tradeoffs between weight, drag, and efficiency. No weight estimation tools with sufficient accuracy are publically available at present, thus a new, component-based preliminary engine design tool, named 'Weight Estimation of Aeronautical Gas Turbine Engines' (or *WEST*), was developed. WEST can be used to predict the weight of novel engine architectures to a reasonable degree of accuracy, all the while accounting for sensitivity to design parameters such as turbine inlet temperature, overall pressure ratio, mass flow rate, power, and choice of turbomachinery configuration. Similar methodologies are able to design components worth between 60 and 110% of the actual weight of an existing engine, whereas WEST was able to account for about 70-90%, thus exceeding initial expectations and improving the reliability of the estimations. This tool can therefore be used to estimate the weight of a variety of existing engines, and is sufficiently flexible to model novel architectures as well, since the results are based on the application-specific design of real engine components. Among the potential uses of WEST, a promising one would be to evaluate the weight of a large set of designs for a particular application. Upon these estimates, single-equation surrogate models could be developed using statistical regression, allowing for these equations to be used as a more computationally-efficient weight estimation methodology in a wide range of aircraft-level design and optimization studies. These equations would build upon the work described in this paper and could be used to accelerate the development and introduction of new aircraft-related technologies.

CONTENTS

List of Figures

List of Tables

NOMENCLATURE

SYMBOLS

Symbol(s)	Units	Description
$A, B, C, ..., H, r, q$	-	Coefficients
A	m^2	Cross-Sectional Area
a	m/s	Speed of Sound, or ...
a	-	Arbitrary Variable Name
AR	-	Aspect Ratio
A_r	-	Bernstein Coefficient
b	m	Blade Height, or ...
b	m	Channel Height, or ...
b	-	Bernstein Basis Polynomial
BPR	-	Bypass Ratio
C	-	Class Function
c	m	Chord, or ...
c	J/kg·K	Specific Heat Capacity
c_{fL}	-	Theoretical Lift Coefficient
c_p	J/kg·K	Specific Heat Capacity (at Constant Pressure)
CPR	-	(HPC) Compressor Pressure Ratio
D	N	Drag (Force), or ...
D	Pa	Stress (Sum and Differences Method), or ...
D	m	Diameter
DF	-	Diffusion Factor
DH	-	DeHaller Number
E	Pa	Elastic (Young's) Modulus, or ...
E	J	Energy
e	-	Cooling Effectiveness
F	N	Force
f	-	Factor
$f(...)$	-	Function of (...)
FPR	-	Fan Pressure Ratio
G	Pa	Shear Modulus
g	-	Row or Stage Gap
g_o	m/s^2	Gravitational Constant/Acceleration
H	-	(Normalized) Maximum Arc Height
h	J/kg	Specific Enthalpy, or ...
h	-	Non-Dimensional Step Size (Finite Differences)
I_{sp}	s	Specific Impulse
k	W/m·K	Thermal Conductivity
K_B	-	Blockage Factor
L	N	Lift (Force)
l	m	(True) Chord, or ...
l	m	Length
L/D	-	Lift-to-Drag Ratio
LER		Leading Edge Radius
LHV	J/kg_f	Lower Heating Value
M	N·m	(Bending) Moment
m	kg	Mass
$\dot{m}$	kg/s	Mass Flow Rate

Symbol(s)	Units	Description
Ma	-	Mach Number
N	RPM	Rotational Speed
n	-	Number of ...
$N1, N2$	-	Class Function Exponents
OPR		Overall Pressure Ratio
P	bar	Pressure
p	Pa	Pressure, or ...
p	m	Pitch
PR	-	Pressure Ratio
Pr	-	Prandtl Number
R	m	Range, or ...
R	-	Degree of Reaction
r	m	Radius, or ...
r	m	Radial-Axis Coordinate
R_g	J/kg·K	Specific Gas Constant
$RTDF$	-	Radial Temperature Distribution Factor
S	Pa	Stress (Sum and Differences Method), or ...
S	-	Scaling Parameter, or ...
S	-	Shape Function
s	J/kg·K	Specific Entropy
S_1	-	Calibration Factor / Correction Coefficient
SF	-	Safety Factor (or Factor of Safety)
SFC	g/kN·s	(Thrust) Specific Fuel Consumption
T	K	Temperature, or ...
T	N·m	Torque
t	m	Thickness
t/c	-	Thickness-to-Chord Ratio
TER		Trailing Edge Radius
U	m/s	Tangential Velocity
V	m/s	Flight Speed, or ...
V	m/s	Absolute Velocity, or ...
V	m^3	Volume
W	kg	Weight (Mass), or ...
W	m/s	Relative Velocity, or ...
W	-	(Normalized) Width
$\dot{W}$	W	Power
w	J/kg	Specific Work
WA	°	Trailing Edge Wedge Angle
x	m	X-Axis Coordinate
x'	m	Coordinate in Transformed X'-Axis
XT	%c	Position of Maximum Thickness (Turbine Blade)
Δx	m	Gap/Displacement/Length (Axial Direction)
y	m	Y-Axis Coordinate
y'	m	Coordinate in Transformed Y'-Axis
Z	-	Zweifel Coefficient
α	rad	Flow Angle, or ...
α	K^{-1}	Coefficient of Thermal Expansion, or ...
α	-	Factor, or ...
α	rad	Shaft Angle
β	rad	Blade Angle, or ...
β	-	Single-Stage Pressure Ratio
δ	m	Thickness Distribution
η	-	Efficiency
γ	-	Ratio of Specific Heats
κ	-	Empirical Coefficient, Shear Portion of Deformation Energy

Symbol(s)	Units	Description
Λ	-	Work Done Factor
λ	-	Taper Ratio
μ	-	Empirical Coefficient, Elastic Portion of Deformation Energy
ν	-	Poisson's Ratio
ω	rad/s	Angular Velocity
φ	rad	Camber Angle
ϕ	-	Flow Coefficient
ψ	-	Work Coefficient
ρ	kg/m^3	Density
σ	-	Solidity, or ...
σ	Pa	(Normal) Stress
$\delta\sigma$	Pa	Change in Stress
τ	Pa	Shear Stress, or ...
τ	s	Time
θ	rad	Tangent Angle, or ...
θ	rad	(Generic) Angle
υ	-	Empirical Coefficient, Ductile Portion of Deformation Energy
ξ	-	Consolidation Coefficient

SUBSCRIPTS

Subscript	Description
0	Original/Initial Value
0,1,2,3	Station Numbering
1,2,3,...	Stage Numbering
1,2,3,4,5,6	Stations in Disk Geometry Formulation
2,21,25,3,4,45,5,...	Engine Station Numbering
A, B	Adjacent Infinitesimal Ring Elements of Disk
a	Aircraft (Excluding Usable Fuel), or ...
a	Blade Root Inner Radius
abs	Absolute (Frame of Reference)
$airfoil$	Airfoil
arc	(Circular) Arc
avg	Average
ax	Axial
bl	Blade(s)
bn	Bending
c	Corrected, or...
c	Mean Camber Line
cas	Casing
cc	Combustion Chamber (Combustor)
cf	Centrifugal
chw	Connecting Hardware
cmp	Compressor
con	Containment
$cooled$	Cooled (Blades)
$cooling$	Coolant,
d	Deviation (Angle)
dd	Dump Diffuser
des	Design
$disk$	Disk
$dome$	Dome
$duct$	Duct
e	von Mises
f	Fuel
fan	Fan
$first$	First
fl	Final, or ...
fl	Flare (Angle)
$fuel$	Fuel
G	Centroid / Centre of Mass
h	Hoop/Tangential (Stress)
HPC	High-Pressure Compressor
HPT	High-Pressure Turbine
hub	(Blade) Hub
i	Inner, or ...
i	Incidence (Angle)
il	Initial
in	Inlet
kin	Kinetic (Energy)
L	Lower Surface
$last$	Last
LE	Leading Edge
$liner$	Liner

Subscript	Description
loc	Local (Spanwise Location)
LPC	Low-Pressure Compressor
LPT	Low-Pressure Turbine
M	Multiplier
m	Mean/Mid, or...
m	Meridional
max	Maximum
$mech$	Mechanical
mid	Mid/Mean (Spanwise Location)
min	Minimum
ml	Meanline
n	Arbitrary Station Number, or ...
n	Neutral Axis, or ...
n	Order of a Bernstein Polynomial
nom	Nominal
o	Origin, or ...
o	Outer
$obj.$	Objective (Function)
op	Operating
out	Outlet
P	Penalty
pl	Planar
plt	(Disk) Platform
pr	Pressure
pt	Polytropic
R	(Temperature) Recovery, or ...
R	Residence
r	Radial, or ...
r	Radial-Axis, or ...
r	Index of a Bernstein Basis Polynomial
ref	Reference
rel	Relative (Frame of Reference)
rim	(Disk Outer) Rim
$root$	(Blade) Root
$rotor$	Rotor (Row/Blade)
row	Row
s	Static Property (Thermodynamics)
seg	(Blade) Segment
sh	Shaft
sk	Skeleton Line
$stator$	Stator (Row/Blade)
stg	Stage(s)
t	Total Property (Thermodynamics), or ...
t	Tangential, or ...
t	(Half-)Thickness Distribution
TE	Trailing Edge
tg	Tangential
tip	(Blade) Tip
$total$	Total Value
trb	Turbine
tt	Total-to-Total
U	Upper Surface
uc	Uncooled
UTS	Ultimate Tensile Strength
x'	Transformed X'-Axis
y	Yield (Stress/Strength)
y'	Transformed Y'-Axis

ABBREVIATIONS

Abbreviation	Description
2D	Two-Dimensional
3D	Three-Dimensional
ACM	Air Cycle Machine
AMRD	Aeronautics Mission Research Directorate
API	Application Programming Interface
APU	Auxiliary Power Unit
ARENA	Airborne Energy Harvesting for Aircraft
BPR	Bypass Ratio
°C	Degrees Centigrade
CAD	Computer Aided Design
CC	Combined-Cycle
CC-APU	Combined-Cycle Auxiliary Power Unit
CCE	Combined-Cycle Engine
CHW	Connecting Hardware
const.	Constant
corr.	Corrected
CPR	(HPC) Compressor Pressure Ratio
CST	Class-function/Shape-function Transformation
D	Difference
deg.	Degree(s)
DLR	German Aerospace Center
e.g.	*exempli gratia* (“for example”)
etc.	et cetera
FEA	Finite Element Analysis
FPR	Fan Pressure Ratio
FPT	Free Power Turbine
g	Gram(s)
GG	Gas Generator
GGT	Gas Generator Turbine
GTlab	Gas Turbine Laboratory
H	Hub (Radius)
HEP	Hybrid-Electric Propulsion
HEX	Heat Exchanger
HPC	High Pressure Compressor
HPT	High Pressure Turbine
Hyp.	Hyperbolic
i.e.	*id est* (“that is”)
in	Inch(es)
IPC	Inter-Pressure Compressor
J	Joule(s)
JPL	Jet Propulsion Library
K	Kelvin
kg	Kilogram(s)
L	Lower
lb	Pound(s)
LE	Leading Edge
LER	Leading Edge Radius
LHV	Lower Heating Value
LPC	Low Pressure Compressor
LPT	Low Pressure Turbine
M	Mid (Radius)
m	Metre(s)

Abbreviation	Description
MEA	More-Electric Aircraft
MJ	Megajoule(s)
mm	Millimetre(s)
MPa	Megapascal(s)
ms	Millisecond(s)
M&S	Modelling and Simulation
MSE	Modelling & Simulation Environment
MW	Megawatt(s)
N	Newton(s)
N/A	Not Applicable
NASA	National Aeronautics and Space Administration
NGV	Nozzle Guide Vane
Nom	Nominal
obj.	Objective
OPR	Overall Pressure Ratio
ORC	Organic Rankine Cycle
Pa	Pascal(s)
Qty	Quantity
rad	Radian(s)
RPM	Revolutions Per Minute
RTDF	Radial Temperature Distribution Factor
S	Sum
s	Second(s)
Sec.	(Report) Section
SF	Safety Factor (or Factor of Safety)
SFC	Specific Fuel Consumption
SI	International System of Units
T	Tip (Radius)
TE	Trailing Edge
TER	Trailing Edge Radius
Temp.	Temperature
TIT	Turbine Inlet Temperature
T-s	Temperature-Entropy (Diagram)
TU Delft	Delft University of Technology
U	Upper
uc	Uncooled
UTS	Ultimate Tensile Strength
vs.	Versus
W	Watt(s)
WEM	Weight Estimation Methodology
WEST	Weight Estimation of Aeronautical Gas Turbine Engines
WHR	Waste Heat Recovery (Unit/System)
°	Degrees (Angle)

1

INTRODUCTION

Aircraft propulsion systems are a feat of both advanced technology and precision engineering. Each of the components (multi-stage axial compressors and turbines, combustion chambers, etc.) are state-of-the-art in their respective fields. Given the highly multi-disciplinary nature of these gas turbine engines, complex couplings exist between the subsystems: a performance gain in one area may lead to penalties in another, and strict operational, material, cost, and environmental limitations mean that the final design is a compromise optimized between various considerations and trade-offs.

Improving aircraft performance and efficiency is essential from both a sustainability and economic perspective. Pre-coronavirus, commercial aviation was responsible for approximately 2.5% of global CO2 emissions, with further industry growth expected [1, 2]. Higher efficiencies mean less fuel consumption, leading to lower operating costs for airlines and a smaller environmental footprint. However, the rate at which engine efficiency can be improved by traditional development methods is slowing [3], thus in order to meet the aggressive emission reduction goals set forth in Flightpath 2050 [4], disruptive engine technologies with non-traditional architectures, energy sources, etc. are required.

One research campaign which aims to tackle such novel engine concepts is the Airborne Energy Harvesting for Aircraft (ARENA) project carried out by the Power & Propulsion group at Delft University of Technology (TU Delft) and several commercial partners [5]. This program targets the conceptual and preliminary design of combined-cycle engines (CCEs) and combined-cycle auxiliary power units (CC-APUs) which utilize an organic Rankine cycle (ORC) power system to recover wasted thermal energy from the engine exhaust. In fact, the thermal energy lost in the hot exhaust gases accounts for over 50% of the fuel's chemical energy, thus even partial energy recovery has the potential to improve the engine's thermal efficiency, with an upper limit of the gains estimated at 15-20% [6]. ARENA seeks to extend the technical readiness level of ORC CCEs from 1 to 4, with a future research and development program envisioned in order to bring this technology to market.

As with any application in aerospace engineering, the weight of the system remains an important factor. In order to design the most optimal CCE for a particular application, tradeoffs must be assessed, and the weight and performance of the various alternatives must be determined to as high of a degree of accuracy as is reasonably possible. This thesis therefore deals with the weight estimation methodology (WEM) of the ARENA project, particularly with regard to the prime mover, or main gas turbine engine (i.e., not the added ORC system). Various component-level design methodologies were sought in scientific literature and then incorporated into the development of a preliminary engine design tool, whose primary objective is weight estimation. The outcome of this thesis is the compiled methodology and the actual design program, which is called 'Weight Estimation of Aeronautical Gas Turbine Engines,' or *WEST* for short.

Chapter 1 of this report presents the background information and motivation (Section 1.1), primary research aim and preliminary expectations (Sec. 1.2), and potential impact (Sec. 1.3) of this thesis. Chapter 2 describes the design methodology for the gas path of axial turbomachines, while Chapters 3 and 4 deal with the design methodologies, validation efforts, and sensitivity analyses of axial compressors and turbines, respectively, which represent the most complex subassemblies in gas turbine engines when viewed from the perspective of preliminary design. Chapter 5 addresses the design, validation, and sensitivity analysis of a complete engine model in WEST, and is then followed by a summary of all relevant project conclusions in Chapter 6. Chapter 7 finishes with a list of recommendations and next-steps for the further, future development of the WEST program.

1.1. MOTIVATION

This section follows the line of thinking which led to the formulation of this thesis and its primary research aim. The starting point is the ARENA project, whose background is presented in Section 1.1.1. The derived need for a suitable modelling and simulation environment (MSE) is later discussed (Section 1.1.2) and explains the requirement of further research efforts regarding weight estimation methodologies (Sec. 1.1.3).

1.1.1. ARENA PROJECT

The novelty and potential of combined-cycle aircraft engines – as are being investigated in the ARENA project, whether that be turbofan or turboshaft – have already been made apparent. The further development of such technologies has the potential to provide a significant step forward with regard to the efficiency of future aircraft and the sustainability of aviation. For this to be accomplished, however, significant challenges must be overcome. Within the ORC concept specifically, advanced design, analysis, and optimization methods must be developed for the ORC-turbine, as well as the progression of high-performance, compact heat exchanger (HEX) technology. Without a lightweight, efficient ORC waste heat recovery (WHR) system, the improvements in thermal efficiency will be eclipsed by the added weight, drag, and installation penalties, leading to a negligible or even non-existent improvement in overall aircraft performance. An exploratory study by de Servi et al. showed that retrofitting an existing engine with an ORC unit using supercritical CO2 as the working fluid had the potential to reduce the specific fuel consumption (SFC) by 2.8%, with an added weight penalty of approximately 3 tonnes per engine [7]. As is clear from this substantial weight penalty, this 'add-on' configuration has strong limitations – due mainly to nacelle spatial constraints and existing HEX technology [7] – thus the need to develop a CCE in which the ORC system is integrated even during the conceptual design stage is apparent.

Examining the cruise condition of flight for a fixed-wing aircraft using Equation 1.1 [8] (also known as the Breguet Range Equation) shows the coupling between efficiency, weight, and drag.

$$R = V \cdot \left(\frac{L}{D}\right) \cdot I_{sp} \cdot \ln\left(\frac{W_{il}}{W_{fl}}\right) \tag{1.1}$$

As shown in Equation 1.1, the range, R, is proportional to the specific impulse, I_{sp}, which is itself inversely proportional to the specific fuel consumption according to Equation 1.2 [9]. Thus, a reduction in SFC clearly produces an increase in expected range.

$$I_{sp} = \frac{1}{SFC \cdot g_o} \tag{1.2}$$

However, the initial weight (mass), W_{il}, and final weight W_{fl}, of the aircraft must also be considered. The fraction composed of these two terms on the right of Equation 1.1 can be expanded as shown in Equation 1.3, where W_a represents the total weight of the aircraft excluding fuel (i.e., the operating empty weight plus the payload) and W_{fuel} represents the usable fuel weight. In this equation, it becomes apparent that W_a is in the denominator, meaning that an increase in aircraft weight results in a decrease in range. This is intuitive, but it is beneficial to note the exact nature of the relationship between the terms and the expected range.

$$\frac{W_{il}}{W_{fl}} = \frac{W_a + W_{fuel}}{W_a} = 1 + \frac{W_{fuel}}{W_a} \tag{1.3}$$

Additionally, the introduction of new heat exchangers will also increase the drag, D, of the aircraft, which will act to further reduce the expected range according to Equation 1.1.

Obviously, the sensitivity of the cruise range of a fixed-wing aircraft with respect to SFC, W_a, and drag is different: range is inversely proportional to SFC and D, while its relationship to W_a is non-linear. Thus, investigation into a particular case study must be performed to obtain a more accurate assessment of the system-level impacts due to the introduction of an ORC WHR unit. Additionally, the actual magnitude of the increase in aircraft weight, drag, and engine thermal efficiency due to the incorporation of such a system is non-trivial; these cannot be determined with a simple, preliminary analysis, but instead require complete performance simulations of a particular case study and relatively-detailed, component-level design and weight estimation of the related configurations. Only then can representative values of SFC, W_a, and D be obtained, which then need to be coupled to other case-specific variables such as the lift, L, flight speed, V, and other variables listed in Equation 1.1 (or a related, higher-fidelity method of analyzing the mission profile).

One of the important research topics – or key questions – of the ARENA project can therefore be formulated as follows:

> What is a quantitative estimation of the improvement in thermal efficiency (i.e., reduction in SFC) and added weight for a combined-cycle aircraft gas turbine engine using an ORC exhaust gas WHR system compared to its single-cycle counterpart when both are optimized for the same application?

To comprehensively evaluate the effect of a combined-cycle engine on aircraft performance and efficiency, the drag and installation penalties need to be considered with an appropriate degree of accuracy. However, this research question provides a sufficient starting point, with the higher-fidelity analysis being something that can be investigated and answered in more depth in the future as the ARENA project progresses and more tools, knowledge, and experience become available.

Addressing such a question requires a suitable numerical setup, i.e., an appropriate modelling and simulation environment for the performance analysis of such engines. This therefore necessitates the following investigation with regard to MSEs:

> What is the most suitable modelling and simulation environment for the preliminary design (including weight estimation) and on/off-design performance analysis of a combined-cycle engine with an ORC WHR system?

Answering this sub-question is the focus of the next section.

1.1.2. MODELLING & SIMULATION ENVIRONMENTS

Modelling and simulation (M&S) marks an important discipline in the research and engineering fields dealing with the development of highly-complex aero engine technology. Thermodynamic cycle codes for gas turbines were introduced as early as the 1950s and since then have continuously evolved to ever-increasing levels of fidelity and utility [10].

Given the objectives of the ARENA project, the selected modelling and simulation environment (MSE) must be capable of on- and off-design performance analysis in steady-state conditions. Optimization will likely be performed accounting for multiple design points, as is the case in modern engine development. Steady-state simulations are sufficient for this purpose, with transient conditions being more critical with regard to controller design, which is not a concern at this stage of development. The MSE must be able to address engine design (including factors such as turbomachinery map scaling, bleed air mass flow calculation, and weight estimation), organic Rankine cycles (heat exchanger sizing, accurate equation of state for the thermodynamic property prediction of organic fluids, and radial turbines dealing with non-ideal compressible flows), and aircraft integration (effects of added weight and drag on flight performance, mission profile, and key performance indicators).

Additionally, it is not sufficient to design the prime mover (i.e., main engine) first and then study the ORC WHR system afterwards. If an existing engine were to be retrofitted, the combined-cycle would produce more power overall due to the energy recovered from the exhaust. This means that derating would be required in order to obtain the same net power output as the original design case. Accordingly, the engine would not be operating at its maximum efficiency, thus negating some of the efficiency gained by the addition of the ORC. It is therefore crucial that the full system is designed and optimized in a coupled way. This is essential if the technology is to provide a competitive option for future aviation applications. Furthermore, retrofitting may also yield higher installation penalties.

It may be that no individual tool can meet all of the main requirements, a likely but less-ideal scenario. In this case, multiple tools will be linked to construct a software framework with the required capabilities.

A broad survey of existing scientific literature reveals several software environments applicable to the modelling and simulation of aeronautical gas turbine engines. The most relevant[1] ones are summarized in Table 1.1. Here, the symbol 'X' is used to indicate fields for which the particular MSE offers functionality, and the symbol tilde (˜) is used where the capability is either limited or unclear. In depth discussions of each MSE will not be included here for the sake of brevity. Also note that these findings are based on what is discernible in literature; this table attempts to classify the programs as best as possible, although the ranges of functionality of the actual programs may vary. Only the practical use of the programs can reveal such details.

As is clear from Table 1.1, only a few MSEs are able to perform weight estimation, with even less featuring compatibility with ORC simulations. Only The Modelon Jet Propulsion Library (JPL) satisfies all the main

[1] Programs which are either rudimentary, outdated, discontinued, or are in-house codes of universities were excluded. The following discussions therefore deal with recognized, state-of-the-art simulation tools. Some of these are more prevalent in literature than others.

Table 1.1: Software environments applicable to the M&S of gas turbine aero engines.

	Performance Analysis					Prelim. Design			Other	
MSE	**Design Point**	**Off-Design**	**Steady-State**	**Transient**	**(Cycle) On-Design**	**Engine Sizing**	**Weight Estimation**	**Component Design**	**ORC Compatibility**	**Optimization**
NPSS	X	X	X	X					~	
WATE++						X	X			X[1]
pyCycle	X	X	X							X[2]
GTlab	X	X	X	X	X	X	X	X		X
PROOSIS	X	X	X	X	X				X[3]	X
GSP	X	X	X	X						
GTPsim	X	X	X	X	~					
GasTurb	X	X	X	X	X	X	X			X
EVA	X	X	X	X						
TURBOMATCH	X	X	X	X						
Modelon JPL	X	X	X	X	~		X		X[4]	

[1] Optimization of flowpath design with respect to weight or dimensions based on fixed thermodynamic cycle. Does not optimize the engine cycle itself.

[2] Provides analytical derivatives for efficient use in gradient-based optimization.

[3] With use of additional Aircraft System Simulation Toolkit.

[4] With use of additional Modelica libraries such as the Modelon Vapor Cycle Library, TU Delft in-house codes, or similar.

requirements (those being design point and off-design steady-state performance simulations, weight estimation, and ORC compatibility). Alternatively, the coupled use of different MSEs like NPSS and WATE++ could potentially satisfy the minimum range of functionality required. Since WATE++ is unavailable outside the United States [11], the only other means of performing weight estimations are GTlab and GasTurb. GTlab — which was developed by the German Aerospace Centre (DLR) -– is also inaccessible [12].

With only two weight estimation options remaining, the Modelon JPL and GasTurb, trial versions of both programs were obtained, and they were subsequently put to use in order to evaluate the software capabilities beyond what is evident in literature. Factors such as thermodynamic analysis, weight estimation results, and computational performance were all considered.

Overall, the Modelon JPL demonstrated a lack of suitability for the ARENA project. The convoluted code, long execution times, and lack of default values for mandatory variables make the program extremely difficult to use and understand. Modelon's own JT9D engine model provides weight estimation results which are demonstratively worse than those published/claimed by the company in 2019 [13], and completely inferior to those of WATE++ (see Appendix A.1 [13]). Additionally, negative component weights were often obtained, as well as trends which appeared to be nonphysical, such as component weights decreasing as engine size, mass flow, and power capacity increase.

The use of GasTurb was much more promising. Fast execution speeds mean that several hundred simulations are possible in a matter of only a few seconds. Built-in iteration and optimization methods are also included, making this program an extremely user-friendly and efficient means of gas turbine engine evaluation and design. Unfortunately, however, GasTurb can only be controlled manually via the user interface, and no application programming interface (API) exists nor is any in development, meaning there is no short-term solution to GasTurb's lack of automated, external controllability. The weight estimation results did show the correct trends (see Figure A.2), but were much lower than historical data compiled from of existing (turboshaft) engine designs (see Table A.2 [14]). It is possible to scale/correct the GasTurb weight estimation results to match the historical data more closely, but the problem with this approach is the fact that, with the application of arbitrary correction factors, all physical meaning of the GasTurb results is lost.

Thus, of the four MSEs which offer weight estimation functionality, two are inaccessible (e.g., WATE++,

GTlab), and two do not provide sufficiently accurate results (e.g., Modelon JPL, GasTurb). With no remaining alternatives, it was decided to focus the thesis project on the implementation of a turboshaft weight estimation method.

1.1.3. WEIGHT ESTIMATION METHODOLOGIES

The decoupling between MSE and WEM opens up new options for weight estimation, but also necessitates further investigation in literature with regard to what sort of tools are available and which ones may be suitable for the purposes of the ARENA project. Overall, three main categories of weight estimation methodologies were found; each one is discussed below. Table 1.2 summarizes the findings and presents advantages/disadvantages of each approach.

Table 1.2: Comparative summary of the three primary weight estimation approaches.

	Weight Estimation Methodology Type		
Attribute	**Historical**	**Component-Based**	**Hybrid**
Accuracy	Low (-)	High(est) (++)	High (+)
Computational Efficiency	High (++)	Low (-)	High (++)
Sensitivity to Key Design Choices (Num. of Inputs)	Low (-)	High (++)	Moderate (+)
Physical-Meaningfulness of Results	Low (-)	High (++)	Moderate (+)
Flexibility (to Model Novel Engines)	Low (-)	High (++)	High (++)
Development Speed	Fast (++)	Slow (-)	Slow(est) (-)

Among the simplest WEMs are single-equation models, in this case based on the regression of historical/statistical data. These offer results at a low computational cost since no preliminary engine design has to be performed. While this can be beneficial in cases where the weight is the only required output, attempting to model an entire engine using only a single equation can lead to accuracy limitations, not to mention an absence of physical meaning. Exact weight values can depend heavily on manufacturer, resulting in a large amount of scatter and therefore uncertainty. Additionally, basing the equations on historical data means the validity of extrapolating the results of these equations for analysis of future engines remains limited.

Lolis et al. [15] cites seven different whole-engine historical data-based models introduced between 1953 and 2012. These equations deal with turbofans and turbojets, with the exact inputs required varying depending on the model. Most commonly, the inputs include one or more of the following parameters: engine mass flow, thrust, bypass ratio and/or fan diameter (in the case of turbofans), overall pressure ratio, and engine thrust [15]. The accuracy of these models ranged from ±25% to ±50%, with more inputs to the equation not necessarily corresponding to improved accuracy. One of the methods with the best accuracy is that proposed by Torenbeek [16]. However, such historically-driven equations do not yet exist for turboshaft engines.

A higher-fidelity approach to weight estimation is to decompose the engine into individual components and subassemblies. The weight of each component can then be estimated using a variety of methods, and the total summation then taken as the full-engine weight.

The exact strategy and fidelity for estimating individual component weights can vary greatly. Onat and Klees proposed in 1979 historically-driven correlations – similar to what was discussed previously – but on an individual part basis [17]. This method has been modified and expanded over the decades since its release and, with the introduction of detailed component design modules such as that for disks presented by Tong et al. [18], has evolved into what is now known as WATE++, with an approximate accuracy of ±10% [19]. In the end, a combination of strategies is the most likely: detailed design of components for which this is possible (e.g., blades, disks, casings), and correlations for those that have a less-direct link to the thermodynamic performance and gas path design (e.g., mounting frames, controls units, other accessories). The detailed design of components offer a clearer link between results and physical reality and are therefore expected to yield higher accuracy. Other component-based design methods include DLR's GTlab [20] and Cranfield University's ATLAS [21].

Overall, the use of component-based methods drastically increases the flexibility of the methodology. While the initial development can (and should) be validated using existing engines, the same procedures can then be used to develop novel engine configurations and architectures, supplying realistic, physically-based solutions as the result, even for engines which do not yet exist and do not have a historical equivalent or closely-related counterpart. These methods are therefore applicable both to studies of existing engines and to evaluations of future types and technologies.

The physical meaningfulness and expanded applicability of such an approach does not come without limitations, however. With preliminary design being performed for a wide range of components, the computation cost and execution times increase dramatically over single-equation models. In WATE++ and ATLAS, for example, every disk in the machine is designed according to its own weight and stress reduction optimization scheme, which drastically increases the time required to retrieve the weight estimation of a single engine, making such an approach unsuitable for integration within aircraft system-level performance and optimization studies. GasTurb is able to execute hundreds of designs in a matter of seconds, meaning a more simplified disk design approach must have been taken in this program.

Some of the conclusions drawn by Lolis et al. [15] can be summarized as follows: that single-equation methods have unacceptably low accuracy, and component-based methods have unacceptably high computational cost. The former of these conclusions led to the development of ATLAS at Cranfield University – an engine preliminary design tool mentioned previously – and the latter to what Lolis describes as a 'hybrid' method. Similar to the methods already discussed, single-equation models can be developed based on the results of component-based models instead of historical data. This allows component-based models to be developed for novel engine configurations and architectures, enabling the weight estimation for new, nonexistent engines. These component-based models can then be used to design numerous engines with varying key input parameters (e.g., overall pressure ratio (OPR), turbine inlet temperature (TIT), bypass ratio (BPR), power, etc.), creating a new result set. Statistical regression can then be used on these result sets, yielding single-equation, surrogate models (with one or more inputs) based on component-level full-engine design tools. This approach has been seen elsewhere as well, for example several studies performed by NASA [22, 23].

For turbofans, Greitzer et al. [22] developed WATE++ models for a variety of modern, high bypass ratio engines, validated these using the real engine data, and then varied the core mass flow, BPR, and OPR to obtain a large result set of yet-nonexistent engine designs. Regression equations were then developed based on this result set. Greitzer et al. presents four sets of equations in total: those for current and advanced level of technologies for both direct drive and geared turbofans [22].

A similar approach is taken by Snyder and Tong [23] for turboshaft engines used in studies relating to NASA's AMRD's Revolutionary Vertical Lift Technology project. Here, WATE++ models are developed for turboshaft engines with power capacities ranging from 485 kW to 5.6 MW divided into small, mid, and large classes. The results of these models were then used to develop two weight estimation equations, one assuming a current level of technology, and the other an advanced level of technology. Unfortunately, the only input to these equations is power output, with consideration for level of technology, meaning weight trends with respect to parameters such as OPR or TIT are not captured, unlike the equations proposed by Greitzer et al. [22] for turbofans, which accounted for core mass flow, OPR, and BPR.

One disadvantage of the hybrid approach is that the component-based models are likely to have some level of error themselves, and the simplified regression equations have error compounded onto this. In the Greitzer et al. study, the error between the WATE++ results and the proposed equations was ±10% [22]. This is reasonable, however, especially given the massively reduced computational cost of a single-equation model compared to a complete engine design. For aircraft system-level optimization studies, this is likely the preferred approach: even if the magnitudes are off by ±10%, it may be that the trends are still captured to a good degree of accuracy.

1.2. RESEARCH AIM

Historically-based single-equation weight estimation models do not provide the necessary accuracy, sensitivity, nor flexibility required for the purposes of the ARENA project. Component-based design methods do, but at a computational cost which is too high for integration into aircraft-level system design and airframe integration optimization studies. Thus, component-based single-equation (hybrid/surrogate) are the only category of weight estimation methodology suitable for the ARENA project. However, with no such tool presently available, at least not one which meets the accuracy requirements, a new component-based preliminary engine design and weight estimation tool must be developed. This tool can be used to generate the weight estimation for novel architectures and turboshaft engines necessary in generating the statistical regression equations according to the hybrid method discussed earlier, which can then be used in optimization studies.

Thus, the development of such a program provides a necessary piece of the puzzle with regard to combined-cycle engine design and research. Improvements in thermodynamic performance and reduction in SFC – outcomes of the modelling and simulation branch of the ARENA project – cannot be correlated to any increase in aircraft range and efficiency without accurate weight estimations of the systems being studied. The

tool-to-be-developed should be capable of reproducing existing engine designs (for validation purposes) but should also be usable in generating new designs, a key objective of the ARENA project. The progression of the ARENA project and similar research campaigns is therefore dependent on such a program, showing its relevance and its potential to impact the future development of more efficient, combined-cycle engines.

A thesis research aim can therefore be formulated as follows:

> To develop the knowledge [and a tool] to perform the preliminary sizing of aeronautical gas turbine engines and predict the trend of weight with respect to power capacity and design parameters such as turbine inlet temperature (TIT), overall pressure ratio (OPR), mass flow rate, number of stages, and choice of turbomachinery configuration (axial, radial, mixed, etc.).

Achieving realistic component designs is an essential factor influencing the success of the proposed tool, since it follows that a realistic design will also lead to a realistic weight estimation for that same part, and then cumulatively for the engine as a whole. It can be beneficial at this stage to lay out what are reasonable expectations for the new weight estimation tool with regard to its potential to (accurately) model and predict the weight of gas turbine engines.

The WATE++ program seeks to be within ±10% of an actual engine weight [19]. Since this is used as a benchmark by many other weight estimation codes and has been developed over several decades with access to a large amount of real engine data and design knowledge, ±10% accuracy would appear to be an upper limit for the expectations for the WEST program being designed as part of this thesis. It is likely that such a range will not be achievable given the much more limited experience and engine data available in this study compared to that which can be accessed by NASA, the developer of WATE++.

GasTurb models components worth only about 60% of the total engine weight [24], so about 40% of the weight of the engine is not accounted for. This may represent a more reasonable underestimation limit for the accuracy obtainable by a new WEM. Thus, accuracy could be expected within the range of +10% to -40% of an actual engine weight. However, it helps also to analyze this hypothesis in slightly more detail.

For example, a study by Greizter et al. [22] lists WATE++ results for seven different turbofan engines, including detailed weight breakdowns by subassembly and component type. If the entire fan module is excluded from these results in order to evaluate the gas generator portion only, the various component types can be compared to the total (remaining) weight to get a quantitative assessment of the relative weight.The results are summarized in Table 1.3 and listed in descending order.

Table 1.3: Average relative weight by component type for the gas generators of seven turbofan engines.

Component Type	**Rel. Weight**
Accessories	21.0%
Disks	19.3%
Other	14.4%
Blades	13.7%
Casings	9.0%
Frames	7.6%
Shafts	6.7%
Burner	6.5%
Ducts	1.7%
Total	**100.0%**

Figure 1.1 provides a generic breakdown of the components and subassemblies found in a typical turboshaft engine. The colour-coding is based on the level of fidelity of the available preliminary design method(s) for that component type, as found in scientific literature. These methodologies are discussed more in depth in Chapters 3 through 5.

As is evident in Table 1.3, different component types have varying degrees of influence on the total engine or gas generator weight. The heaviest type is accessories, for which the WEM found in literature is only an empirical correlation (as will be discussed in Section 5.1.4). The category of 'other' has no WEM at all, meaning the 14.4% (on-average) fraction of engine weight which falls under this category is left entirely unmodelled. An underprediction of actual engine weight is therefore generally expected. Disks and blades are the second- and fourth-heaviest component types, respectively, which is positive since it is these components for which

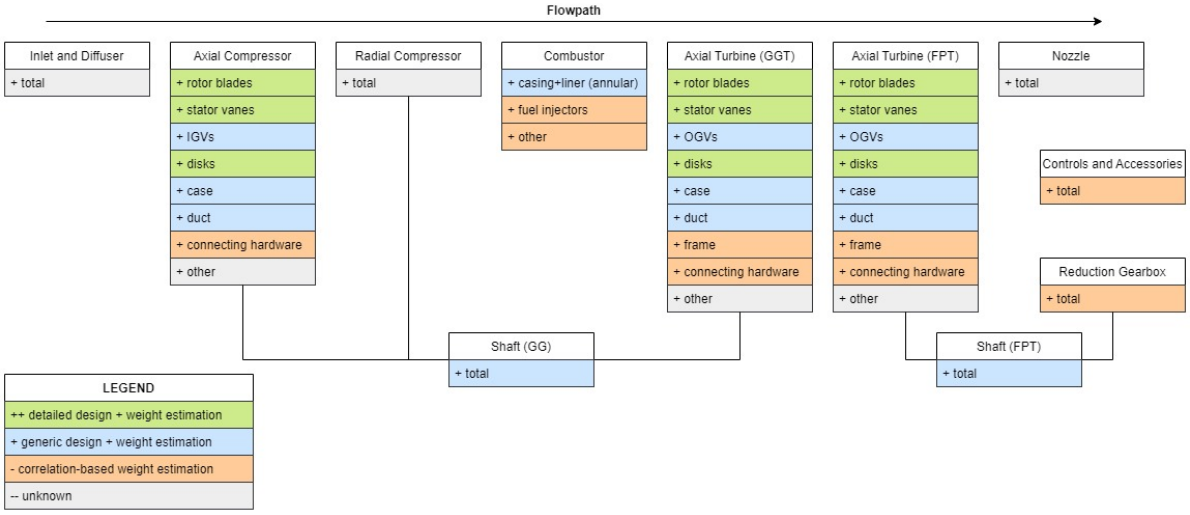

Figure 1.1: Breakdown of a turboshaft engine by subassembly and component type.

the most detailed design methodologies exist (as shown in Figure 1.1 and described in Chapters 3 and 4). Most of the remaining, lighter components can be estimated using generic design methods.

With the relative weights listed in Table 1.3, a rough analysis can be performed on the expected accuracy of the new program. If, for example, components with detailed design methodologies (blades and disks) are (arbitrarily) assumed to have an expected accuracy of ±10%, those with generic design methodologies (casings, shafts, burner, and ducts) an expected accuracy of ±25%, and those with correlation-based WEMs (accessories and frames) an expected accuracy of ±40%, and 'other' not modelled, then lower limit of expected accuracy range is 64.8% of the total engine weight and upper limit of 106.2%. This corresponds to +6.2% and -35.2%, which is fairly consistent with the +10% and -40% discussed earlier, as was expected based on literature describing WATE++ and GasTurb.

Even if such accuracy wasn't obtained, this would still be a scientific finding in itself and a valid conclusion of the project. It may be that the newly-developed tool does not meet the accuracy requirements of the ARENA project and related studies, but it is important to find this out instead of using existing programs which are guaranteed not to. Additionally, further/future development of the program may lead to improved accuracy. WATE++ was developed over several decades, and so once more experience is gained by researchers at the TU Delft and when more engine data becomes publicly available in the future, the WEST program may continue to be refined, leading to an ever-bettering of the results.

1.3. IMPACT

The applicability of the envisaged weight estimation method is not only limited to combined-cycle engines. A component-based WEM has the potential to influence and impact any research campaign which involves the design of turbofan and/or turboshaft engines and for which weight of the engine is an important factor. For higher-fidelity designs which account for the couplings between the numerous subsystems present in a single aircraft, the importance of accurate engine weight estimation and design is no longer reserved for propulsive system analysis only, but affects a much wider range of aircraft-level performance and efficiency studies. But how impactful would such a tool be, and is it necessary? The following sections address some current trends in aeronautical engineering research and explore the potential impact of the WEST program, not only within the research projects taking place at the TU Delft (e.g., ARENA), but also as an open-source tool which could be made available to researchers around the globe.

The WEST tool is useful for the design of turbofan and turboshaft engines, both of which are relevant in the ARENA project since CCEs and CC-APUs are to be studied. However, turboshafts are of particular importance for several applications. First, because of their upcoming relevance in various areas of aviation research, such as hybrid-electric propulsion, more-electric aircraft, and urban air mobility, and second, because of the limited amount of related scientific research studies. The literature related to the design and weight estimation of turbofans is far more extensive than that of turboshafts, and methods like regression equations – such as those developed by Greitzer et al. [22] – do not exist for turboshafts. Such equations, which estimate engine

weight with a good degree of accuracy while accounting for sensitivity to factors such as core mass flow, OPR, and BPR, can only be developed for turboshafts (excluding the BPR, of course, but possibly accounting for other high-level design variables such as TIT) once a validated, component-based turboshaft design tool has been established.

Section 1.1.1 has already addressed combined-cycle engines and auxiliary power units being researched in the ARENA project, thus this discussion will not be repeated here. It is useful to note, however, the potential of this novel engine architecture to increase the efficiency of future power units and therefore improve the sustainability in aviation, and the importance of a suitable weight estimation methodology in furthering this research and making such technologies a reality.

One trend in aeronautical engineering research is the tendency towards more-electric aircraft and hybrid-electric propulsion (HEP). de Vries et al. defines HEP as any concept in which electrical energy is used either to generate or transmit the power (either in whole or in part) required for propulsion [25], thus a wide spectrum of potential architectures exist. Jansen et al. [26] identifies three electrified aircraft propulsion configurations: partially turboelectric, fully turboelectric, and hybrid-electric. However, hybrid-electric can itself be split into series, parallel, or series/parallel subcategories [27], and fuel cells may be added to any of the aforementioned configurations – as was proposed in Boeing's Subsonic Ultra Green Aircraft Research Freeze concept [26] – to further expand the range of possible architectures. Since the goals of such investigations are typically the reduction of noise, emissions (i.e., improvement of efficiency), and/or operating costs [25], few bounds are placed on the initial concepts, yielding a very open-ended problem with a long and widely-varied list of potential solutions.

Among all HEP concepts, turboelectric configurations are quite prevalent: NASA's N3-X [28], the ECO-150 [29], and ONERA's DRAGON [30] are all examples of projects which feature turboshaft engines for power generation. The relevance of turboshafts in future hybrid-electric aircraft powertrains is therefore apparent, meaning that a turboshaft weight estimation tool – one which is able to correctly assess the weight trends with varying levels of power capacity and hybridization – could be an invaluable asset in furthering the research that has been introduced in these studies and others.

One of the main applications of – and closely linked to – hybrid-electric propulsion is the concept of more-electric aircraft. While HEP is a subset of MEA dealing with the electrification and hybridization of the power generation system, MEA can be understood from a full propulsion- and system-level context as well. For the purposes of this discussion, HEP will refer to strategies of improving the powertrain efficiency, and MEA will deal with strategies of improving the aeropropulsive efficiency of the aircraft. The former can deal with factors such as engine and/or power transmission and conversion efficiencies, the latter dealing with the lift-to-drag or thrust-to-power ratios of the propulsive devices [25].

Taking MEA beyond the power system alone results in full aircraft-level configuration changes, such as the introduction of concepts like distributed propulsion [30], boundary layer ingestion [28], tip-mounted propulsion [31], and propulsive fuselage [32, 33]. Such technologies require airframe-level changes and integration studies, and while technologies such as boundary layer ingestion and propulsive fuselage do not necessarily require hybridization of the powertrain, hybridization can still be beneficial. Concepts such as distributed and tip-mounted propulsion are especially aided by HEP due to the flexibility to, for example, implement a large number of propulsors at nearly any location on the aircraft, since these can be powered by electric motors. Thus, the emergence of turboelectric powertrains has enabled a much wider range of aircraft concepts to be investigated, ones which may not have been possible (or nearly as feasible) several decades ago with gas turbine engines alone.

The three HEP projects using turboshafts mentioned previously [28–30] are implementations of the concept of distributed propulsion. Each of these projects require varying level of development of the associated technologies, with the ECO-150 and DRAGON concepts envisioning introduction dates around 2035 [29, 30], and the N3-X providing an even larger improvement in aircraft efficiency but with an introduction date targeted around 2045 [26, 28].

The development and accurate assessment of the viability of MEA concepts requires analysis not only of the propulsion subsystem, but of the full aircraft and system-integration levels as well. When this is the case, the weight of the proposed engine architecture becomes a very important factor, thus a tool which can accurately estimate the weight of a variety of turboshaft engines is needed in most of these projects if they are to continue further. The potential impact of the development of such a tool is therefore apparent for a wide range of up-and-coming research projects in aviation. System-level optimization studies would also benefit from the much more computationally-efficient component-based single-equation weight estimation models that are a potential outcome of the development of a novel, component-based turboshaft design tool.

In contrast to the above-mentioned aircraft trends, implementation of MEA does not always have to involve large-scale architecture changes. For example, the environmental control systems of commercial aircraft often employ air cycle machines. These are operated using bleed air from the prime movers; they have low efficiencies, but make up for this with their light weight. One possibility is to replace air cycle machines with vapour compression cycles, a thermodynamic cycle with a higher coefficient of performance, but more components and higher weight. The compressor used in the vapour compression cycles would likely need to be electrically-powered, and such power could be drawn from the APU, for example. However, changing the environmental control system from being powered using compressed air to electricity generated by the APU may result in a further reduction in efficiency because the main engines are quite efficient already due to the high level of design refinement and the effect of ram compression, whereas APUs have not experienced the same level of development as turbofans. Thus, if the environmental control systems or any other onboard system becomes electrically-powered as part of the trend towards MEA, more power demand may be placed on the APU, meaning that the efficiency of the APU should be improved simultaneously to ensure the viability of the electrification of such systems. The ARENA project seeks to address this dilemma using a combined-cycle approach, but in general it is important to note that, before the full propulsion system becomes electrically-driven, smaller systems may transition first, creating the need for APUs with improved performance. Since auxiliary power units are turboshaft engines, the relevance of a turboshaft design tool for MEA research becomes all the more evident.

Another field of growing relevance for turboshaft engines is vertical takeoff and landing and urban air mobility. Researchers at NASA have sought to revolutionize vertical lift technology through the introduction of large, civil tiltrotor vehicle platforms [23, 34]. Such vehicles rely heavily on turboshaft engines, either in direct-drive or turboelectric configurations. The use of a large number of propellers suits a turboelectric configuration well, but in general the limitations of the power density of current battery technology necessitates the use of onboard (turboshaft) engines for power generation, especially when designed for larger payloads or extended ranges. The same is true for urban air mobility, for which several research projects and industrial design efforts have been targeted [35, 36], with numerous potential configurations having been proposed. In each of these examples, it is the use of turboshaft engines which make such concepts possible, and since many of these investigations are still in a conceptual phase, the availability of a turboshaft weight estimation tool could prove beneficial.

As discussed in the preceding paragraphs, the range of potential use cases for turboshaft engines within the aviation industry is growing, and in order to provide continual technological advancements for these areas of research, an engine preliminary design tool is required. This is necessary not only for the analysis of weight trends of the engine itself, but also for inclusion in multidisciplinary, system-level aircraft performance studies. The development of such a tool holds particular relevance for applications involving turboshafts, as previously discussed, since no such tool yet exists; however, even for turbofan engines (for which similar programs do already exist) the relevance remains high. As investigated in the preceding chapters, existing tools are either unavailable (i.e., inaccessible (WATE++, GTlab)) or unsuitable (i.e., do not provide a sufficient level of accuracy (Modelon JPL) or autonomy (GasTurb)).

Therefore, by making the new weight estimation tool open-source, the potential impact of such a development effort increases greatly. With so many tools already existing but remaining inaccessible, aerospace researchers are left to either use lower-fidelity methods or to develop their own component-based models, as is the case with this thesis. This limits either the quality of specific research being performed or delays the production of useful results due to the longer development and analysis times. Making WEST open-source gives smaller-scale public and private researchers alike access to a tool which meets a need that has not yet currently been met, and does so at no cost to themselves. The aim of this more widespread adoption broadens its usefulness from the context of TU Delft alone to any research projects with a similar need and which do not already have direct access to such a preliminary design and weight estimation tool. Python represents a viable development platform due to its free availability, widespread use within the scientific community, and compatibility with many software APIs.

Ideally, the tool would include as many informed default values as possible, making preliminary design and weight estimations accessible for both beginner users and designers, with further refinement achievable depending on the level of user experience and technical knowledge. This keeps the tool as accessible and widely-usable as possible, without forcing the user to make uninformed design decisions. It should also include gas path synthesis, enabling novel engines to be developed, instead of limiting analysis to the recreation of existing engines alone. All of these considerations contribute to extending the potential impact of this thesis.

1.4. SUMMARY

- Increasing economic, legislative, and environmental considerations have heightened the need for aircraft with reduced fuel consumption, leading to the exploration of novel engine architectures – such as the combined-cycle engine proposed in the ARENA project – with the aim of improving efficiency. This particular architecture uses a secondary thermodynamic cycle – a Rankine cycle using an organic working fluid – to recover wasted thermal energy from the exhaust gases of the main power unit.

- While improving efficiency is the primary goal of the combined-cycle engine concept, weight remains a critical component in aerospace engineering systems, meaning that the weight of such engines has the potential to make or break the ARENA project with regard to its real-life plausibility. Of the four modelling and simulation environments which offer weight estimation functionality, WATE++ (used in combination with NPSS) and GTlab are inaccessible, and the Modelon Jet Propulsion Library and GasTurb do not offer results with sufficient accuracy. The lack of appropriate weight estimation options motivates the need for further research into weight estimation methodologies.

- Of the various weight estimation methodologies, single-equation models do not offer the necessary accuracy for the purposes of the ARENA project, nor the sensitivity to more than just a few of the key engine design parameters, nor the flexibility to predict weight of novel engine architectures. Component-based preliminary engine design tools have the potential to offer the necessary accuracy, sensitivity, and flexibility, but at a significant computational cost. Several studies have used a method hybridizing the two, using component-based tools to design novel engines and then combining these with statistical regression to develop single-equation, surrogate models. These models offer lower accuracy than the initial component-based designs, but at a significantly lower computation cost, enabling them to be used in aircraft-level performance and optimization studies.

- Stemming from the lack of public/commercial availability of suitable component-based engine design tools, the present thesis focuses on preliminary engine design for the purposes of weight estimation. A new, component-based design tool was therefore developed. Overall, it was expected that the tool will capture between 60 and 110% of the actual weight of an engine. In general, underprediction is expected.

- Of the theoretical framework which was used to construct the new weight estimation tool, blades and disks have the most advanced design methods. Casings, ducts, shafts, and combustors all offer meaningful but somewhat more generic design methods, with the weight of frames, hardware, and accessories all being estimated using empirical correlations.

- A new turboshaft preliminary design and weight estimation tool has the potential to provide valuable assistance with respect to ongoing research in the field of aeronautical engineering. Current design trends include combined-cycle engines, hybrid-electric propulsion, more-electric aircraft, and urban air mobility, all of which require engine sizing for the development of meaningful results. Turboshaft engines are of particular relevance in each of these fields. Keeping the newly-developed tool open-source ensures that it is accessible to as wide of a range of researchers as possible, increasing its potential impact within the larger scientific community.

2

GAS PATH

Gas turbine engines operate on the thermodynamic *Brayton* cycle. In order to produce work and power, they require a (gaseous) working fluid, which passes through a full-engine-length region known as the *gas path*. While the gas path (also known as the 'flow path' or 'meridional channel') is not actually a physical component of the engine in and of itself, its layout influences the design of – and defines the geometrical restrictions applied to – the blades, disks, and casing. A sensible gas path design is therefore the fundamental first step in preparing for the subsequent component-level design of an axial turbomachine. The synthesis of the gas path is also closely linked to the meanline thermodynamic performance of the same machine, meaning that together these set the stage for the preliminary assembly-level (e.g., compressor or turbine) and engine-level (e.g., core/gas-generator) designs.

The objective of this chapter is to supplement the axial compressor design methodology discussed later in Chapter 3. Here, the gas path design methodology for a single axial compressor is described , which can then be used as a starting point for the subsequent 3D mechanical design of the compressor components outlined in Section 3.1. Differences exist between the methodologies used for the gas paths of axial compressors and turbines; the differences for turbines are discussed in its respective chapter in Section 4.1.1.

2.1. DESIGN METHODOLOGY

In this section, the design of the gas path for a single axial compressor will be addressed. By approaching the gas path design of each turbomachine individually, the problem is simplified, and several of these assemblies can then be combined to form, for example, the core of a turbofan engine (e.g., low-pressure compressor (LPC), high-pressure compressor (HPC), high-pressure turbine (HPT), and low-pressure turbine (LPT)). Section 2.1.1 begins with the meanline performance analysis, which includes the radial dimensions associated with the gas path design, i.e., the mean radii and local blade heights, which also define the local hub and tip radii. This is followed by design in the streamwise (or axial) direction in Section 2.1.2, which defines the 2D shape of the blades when viewed in the axial/radial plane.

2.1.1. MEANLINE PERFORMANCE AND RADIAL DIMENSIONS

Figure 2.1 shows a simplified, two-dimensional side view of a gas path cross-section. Here, rotor and stator blades are seen in succession, forming a multi-stage compressor. Note how the cross-sectional area (and thus the blade height, b) decreases along the flow path from left to right as the working fluid is compressed. The tip, mean, and hub radii are shown: this particular machine has a fixed (or constant) hub radius, although machines with constant mean or tip radii are also possible. The station numbering of Stage 2 is indicated: Station 1 corresponds to the rotor inlet, Station 2 to the rotor outlet / stator inlet, and Station 3 to the stator outlet. The outlet station of a particular row or stage corresponds to the inlet station of the next. Finally, the location and meaning of row and stage gaps are indicated; row gaps refer to the spacing between two rows in the same stage, and stage gaps refer to the spacing between two rows of adjoining stages.

In gas turbine design, the stator vanes are attached to the non-rotating casing, while rotor blades are attached to the rotating hub. Thus, the roots of rotor blades occurs at the hub, and their tips at the casing, while the opposite is true for stator vanes. Each rotor blade has a root, which is contained in the disk corresponding to that row. The disks are connected via hardware to transmit torque throughout the hub.

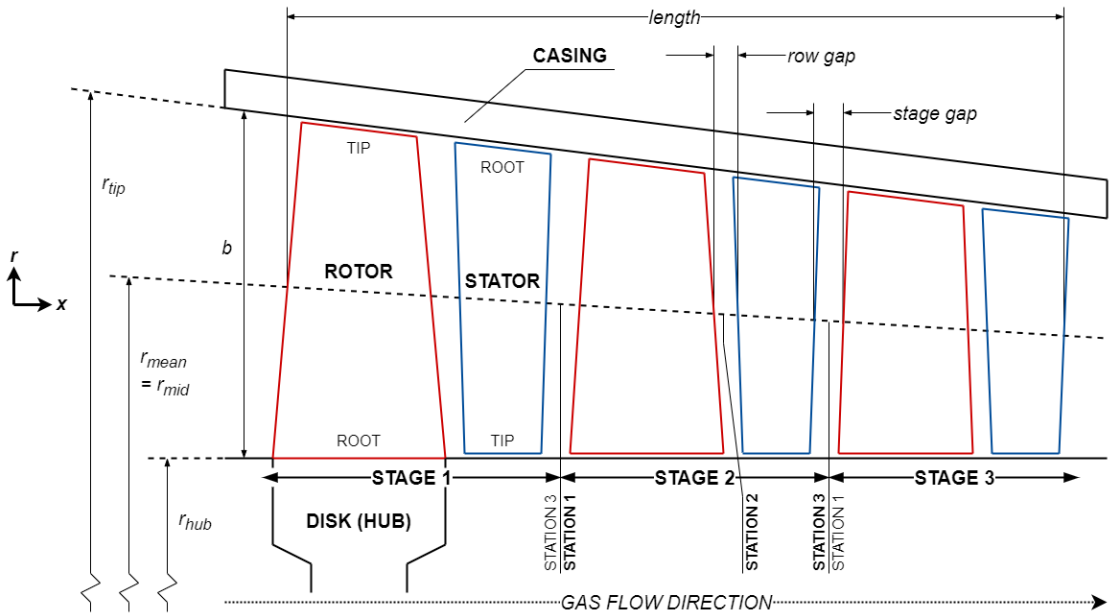

Figure 2.1: Simplified visualization of a multi-stage axial compressor gas path.

2.1.1.1. REQUIRED INPUTS

Table 2.1 shows the inputs required to perform meanline analysis of a single axial compressor. The only value not listed here is either the total-to-total isentropic or polytropic efficiency (η_{tt} and η_{pt}, respectively), one of which is required but will be assumed based on the prescribed duty coefficients, as will be discussed shortly.

Table 2.1: Required inputs for meanline analysis and preliminary gas path design of axial compressors.

Category	#	Input Parameter	Symbol	Units
Performance	1	Mass Flow Rate	$\dot{m}$	kg/s
	2	Pressure Ratio	PR	-
	3	Rotational Speed	N	RPM
	4	Inlet Total Pressure	$P_{t,in}$	bar
	5	Inlet Total Temperature	$T_{t,in}$	K
Duty Coefficients	6	Flow Coefficient	ϕ	-
	7	Work Coefficient	ψ	-
	8	Degree of Reaction	R	-
Working Fluid	9	Specific Gas Constant	R_g	J/kg·K
	10	Specific Heat Capacity[1]	c_p	J/kg·K
	11	Ratio of Specific Heats	γ	-
Design	12	Number of Stages[2]	n_{stg}	-
	13	Annulus Type[3]		

[1] At constant pressure. [2] Optional. [3] Fixed hub, mid, or tip diameter.

The first five input parameters relate to the thermodynamic performance of the machine. The *duty coefficients* – the flow coefficient (ϕ), work coefficient (ψ), and degree of reaction (R), which are defined in Equations 2.1 through 2.3, respectively – give the user control over the design and relative performance of the machine. Only one value is specified for each of these coefficients since the assumption of repeated stages is made, i.e., every stage has the same duty coefficients.

$$\phi = \frac{V_m}{U} \tag{2.1}$$

$$\psi = \frac{w}{U^2} \tag{2.2}$$

$$R = \frac{\Delta h_{s,rotor}}{w} \tag{2.3}$$

The working fluid in this case requires only two inputs, although three are listed in Table 2.1. This is because the working fluid is modelled as a *calorically-perfect gas*, thus the three properties are related though the following relationship, meaning only two are needed to define the full set:

$$\gamma = \frac{1}{1 - \left(R_g / c_p\right)} \tag{2.4}$$

This simplifying assumption, which means that all the properties of the working fluid are independent of temperature, is done for the sake of simplicity, as well as to expedite the program's development time and reduce computational cost. It is recommended to reevaluate this assumption in the future by reviewing both the potential improvements in accuracy and increased computational cost of other working fluid models – for example, a model which takes into account the temperature-dependence of the specific heat capacity, c_p (i.e., a thermally-perfect gas model, as is used in GTlab [37]), and/or the impact of varying flow composition (i.e., fuel-to-air ratio) on R_g and c_p – to determine if the program would benefit from a different model.

Typical values for the duty coefficients and working fluid parameters (i.e., fields 6 through 11 of Table 2.1) of an axial compressor are shown in Table 2.2 [38–40]. Note that the working fluid is assumed to be dry air, and the value of γ is shown for reference only, since it can be calculated using Equation 2.4.

Table 2.2: Typical ranges/values for axial compressor duty coefficients and (dry air) working fluid properties [38–40].

Parameter	Units	Range/Value
ϕ	-	0.4 - 1.1
ψ	-	0.3 - 0.6
R	-	0.5 - 0.9
R_g	J/kg·K	287
c_p	J/kg·K	1000
γ	-	(1.40)

The last design parameters listed in Table 2.1 can be specified by the user in order to influence the machine design. The number of stages is optional since the program will select an appropriate number if none is otherwise present. The annulus type is specified by fixing either the hub ("H"), mid ("M"), or tip ("T") diameter of the machine, thus affecting its shape and general appearance. Choosing one of these diameters to be constant across the entire flow path is important as it affects the distribution of work across the stages and the overall weight of the machine. The sensitivity of weight to this parameter will be discussed in Section 3.3.

Differences in Present Approach One of the most fundamental differences between the meanline methodology presented here and those of programs such as ATLAS (developed at Cranfield University [21]) and GTlab (developed by the DLR [20]) is the way in which the geometry is defined. In other programs, the user has more direct control over the geometry, allowing them to specify either the hub, mid, or tip diameter, or the hub-to-tip ratio at the inlet, which also necessitates the inlet Mach number, inlet flow angle, and an estimate of either the polytropic or isentropic efficiency as additional inputs. In the present methodology, however, the three duty coefficients are used as inputs instead since these have a direct influence on the machine's performance, not geometry. This means that, with the aid of *Smith charts* or equivalent relationships available in literature, the polytropic efficiency of each stage can be estimated automatically based on the duty coefficients, eliminating the need for this as an input. They also fully define the velocity triangles at each stage, eliminating the need for the inlet flow angle and Mach number as inputs. If needed, one of the aforementioned diameter values can be obtained by choosing the corresponding rotational speed.

Furthermore, this program aims to enable the weight estimation not only of existing engines, but new and even novel engine designs and configurations as well, thus starting from performance parameters such as the duty coefficients and not the geometry of a specific example is preferred. That said, in some occasions – such as validation cases – recreating existing engines is desirable, and a function has been built into the program such that the user can specify the outer radius and total length of a specific compressor or turbine, and the program will then optimize the duty coefficients to obtain the corresponding geometry. Such functionality allows the user to accurately manipulate the geometry despite the somewhat obscured relationship between duty coefficients and machine dimensions.

Unit Conversions Before calculations commence, it is important to ensure that all values are present in relevant and consistent units. In this case, the rotational speed, N – specified in RPM – should be converted to angular velocity, ω, with units of radians per second (rad/s). The total pressure at the inlet can be converted from bar to the SI unit of Pascals.

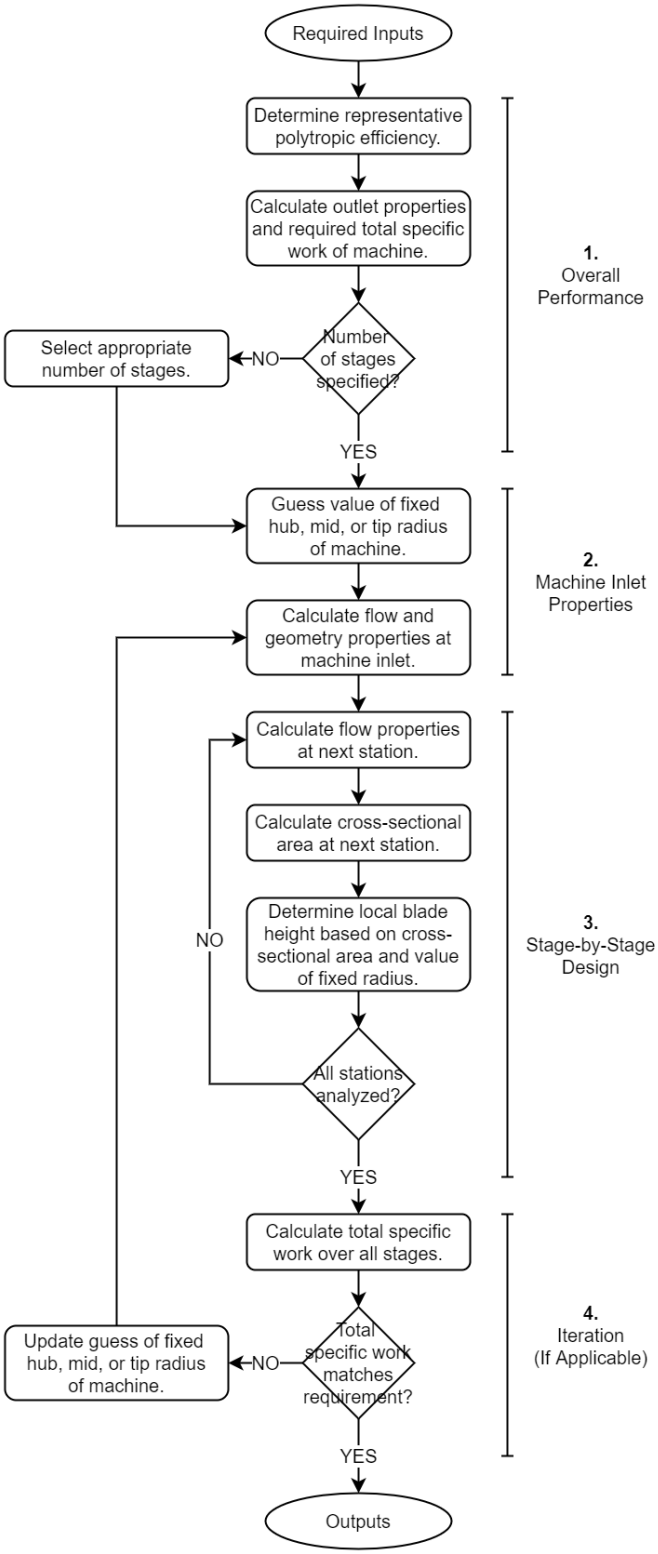

Figure 2.2: Flow chart describing the meanline analysis and preliminary gas path design procedure.

2.1.1.2. OVERALL PERFORMANCE

An overview of the procedure for analyzing meanline performance and designing the radial dimensions of the gas path is shown in Figure 2.2. As shown in this figure, the first step in evaluating compressor performance is to obtain an estimate of the polytropic efficiency. Instead of requiring this as an input from the user, this value can be predicted based on the specified duty coefficients since, as previously discussed, duty coefficients have a direct link with machine performance. Figure 2.3 shows equivalent Smith charts for axial compressors assuming well-designed, repeated stages; these were originally proposed by Casey and reproduced by Lewis [39, 41]. Each chart requires the flow and work coefficient as input, is valid for a fixed degree of reaction (either 0.5, 0.7, or 0.9), and provides the polytropic efficiency, η_{pt}, of a single stage as output. Interpolation can be used to retrieve an estimation of efficiency for degrees of reaction lying between those values listed. The original figures were digitized and then implemented into the meanline calculation procedure.

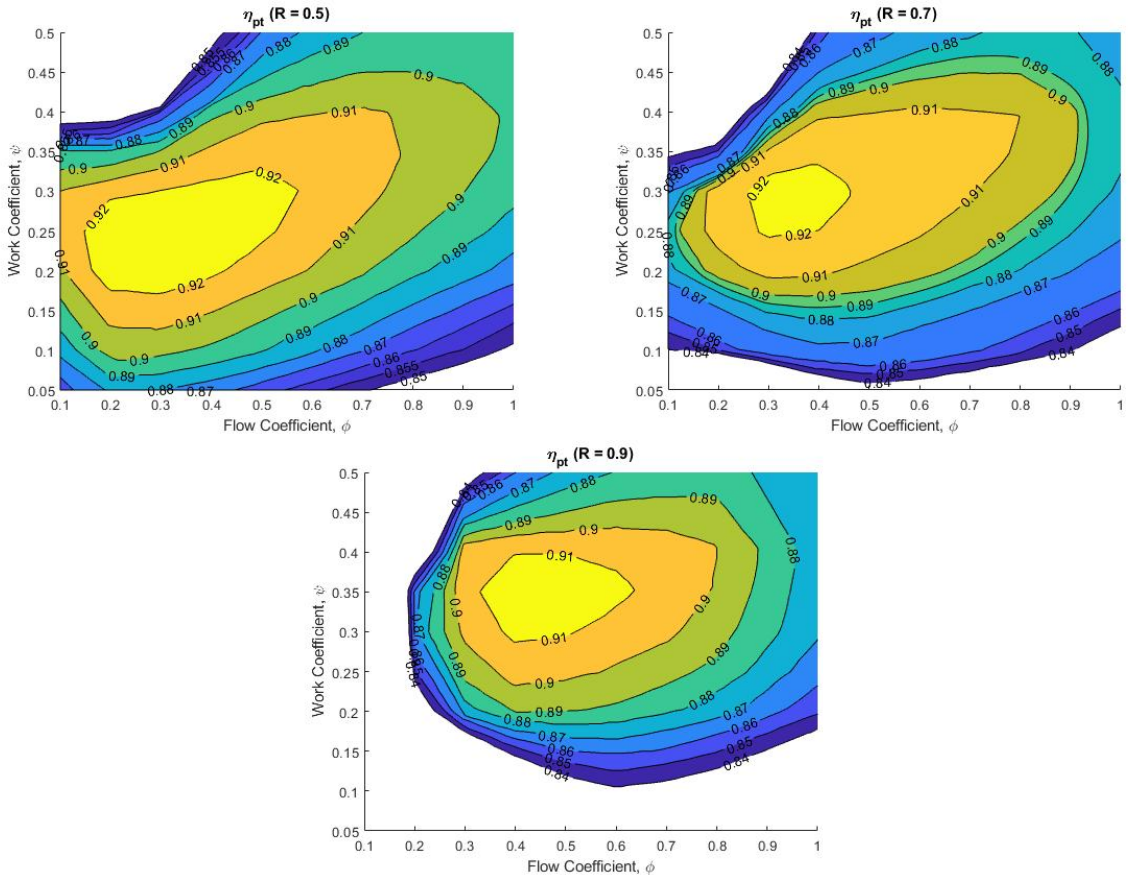

Figure 2.3: Equivalent Smith charts for axial compressors at varying degrees of reaction [39, 41].

Next, the total pressure and temperature at the compressor outlet can be calculated using Equations 2.5 and 2.6, respectively. Note that Equation 2.6 is only valid for calorically-perfect gases since the assumption of constant specific heats means that the ratio of specific heats, γ, is also fixed.

$$p_{t,out} = p_{t,in} \cdot PR \tag{2.5}$$

$$T_{t,out} = T_{t,in} \cdot PR^{\frac{\gamma-1}{\gamma \cdot \eta_{pt}}} \tag{2.6}$$

With the outlet properties known, the total specific work, $w_{t,total}$, done to the working fluid by the compressor can be calculated using Equation 2.7, followed by the consumed power, $\dot{W}$, in Equation 2.8.

$$w_{t,total} = c_p \cdot \left(T_{t,out} - T_{t,in}\right) \tag{2.7}$$

$$\dot{W} = \dot{m} \cdot w_{t,total} \tag{2.8}$$

The total-to-total isentropic efficiency of the compressor, η_{tt}, may be calculated for reference according to the following relation:

$$\eta_{tt} = \frac{PR^{\frac{\gamma-1}{\gamma}} - 1}{PR^{\frac{\gamma-1}{\gamma \cdot \eta_{pt}}} - 1} \tag{2.9}$$

Finally, an appropriate number of stages, n_{stg}, can be determined if this value has not already been set as an input by the user. An approximate single-stage pressure ratio of 1.3 is selected to represent a moderate level of technology [42], although the user is free to modify (increase) this value if they want to assume a higher level of technology. The outcome of Equation 2.10 can then be rounded to the nearest integer to obtain the final result. More advanced checks on design feasibility may be performed at the end of the analysis and the number of stages updated accordingly; however, no such procedure is yet implemented in the present methodology. The number of stages is therefore currently based solely on machine pressure ratio.

$$n_{stg} \approx \log_{1.3}(PR) \tag{2.10}$$

Note that Equation 2.10 – and the logarithmic base of 1.3 – is used only to estimate an appropriate number of stages; the actual pressure ratio over each stage is a calculated value, not fixed, and is determined once the number of stages has been established and the full gas path design is completed. Thus, the pressure ratio will vary per stage and will not necessarily be equal to 1.3, since the actual distribution is based on specific work, not single-stage pressure ratio.

2.1.1.3. STAGE-BY-STAGE DESIGN

If the thermodynamic state and geometry are fully-defined at a particular station – for example, the inlet of a stage – then the properties at the next station(s), i.e., the intermediate station and outlet of that same stage, can be calculated using the following procedure. The outlet properties of one row or stage are considered the inlet properties of the next, meaning that this stage-by-stage design procedure can be repeated indefinitely, one stage at a time, in order to generate the complete meanline thermodynamic data set and preliminary gas path design. Obviously, a starting point is required, i.e., one location for which all properties are fully-defined, in order to trigger the domino of subsequent calculations. For convenience, this starting point is chosen as the machine inlet, and the methods for determining the properties at the inlet are described in Section 2.1.1.4.

Nomenclature Figure 2.4 shows the station numbering and nomenclature for a single stage of an axial compressor at a fixed radial coordinate. In the present study, absolute, relative, and tangential velocities are represented by V, W, and U, respectively. Flow (absolute) and blade (relative) angles are represented by α and β, respectively. The inlet to the rotor is considered Station 1 and the rotor outlet Station 2. The third and final station in the case of compressors is denoted as Station 3 and occurs at the stator outlet.

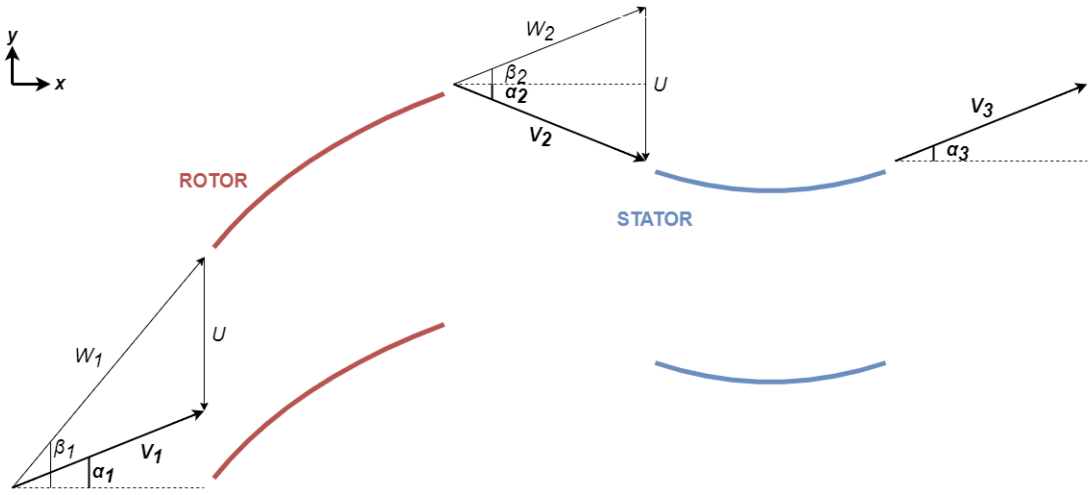

Figure 2.4: Station numbering and nomenclature of a single axial compressor stage.

For axial compressors with repeated stages (i.e., the same duty coefficients applied to each stage, an assumption that is made in the present analysis), α_3 is equal to α_1. If the machine also has a constant mean radius, then V_3 is equal to V_1 in the subsequent stages. If the mean radius is not constant, however, which may be the case if the machine is designed to have a constant hub or tip diameter, then $\alpha_3 = \alpha_1$ is still true, whereas the actual velocity values (V_3 and V_1) may differ due to the changing tangential velocity with varying mean radius. For simplicity, however, it is convenient to assume a constant or nearly-constant mean radius when analyzing a single stage in isolation, which leads to constant tangential (U) and meridional/axial (V_m) velocities over the entire stage.

Angles The flow and blade angles are calculated based on the prescribed duty coefficients, as shown in Equations 2.11 through 2.14. These can be calculated once for the entire machine, since the assumption of repeated stages, and therefore constant duty coefficients, also implies repeated flow angles, making the relationship shown in Equation 2.15 true as well.

$$\alpha_1 = \tan^{-1}\left(\frac{1 - \frac{\psi}{2} - R}{\phi}\right) \tag{2.11}$$

$$\beta_1 = \tan^{-1}\left(\tan(\alpha_1) - \frac{1}{\phi}\right) \tag{2.12}$$

$$\beta_2 = \tan^{-1}\left(\frac{\phi \cdot \tan(\alpha_1) + \psi - 1}{\phi}\right) \tag{2.13}$$

$$\alpha_2 = \tan^{-1}\left(\tan(\beta_2) + \frac{1}{\phi}\right) \tag{2.14}$$

$$\alpha_3 = \alpha_1 \tag{2.15}$$

Total Properties The tangential velocity can be calculated using Equation 2.16. For simplicity, the mean radius, r_m, is taken at the stage inlet (Station 1) to avoid the need for iterative calculations. The tangential velocity, U, is assumed constant over the entire stage despite the possibility of variation in the mean radius, and the result of Equation 2.16 is taken as the approximate average over the whole stage despite only being calculated at the inlet.

$$U_{stg} = \omega \cdot r_{m,1} \tag{2.16}$$

The meridional velocity and absolute velocities at each station can be calculated using Equations 2.17 through 2.20. Note that the relation presented in Equation 2.20 is only valid under the assumptions of repeated stages and constant mean radius.

$$V_m = \phi \cdot U_{stg} \tag{2.17}$$

$$V_1 = \frac{V_m}{\cos\alpha_1} \tag{2.18}$$

$$V_2 = \frac{V_m}{\cos\alpha_2} \tag{2.19}$$

$$V_3 = V_1 \tag{2.20}$$

The total specific enthalpy, h_t, at the rotor inlet is calculated using Equation 2.21 assuming the total temperature, T_t, is already known at this location, and using a reference temperature, T_{ref} of zero kelvin:

$$h_{t,1} = c_p \cdot \left(T_{t,1} - T_{ref}\right) \tag{2.21}$$

The total specific work of the stage can be calculated using Equation 2.22. For machines which have a constant mean radius and repeated stages, this value is the same for all stages. For machines with either a constant hub or tip diameter, the mean radius varies along the flow path, leading to an unequal amount of work performed by each stage. This is discussed more in Section 2.1.1.5.

$$w_{t,stg} = \psi \cdot U_{stg}^2 \tag{2.22}$$

The change in total enthalpy across the rotor is equal to the specific work of that stage. The total enthalpy at the rotor outlet is therefore calculated using Equation 2.23:

$$h_{t,2} = h_{t,1} + w_{t,stg} \tag{2.23}$$

Regardless of the machine type, the total specific enthalpy remains constant across stator rows, although the static properties may vary. This fact is reflected in the relation presented in Equation 2.24:

$$h_{t,3} = h_{t,2} \tag{2.24}$$

Finally, the total temperature and pressure at any row and/or stage outlet can be calculated using Equations 2.25 and 2.26, respectively. In these equations, the subscript n denotes any arbitrary station number (e.g., 2 or 3) in the single-stage nomenclature convention (Figure 2.4), and $n-1$ the station preceding the current one (e.g., 1 or 2). Note that the reference temperature is still assumed to be zero kelvin.

$$T_{t,n} = \frac{h_{t,n}}{c_p} + T_{ref} \tag{2.25}$$

$$p_{t,n} = p_{t,n-1} \cdot \left(\frac{T_{t,n}}{T_{t,n-1}} \right)^{\frac{\gamma \cdot \eta_{pt}}{\gamma - 1}} \tag{2.26}$$

Station Cross-Sectional Area Starting with the total specific enthalpy, h_t, total pressure, p_t, absolute flow velocity, V, and meridional velocity, V_m, of any particular station in the machine, the required cross-sectional area of the flow path at that station can be calculated using the static quantities as an intermediate step. This procedure is shown in Equations 2.27 through 2.33 and is necessary for determining the blade height and mean radius of the station, which is required in the design of subsequent stages and in analysis of overall machine performance. For clarity, what is meant by 'cross-sectional area' is the flow path area, i.e., the space available for the gas to occupy, in the plane normal to the axial – or meridional – direction.

$$h_s = h_t - \frac{V^2}{2} \tag{2.27}$$

$$T_s = \frac{h_s}{c_p} + T_{ref} \tag{2.28}$$

$$a = \sqrt{\gamma \cdot R_g \cdot T_s} \tag{2.29}$$

$$Ma = \frac{V}{a} \tag{2.30}$$

$$p_s = p_t \cdot \left(1 + \frac{\gamma - 1}{2} Ma^2 \right)^{\frac{-\gamma}{\gamma - 1}} \tag{2.31}$$

$$\rho = \frac{p_s}{R_g \cdot T_s} \tag{2.32}$$

$$A = \frac{\dot{m}}{\rho \cdot V_m} \tag{2.33}$$

Blade Height and Mean Radius If local blockage factors, K_B, are being applied, then the corrected cross-sectional area can be calculated using Equation 2.34. *Blockage factors* are defined and discussed in more detail in Appendix B.2. If not applicable, then a value of $K_B = 1$ can be used.

$$A_c = \frac{A}{K_B} \tag{2.34}$$

If the machine has a constant mean radius, then the procedure for determining the blade height, b, and mean radius at subsequent stations is quite straightforward. In this case, the mean radius at any station is the same as at the previous (Equation 2.35), meaning the blade height can be calculated using Equation 2.36.

$$r_{m,n} = r_{m,n-1} \tag{2.35}$$

$$b = \frac{A_c}{2 \cdot \pi \cdot r_m} \tag{2.36}$$

If the machine has a constant hub or tip diameter, then iteration is necessary. Equation 2.35 can be used as a first guess for the mean radius of the next station, with the hub or tip radius calculated using Equation 2.37 or 2.38, respectively.

$$r_{hub} = r_m - \frac{b}{2} \tag{2.37}$$

$$r_{tip} = r_m + \frac{b}{2} \tag{2.38}$$

In such cases, the fixed radius (hub or tip) is known from the previous station, which was initially determined at the inlet of the first stage. The value of the mean radius is then iterated such that the blade height calculated using Equation 2.36 and the result of either Equation 2.37 or 2.38 satisfy Equation 2.39 or 2.40, respectively, depending on which of the radial coordinates is fixed.

$$r_{hub,n} = r_{hub,n-1} \tag{2.39}$$

$$r_{tip,n} = r_{tip,n-1} \tag{2.40}$$

Repetition The procedure specified in Equations 2.23 through 2.40 can be repeated for each row in the stage (i.e., twice). The procedure outlined in Section 2.1.1.3 can then be repeated for every stage in the machine. The outlet properties of one row are taken as the inlet properties of the next, just as the outlet properties of one stage are taken as the inlet properties of the next. For example, the total specific enthalpy at the outlet of stage n ($h_{t,3}$) is the same as the value of $h_{t,1}$ required in Equation 2.23 when analyzing stage $n+1$. By repeating this procedure for each stage in the machine, the complete thermodynamic cycle can be defined, as well as some preliminary geometry (mean radii and blade heights) for the gas path design.

2.1.1.4. MACHINE INLET PROPERTIES

In order to begin the stage-by-stage design procedure described in Section 2.1.1.3, the thermodynamic state and geometry must be fully-defined at a particular station. The machine inlet is chosen as this location for convenience, since the fluid properties are typically known here. For example, the first component in the engine will have inlet flow properties corresponding to ambient conditions, and the other machines have inlet properties equal to the outlet properties of the previous. So, if compressors, turbines, and combustors are designed in the order in which they appear in the engine gas path, then the complete engine design is a relatively simple combination of the individual designs of multiple machines.

With the total specific work over the entire machine calculated in Equation 2.7, the specific work over the first stage, $\left(w_{t,stg}\right)_1$, can be estimated using Equation 2.41:

$$\left(w_{t,stg}\right)_1 = \frac{w_{t,total}}{n_{stg}} \tag{2.41}$$

The tangential velocity, mean (or mid) radius, and meridional velocity at the inlet can then be calculated using Equations 2.42, 2.43, and 2.44, respectively.

$$U = \sqrt{\frac{(w_{t,stg})_1}{\psi}} \tag{2.42}$$

$$r_m = \frac{U}{\omega} \tag{2.43}$$

$$V_m = \phi \cdot U \tag{2.44}$$

The flow angles can be used to calculate the absolute flow velocities, V_1 and V_2, according to Equations 2.18 and 2.19, with the flow and blade angles being calculated using Equations 2.11 through 2.15. Finally, the total specific enthalpy can be calculated using Equation 2.21, where $T_{t,1}$ in this case is equal to the machine-level input parameter $T_{t,in}$ as specified in Table 2.1.

At this point, the values necessary for calculating the cross-sectional area at the inlet are all known, and this can be done using the procedure described in Equations 2.27 through 2.33. The mean radius at the inlet was already calculated using Equation 2.43, thus the blade height at the inlet can be calculated using Equations 2.34 and 2.36. If the machine has a constant hub or tip radius, then this dimension is determined using either Equation 2.37 or 2.38. This value is then fixed for the stage-by-stage analysis which follows.

2.1.1.5. ITERATION

As shown in Equation 2.22, the specific work done by a stage, $w_{t,stg}$, is dependent upon the tangential velocity, U_{stg}, which is itself dependent on the local mean radius according to Equation 2.16. Therefore, for machines which have either a constant hub or constant tip diameter, the mean radius varies along the flow path, meaning a different amount of work is done by each stage. The total specific work actually done by the entire machine according to the present design can therefore be calculated using Equation 2.45:

$$(w_{t,total})_{des} = \sum_{i=1}^{n_{stg}} (w_{t,stg})_i \tag{2.45}$$

However, as discussed in Section 2.1.1.2 and calculated using Equation 2.7, the required total specific work is already known, thus there may be a discrepancy between the results of Equations 2.7 and 2.45. For the case of constant mean radius, there is no variation in this dimension, meaning that every stage performs the same amount of work. The work done by any given stage can therefore accurately be assumed as the total divided by the number of stages, as was done in Equation 2.41. However, this assumption becomes inaccurate for machines with a fixed hub or tip diameter.

Therefore, to design such a machine which satisfies the design requirement set forth by Equation 2.7, iteration is necessary. Since the selection of the fixed radial value affects the work done by any given stage, this value needs to be adjusted (or iterated) to obtain the desired effect. As shown in Section 2.1.1.4, the work done by the first stage has a direct influence on the mean, hub, and tip radii of the first stage. In the present methodology, it is one of these radial values which is taken, fixed, and then adhered to by all other stages in the machine, thus manipulation of the work performed by the first stage is essentially an indirect way of manipulating the fixed radius and therefore the specific work done by all other stages. Thus, the first stage work – initially estimated using Equation 2.41 – can be iterated using the Newton-Raphson iteration method and the procedure described in Sections 2.1.1.3 and 2.1.1.4 repeated until convergence is obtained between the required $w_{t,total}$ calculated in Equation 2.7 and the actual value achieved by the design, $(w_{t,total})_{des}$, found using Equation 2.45. The formulation of the Newton-Raphson method is described in Appendix B.1.

2.1.2. AXIAL DIMENSIONS

Meanline analysis provides the mean radius and local channel height at every station in the machine. As is evident in Figure 2.1, these dimensions are synonymous with the blade properties as well, i.e., the blade mean radius and local height, respectively. However, both of these dimensions apply in the radial direction only and give no information regarding the axial chord length or relative axial positioning/spacing of the rows. Thus, to complete the design of the blades in the axial/radial plane, several additional input parameters are required. These are presented in Table 2.3.

Aspect ratio is defined as the blade span (or height, b) divided by the chord, as shown in Equation 2.46. The aspect ratio of a particular row depends on the row type (i.e., rotor vs. stator) and relative location (i.e., stage i of a machine with n stages). As seen in the last column of Table 2.3, four aspect ratios are provided as

Table 2.3: Additional inputs required for completion of turbomachinery gas path design in axial direction.

Category	#	Input Parameter	Symbol	Units	Qty
Axial	14	Aspect Ratios	AR	-	4
	15	Row and Stage Gaps	g	-	2
	16	Taper Ratios	λ	-	2

inputs: one for the first rotor row, one for the first stator row, one for the last rotor row, and one for the last stator row. The aspect ratios of any row in between are determined using linear interpolation between the two input values corresponding to that row type.

$$AR = \frac{b}{c} \tag{2.46}$$

For validation cases using existing engines, cross-sections of these engines can be digitized, and the (approximate) non-dimensional aspect ratios can then be measured and used as inputs in the present methodology. To improve the program's applicability to the design of novel engines, it is recommended to embed loss models into the current meanline performance analysis, models which are sensitive to the factors such as the aspect ratios of the blades, row and stage gaps, etc. This would allow the aspect ratios and other such variables to be defined by the program automatically based on a specified set of criteria: the values could be selected or even optimized to, for example, maximize efficiency or reduce weight. This would allow a more ideal final design to be achieved, all the while eliminating the need for these values as inputs.

Two taper ratios, λ, and two maximum thickness-to-chord ratios, $(t/c)_{max}$, are also required, one of each applying for all rotor blades and one of each applying for all stator vanes. Taper ratio is defined in Equation 2.47, while $(t/c)_{max}$ is discussed further in Section 3.1.1.2.

$$\lambda = \frac{c_{tip}}{c_{root}} \tag{2.47}$$

Finally, two row/stage gaps, g, are provided: one for the gap between the first and second blade row in a single stage (i.e., row gap), and one for the gap between two rows of consecutive stages (i.e., stage gap). Both are dimensionless quantities expressed as fractions of the mean axial chord of the preceding blade row, which is the same formulation as used in the meanline design code Meangen [43]. The concept of row and stage gaps are illustrated in Figure 2.1. Typically, stage gaps are larger than row gaps, although this does not always have to be the case.

Figure 2.5 shows a view of a generic, tapered, axial compressor rotor blade in the axial/radial plane, similar to what was shown in Figure 2.1 but with additional dimensions (and, in this case, a constant mean radius). As previously mentioned, the radii and blade heights at every station have already been determined as part of the meanline analysis. For the blade shown in Figure 2.5, this is a total of four dimensions: the mean radii r_1 and r_2, and the blade (or channel) heights b_1 and b_2. Here, 1 and 2 are used to denote the inlet and outlet (or leading and trailing edges) of that particular blade row, respectively.

The average height of the blade can be calculated using Equation 2.48. In the present methodology, the *axial chord*, c_{ax}, will be used when dealing with aspect ratios, taper ratios, row and stage gaps, thickness-to-chord ratios, etc. This was done since, in the case of turbomachinery design, the amount of blade twist can be significant, thus axial chord provides a more consistent unit of measure (or reference value) than true chord, and varies less along the span. The axial chord can therefore be calculated using Equation 2.49.

$$b_{avg} = \frac{b_1 + b_2}{2} \tag{2.48}$$

$$c_{ax} = \frac{b_{avg}}{AR} \tag{2.49}$$

Three different axial chord values are shown in Figure 2.5, one for the tip, root, and mid-span. Those at the tip and root are distinguished using their respective subscripts, but that of the mid-span (or mean radius) is denoted simply as c_{ax}. This is for simplicity, but note that c_{ax}, $c_{ax,mean}$, and $c_{ax,mid}$ can be used interchangeably in the present convention.

The gaps between rows are simply displacements in the axial direction, and can therefore be represented as Δx. The gap between the first and second row in the same stage can be calculated using Equation 2.50, with

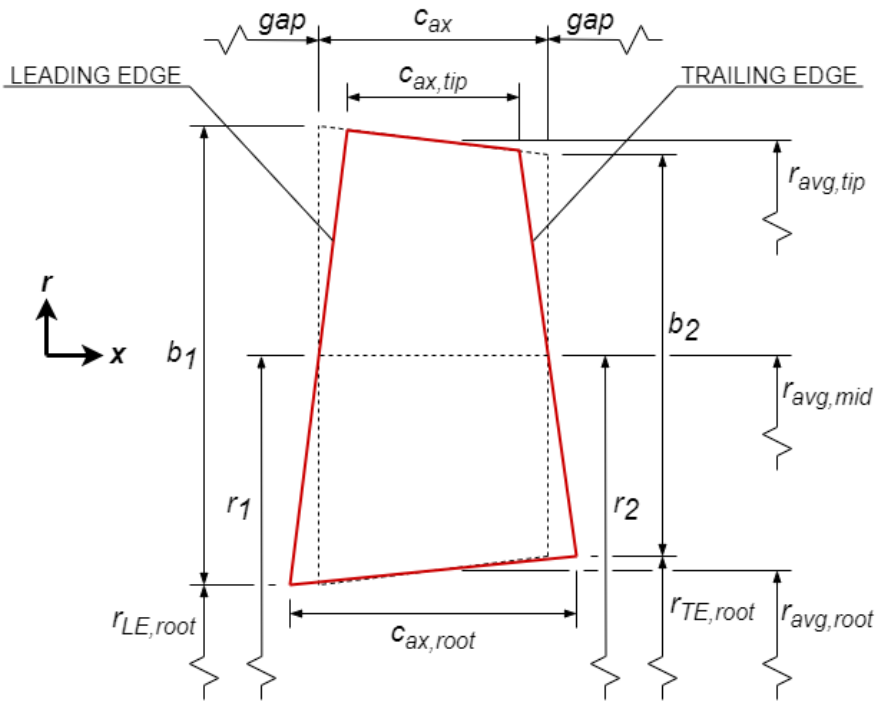

Figure 2.5: Gas path side view of a generic axial compressor blade (axial/radial plane).

the gap between two rows in different stages using Equation 2.51. Note once again that the non-dimensional parameter g is expressed as a fraction of the axial chord of the blade row immediately upstream of the gap in question (i.e., c_{ax} of a particular row determines the length of the gap immediately downstream of itself).

$$\Delta x_{row} = g_{row} \cdot c_{ax} \tag{2.50}$$

$$\Delta x_{stg} = g_{stg} \cdot c_{ax} \tag{2.51}$$

Finally, blade taper can be applied. Since axial chords are being used, the taper ratio can be redefined according to Equation 2.52. Stator vanes often feature less taper, thus λ_{stator} will usually be closer to unity than λ_{rotor}.

$$\lambda = \frac{c_{ax,tip}}{c_{ax,root}} \tag{2.52}$$

In the present methodology, taper is applied such that the mean axial chord of the blade is kept constant according to the value calculated in Equation 2.49. This allows the user to modify the taper ratios without affecting the total machine length. In theory, this method could lead to interference between blade rows; however, no such interference was observed in any of the validation cases due to the use of realistic (and relatively high) aspect ratios. The dashed lines in Figure 2.5 represent the blade pre-taper, while the solid lines represent the finalized profile of the blade in the axial/radial plane once taper has been applied.

Thus, if c_{ax} is assumed fixed, then it is the chord at the root and tip which will be affected by the introduction of taper. If the axial chord at the mean radius is the average of the root and tip chords (Equation 2.53), then it follows that the root and tip axial chords can be calculated using Equations 2.54 and 2.55, respectively:

$$c_{ax} = \frac{c_{ax,tip} + c_{ax,root}}{2} \tag{2.53}$$

$$c_{ax,root} = c_{ax}\left(\frac{2}{1+\lambda}\right) \tag{2.54}$$

$$c_{ax,tip} = c_{ax}\left(\frac{2\lambda}{1+\lambda}\right) \tag{2.55}$$

When taper is applied, the axial location of the leading and trailing edges changes. Note that, for locations where the axial chord decreases due to taper (e.g., the blade tip shown in Figure 2.5), the radial coordinates are also updated (interpolated) such that the new blade boundary lies directly overtop of the original. However, when the axial chord increases (e.g., the blade root shown in Figure 2.5), the radial coordinate is held constant to avoid the presence of short divergent sections in the gas path channel and to maintain continuity with the rows immediately up- and downstream of the current row.

2.2. SUMMARY

- The Weight Estimation of Aeronautical Gas Turbine Engines (WEST) tool's meanline analysis and gas path design tool is founded on the use of duty coefficients as inputs, not geometry (see Section 2.1.1.1). This allows engines to be designed based on their performance first, with less direct control over the dimensions of the machine, instead of the other way around. Doing so is beneficial in the case of novel architectures, since little may yet be known about the expected geometry/profile.

3

AXIAL COMPRESSORS

Compressors, combustors, and turbines form the backbone of modern aircraft engines. Each of these performs an essential role with regard to the practical realization of the discrete processes involved in the Brayton cycle. The use of axial turbomachinery is necessary to achieve the considerable mass flow rates required by large turbofan engines, with smaller turboshafts typically accomplishing compression through axial devices, radial devices, or a combination of these.

Turbomachinery constitutes a large share of total engine weight, thus the design of such components has a significant impact on overall weight estimation. Representative designs of blades, disks, casings, etc., are therefore important, since it follows that a realistic design will also lead to a realistic weight estimation for that same part. The objective of this chapter is to describe the methodology used in the design of axial compressors (Section 3.1), as well as documentation of the validation efforts (Sec. 3.2), finishing with a discussion of the sensitivity of the results to the variation of key parameters (Sec. 3.3). While the general procedure for designing axial turbomachinery is fairly consistent regardless of whether the device is used for compression or expansion, only compressors will be discussed here, with the differences in methodology for axial turbines presented in Chapter 4.

3.1. DESIGN METHODOLOGY

The following sections discuss the methodologies used in the blade, disk, casing, and connecting hardware designs for axial compressors. Figure 3.1 shows an overview of this procedure. Section 3.1.1 begins with the blade design procedure, which builds upon the two-dimensional (2D) outline of the blade when viewed in the axial/radial plane, which has already been designed as described in Chapter 2. The three-dimensional (3D) blade design can then be completed to determine its weight, which is a requirement for the subsequent design of disks (Section 3.1.2). Note that disks are only present in the case of rotor rows. This is followed by the design of the casing (Sec. 3.1.3) and a weight estimation of the stator shrouds and connecting hardware (Sec. 3.1.4). The weight of all subcomponents can then be combined into an assembly-level weight estimation.

3.1.1. BLADES

There can be hundreds or even thousands of blades in a single multi-stage machine, thus an appropriate design methodology is imperative for a realistic weight estimation. The weight of the blades also determines the stresses applied to the disks (and casing in the event of blade failure) – this will be discussed further in Sections 3.1.2 and 3.1.3 – which in turn affects the designs and weight estimations of these component types. Thus, blade design has a 'downstream' effect (figuratively speaking) on the component-level design of turbomachinery and therefore an important influence on total weight estimation. Figure 3.2 shows an overview of the procedure followed in the design of a single axial compressor blade.

In order to complete the 3D blade shape, one other input is required, in addition to those already listed in Table 2.1 and Table 2.3. This is the maximum thickness-to-chord ratio, and is shown in Table 3.1.

3.1.1.1. LEADING AND TRAILING EDGE BLADE ANGLES

The leading and trailing edge blade angles of the rotor, β_1 and β_2, respectively, were calculated at the mid radius for each blade row using Equations 2.12 and 2.13 during the meanline analysis. The blade angles

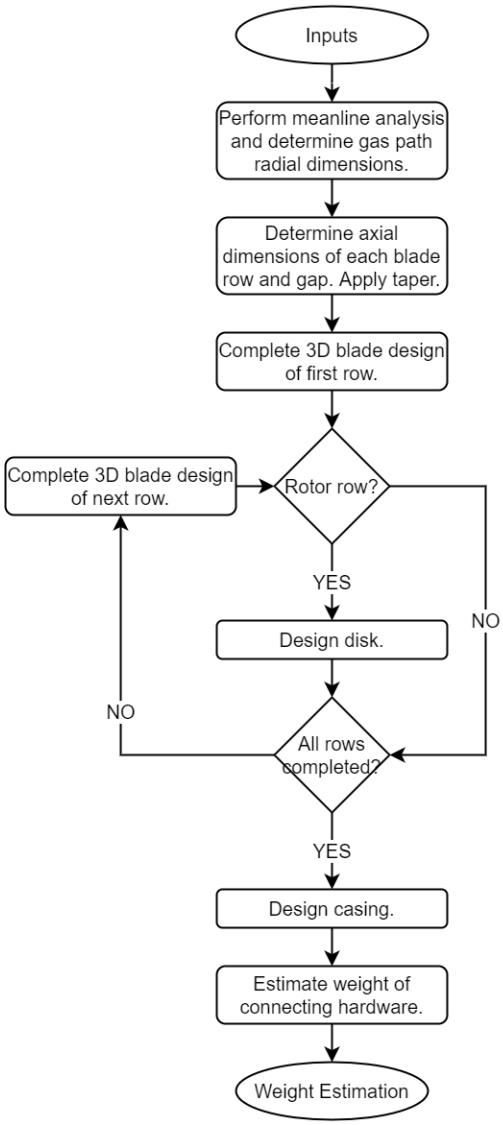

Figure 3.1: Flow chart describing the axial compressor design procedure.

of stator vanes are the same as the flow angles, α, since they do not rotate, meaning there is no difference between the absolute and relative frames of reference in this case. With the assumption of repeated stages, α_3 is equal to α_1 as shown in Equation 2.15, thus the blade angles of the stators are also fully-defined.

The blade angles define part of the local airfoil design, particularly with regard to the camber line, which should be tangent to these angles at its leading and trailing edges. Before such profile design can be completed for each spanwise location, however, the blade angles at each spanwise location must be known, whereas only those at the mid radius have yet been calculated. In order to determine this missing information, the Free Vortex design methodology is employed in order to provide a representative picture of what a blade could look like once spanwise twist is applied. In modern engine design, other methodologies may be used for determining the amount of twist in the blades (e.g., the forced vortex, constant reaction, exponential vortex, and/or general vortex design methods [44], or some higher-fidelity analysis), but for the purposes of preliminary design for weight estimation, the Free Vortex approach is sufficient, as is evidenced by its use in other engine design and weight estimation tools such as ATLAS and GTlab [20, 21].

The Free Vortex method is summarized in Equations 3.1 and 3.2 [20]. Equation 3.1 implies that the meridional (or axial) velocity is not a function of radius, i.e., it is constant across all spanwise locations. Equation 3.2 shows that the product of the tangential component of flow velocity and radius is constant, implying that the tangential component of velocity decreases with increasing radial coordinate. A more complete description

Table 3.1: Additional inputs required for completed gas path and detailed blade design of axial compressors.

Category	#	Input Parameter	Symbol	Units	Qty
Profile	17	Max. Thickness-to-Chord Ratio	$(t/c)_{max}$	-	2

of the procedure used, which is based on these equations, is described in detail in Appendix B.3. Figure 3.3 shows examples of what rotor blade velocity triangles may look like when blades are designed according to the Free Vortex approach.

$$V_m \neq f(r) \tag{3.1}$$

$$V_t \cdot r = const. \tag{3.2}$$

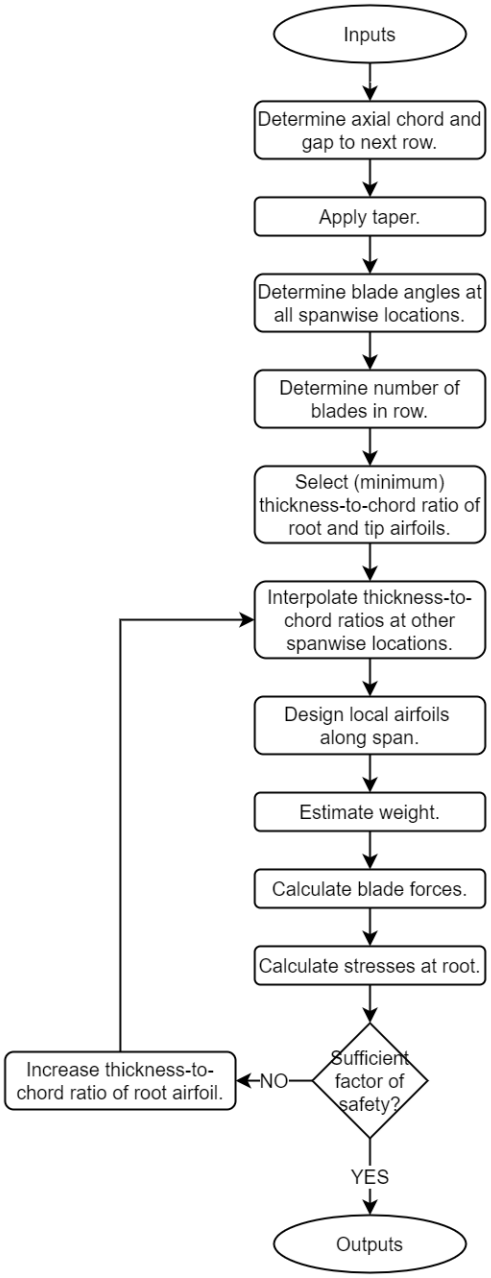

Figure 3.2: Flow chart describing the axial compressor blade design procedure.

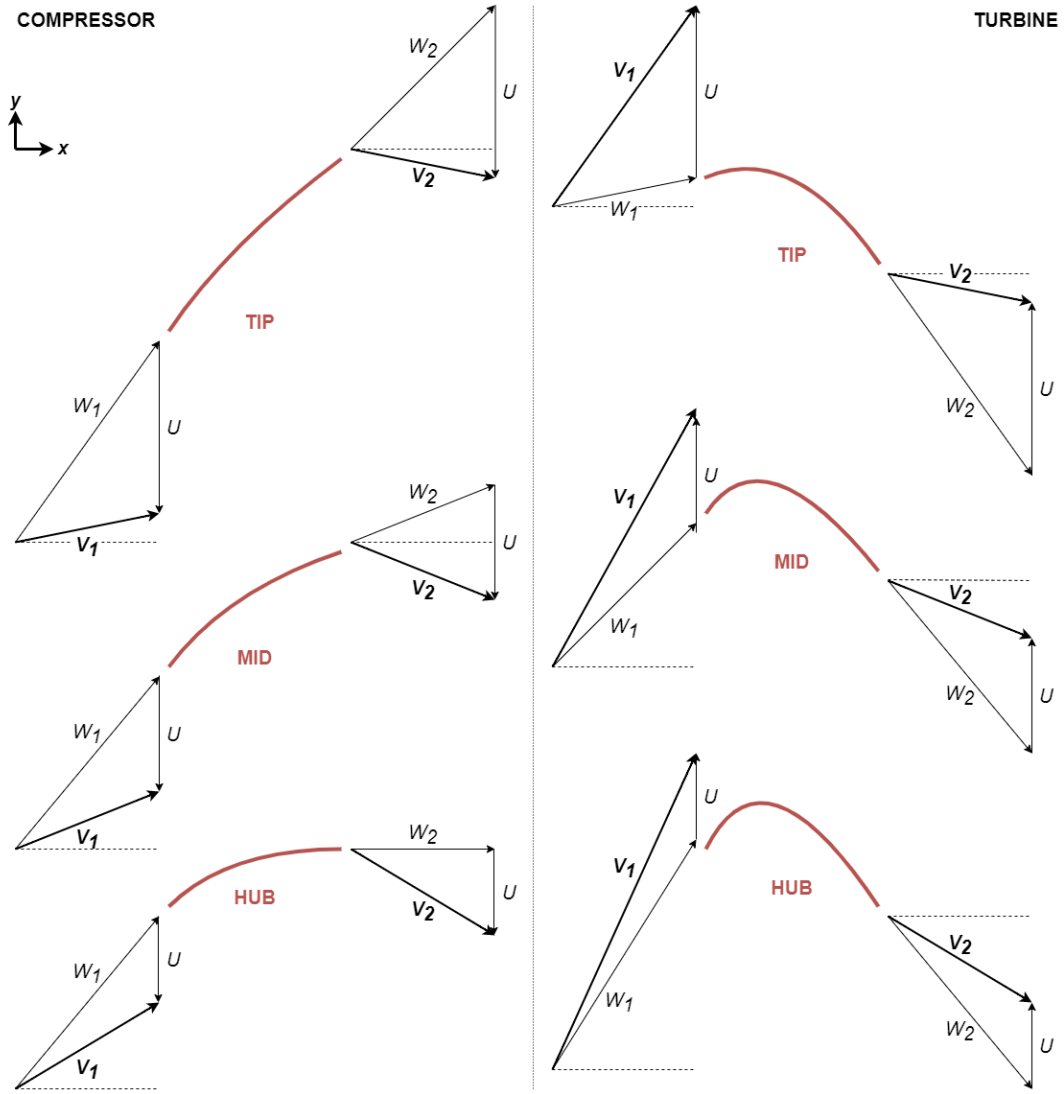

Figure 3.3: Example of rotor blade velocity triangles when designed according to the Free Vortex design methodology.

3.1.1.2. AIRFOILS

With a 2D outline of each blade determined according to the format shown in Figure 2.5, and with the leading and trailing edge blade angles known at every spanwise location, local two-dimensional airfoils/profiles (e.g., Figure 3.4) are required in order to complete the missing dimensions and convert the existing results into a 3D blade design. In the subsequent airfoil design procedure, three main aspects must be considered:

1. Camber line equation.
2. Thickness distribution.
3. Maximum thickness-to-chord ratio.

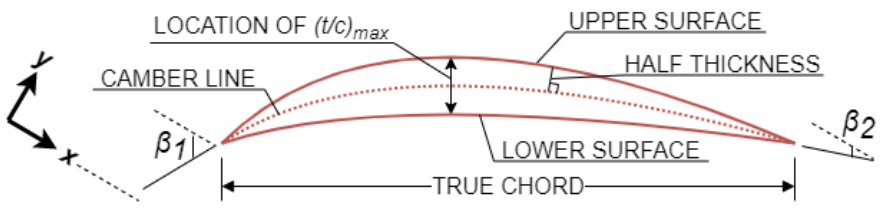

Figure 3.4: Composition of a compressor blade local airfoil section.

Maximum Thickness-to-Chord Ratio One important design parameter regarding airfoil design is the maximum thickness-to-chord ratio, $(t/c)_{max}$. As seen in Table 2.3, this value is an input for the airfoil/profile design procedure which follows, but does not necessarily need to be input by the user, unless they wish to specifically override the default values provided. The values shown in Table 3.2 are the default maximum thickness-to-chord ratios for compressor blades corresponding to those row types in the turbomachinery design programs Meangen and Stagen [43] and are therefore taken as representative values.

Table 3.2: Default thickness-to-chord ratios for different row types of an axial compressor [43].

Row Type	Minimum $(t/c)_{max}$ [%]
Rotor	7.5
Stator	10.0

Here, the term 'minimum $(t/c)_{max}$', or 'minimum-maximum thickness-to-chord ratio', is not contradictory. What this means is that, at any fixed spanwise location of the blade, there is a maximum thickness-to-chord ratio of that local airfoil. However, the value that this $(t/c)_{max}$ must take, either here or at any other spanwise location, must be minimally equal to the value specified in Table 3.2. In other words, these values are the minimum $(t/c)_{max}$ values used. The reason these are a minimum – and are not necessarily applied directly at every spanwise location – is due to stress considerations. As will be discussed in more detail later, the blades in axial turbomachinery are subject to large stresses (rotors in particular, due to the high rotational speeds and therefore large centrifugal stresses). It may therefore be beneficial to reduce the thickness of the blade at the tip to reduce weight and the magnitude of the centrifugal force. It may also be beneficial to increase the thickness of the root in order to increase the root cross-sectional area and therefore reduce the local stresses. Thus, the values presented in Table 3.2 are the minimum values, i.e., what is likely found at the blade tip, but the actual local $(t/c)_{max}$ may increase at other spanwise locations depending on the results of the stress analysis.

It is also important to note that, in the present methodology, the value of $(t/c)_{max}$ can be used as either a maximum thickness-to-*true*-chord ratio or as a maximum thickness-to-*axial*-chord ratio. It is recommended to use the latter since, in the case of compressor rotor blades which feature a large amount of twist when designed according to the Free Vortex method, the true chord at the tip can be quite large. So, if $(t/c)_{max}$ is used as the thickness-to-true-chord ratio, the thickness will also be high at the tip, leading to a heavy blade with a large centrifugal force and therefore large stresses at the hub. By instead applying $(t/c)_{max}$ as a thickness-to-axial-chord ratio, the thicknesses across the span of even of highly-twisted blades remains reasonable, and stresses at the blade root are mitigated.

Camber Line The work of Carolus [45] provides a comprehensive means of compressor blade profile design – including both the camber line equation and thickness distribution – using NACA 65-series airfoils. Studies exist for this series of airfoils for blades in cascade arrangement and in highly-cambered configurations, hence its applicability to compressor blade design. It therefore offers accurate modelling in terms of fluid dynamic performance, which in turn will yield dependable weight estimation results. The complete procedure for determining the y-coordinates of a circular arc mean camber line, y_c, is described in Appendix B.4.1.

Thickness Distribution Carolus [45] provides the thickness distributions, y_t, of several symmetric NACA 65-series airfoils, with thickness-to-chord ratios varying from 6% to 15%. This data is reproduced in Table B.2 in Appendix B.4.2. Note that the thicknesses listed in Table B.2 are *half-thicknesses*, i.e., they are a measure of the distance between the mean camber line and either the upper or lower airfoil surfaces. The values in Table B.2 are presented as discrete $(t/c)_{max}$ values and not in analytical form, meaning that for $(t/c)_{max}$ values between any of those listed, linear interpolation between the closest distributions can be used, and for $(t/c)_{max}$ values lower than 6% or higher than 15%, scaling of the closest distribution can be used.

Since these thickness distributions are for symmetric airfoils, they yield the upper (U) and lower (L) surface coordinates for that airfoil. However, in the case of cambered airfoils, the thickness distribution must be combined with the mean camber line calculated in Equation B.41. This can be done using Equations 3.4 through 3.7 [46], where the local tangent angle of the camber line, θ, is defined in Equation 3.3.

$$\theta = \tan^{-1}\left(\frac{dy_c}{dx}\right) \tag{3.3}$$

$$x_U = x - y_t \cdot \sin\theta \tag{3.4}$$

$$y_U = y_c + y_t \cdot \cos\theta \tag{3.5}$$

$$x_L = x + y_t \cdot \sin\theta \tag{3.6}$$

$$y_L = y_c - y_t \cdot \cos\theta \tag{3.7}$$

It is important to note that there is some limited flexibility in the compressor blade profile design method presented here. For example, only NACA 65-series airfoils are considered at present, and all of these have a maximum thickness occurring at 40% chord. However, since these profiles are representative of real gas turbine compressor blades, and since the main objective of the methodology presented in this report is to design components for accurate weight estimation – not necessarily ideal fluid dynamic performance – these limitations are considered acceptable at the current stage. Variation of the point of maximum thickness or even application of different compressor-blade airfoils with the same $(t/c)_{max}$ values are likely to produce only small differences in weight estimation. Thus, if the program were to be used for mechanical design of actual components, then it may be beneficial to further expand the blade design methods at that time.

Dimensionalization A final, important step in designing the compressor blade profiles is converting the normalized profile into actual dimensions. As previously stated, the leading and trailing edge points were taken at (0,0) and (1,0), respectively, when defining the circular arc mean camber line. The coordinates of the upper and lower surfaces can therefore be rotated around the centre point (0.5,0) until the angle at the leading edge matches the leading edge blade angle, β_1, (or α_2 in the case of stator vanes) calculated during the blade design procedure. The profile can then be scaled again such that the axial chord length is equal to unity. Finally, when the axial chord for the profile in question is known (calculated in Equation 2.49), further scaling can be done such that the axial chord of the profile matches this value. This concept is shown in Figure 3.5. With these final steps, a dimensioned blade profile can be obtained for every section along the span of every blade in the compressor.

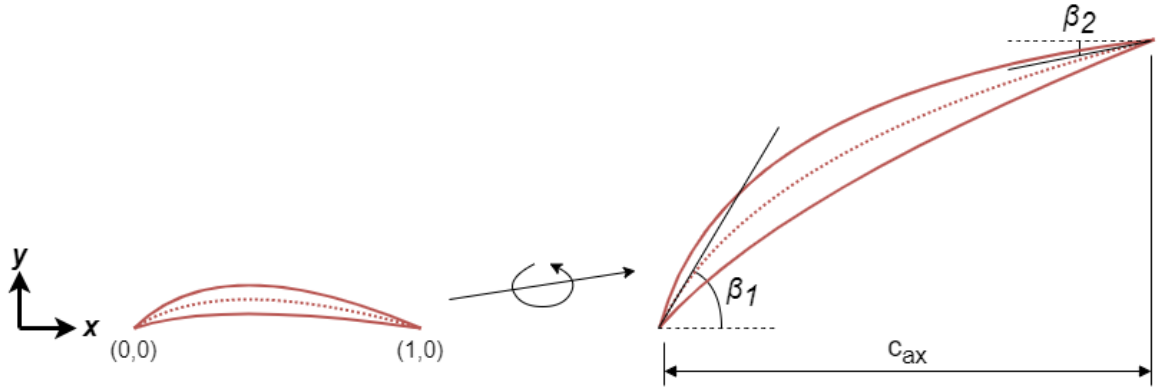

Figure 3.5: Dimensionalization of a compressor blade local airfoil section.

3.1.1.3. WEIGHT

The first step in calculating blade weight is to analyze the properties of each local section, i.e., the average radius and cross-sectional area of the blade at its hub, mid, and tip. The annular through-flow area of the gas path varies along the machine, so even though one radial coordinate is fixed (i.e., the machine may have a constant hub, mean, or tip diameter), the radii at the other two sections are varying even across the chord of a single blade. Thus, the *average radius* of a particular blade section refers to the mean/average radius of that blade *section*, but is not to be confused with the mean (or mid or meanline) radius of the blade as a whole. This concept is shown in Figure 2.5, where the leading edge (LE) radius, r_{LE}, trailing edge (TE) radius, r_{TE},

and average radius, r_{avg}, are shown explicitly for the root/hub section (shown with the additional subscript $root$). Such local radii can be defined for the mid and tip sections as well, as seen in Figure 2.5.

When calculating average radius for the purposes of estimating blade weight, a weighted average can be used based on the location of maximum thickness. In compressor blades designed using NACA 65-series airfoils, the location of maximum thickness occurs at 40% chord [45]. Thus, an approximate thickness-weighted average radius, calculated using Equation 3.8, is used.

$$r_{avg} = (0.6 \cdot r_{LE}) + (0.4 \cdot r_{TE}) \tag{3.8}$$

The cross-sectional area of the blade refers to the area outlined by the airfoil/profile of that local section, as designed in Section 3.1.1.2. Despite the varying radial coordinates to which these airfoils are applied, the area is calculated based only on their flattened (or projected) two-dimensional profile, and the radial variation is accounted for by the average radius values just discussed.

With the average radius and cross-sectional area of the blade calculated for each major section, the blade can be subdivided along the span into discrete volumetric segments. For example, two segments may be analyzed: the segment composing the volume between the hub and mid sections, and the segment composing the volume between the mid and tip sections, as shown in Figure 3.6.

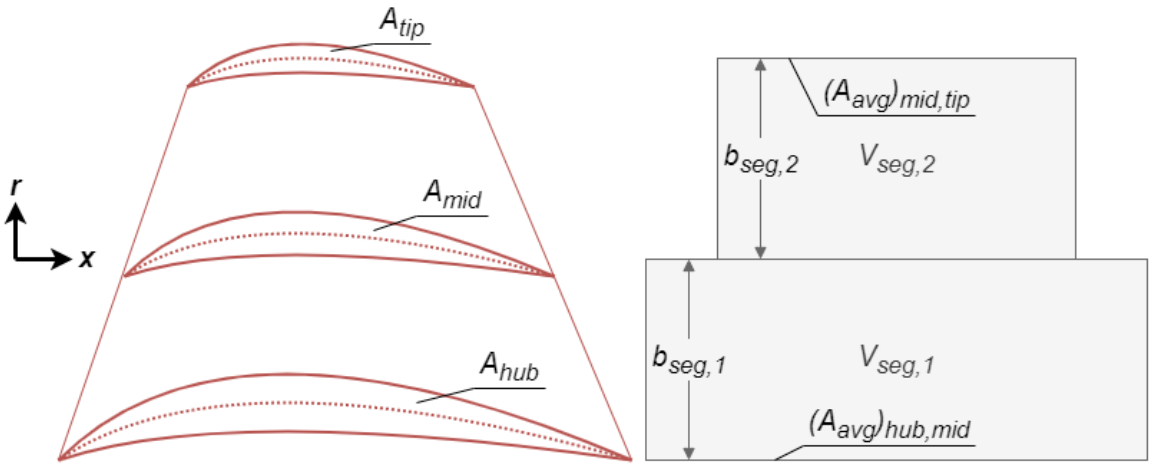

Figure 3.6: Segmentation of a compressor blade for approximate weight estimation.

If i is used to denote the inner section, and o the outer section, then the average cross-sectional area (i.e., the airfoil area, or the area bounded by the upper and lower surfaces as shown in Figure 3.4), height of the blade segment, and volume of the blade segment can be calculated using Equations 3.9, 3.10, and 3.11, respectively.

$$A_{avg} = \frac{A_i + A_o}{2} \tag{3.9}$$

$$b_{seg} = r_{avg,o} - r_{avg,i} \tag{3.10}$$

$$V_{seg} = A_{avg} \cdot b_{seg} \tag{3.11}$$

The total volume of the blade, V_{bl}, can then be calculated using Equation 3.12:

$$V_{bl} = \sum V_{seg} \tag{3.12}$$

Finally, the mass of the blade (colloquially referred to as the 'blade weight') can be calculated using Equation 3.13 once the blade material, and thus the material density, ρ, is known. The material selection procedure is described in Section 3.1.1.6.

$$m_{bl} = \rho \cdot V_{bl} \tag{3.13}$$

It is important to note that the blade weight estimation accounts only for the aerodynamic body; it does not account for the blade root or platform. Instead, these parts of the blade will be included in the disk design and weight estimation procedure described in a later section according to the methodology proposed by Lolis [21]. This means that, compared to the actual component weights of a given engine, the present study will underestimate the weight of the blades and overestimate the weight of the disks. When combined, however, the total weight of these two component types should be comparable to the real engine.

The centroid radius (i.e., the radial coordinate of the centre of mass), r_G, of a single blade segment can be calculated using Equation 3.14:

$$r_{G,seg} = \frac{(r_i \cdot A_i) + (r_o \cdot A_o)}{A_i + A_o} \tag{3.14}$$

The centroid radius of the entire blade can then be calculated using Equation 3.15:

$$r_{G,bl} = \frac{\sum \left(r_{G,seg} \cdot V_{seg}\right)}{V_{bl}} \tag{3.15}$$

This value is not needed in calculating the blade weight, but is a property of the centre of mass, which will be important later when determining the centrifugal forces acting on the blade and therefore the centrifugal forces acting at the blade root and disk hub. These influence the stress calculations and therefore the design and sizing of the blades and disks.

3.1.1.4. NUMBER OF BLADES IN ROW

Next, the number of blades in the row can be determined. This is useful when calculating the forces applied to a single blade and in finding the total weight of all blades in a row. The first step in determining a suitable number of compressor blades is to calculate the required solidity, σ, using Equation 3.16 for rotor rows and Equation 3.17 for stator rows [20]. This is the same procedure as used in GTlab [20].

$$\sigma_{min,rotor} = \left| \frac{W_{2,t} - W_{1,t}}{2 \cdot W_1 \cdot (DF + DH - 1)} \right| \tag{3.16}$$

$$\sigma_{min,stator} = \left| \frac{V_{3,t} - V_{2,t}}{2 \cdot V_2 \cdot (DF + DH - 1)} \right| \tag{3.17}$$

In these equations, two new terms are presented: the diffusion factor, DF, and the DeHaller number, DH. The DeHaller number for rotors and stators can be calculated using Equations 3.18 and 3.19 [20].

$$DH_{rotor} = \frac{W_2}{W_1} \tag{3.18}$$

$$DH_{stator} = \frac{V_3}{V_2} \tag{3.19}$$

Regarding the diffusion factor, a limiting value of **0.6** should be applied at the hub, and **0.4** at the tip [21], allowing for the minimum local solidity to be calculated at these two outermost blade locations.

Next, the maximum pitch at the hub and tip can be calculated by applying Equation 3.20 at both of these locations [20]. Here, the local *axial* chord is used for simplicity.

$$p_{max} = \frac{c_{ax}}{\sigma_{min}} \tag{3.20}$$

Finally, the minimum number of blades, n_{bl}, can be calculated using Equation 3.21 [20]:

$$n_{bl,min} = \frac{2 \cdot \pi \cdot r_{loc}}{p_{max}} \tag{3.21}$$

By applying Equation 3.21 to two local spanwise sections, the hub and the tip, the minimum required number of blades can be calculated at those two locations. The maximum of the two results can then be taken and rounded up to the nearest integer in order to determine the minimum number of blades of the entire row.

The weight of all blades in the row can be calculated simply by multiplying the result of Equation 3.13 with the number of blades calculated in the preceding steps, as shown in Equation 3.22:

$$m_{bl,row} = m_{bl} \cdot n_{bl} \tag{3.22}$$

3.1.1.5. STRESS ANALYSIS

To ensure feasible blade design, the forces acting on each blade and the resulting stresses must be calculated, and these compared to some stress criteria in order to ensure a blade which can function in its given application and operating conditions. If necessary, the design can be iterated until all structural design requirements are satisfied. With a preliminary blade design accomplished as outlined in the preceding sections, the next step is the calculation of forces and stresses. The methodology for this, which was developed as part of the WEST program, is described in detail in Appendix B.5. The outcome of this procedure is the maximum von Mises stress in the blade, $\sigma_{e,max}$.

Yield Criterion The factor of safety (or safety factor), SF, with respect to plastic deformation of the material (i.e., *yield*) can be calculated using Equation 3.23:

$$SF = \frac{\sigma_y}{\sigma_{e,max}} \tag{3.23}$$

If the safety factor satisfies the criterion specified by the user, then the blade design is complete. If not, then thickness-to-chord ratio of the root can be iterated using the Newton-Raphson method (Appendix B.1) until the required factor of safety is obtained. By increasing the maximum thickness-to-chord ratio at the root (and interpolating the value at the mid-span to be the average of the root and tip values), the root area increases, thus decreasing the stresses. The weight of the blade also increases, which will cause the centrifugal force to grow; however, this effect is typically eclipsed by the increased root area (up to a certain limit). It is suboptimal to increase the thickness at the blade tip, since this increases the blade weight without increasing the cross-sectional area at the root. The stresses are therefore guaranteed to increase in this case.

To reduce high-cycle fatigue in the blades, the allowable stress should typically be limited to around 0.7 of the material yield strength in order to create a margin for vibratory stresses [47]. This corresponds to a recommended blade factor of safety of **1.43** (1/0.7 = 1.4285) with respect to the yield stress criterion.

3.1.1.6. MATERIALS

Material-depedent properties have already been invoked in several equations, such as density in Equation 3.13 and yield strength in Equation 3.23. Material selection is an important part of mechanical design; aircraft engines are subject to extreme temperatures, and their components to extreme stresses, thus the selection of suitable, aerospace-grade materials is an essential step in component development. For this reason, a database of relevant materials can be compiled, one which accounts for the temperature-dependence of various material properties.

Materials Database Table 3.3 shows the physical properties listed for each material in the WEST material database (density being the only temperature-indepdendent property), and Table 3.4 lists the various alloys currently available in the database. The structure shown in Table 3.3 is the same as the one used in GTlab [20]. The material-specific data was compiled from a variety of sources [48–57], and the specific materials selected are consistent with the material databases of other aircraft engine design programs, such as WATE++ and GTlab [18, 20, 22]. However, the material options in these other programs are somewhat more numerous, thus it is recommended to further expand the list of alloys available in WEST's database in order to extend the program's applicability to a wider range of engines.

Table 3.3: Physical material properties accessible through the WEST material database.

	Property	**Symbol**	**Units**
	Density	ρ	kg/m^3
Temp.-Dependent	Elastic (Young's) Modulus	E	Pa
	Shear Modulus	G	Pa
	Ultimate Tensile Strength	σ_{UTS}	Pa
	Yield Strength	σ_y	Pa
	Poisson's Ratio	ν	-
	Coefficient of Thermal Expansion	α	K^{-1}
	Thermal Conductivity	k	W/m·K^1
	Specific Heat Capacity	c	J/kg·K^1

Table 3.4: Materials currently available in the WEST material database [48–57].

Category	Designation
Steel Alloys	17-4PH AISI 4340[1]
Titanium Alloys	Ti-17 Ti-6242 Ti-6Al-4V
High-Temp. Super-Alloys	HASTELLOY S INCONEL 600, 718 NIMONIC 105

[1] Temperature-dependence not accounted for.

While general knowledge of which materials are used in aerospace applications is beneficial, specific alloys must still be selected for particular components/applications. For the study of existing engines where such information is available, the material can be specified directly by the user according to its designation. For components where the material or alloy is unknown – as is usually the case – and for designs of new engines, a material selection procedure is required.

Material Selection In the present methodology, a simple strategy is taken, with material selection depending solely on the maximum local operating temperature, $T_{op,max}$. Determining the operating temperature is a matter in itself and will be discussed in Section 3.1.1.7 for the case of axial compressor blades. For the time being, however, it can be assumed that the maximum local operating temperature of the blade is known. In this case, the material can be determined based on the range of operating temperatures shown in Table 3.5. Note that temperatures in this table are listed in degrees centigrade (°C).

Table 3.5: Material selection based on local maximum operating temperature.

Range of $T_{op,max}$ [°C]	Material
≤ 370	Ti-17
370 - 650	INCONEL 718
> 650	NIMONIC 105

As seen in Table 3.5, no steel alloy will be applied by the program unless specifically chosen by the user. The temperature ranges shown are based on either the maximum operating temperature of that material as listed by the supplier or by the limiting temperatures with regard to the availability of temperature-dependent material properties. Thus, Ti-17, INCONEL 718, and NIMONIC 105 have maximum operating temperatures of 370°C [50], 650°C [54], and 950°C [56], respectively.

3.1.1.7. OPERATING TEMPERATURE

As discussed in the preceding section, all physical material properties except density are temperature-dependent, thus a reasonable estimation of the blade temperature must be obtained in order to evaluate the local material properties accurately. For this, the results of the meanline analysis and preliminary gas path design can be reintroduced, since part of these results include the local gas temperature, which will have a direct effect on the blade surface temperature.

The first step in determining the maximum surface temperature of the blade (and therefore its maximum operating temperature) is the calculation of the average static and total gas temperatures across that row. The average static gas temperature, $T_{s,avg}$, can be calculated using Equation 3.24. In this equation, subscripts n and $n+1$ again denote local station numbering (Figure 2.4), thus $n = 1$ for rotor rows and $n = 2$ for stator rows.

$$T_{s,avg} = \frac{T_{s,n} + T_{s,n+1}}{2} \tag{3.24}$$

Regarding total temperature, this is constant across stator rows, thus for stator rows in the absolute frame of reference, the average total temperature is determined according to the following relation:

$$\left(T_{t,avg}\right)_{stator} = T_{t,2} = T_{t,3} \tag{3.25}$$

For rotor rows, the total temperature should be evaluated in the *relative* frame of reference. Coincidentally, the total temperature is constant across a rotor row when viewed in this reference frame. The average (relative) total temperature for rotor rows can therefore be calculated using Equation 3.26:

$$\left(T_{t,avg}\right)_{rotor,rel} = \left(T_{t,1}\right)_{rel} = \left(T_{t,2}\right)_{rel} = c_p \cdot T_{s,1} + \frac{W_1^2}{2 \cdot c_p} \tag{3.26}$$

Next, the *adiabatic wall* temperature, T_{aw}, can be calculated according to Equation 3.27 [58]:

$$T_{aw} = T_{s,avg} + f_R \left(T_{t,avg} - T_{s,avg}\right) \tag{3.27}$$

In this equation, f_R represents a *recovery factor*. This can be estimated using Equation 3.28 [59] for Prandtl numbers close to unity:

$$f_R = \sqrt[3]{Pr} \tag{3.28}$$

Assuming a representative Prandtl number for air of 0.71 [60], this yields a recovery factor of **0.892**, which is slightly lower than, but comparable to, the value of 0.94 suggested by Walsh and Fletcher [58].

The adiabatic wall temperature resulting from Equation 3.27 can then be used as the relevant operating temperature at which to evaluate material properties for use in the blade stress calculations.

3.1.2. DISKS

The high rotational speeds present in gas turbine engines – partnered with the weight of the blade rows – means that very large centrifugal forces are generated: disks are therefore used to keep the engine from tearing itself apart. They not only hold the blades in place, but they also absorb large stresses and temperature gradients, making them an extremely critical component when viewed from the perspective of mechanical design and material selection. As previously discussed, disks are also a component type responsible for one of the largest shares of total engine weight, meaning that a suitable disk design methodology is imperative in achieving realistic full-engine weight estimations. The methodology presented in this section mainly follows the one proposed by Lolis [21], with the addition of some modifications/corrections, which will be noted. Lolis claims that this method is both a simplified and improved version of the WATE++ methodology proposed by Tong et al. [18].

Figure 3.7 shows an overview of the disk design procedure. If no disk type is specified by the user, then this procedure will be repeated for each of the three available geometry formulations, and the lightest disk which satisfies the stress criteria will be selected. If no disks satisfy the stress criteria, then the one with the smallest violation will be selected. While it is possible to reach a more optimal solution this way, the computational cost increases substantially when all options are evaluated, thus it is recommended to only select the most applicable disk type for a particular application.

3.1.2.1. GEOMETRY

Three disk types will be considered in the present methodology. These are: web disks (Figure 3.8), hyperbolic disks (Figure 3.9), and ring disks (Figure 3.10), which are common in HPCs, HPTs, and LPCs, respectively. The figures below show the relevant dimensions of interest, mainly the radial stations and local thicknesses. Note that the blade airfoil is also shown in each of these figures, but is not actually part of the disk. A real disk may have additional features and connecting hardware, but these slightly simplified representations capture the majority of disk weight and are therefore sufficient for the purposes of weight estimation.

One of the main differences between the methods used by Lolis and Tong et al. is the inclusion/exclusion of the blade root in the disk design and weight [18, 21]. In Lolis' method, everything below r_{hub} is considered to be the disk, when in reality the region between r_6 and r_{hub} is composed partially of blade roots and partially of disk posts. This work follows the simplified approach of Lolis. This assumption means that the weight estimation of the disks will be slightly higher than the real engine components due to the added mass of the blade roots, and the weight estimation of the blades will be lower due to the removal of the blade roots, meaning a direct comparison for these individual component types isn't entirely meaningful. However, the summation of the blade and disk weight estimations should be comparable to the combined weights of the blades and disks in the real engine, thus adding these two component types together provides a means for the meaningful comparison of results.

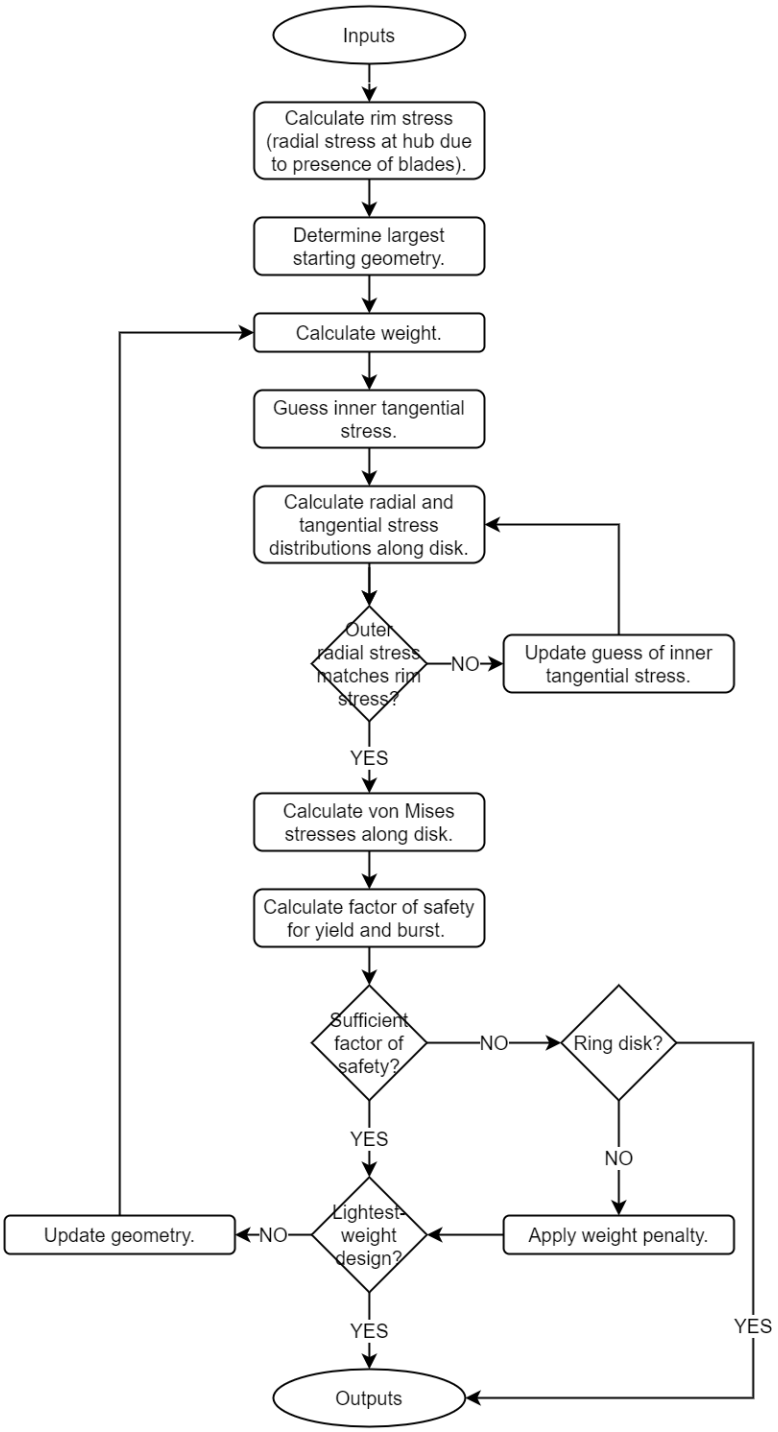

Figure 3.7: Flow chart describing the disk design procedure.

In typical mechanical design, increasing the cross-sectional area results in a decrease of internal stresses, since the forces acting on the object are dispersed over a larger area. With the design of disks, however, increasing the thicknesses also results in more rotating mass, which yields larger centrifugal forces and may actually increase the stresses, having the opposite effect than originally intended. Thus, the disk design with the lowest stresses is some optimized combination of the design variables r_1 through r_6 and t_1 through t_6, with the solution itself not being self-evident. Additionally, reduction of component weight is critical in the design of aeronautical gas turbine engines, so optimization is also required to achieve the lowest-weight design while still adhering to structural requirements. For these reasons, optimization should be employed for the design of every disk in the machine. For a gas turbine engine with several multi-stage compressors and

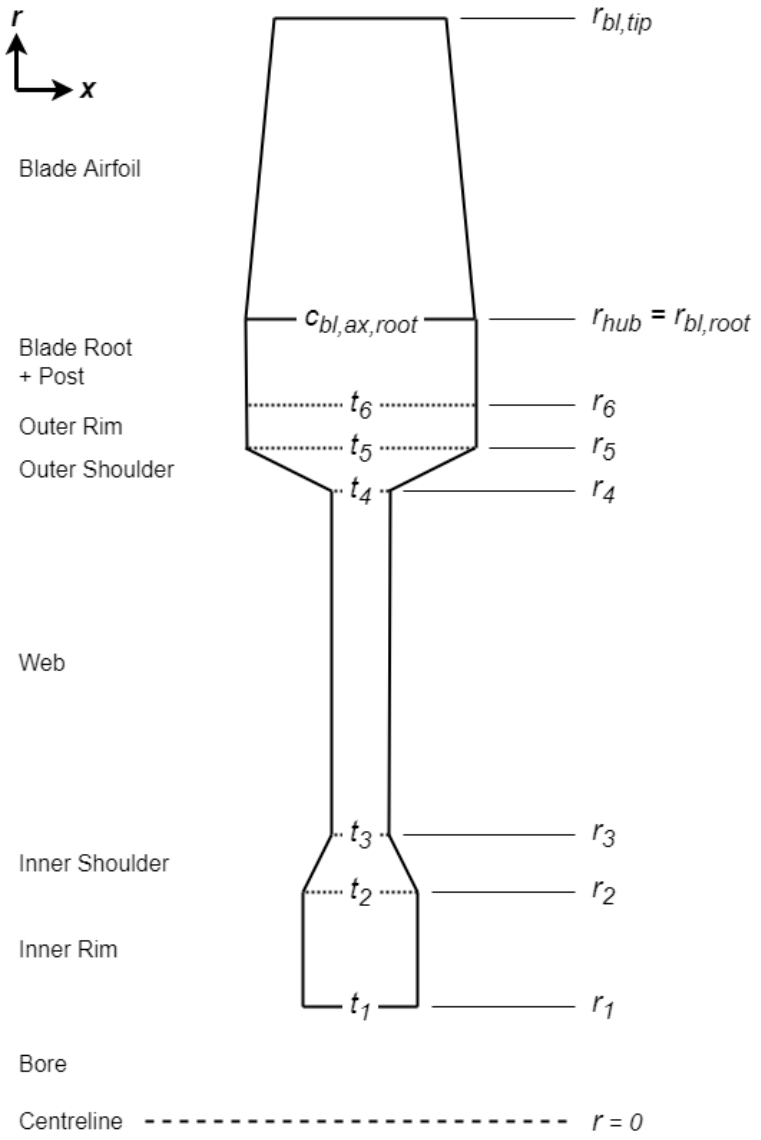

Figure 3.8: Geometry formulation of a web disk [18].

turbines, however, optimizing every disk has the potential to drastically increase the computational cost of the weight estimation simulation. Maintaining a large number of design variables also increases the computation cost, making it beneficial to simplify the design through reducing the number of free variables in the geometry formulation in order to accelerate the design process. Such simplifications will now be discussed for each disk type.

Web Disk For the web disk shown in Figure 3.8, Lolis proposes the following design choices described by Equations 3.29 through 3.35 [21].

$$t_5 = t_6 = c_{bl,ax,root} \tag{3.29}$$

$$t_3 = t_4 \tag{3.30}$$

$$t_1 = t_2 \tag{3.31}$$

$$r_6 = r_{hub} \tag{3.32}$$

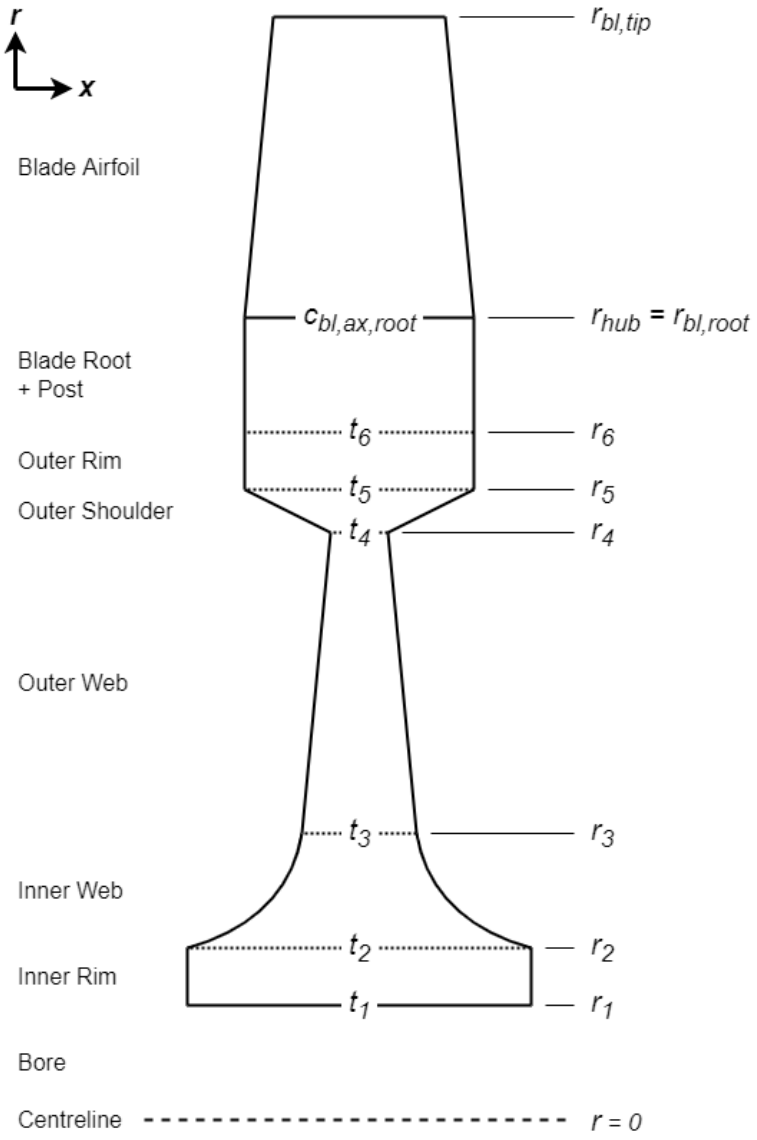

Figure 3.9: Geometry formulation of a hyperbolic disk [18].

$$r_5 = r_6 - \min\left(0.75 \cdot b, \quad 0.75 \cdot t_6\right) \tag{3.33}$$

$$r_3 = r_2 + 0.5 \cdot \frac{t_2 - t_3}{\tan\left(30°\right)} \tag{3.34}$$

$$r_4 = r_5 - 0.5 \cdot \frac{t_5 - t_4}{\tan\left(60°\right)} \tag{3.35}$$

The design assumptions shown in Equations 3.29 through 3.32 are relatively straightforward, and seem to agree well with the general shape of web disks as shown in Figure 3.8. Equation 3.32 accounts for the fact that the blade root is incorporated into the disk weight, not the blade weight, as previously discussed. Equation 3.33 gives an approximate height for the combined blade root and outer rim sections, which is compatible with representative values for blade root height presented by Tong et al. [18]. Finally, Equations 3.34 and 3.35 define radial values r_3 and r_4, respectively, based on assumed shoulder angles. Note that Lolis includes half-angles of $\pi/5$ radians (36 degrees) in both of these equations [21]; however, these were modified to 30° and 60° with respect to the radial axis to be more consistent with the geometry presented in Tong et al. [18].

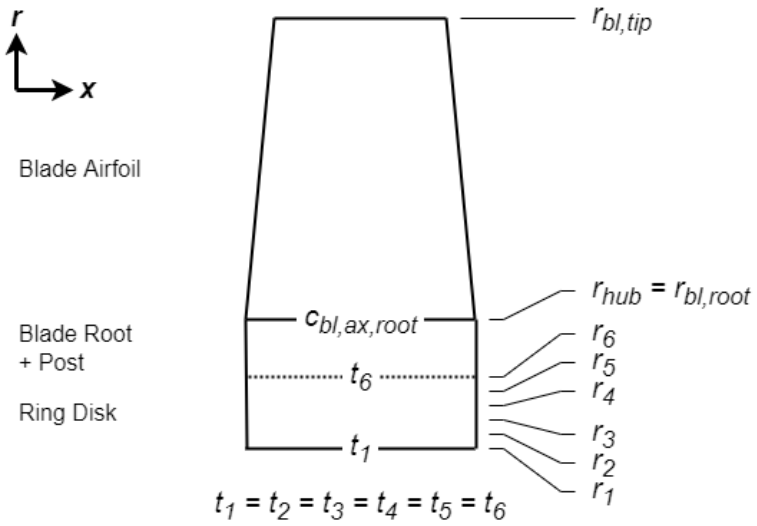

Figure 3.10: Geometry formulation of a ring disk [18].

Equations 3.29 through 3.35 specify eight of the original 12 design variables (r_1 through r_6 and t_1 through t_6), leaving a design vector of only four variables: r_1, r_2, t_2, and t_4. The adopted design choices will therefore significantly reduce the computational cost of the disk optimization procedure, while still allowing for a considerable amount of design freedom.

Next, constraints can be added to design vector variables to constrain the problem such that feasible, realistic designs are obtained. Lolis proposes the constraints shown in Equations 3.36 through 3.40.

$$r_1 \geq 1.1 \cdot r_{sh,max} \tag{3.36}$$

$$r_2 \geq 1.1 \cdot r_1 \tag{3.37}$$

$$r_4 \geq 1.1 \cdot r_3 \tag{3.38}$$

$$1.5 \cdot t_4 \leq t_2 \leq 2 \cdot t_6 \tag{3.39}$$

$$0.3 \cdot t_6 \leq t_4 \leq 0.8 \cdot t_6 \tag{3.40}$$

The first three constraints ensure that radial positions are sufficiently spaced to avoid excessively small geometry features, and to ensure sufficient clearance between the inner rim of the disk and the shaft which may pass through the bore, whose maximum radius is represented by $r_{sh,max}$. The last two constraints provide reasonable bounds for the local thicknesses. The upper limit of $2 \cdot t_6$ for t_2 shown in Equation 3.39 restricts the width of the inner rim to ensure that it does not interfere with the disks of adjacent stages.

Hyperbolic Disk For hyperbolic disks, the same correlations and constraints apply as the web disk, with two exceptions. The location of r_3 is assumed to be one-third of the distance between r_2 and r_4, as shown in Equation 3.41 [21]. Additionally, the inner web is assumed to be straight, for simplicity, instead of curved as is shown in Figure 3.9. Next, the half-angle of this straight section is assumed to be $\pi/4$ radians (or 45 degrees) with respect to the radial direction, meaning that t_3 is a function of t_2 and the difference between r_2 and r_3, as shown in Equation 3.42 [21].

$$r_3 = r_2 + \frac{r_4 - r_2}{3} \tag{3.41}$$

$$t_3 = t_2 - \frac{2 \cdot (r_3 - r_2)}{\tan(\pi/4)} \tag{3.42}$$

One problem that exists in Lolis' formulation is that nothing prevents the value of t_3 from being less than t_4 or even negative (leading to infeasible geometry), which can occur if r_2 is too low. To account for this, an additional constraint can be added in the case of hyperbolic disks, one which ensures that t_3 is no smaller than t_4. Through a combination of several previous correlations, the constraint shown in Equation 3.43 can be derived. This places limitations on the design vector variables r_2, t_2, and t_4 to ensure that $t_3 \geq t_4$.

$$\frac{(t_2 - t_4) \cdot \tan(\pi/4)}{2} - (r_3 - r_2) \geq 0 \tag{3.43}$$

Finally, it is important to note that, in the case of web and hyperbolic disks, *normalized* versions of the constraints are used in the actual code implementation of the WEST disk optimization procedure. This improves the numerical results and the sensitivity of the optimizer to all variables in the design vector. The normalizing parameters can simply be found by evaluating the expressions with the initial disk geometry and then using these as denominators for normalizing the results of the constraints found in each subsequent iteration and/or design vector perturbation.

Ring Disk As shown in Figure 3.10, ring disks feature much simpler geometry than the previous types discussed. The thickness of the disk is constant (Equation 3.44 [21]) and equal to the axial chord of the blade root (Equation 3.29). Radii r_2 through r_6 are also trivial, since they can simply be assumed to be equally spaced between r_1 and r_{hub}. Thus, only one design variable remains – the inner radius, r_1 – changing the design from an optimization problem to an *iteration* problem. The value of r_1 can therefore be modified using the Newton-Raphson iteration method (Appendix B.1) to reduce weight up to the point just before the maximum allowable stresses are exceeded. Calculation of the internal disk stresses and the evaluation of the yield and burst stress criteria are the subject of Section 3.1.2.3.

$$t_1 = t_2 = t_3 = t_4 = t_5 = t_6 \tag{3.44}$$

The same lower limit as web and hyperbolic disks can be used for the ring disk iteration variable r_1, as shown in Equation 3.36. Regarding the upper limit, a typical height of the blade root used in a ring disk is 17.65% of the airfoil height [18]. Multiplying this value by a factor of 1.3 to allow for some ring disk thickness below the lowest point of the blade root means that r_1 should be no larger than the value shown in Equation 3.45:

$$r_1 \leq r_6 - (0.1765 \cdot b \cdot 1.3) \tag{3.45}$$

3.1.2.2. WEIGHT

The weight of any given disk design can be calculated by integrating the circumference and thickness over the full range of radii, as shown in Equation 3.46. This problem can be solved numerically by dividing the disk into discrete, infinitesimal ring elements, calculating the volume of each element, adding them together, and then multiplying by the selected material density for a total disk weight. Determining an appropriate material, and therefore the material density, ρ, is the subject of Section 3.1.2.4.

$$m_{disk} = \rho \cdot \int_{r_1}^{r_6} (2 \cdot \pi \cdot r \cdot t)\, dr \tag{3.46}$$

3.1.2.3. STRESS ANALYSIS

The first step in calculating the stresses in the disk is to determine the rim stress, σ_{rim}, using Equation 3.47 [21]. This is the average stress present at hub, i.e., the root of the blade or the outer radius of the disk, due to the presence of the blades. While the blades are attached only at discrete locations, the force is applied over the entire surface, resulting in the assumption of a uniform rim stress.

$$\sigma_{rim} = \frac{n_{bl} \cdot m_{bl} \cdot r_{G,bl} \cdot \omega^2}{2 \cdot \pi \cdot r_{hub} \cdot c_{bl,ax,root}} \tag{3.47}$$

As is evident from Equation 3.47, the rim stress depends on the number of blades, n_{bl}, the mass of each individual blade, m_{bl}, the radial coordinate of the blades' centre of gravity, $r_{G,bl}$, angular velocity, ω, hub radius, r_{hub}, and the axial chord of the blade at its root, $c_{bl,ax,root}$. All of these values were determined in Sections 2.1.1 and 3.1.1, meaning the calculation of the rim stress is quite straightforward.

If a particular disk geometry is selected, then the stress distribution throughout that disk can be calculated. For this, a guess must be made of the tangential (or hoop) stress at the inner radius (r_1) of the disk, denoted as $\sigma_{h,1}$. With this value assumed, the radial and tangential stresses can be calculated throughout the entire disk, starting at the inner radius and ending at the rim (or hub). For this, the disk can be discretized into infinitesimal ring elements which together compose the entire disk. The methodology for this and subsequent element-by-element stress analysis is described in detail in Appendix B.6. The outcome of this procedure is the distribution of von Mises stress, σ_e, throughout the disk, as well as the average tangential stress, $\sigma_{h,avg}$.

Stress Criteria Two relevant design criteria for disks can now be analyzed using the stresses determined in the preceding calculations. These are the yield criterion and the burst criterion [18]. The von Mises stress, σ_e, can be compared to the yield stress of the material at each local section (accounting of course for the variation in σ_y depending on the local operating temperature) to determine its factor of safety with regard to material yield, as is shown in Equation 3.48. For this criterion, Tong et al. [18] recommends a factor of safety, SF, equal to **1.1**. The burst criterion – shown in Equation 3.49 – compares the ultimate tensile strength of the material, σ_{UTS}, to its average tangential stress, $\sigma_{h,avg}$, and captures plastic material behaviour which is of particular relevance at overspeeds [21]. As will be seen in later validation sections, the results of WEST are compared to WATE++ results developed by Greitzer et al. [22]; in both cases, the engines and their components are sized for take-off conditions, which reduces the likelihood of disk failure.

$$1 - \frac{SF \cdot \sigma_e}{\sigma_y} > 0 \tag{3.48}$$

$$1 - \frac{\sigma_{h,avg}}{0.47 \cdot \sigma_{UTS}} > 0 \tag{3.49}$$

Both the yield and burst criterion are reformulated compared to their forms presented by Lolis and/or Tong et al. [18, 21]. The reformulations – shown in Equations 3.48 and 3.49 – ensure that the calculated stresses appear in the numerator, and the non-zero material properties (σ_y and σ_{UTS}), in the denominator. This was found to improve the numerical stability of the disk design and stress calculation procedure.

3.1.2.4. MATERIALS

The material used in any particular disk can be specified explicitly by the user and selected from the WEST material database. If no material is specified, then one will be chosen automatically with the same procedure as was used for determining blade materials. This methodology is described in Section 3.1.1.6.

3.1.2.5. OPERATING TEMPERATURE AND TEMPERATURE PROFILE

Calculation of material properties, such as the Poisson's ratio, elastic moduli, and coefficients of thermal expansion shown in Equation B.66 or the yield and ultimate tensile strengths shown in the stress criteria (Equations 3.48 and 3.49), depend on the local material temperature. For this, it is important to have an accurate temperature profile applied to the disk, so that the evaluation of such properties are representative of a real component, leading to a final disk design which is as realistic as possible. The temperature profile in compressor disks is relatively trivial, unlike the case for turbine disks, which will be discussed in the next chapter. For compressor disks, Kurzke and Halliwell suggest a uniform temperature equal to the local gas temperature in steady-state operation [24]. Thus, the temperature of the entire disk is assumed equal to the adiabatic wall temperature, T_{aw}, of the corresponding rotor row as calculated in Equation 3.27 during the blade design procedure.

3.1.2.6. OBJECTIVE FUNCTION

As previously discussed, the design of web and hyperbolic disks require optimization. For this, it is beneficial to briefly address a suitable objective function, f_{obj}, with the goal of minimizing this value. The main objective is the reduction of disk weight, with the added constraint that both the yield and burst stress criteria (Equations 3.48 and 3.49, respectively), must be satisfied. Depending on the optimization algorithm and the particular implementation and/or solver, the solution may not always strictly adhere to the specified constraints. For these cases, it is beneficial to add a penalty factor, f_P, to the objective function as shown in Equation 3.50.

$$f_{obj} = \frac{m_{disk}}{(m_{disk})_0} + f_P \tag{3.50}$$

In this equation, the weight of the disk, m_{disk}, is normalized using whatever the weight of the disk was corresponding to the initial design vector, $(m_{disk})_0$. The penalty factor is calculated using Equation 3.51, with the penalty multiplier, f_M, defined in Equation 3.52.

$$f_P = \left| \min\left(1 - \frac{SF \cdot \sigma_e}{\sigma_y}, \quad 1 - \frac{\sigma_{\theta,avg}}{0.47 \cdot \sigma_{UTS}}\right) \right| \cdot f_M \tag{3.51}$$

$$f_M = \begin{cases} 0, & \min\left(1 - \frac{SF \cdot \sigma_e}{\sigma_y}, \quad 1 - \frac{\sigma_{h,avg}}{0.47 \cdot \sigma_{UTS}}\right) \geq 0 \\ 20, & \min\left(1 - \frac{SF \cdot \sigma_e}{\sigma_y}, \quad 1 - \frac{\sigma_{h,avg}}{0.47 \cdot \sigma_{UTS}}\right) < 0 \end{cases} \tag{3.52}$$

In these equations, the absolute value of the minimum stress criteria (which is already normalized) is added to the normalized weight in the objective function, multiplied by a certain factor. For designs which satisfy the stress criteria, this multiplication factor is zero, as shown in Equation 3.52, meaning the objective function is based solely on the minimization of disk weight. For designs which violate the stress criteria, the normalized stress is multiplied by a factor of **20**. This value was carefully tuned in order to provide the desired optimization results: a lower penalty factor means the stress criteria is not as heavily enforced, meaning some designs could turn out to have factors of safety slightly lower than the requirements. A higher penalty factors and the optimizer will be so heavily influenced by the stresses that the optimal, lowest-weight disk will not be selected. Thus, a factor of 20 was found through trial and error, although the preferred value of f_M may depend on the particular implementation of this methodology or the particular machine used to run WEST.

3.1.3. CASING

Like ducts, casings form part of the gas path channel and must therefore be able to contain the high pressures present in the working fluid. Casings must also be designed to contain blade fragments in case of failure and subsequent detachment, since blades have a large amount of kinetic energy due to the high rotational speeds present in gas turbine engine spools. The kinetic energy of disks and/or disk fragments is generally too large to absorb, meaning this is not part of the design criteria. Thus, while detailed aspects of casings such as flanges, connecting hardware, and actuators for variable stator vanes (if applicable) will not be modelled in the present methodology, a representative idea of total casing weight is still possible through calculation of local thicknesses using a physically-based approach to pressure and blade fragment containment.

3.1.3.1. LOCAL THICKNESSES

With meanline analysis and stage design completed in the preceding sections, all information required for estimating necessary casing thicknesses is known. This can be done on a row-by-row basis, with the final casing design being a connection of these discrete calculation points, resulting in a variable-thickness component.

Blade Containment The first step in calculating local casing thickness in the case of rotor rows is to determine the kinetic energy, E_{kin}, of the blade fragment/segment which detaches. To analyze the most critical scenario, it will be assumed that the entire blade airfoil detaches, thus the full weight of the blade can be used as shown in Equation 3.53 [61]:

$$E_{kin,bl} = \frac{m_{bl} \cdot r_{G,bl}^2 \cdot \omega^2}{2} \tag{3.53}$$

Next, the casing thickness required for blade containment, $t_{con,bl}$, is determined using Equation 3.54 [61]. In this equation, variables S_1 and ξ represent a calibration factor and consolidation coefficient, respectively. Variables υ, μ, and κ are empirical coefficients representing the ductile, elastic, and shear portions of the overall deformation energy, respectively. Each of these is defined in Equation 3.55 [61].

$$t_{con,bl} = S_1 \sqrt{\frac{E_{kin,bl}}{0.65 \cdot \xi \cdot \sigma_{bn,max} \cdot \left(\upsilon + \mu + \frac{\kappa}{2}\right) \cdot l^*}} \tag{3.54}$$

$$S_1 = 2.0, \quad \xi = 1.3, \quad \upsilon = 0.7, \quad \mu = 0.05, \quad \kappa = 2.5 \tag{3.55}$$

The term $0.65 \cdot \xi \cdot \sigma_{bn,max}$ in the denominator of Equation 3.54 represents the maximum impact strength, with $\sigma_{bn,max}$ being the maximum bending stress. In this present analysis, $\sigma_{bn,max}$ will simply be assumed equal to the yield strength of the material, σ_y, at the local temperature, since no further explanation regarding

the definition of maximum bending stress is given by Bretschneider et al. [61]. The reference length, l^*, is chosen as the perimeter length of the blade tip airfoil, since this is the point of impact where the rotor blade contacts the casing [61]. This can be calculated explicitly using the tip airfoil designed during the blade design procedure.

Pressure Containment The casing thickness required for pressure containment, $t_{con,pr}$, can be calculated using Equation 3.56 [21]. In this equation, p_s represents the static pressure at the local station, r the local radius (i.e., the blade tip radius, since this is synonymous with the casing inner radius), and σ_y the local yield strength of the material. SF represents an optional factor of safety, although since the thickness for containing blade fragments far surpasses the one for pressure containment [61], this safety factor is not particularly relevant.

$$t_{con,pr} = SF \cdot \frac{p_s \cdot r}{\sigma_y} \tag{3.56}$$

Equation 3.56 can be repeated for the inlet (i) and outlet (o) stations of the particular blade row, since the static pressure will be different between these two locations. The minimum required local casing thickness can therefore be calculated using Equation 3.57:

$$t_{cas} = \max\left(t_{con,bl}, \quad \left(t_{con,pr}\right)_i, \quad \left(t_{con,pr}\right)_o\right) \tag{3.57}$$

It is important to note at this stage that the method for joining the discrete thickness values has an effect on total casing weight estimation. A smoothing between values to produce a more continuous outer profile of the casing will result in additional volume and therefore a higher weight estimation, which is not necessarily negative since some aspects of the casing are not modelled, as previously mentioned. Depending on the manufacturing methods used, smoother geometry may also be preferred, meaning this may also be the more realistic approach. However, without detailed knowledge of the casing designs of real engines, it is difficult to determine the ideal method of joining the discrete thicknesses into a continuous casing design.

3.1.3.2. TEMPERATURE

The maximum operating temperature of the casing can be determined in a similar as was done for blades in Section 3.1.1.7. For this, the adiabatic wall temperature can be calculated using Equation 3.27, with the same recovery factor and method for calculating static temperature. The only exception is the way in which total temperature is determined: since the casing is non-rotating, total temperature should be calculated in the absolute frame of reference, thus Equation 3.26 should be replaced by Equation 3.58:

$$\left(T_{t,avg}\right)_{rotor} = \frac{T_{t,1} + T_{t,2}}{2} \tag{3.58}$$

For selecting a suitable material, the maximum operating temperature for all locations in the casing should be used, whereas the yield strength used in thickness calculations (Equations 3.54 and 3.56) should be determined based on the local operating temperature of the specific row.

3.1.4. OTHER

This section discusses the weight estimation of other components of compressors, which do not contribute a large share to compressor weight and for which the design methodology is either very simple, e.g., stator vane shrouds, or nonexistent, e.g., connecting hardware, which uses an empirical correlation for weight prediction. These components are addressed in Sections 3.1.4.1 and 3.1.4.2, respectively. Figure 3.11 [17] illustrates the typical components used in a single stage of an axial turbomachine, showing the relationship between inner shrouds, connecting hardware, and the components already discussed (e.g., blades, disks, and casing).

3.1.4.1. INNER SHROUD

While the casing represents the outer portion of the gas path channel, the inner portion has not yet been accounted for. Shrouded tips can be applied to all stator vanes in order to define the shape of the gas path and to provide the necessary pressure containment. Thus, shrouds apply to stator rows only. Additionally, the weight of the shroud will be included in the weight estimation of the *stator vanes* (blades), not as a separate component.

The thickness of the shroud will depend on the specific row being analyzed. Using the pressure containment equation shown in Equation 3.56 and used during the casing design, the minimum required thickness

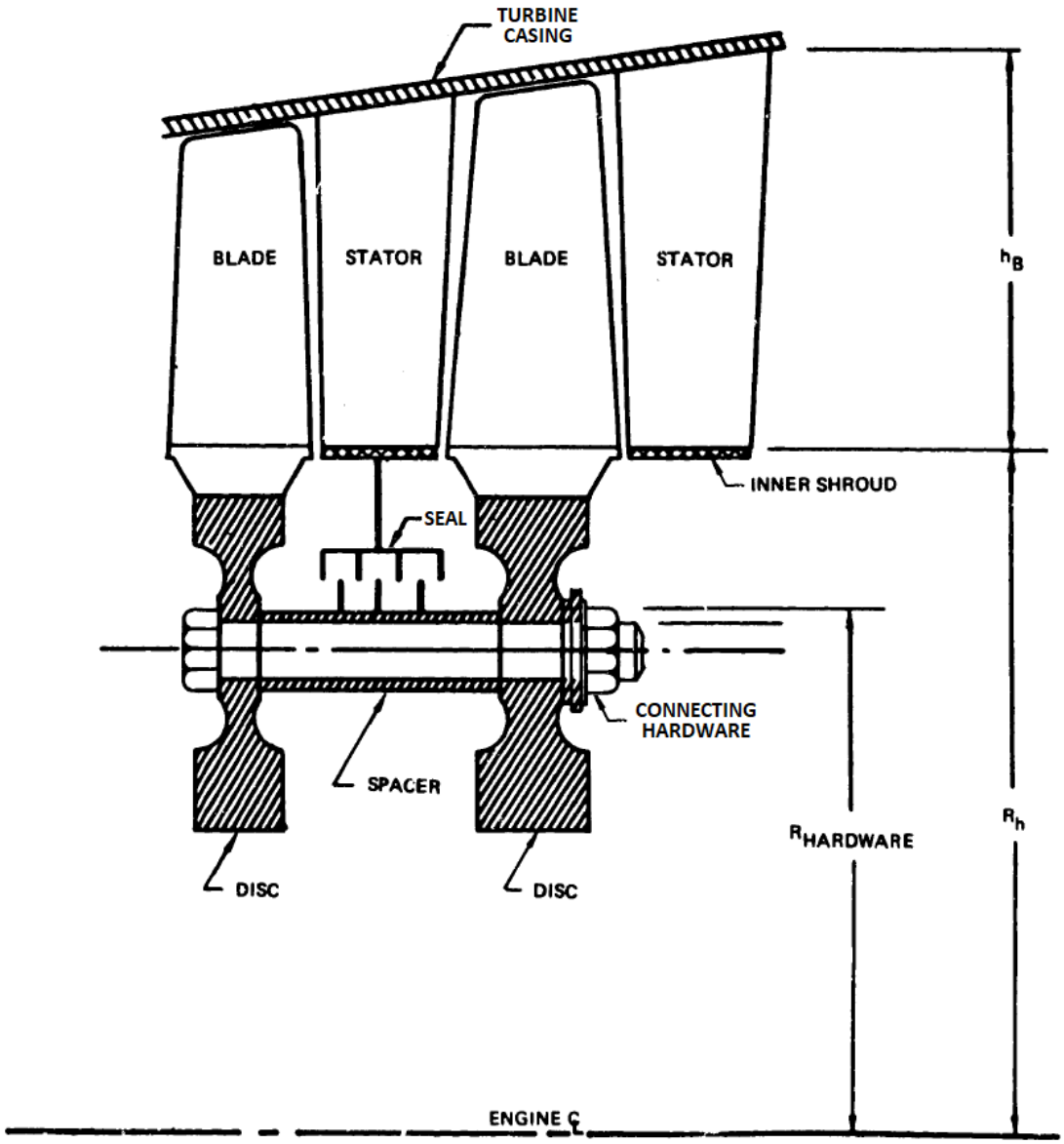

Figure 3.11: Typical stage components of an axial turbomachine [17].

of the shroud can be determined, one which can sufficiently contain the pressure of the working fluid. The static pressure is available from the meanline analysis, and the material and local temperature (which are necessary for determining the local yield strength) are assumed to be the same as the blade. The radius is simply the inner radius of the gas path at that location.

With the compressor casing, variable thickness was accepted since the probable manufacturing methods (e.g., casting, forging, machining) allow for this. However, in the case of stator vane inner shrouds, a fixed sheet metal thickness is likely preferable, meaning that the required thickness should be calculated using Equation 3.56 at both the leading and trailing edges of the row, and then these two results combined (i.e., the larger of the two used) such that the component has a single, uniform thickness. This thickness can then be rounded *up* to the nearest sheet- or plate-metal gauge according to the standardized sizes listed in Table 3.6 [62, 63]. For example, a required thickness of 6.789 mm should be rounded up to the nearest multiple of 2.00 mm (i.e., 8.0 mm) based on the increment(s) listed in Table 3.6.

The weight of a particular shroud is therefore the volume of a conical shell multiplied by the (blade) material density. The LE/TE radii of the shell and its length correspond to the gas path design for that particular row, and the thickness corresponds to the sheet metal thickness determined using Equation 3.56 and Table 3.6. Note that a minimum thickness of 1.00 mm is enforced for ducts and shrouds.

Table 3.6: Standardized sheet and plate metal thickness increments [62, 63].

Range of t [mm]	**Increment [mm]**
≤ 1.0	0.10
1.0 - 2.0	0.25
2.0 - 3.0	0.50
3.0 - 3.2	0.20 (= 3.2)
3.2 - 6.0	1.00
6.0 - 10.0	2.00
10.0 - 15.0	2.50
15.0 - 20.0	5.00 (= 20.0)
20.0 - 22.5	2.50 (= 22.5)
22.5 - 30.0	5.00
30.0 - 32.0	2.00 (= 32.0)
32.0 - 80.0	5.00
80.0 - 130.0	10.0
130.0 - 150.0	20.0 (= 150.0)
150.0 - 200.0	20.0
≥ 200.0	50.0

3.1.4.2. CONNECTING HARDWARE

The last component type which can be considered a part of an axial compressor and which requires weight estimation is the connecting hardware. Shafts are used to transmit torque and power between devices, e.g., a compressor and turbine, but it is the connecting hardware which is used to connect multiple rotor stages of the same turbomachine and transmit torque between them. Suitable design methods for such hardware do not exist in open literature [21], so the weight of these components will be estimated using a modified version of the empirically-based correlation proposed by Onat and Klees [17], which represents the hardware as thin-walled cylindrical elements. The connecting hardware (denoted with subscript chw) can be divided into discrete segments, each segment representing the hardware connecting the disks of two consecutive stages. The mass of such a segment, $m_{chw,seg}$, can be estimated using Equation 3.59 [17]:

$$m_{chw,seg} = 2 \cdot \pi \cdot r_{chw,avg} \cdot l_{seg} \cdot t_{chw} \cdot \rho \tag{3.59}$$

In this equation, $r_{chw,avg}$ represents the average hardware radius, which can be calculated for each of the joined rotor disks using Equation 3.60, and the average taken.

$$r_{chw} = r_1 + 0.75 \cdot (r_6 - r_1) \tag{3.60}$$

The length of the segment, l_{seg}, can be determined based on the axial distance between the two disks as found during the gas path and disk design procedures. The wall-thickness of the cylindrical element, t_{chw}, is assumed to be **2.0 mm**, and the material is assumed to be steel [17].

In Onat and Klees' original formulation, the hardware radius is assumed to be 75% of the disk outer radius (r_6), but for short ring disks, this means that these components would not even connect to the disk. Thus, the methodology was updated to calculate the radius using Equation 3.60 so that the hardware will always be in contact with adjoining disks.

Finally, the total connecting hardware weight can be estimated using Equation 3.61:

$$m_{chw} = \sum m_{chw,seg} \tag{3.61}$$

3.2. VERIFICATION AND VALIDATION

Verification and validation are important steps in the development of scientific design methodologies and their practical implementation with respect to software development. The objective of this section is to describe the validation efforts relating to axial compressors and the methodologies presented in Section 3.1. Such analysis aims at improving confidence in the final results and providing an evaluation of their accuracy. Since axial compressors represent an important building-block in engine design, this section will also give an initial idea of WEST's potential in generating realistic preliminary engine designs and weight estimations, although validation efforts of other components and of full engine designs are relegated to later chapters. Section 3.2.1 provides an in-depth description of the inputs used so that the results (Section 3.2.2) can be reproduced. Finally, the results are discussed in Section 3.2.3.

3.2.1. INPUTS

Two engines will be used for validation, the CFM56 and the PW2037, which provides four validation cases for axial compressors since each of these has both a low-pressure and high-pressure compressor. Performance data for these engines is shown in Table 3.7 [22] for sea-level static conditions.

Table 3.7: Sea-level static performance of existing engines [22].

Parameter	Symbol	CFM56-7B27	PW2037	Units
Mass Air Flow Rate	$\dot{m}_2$	351.1	547.5	kg/s
Bypass Ratio	BPR	5.0	5.77	-
Fan Pressure Ratio	FPR	1.72	1.61	-
Overall Pressure Ratio	OPR	27.8	26.4	-
Compressor Pressure Ratio[1]	CPR	10.3	10.5	-
Spool 1 Speed	N_1	5380	4575	RPM
Spool 2 Speed	N_2	15183	12250	RPM
Stage Count[2]	n_{stg}	1/3/9/1/4	1/4/12/2/5	-
Fan Diameter	D_{fan}	1.549	1.994	m
Weight/Mass	m	2400	3311	kg

[1]Of high-pressure compressor (HPC). [2]Of fan/LPC/HPC/HPT/LPT.

In Table 3.7, the air mass flow rate, $\dot{m}$, (i.e., the total for both the core and bypass flows) has the subscript 2. This subscript corresponds to the engine-level thermodynamic station nomenclature described by SAE Aerospace Standard AS755 and shown in Figure 3.12 [24]. As is evident in this figure, neither the mass flow rate nor the thermodynamic properties at the engine inlet will be the same as those of the LPC inlet (station 21) or HPC inlet (station 25). Thus, a few steps must be taken to convert the data in Table 3.7 into useful, compressor-specific inputs.

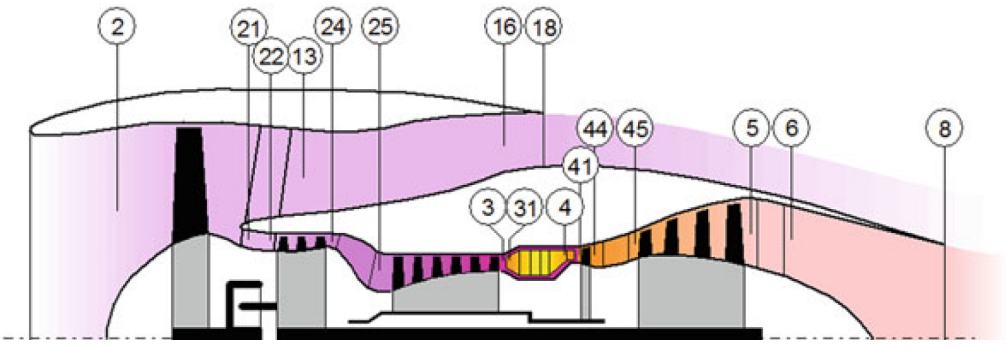

Figure 3.12: Thermodynamic station nomenclature of turbofan engine [24].

Firstly, the total air mass flow rate, $\dot{W}T_2$, can then be converted into the core mass flow rate, $\dot{m}_{21}$, using the bypass ratio as shown in Equation 3.62.

$$\dot{m}_{21} = \frac{\dot{m}_2}{1+BPR} \tag{3.62}$$

Since the fan is not part of the engine's core – or gas generator – it is currently not modelled in WEST, thus the fan's outlet properties can be estimated using a few simple correlations. The total pressure at the fan outlet can be calculated using Equation 3.63. Assuming a fan polytropic efficiency of **0.85**, the total temperature at the fan outlet can be calculated using Equation 3.64.

$$P_{t,21} = P_{t,0} \cdot FPR \tag{3.63}$$

$$T_{t,21} = T_{t,0} \cdot FPR^{\frac{\gamma-1}{\gamma \cdot \eta_{pt,fan}}} \tag{3.64}$$

Since the properties in Table 3.7 are for sea-level static conditions [22], the total temperature ($T_{t,0}$) and pressure ($P_{t,0}$) at the engine inlet can be taken as **298.15 K** and **1.01325 bar**, respectively. Also, the working fluid is assumed to be dry air, just as with axial compressors, thus the properties of the working fluid are also known (see Table 2.2). The total specific work done by the fan can therefore be calculated using Equation 3.65, followed by the power in Equation 3.66.

$$w_{t,fan} = c_p \cdot \left(T_{t,21} - T_{t,0}\right) \tag{3.65}$$

$$\dot{W}_{fan} = \dot{m}_2 \cdot w_{t,fan} \tag{3.66}$$

The pressure ratio of the high-pressure compressor, PR_{HPC}, is already known: this the value of CPR listed in Table 3.7. The pressure ratio of the low-pressure compressor, PR_{LPC}, can therefore be calculated using Equation 3.67:

$$PR_{LPC} = \frac{OPR}{FPR \cdot CPR} \tag{3.67}$$

Thus, the thermodynamic inputs for the LPCs of the CFM56 and PW2037 engines can be calculated using the data in Table 3.7 and the procedure described above. The input parameters for the HPCs correspond to the outlet properties of the LPCs, thus these can be determined using the meanline performance calculations described in Section 2.1.1.2, or simply by running a full-engine model in WEST, which automatically links the inputs/outputs of these two components. The data needed to perform the preliminary sizing of the CFM56 and PW2037 at take-off conditions are summarized in Table 3.8. Note that data corresponding to the HPCs are for reference only, since these are calculated by the program automatically.

Table 3.8: Thermodynamic input parameters for compressors of CFM56 and PW2037.

		CFM56		PW2037	
Parameter	**Units**	**LPC**	**(HPC)**	**LPC**	**(HPC)**
$\dot{m}$	kg/s	58.5	58.5	80.9	80.9
PR	-	1.57	10.3	1.56	10.5
N	RPM	5380	15183	4575	12250
$P_{t,in}$	bar	1.74	2.73	1.63	2.55
$T_{t,in}$	K	357.8	412.9	349.9	403.0

As seen in Table 2.1 and Table 2.3, more information is required in order to close the model for the estimation of the axial compressor weight. For this, cross-sections of the CFM56-5B and PW2037 were obtained from Jane's Aero-Engines [64, 65]. Digitization was performed on these cross-sections in order to make estimates of the blade aspect ratios, row and stage gaps, and taper ratios. In addition to these non-dimensional design parameters, the maximum outer diameter, total length (excluding inlet guide vanes), and shaft radius were also measured. These results are presented in Table 3.9.

The outer radius and length of the compressors are included in Table 3.9 for reference only, since these are not explicit inputs of the program, while other parameters such as the duty coefficients were then optimized in order to obtain the prescribed outer radius and length. This was performed using a built-in optimization function specifically designed for this purpose. Some of these parameters, such as row/stage gaps or taper ratios, vary per stage, thus measurements of multiple rows were made (e.g., first and last) during the digitization process and the averages were then taken and used as inputs.

Table 3.9: Mechanical design input parameters for compressors of CFM56 and PW2037.

			CFM56		PW2037	
Category	**Parameter**	**Units**	**LPC**	**HPC**	**LPC**	**HPC**
Dimensions	Outer Radius	m	(0.494)	(0.306)	(0.554)	(0.330)
	Length[1]	m	(0.379)	(0.488)	(0.379)	(0.860)
Duty Coefficients[2]	Flow Coefficient, ϕ	-	0.719	0.495	0.713	0.586
	Work Coefficient, ψ	-	0.212	0.333	0.234	0.317
	Degree of Reaction, R	-	0.555	0.598	0.556	0.631
General Design	Working Fluid		Air	Air	Air	Air
	Number of Stages, n_{stg}	-	4	9	4	12
	Fixed Diameter[3]		Hub	Hub	Hub	Mid
	Inlet Guide Vane		Yes	Yes	Yes	Yes
Aspect Ratios, AR	First Stage Rotor	-	1.80	2.1	2.562	2.997
	Last Stage Rotor	-	1.54	1.7	2.569	1.597
	First Stage Stator	-	2.60	3.7	2.761	2.636
	Last Stage Stator	-	2.12	1.7	2.808	1.369
Gaps, g	Row	-	0.28	0.25	0.312	0.503
	Stage	-	0.425	0.45	0.292	0.478
Taper Ratios, λ	Rotor	-	0.847	0.85	0.774	0.740
	Stator	-	1.0	1.0	1.053	0.978
Disk Design	Disk Type		Ring	Web	Ring	Web
	Max. Shaft Radius	m	0.305	0.058	0.328	0.070
Materials	Rotor Blade Material 1		Ti-17	Ti-17	17-4PH	17-4PH
	→ Stages	-	All	1-3	All	1-9
	Rotor Blade Material 2			17-4PH		IN 718[4]
	→ Stages	-		4-9		10-12
	Stator Vane Material 1		Ti-17	17-4PH	17-4PH	17-4PH
	→ Stages	-	All	All	All	All
	Stator Vane Material 2					
	→ Stages	-				
	Disk Material 1		Ti-17	Ti-17	17-4PH	17-4PH
	→ Stages	-	All	1-6	All	1-9
	Disk Material 2			IN 718[4]		IN 718
	→ Stages	-		7-9		10-12
	Casing Material		17-4PH	17-4PH	17-4PH	17-4PH

[1]Total length excluding guide vane. [2]Obtained by optimizing for the prescribed bounding dimensions using the other inputs as listed below. [3]I.e., annulus type. [4]INCONEL 718.

Information about compressor materials was also not always available. The titanium and INCONEL alloys shown are the same as those used by Greitzer et al. in developing WATE++ models of the same engines [22]. The stage at which materials change was not noted. For these cases, the temperature-dependent material selection procedure described in Section 3.1.1.6 was used. In other cases, material data was available. For example, the HPC of the CFM56 uses titanium for the first three rows of rotor blades and steel for everything after, as well as for all stator vanes [64]. However, the exact alloys of titanium and steel were not specified, so Ti-17 and 17-4PH were assumed, respectively, to be consistent with Greitzer et al. [22].

Even less was known about the materials used in the PW2037 than the CFM56. In general, a largely steel-based material selection was used since doing so yields results more consistent with the WATE++ results (as will be discussed in the next sections), although this remains an open-ended assumption. Visual inspection of the PW2037 shows a noticeable difference in disk design for stages 10 to 12 of the HPC, implying a different material for these rows compared to the first nine. Thus, higher-temperature alloys were used for the last few rows of the HPC, beginning at stage 10.

Overall, the numerous material-related assumptions will have a large effect on weight estimation, and since it is unclear whether steel is the most-used material in the PW2037, a second material combination will be applied as well to investigate the sensitivity of the results to choice of material. This is discussed more in depth in a later section (Section 3.3.6).

3.2.2. RESULTS

Figure 3.13 shows the meanline performance analysis as well as the gas path, blade, disk, and casing design results of the CFM56 high-pressure compressor, the latter being displayed in the form of an engine cross-sectional side view. Similar plots are provided in Appendices C.1.1.1 through C.1.1.3 for the other axial compressor validation cases. Since the engine cross-section does not show the blade airfoils nor their spanwise twist distribution, representative top-view blade design results are shown in Figure 3.14. These correspond to the first stage of the CFM56 HPC. Figure 3.15 shows an example of the distribution of stresses throughout a disk, also for the first stage of the CFM56 HPC. Figure 3.16 shows the same plot, only assuming this was designed with a ring disk instead of a web disk. Table 3.10 gives the weight estimation results of the compressors, including a breakdown by component type. These are compared to benchmark WATE++ results provided by Greitzer et al. [22], which are used to evaluate the accuracy of the WEST design methodology and its practical implementation. Finally, Figure 3.17 shows real CFM56 HPC rotor blades (stages 3 and 6), with Table 3.11 [64] offering a comparison between the properties of these blades and the design results generated by WEST.

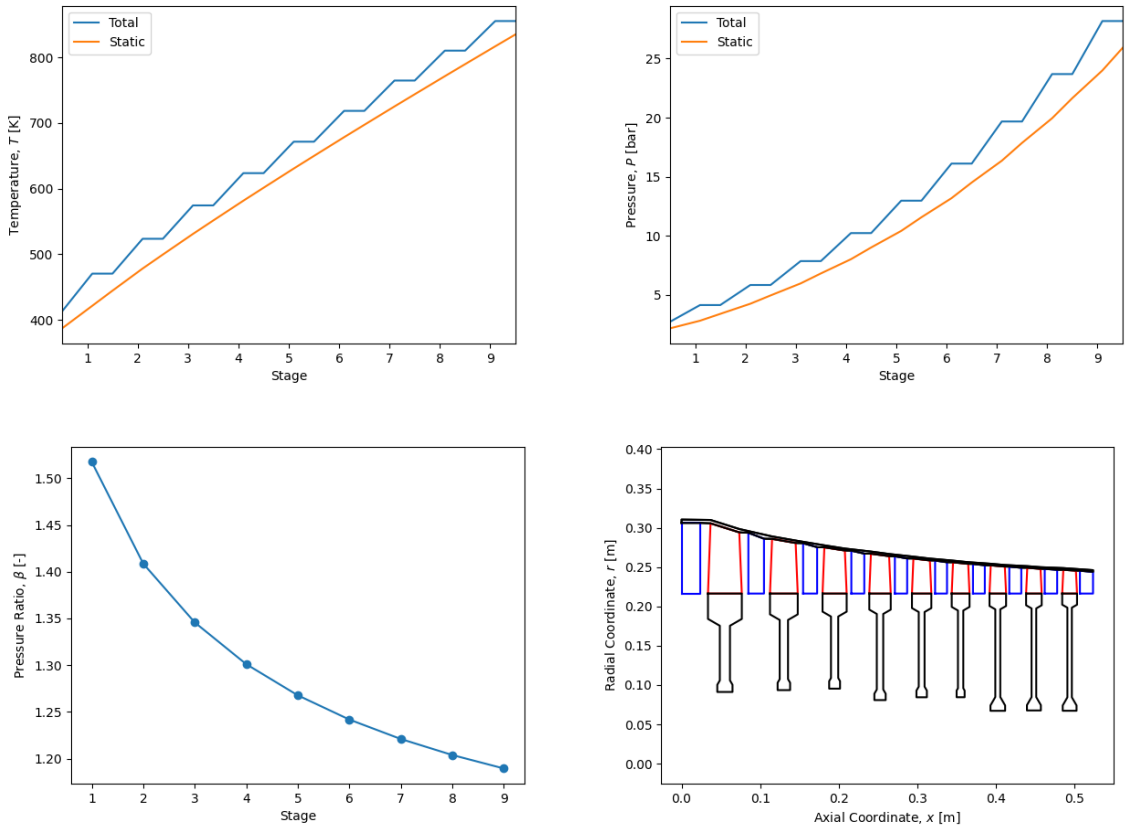

Figure 3.13: Meanline performance and mechanical design results of CFM56 HPC.

3.2.3. DISCUSSION

As shown in Figure 3.13 (as well as Figure C.1, Figure C.2, and Figure C.3 for the other axial compressor validation cases), the results of the meanline analysis are consistent with expectations and do not present any unexpected trends: the total temperature and pressure increase over rotor rows, implying addition of work, and are constant across stator rows, while the static properties increase continually. For machines with constant hub diameter, the amount of specific work done per stage decreases slightly along the flow path, which is expected based on the adoption of the same duty coefficients for the repeating stages. The individual-stage pressure ratio decreases along subsequent stages, which can be explained by the fact that the specific work is decreasing and the magnitude of the pressures is rising, meaning the ratio of outlet/inlet pressure will decrease. All the results in the plots exhibit physical behaviour and therefore provide some level of verification with regard to the implementation of the meanline design code.

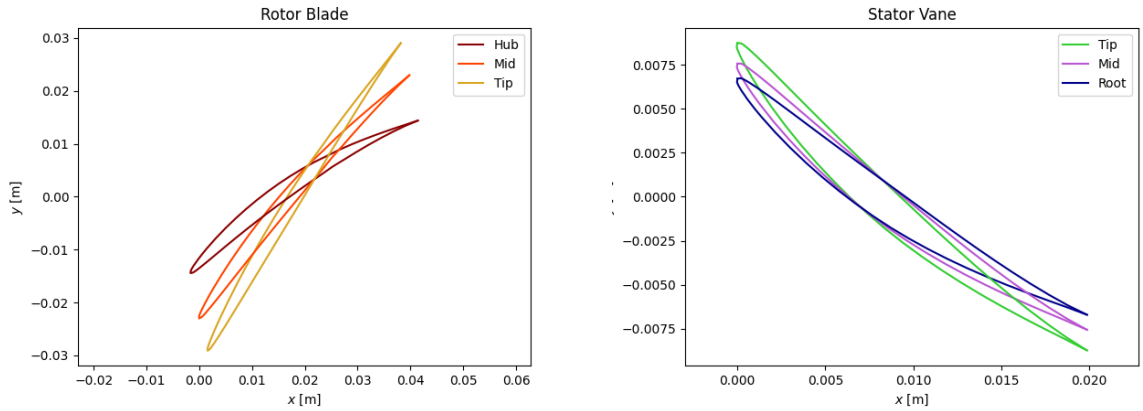

Figure 3.14: Spanwise blade profiles of CFM56 HPC first stage.

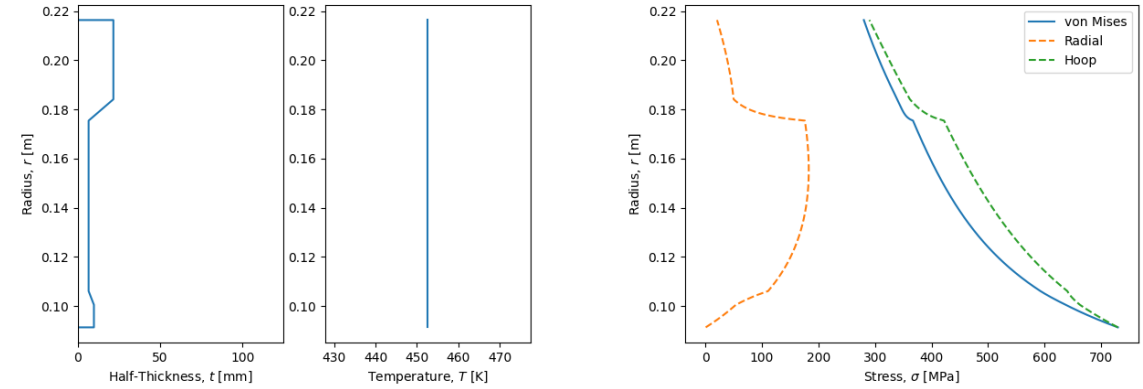

Figure 3.15: Stress distributions of CFM56 HPC first stage (web) disk.

The compressor cross-section shown in Figure 3.13 also represents a reasonable design solution, with the gas path channel height decreasing along the flow path in order to maintain a constant mass flow rate despite the rising pressures. The disk designs are consistent with the (web) disk geometry formulation, and the slightly different design shown in the last three disks should be expected since the material changes for these final stages. The blade profiles in Figure 3.14 also exhibit twist, with the rotor rows having higher angles close to the tip due to the higher tangential velocity at these locations and the assumption of constant meridional velocity with application of the Free Vortex design method. Thus, all mechanical design results appear reasonable.

For both the CFM56 and PW2037 cases, an additional, high-level source of validation relating to the meanline and gas path design are the duty coefficients obtained using the built-in optimization method. While many non-dimensional design parameters (aspect ratios, taper ratios, row/stage gaps) were estimated using the engine cross-sections and then applied to the compressor model, the duty coefficients were optimized to achieve the same outer radius and total length as the actual engine (these dimensions also being determined using digitization). The results of this data fitting procedure are exceedingly promising, with all of the duty coefficients (Table 3.9) falling within the expected ranges laid out previously in Table 2.2. The only exception to this are the work coefficients of the two low-pressure compressors, which fall below the expected range. This makes sense, however, since LPCs do not perform a significant amount of work. For example, the LPC pressure ratios of the CFM56 and PW2037 are 1.57 and 1.56, respectively, according to the data presented in Table 3.7, while both of these compressors have four stages. This is far below the pressure ratio of 10.3 accomplished by the CFM56 HPC in only nine stages. Thus, the fact that the optimized duty coefficients all lie within or very close to typical values expected for axial compressors validates the implementation of the meanline and gas path design procedure and builds confidence in the methodology for the purposes of engine preliminary design.

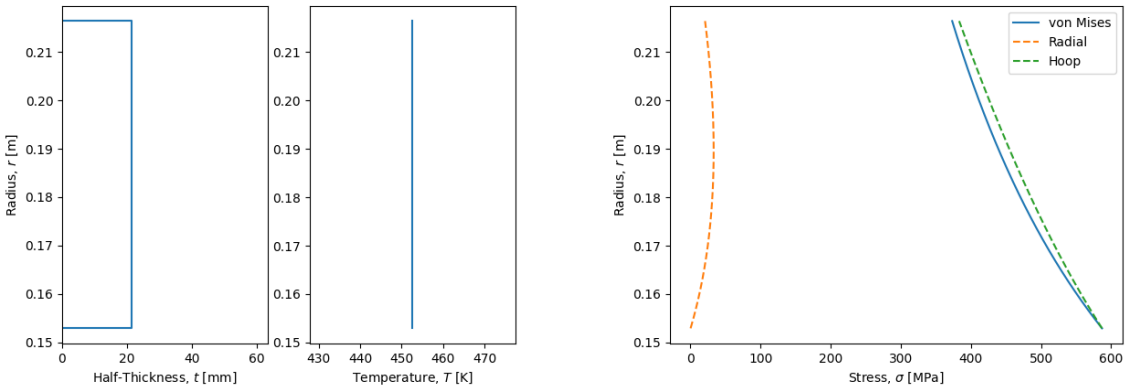

Figure 3.16: Stress distributions of CFM56 HPC first stage (ring) disk.

Figure 3.16 shows the stress distribution through the CFM56 HPC first stage disk when it is designed as a *ring* disk. As is evident from this figure, the radial stresses are zero at the inner radius and non-zero at the outer radius, which is expected since the blades impose a radial stress at the disk hub. The tangential/hoop stresses are significantly larger, but decrease gradually towards the hub. The inner radius of the disk is typically the critical stress region [24], so these results are consistent with expectations in that regard. The constant thickness of the ring disk means smooth geometry, and since the stress distributions are also smooth, all of the results appear to be feasible and physically-sound. As is apparent from the nearly 600 MPa maximum stress, high-strength aerospace-grade materials are required for the construction of gas turbine disks.

With the stress distribution of ring disk appearing quite reasonable, those of web disks can now be examined. Web disks feature variable thicknesses, meaning corners – and therefore stress concentrations – will be present, thus leading to more complex stress distributions. Figure 3.15 shows the stresses throughout the CFM56 HPC first stage disk that is of the web type. Here, stress peaks are indeed observed in locations where the thickness changes sharply. Overall, however, the profiles shown in Figure 3.15 appear fairly consistent with the stress distribution examples given by Kurzke and Halliwell and reproduced in Figure 3.18 [24]. The main difference exists near the hub of the disk, where Kurzke and Halliwell's stress results drop sharply. This is not the case in the present results due to the assumption that blade roots are part of the disk: if blade roots were to be modelled individually, then the radial stresses would apply throughout the root region and drop off near the hub, and the hoop stresses would also reduce substantially near the outer radius since the disk outer region is discontinuous due to the presence of the blade post. Thus, the disk stress results appear physical, with the exception of some small effects due to the simplifying assumptions of the present disk design and stress analysis methodology.

The predicted weight of the compressors and related subcomponents provide some level of insight into the validity of the implemented methodology. See Table 3.10. If the design and weight estimation of each component and subassembly is realistic, then it is more likely that that of the total engine will be as well.

As shown in Table 3.10, the weight estimation results of the present methodology appear roughly consistent with the benchmark WATE++ data. At the very least, all components are within the right order of magnitude. The relative error between the two result sets varies from -11.2% to -26.9% for compressor-level assemblies, which seems quite good, although the variance for specific component types is sometimes much larger (up to -52.9%). This shows that underprediction is nearly always the case, which is also consistent with expectations, especially in the case of assembly-level weight estimations where what is meant by the 'other' category of the WATE++ results is not defined nor is a methodology provided. Thus, this is left entirely unmodelled in the present program. The fact that the components under the 'other' category (besides connecting hardware) are not considered therefore accounts for a large share of the underpredicted weight.

The weight of rotor blades is quite low as well, but this makes sense since the weight of the blade root is incorporated into the weight estimation of the disk, not the blade, which is a difference between the WATE++ and present methodologies. Stator vane weight estimations are also lower, which makes sense since the vane airfoils and shrouds are modelled, but the attachment method to the casing is not. Casings are in general much lighter as well, and since detailed aspects of the casing such as flanges, connecting hardware, and variable stator vane actuators are not accounted for, underprediction should be expected.

Table 3.10: Comparison of weight estimation results for CFM56 and PW2037 axial compressors [22].

Engine	Component	WATE++ [kg]	WEST [kg]	Rel. Error [-]
CFM56	**LPC (Total)**	**97.1**	**83.7**	**-13.8%**
	Rotors + Disks	37.2	41.1	10.5%
	Rotor Blades	10.9	4.20	
	Disks	26.3	36.9	
	Stator Vanes	14.5	7.01	-51.7%
	Casing	25.9	23.9	-7.7%
	Connecting Hardware		11.7	
	Other	19.5		
CFM56	**HPC (Total)**	**184.2**	**134.6**	**-26.9%**
	Rotors + Disks	101.6	91.0	-10.4%
	Rotor Blades	16.3	9.19	
	Disks	85.3	81.8	
	Stator Vanes	21.8	16.1	-26.0%
	Casing	41.3	19.4	-52.9%
	Connecting Hardware		8.07	
	Other	19.5		
PW2037	**LPC (Total)**	**189.6**	**168.4**	**-11.2%**
	Rotors + Disks	76.7	98.5	28.5%
	Rotor Blades	25.4	11.5	
	Disks	51.3	87.1	
	Stator Vanes	30.8	21.8	-29.5%
	Casing	46.7	35.3	-24.5%
	Connecting Hardware		12.8	
	Other	35.4		
PW2037	**HPC (Total)**	**352.9**	**267.6**	**-24.2%**
	Rotors + Disks	196.9	180.7	-8.2%
	Rotor Blades	37.2	14.3	
	Disks	159.7	166.3	
	Stator Vanes	43.5	29.0	-33.3%
	Casing	75.7	41.6	-45.0%
	Connecting Hardware		16.2	
	Other	36.7		

Overall, the weight estimation results presented in Table 3.10 can be considered quite usable. Since the goal is to use WEST results in aircraft-level design and optimization studies, the change in weight for different input parameters (i.e., the *deltas*) will be important, not just the magnitudes themselves, meaning that *consistent* underprediction is not entirely problematic. However, a word of caution is also beneficial at this stage. In the case of the CFM56 and PW2037 LPCs, some component types (rotors and disks) are overpredicted, while others are underpredicted (stator vanes, casing), and these errors tend to cancel each other out, resulting in what would otherwise appear to be 'accurate' compressor-level weight estimations. On the other hand, most component types are underpredicted, so there is only a limited amount of error compounding, meaning that the compressor weight estimations can be taken as reasonably trustworthy, albeit always on the lower end of what should be expected.

Additionally, in the field of aircraft engine design, where so much data remains proprietary and is unavailable to the present study, a large amount of uncertainty exists simply due to what is unknown, most notably material and alloy selection. Since such data is not, for the most part, provided by the manufacturer or publicly available, assumptions must be made in order to fill in the missing information. These assumptions can have a significant effect on overall weight estimation. Results can be change significantly based on

Figure 3.17: CFM56-5C HPC stage 3 (left) and stage 6 (right) rotor blades.

Table 3.11: Comparison of WEST design and weight estimation results with real engine components [64].

Category	Parameter	Units	WEST[1]	CFM56[2,3]
HPC Stage 3 Rotor Row	Blade Weight, m_{bl}	g	15.9	22
	Thickness-to-Chord Ratio, $(t/c)_{max}$ (At Tip)	%	7.5	3.7
HPC Stage 6 Rotor Row	Blade Weight, m_{bl}	g	9.92	12
	Thickness-to-Chord Ratio, $(t/c)_{max}$ (At Tip)	%	7.5	4.2
HPC	Total Number of Rotor Blades	-	694	968[1]

[1]CFM56-5B. [2]CFM56-5C. [3]Approximate (based on measurements of real components).

material/alloy selection, meaning that the results shown in Table 3.10 are only as good as the assumptions. For example, in the case of disk design, a titanium alloy with significantly lower strength than a steel alloy may still produce a lighter disk. This is because, despite its lower strength, the lower density also results in less rotating mass and therefore less centrifugal forces to counteract. In other words, the titanium disk could be much lighter, resulting in a lower weight estimation, which in this case would appear to be less accurate when compared to the WATE++ results. For engines where it is not clear what materials are used – such as the PW2037 and most of the CFM56 – the results can vary substantially depending on what material assumptions are made. The sensitivity of the weight results to material selection is discussed more in Section 3.3.6, but it is important to note here that there are limitations in the degree to which the results can be validated since there is still such a great deal of uncertainty with regard to the design assumptions.

Finally, some components of an actual CFM56-5C engine were procured, which offers a limited but insightful opportunity to validate some of the results against the real engine. As seen in Table 3.11 [64], WEST underpredicts the weight of the blades compared to the real engine components. This is expected, however, since the present methodology accounts for the blade root in the *disk* weight estimation, not that of the blade. Tong et al. [18] estimates that, for rows using web disks, the blade root and blade post each accounts for 20% of the total blade weight, meaning that the blade airfoil should account for about 60% of the total blade weight. If the WEST results are compared to the real components as shown in Table 3.11, then the WEST weight estimation is 72.3% of the real blade for the third stage HPC rotor and 82.7% for the sixth stage HPC rotor. Both of these values are above the anticipated value of 60%, but show that the weight estimations are still considerably close. The underprediction observed in Table 3.10 for the combined rotor and disk weight of HPCs is therefore likely due to underestimation of the *number* of blades since, as shown in Table 3.11, the

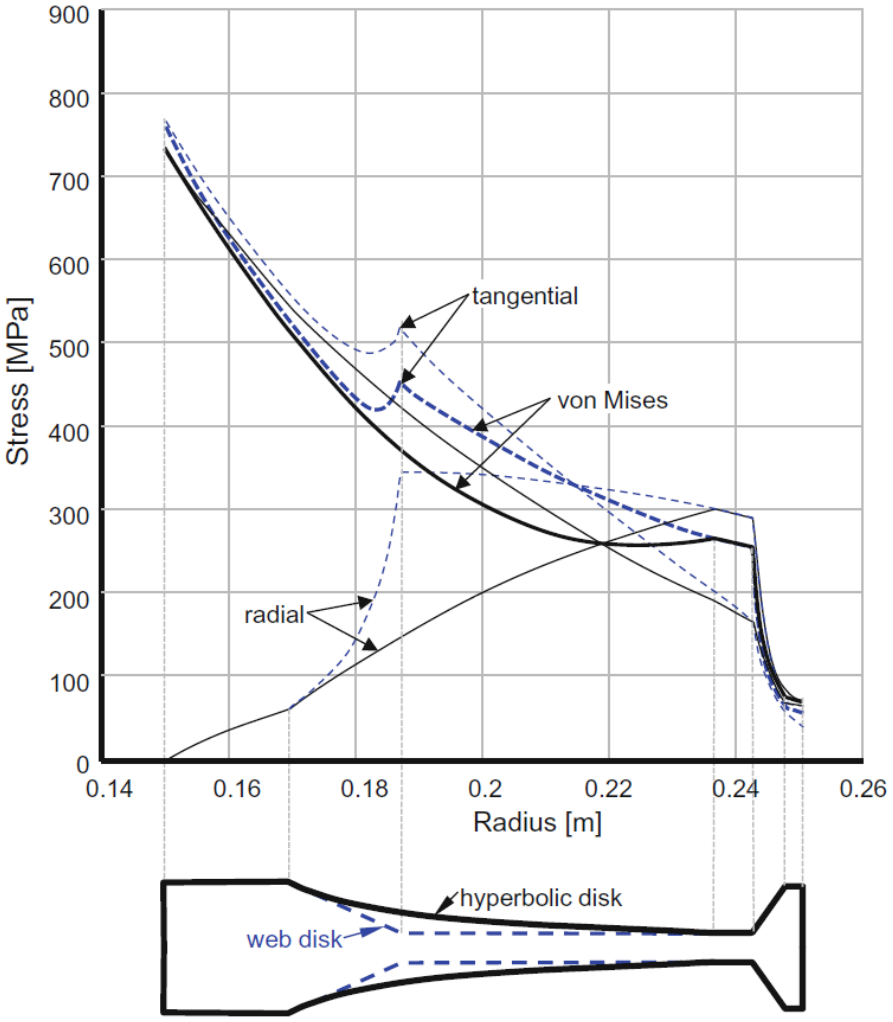

Figure 3.18: Examples of stress distributions in web and hyperbolic disks [24].

number of HPC blades is significantly underpredicted by WEST.

Furthermore, measurements of the real components show that the thickness-to-chord ratio at the tip of the blades is much lower than the default value of 7.5% assumed by WEST. This methodology may therefore be improved by reducing the minimum $(t/c)_{max}$ values shown in Table 3.2 to match more closely the design trends of real engines.

3.3. SENSITIVITY ANALYSIS

It is beneficial to evaluate the sensitivity of the weight estimation results with regard to a variety of design inputs and assumptions of interest. This provides an idea of the variability of the presented results and their level of dependence on the background knowledge of the specific application. It also provides novel insight regarding weight trends with respect to user-defined design choices. The objective of this section is therefore to evaluate the sensitivity of the WEST program's axial compressor model with regard to variations in key input parameters; the factors which will be addressed are annulus type (Section 3.3.1), number of stages (Sec. 3.3.2), main parameters of the engine system model (Sec. 3.3.3), duty coefficients (Sec. 3.3.4), disk design (Sec. 3.3.5), material selection (Sec. 3.3.6), and numerical settings of the software implementation (Sec. 3.3.7).

3.3.1. ANNULUS TYPE

The annulus type, i.e, the selection of whether to fix the hub, mid, or tip diameter of the machine, has a large impact on the gas path design and is therefore expected to influence the total weight estimation as well. For evaluating the sensitivity of this parameter, two scenarios will be considered. The first is the evaluation of the three annulus types such that they all have the same outer dimensions, and the second is for compressors that all have the same duty coefficients, but whose maximum tip radius and length may vary.

3.3.1.1. FIXED OUTER DIMENSIONS

The outer radius and total length of the CFM56 HPC were previously measured to be 0.306 m and 0.488 m, respectively. The duty coefficients, which affect the machine geometry, can be optimized for each of the three annulus types in order to achieve the same outer dimensions as the original CFM56 HPC. Doing so provides insight into the variation of machine weight when the same geometrical restrictions are applied to each gas path sizing approach. Table 3.12 lists the duty coefficients necessary to achieve the specified outer radius and length for the three cases being investigated. All other design input parameters are the same as those listed in Table 3.8 and Table 3.9. The same is true for all instances of sensitivity analysis carried out for the compressor design: the input values are equal to those recorded in Section 3.2 unless otherwise noted. Additionally, the term *nominal* is used throughout this section to distinguish the original design from those using modified input parameters.

Table 3.12: Duty coefficients of CFM56 HPC model for various annulus types (fixed outer dimensions).

Category	Parameter	Units	Value		
General Design	Fixed Diameter	-	Hub[1]	Mid	Tip
Dimensions	(Max) Outer Radius	m	(0.306)	(0.306)	(0.306)
	Length[2]	m	(0.488)	(0.488)	(0.488)
Duty Coefficients	Flow Coefficient, ϕ	-	0.495	0.422	0.429
	Work Coefficient, ψ	-	0.333	0.306	0.246
	Degree of Reaction, R	-	0.598	0.569	0.552

[1]Nominal. [2]Total length excluding guide vane.

Table 3.13 presents the weight estimation results for the CFM56 HPC for the three annulus types assuming fixed outer dimensions. Figure 3.19 shows a side-by-side comparison of the designs.

Table 3.13: Comparison of weight estimation results of CFM56 HPC model for various annulus types (assuming fixed outer dimensions).

Component	Weight [kg]		
	Hub[1,2]	Mid[1]	Tip[1]
Total	**134.6**	**155.4**	**185.6**
Rotors + Disks	91.0	99.3	131.5
Rotor Blades	9.19	10.8	7.81
Disks	81.8	88.5	123.7
Stator Vanes	16.1	22.9	16.5
Casing	19.4	24.7	28.3
Connecting Hardware	8.07	8.45	9.28

[1]Fixed diameter. [2]Nominal.

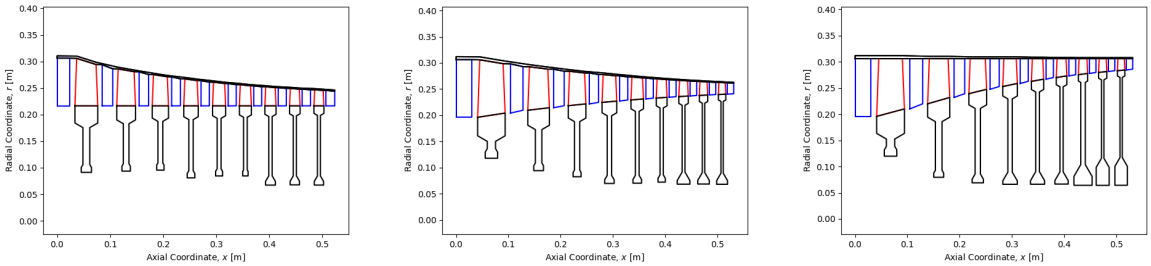

Figure 3.19: Design results of CFM56 HPC for fixed hub (left), mid (middle), and tip (right) diameters (assuming fixed outer dimensions).

As is evident in Table 3.13, the machine with a constant hub radius results in the lowest weight when adhering to fixed geometrical constraints, while the one with a constant tip radius is the heaviest. This is due largely to disk weight. In the case of constant mid and tip diameter designs, the axial chord of some rotor blade rows increases due to the way in which the gas path design procedure is formulated and the fact that the same aspect ratios are used in all cases. This creates wider disks, which in turn leads to higher weights. Thus, for applications where the outer dimensions of the compressor must be strictly adhered to, designs using a fixed hub diameter are expected to have the lowest weight. Otherwise, the user can modify the axial chords through manipulation of the aspect ratios to mitigate the growth in weight.

3.3.1.2. FIXED DUTY COEFFICIENTS

The same investigation is now repeated while holding the duty coefficients constant. This leads to different lengths and outer diameters as outputs of the gas path design (see Table 3.14). Table 3.15 presents the weight estimation results.

Table 3.14: Outer dimensions of CFM56 HPC model for various annulus types (fixed duty coefficients).

Category	**Parameter**	**Units**	**Value**		
General Design	Fixed Diameter	-	Hub[1]	Mid	Tip
Duty Coefficients	Flow Coefficient, ϕ	-	*0.495*	*0.495*	*0.495*
	Work Coefficient, ψ	-	*0.333*	*0.333*	*0.333*
	Degree of Reaction, R	-	*0.598*	*0.598*	*0.598*
Dimensions	(Max) Outer Radius	m	(0.306)	(0.293)	(0.273)
	Length[2]	m	(0.488)	(0.452)	(0.575)

[1]Nominal. [2]Total length excluding guide vane.

Table 3.15: Comparison of weight estimation results of CFM56 HPC model for various annulus types (constant duty coefficients).

Component	**Weight [kg]**		
	Hub[1,2]	Mid[1]	Tip[1]
Total	**134.6**	**122.4**	**174.8**
Rotors + Disks	91.0	80.9	110.1
Rotor Blades	9.19	8.30	11.8
Disks	81.8	72.6	98.4
Stator Vanes	16.1	15.3	22.5
Casing	19.4	18.5	32.9
Connecting Hardware	8.07	7.73	9.28

[1]Fixed diameter. [2]Nominal.

The results are noticeably different from the previous case. The machine with a constant mean diameter is now the lightest of any design yet seen. It also has the shortest length, suggesting that length has a significant influence on weight (more so than outer radius), which makes sense considering the fact that the thicknesses of disks – which are the heaviest component type in axial compressors – depend heavily on the axial chord length of the blades. This emphasizes the need for the program to select aspect ratios (and thus axial chords) automatically based on, for example, losses and loss models, since doing so significantly affects total weight.

3.3.2. NUMBER OF STAGES

Table 3.16 shows the outer dimensions of a CFM56 high-pressure compressor designed with 8, 9, and 10 stages, while keeping the machine pressure ratio constant. Cross-sections are shown in Figure 3.20.

Table 3.16: Outer dimensions of CFM56 HPC model for various number of stages.

Category	Parameter	Units	Case 1	Case 2	Case 3
General Design	Number of Stages, n_{stg}	-	8	9[1]	10
Dimensions	(Max) Outer Radius	m	(0.316)	(0.306)	(0.298)
	Length[2]	m	(0.390)	(0.488)	(0.596)

[1] Nominal. [2] Total length excluding guide vane.

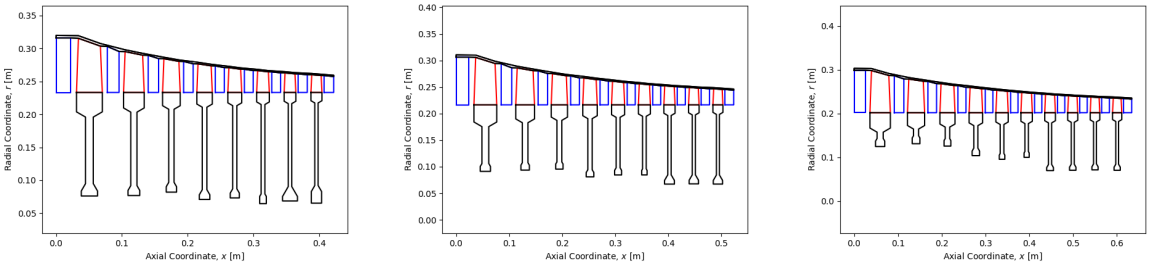

Figure 3.20: Design results of CFM56 HPC for 8 (left), 9 (middle), and 10 (right) stages.

As seen in Table 3.17, increasing the number of stages results in an increase in compressor weight, as should be expected. In theory, further weight reduction is possible by continually reducing the number of stages; however, there is, of course, a practical limit to this.

Table 3.17: Comparison of weight estimation results of CFM56 HPC model for various annulus types (constant duty coefficients).

Component	Weight [kg]		
	8[1]	9[1,2]	10[1]
Total	**115.1**	**134.6**	**152.8**
Rotors + Disks	80.3	91.0	99.4
Rotor Blades	7.30	9.19	11.2
Disks	73.0	81.8	88.2
Stator Vanes	13.1	16.1	19.3
Casing	15.0	19.4	24.6
Connecting Hardware	6.74	8.07	9.57

[1] Number of stages. [2] Nominal.

Table 3.18 shows the maximum and average single-stage pressure ratios for the three designs considered in Table 3.17. As discussed in Section 2.1.1.2, a pressure ratio of 1.3 represents a moderate level of technology for a single axial compressor stage. If 1.6 is considered highly-advanced, then the 8-stage machine is already approaching this rather closely, meaning that designing a machine with less than eight stages (in this example) may simply be infeasible. With the way in which specific work is distributed in the present methodology, the maximum single-stage pressure ratio for the (nominal) 9-stage design is 1.518, which is already quite high. Thus, careful attention must be paid by the designer to select a number of stages which is both lightweight and realistic given the assumed level of technology and (off-design) performance requirements.

Table 3.18: Comparison of single-stage pressure ratio of CFM56 HPC model for various number of stages.

Type	PR_{stg} [-]		
	8[1]	9[1,2]	10[1]
Maximum	1.581	1.518	1.469
Average	1.343	1.300	1.266

[1] Number of stages. [2] Nominal.

3.3.3. MAIN PARAMETERS OF THE ENGINE SYSTEM MODEL

Next, it is useful to evaluate the effect of various thermodynamic/process-related input parameters, namely the pressure ratio, mass flow rate, and rotational speed of the machine. For this, each of these is varied by ±25% from the nominal value. The results of these studies are included in Appendix C.2.1.1, with Table 3.19 summarizing some of these findings. The values in this table for ±25% are those measured, and the values for ±1% are simply proportionality constants, i.e., the averages over the ranges studied.

Table 3.19: Comparison of weight estimation results of CFM56 HPC model for the main parameters of the engine system model.

Parameter	**Rel. Weight [-]**		
	-25%[1]	+25%[1]	±1%[1]
Pressure Ratio, PR	+18.3%	-10.3%	∓0.57%[2]
Mass Flow Rate, $\dot{m}$	-32.4%	+38.0%	±1.41%[2]
Rotational Speed, N	+8.32%	-1.04%	∓0.19%[2]

[1]Variation in parameter of interest. [2]Proportionality constant.

As seen in Table 3.19, the weight of the compressor is inversely proportional to both pressure ratio and rotational speed, since increasing these values act to reduce the size of the gas path. Mass flow rate follows the opposite trend and has the most significant effect in terms of magnitude: a 1% change in mass flow rate (with respect to the nominal) produces, on average, a 1.41% change in total compressor weight. It is important to note that, since the pressure ratio and mass flow rate were changed independently, the consumed power also changes (see Table C.1 and Table C.4). The results may differ if their values were varied simultaneously to keep the power level constant. This should consequently be taken into account when drawing higher-level conclusions, although the sensitivities in Table 3.19 are still of interest.

3.3.4. DUTY COEFFICIENTS

As discussed in Section 2.1.1.1, duty coefficients have a large influence on machine performance, while the effect on machine dimensions is less clear. A designer of novel engines and architectures may therefore find it useful to define the engine based on these duty coefficients (and therefore performance level) instead of arbitrarily choosing dimensions. Thus, it is beneficial to have a rough idea of what may be expected with regard to compressor size and weight when tuning the flow coefficient, work coefficient, and degree of reaction.

Table 2.2 showed a range of typical values for duty coefficients which may be expected in axial compressors. Taking these ranges and limiting them slightly more based on the range of applicability of the equivalent Smith charts shown in Figure 2.3, flow coefficients, work coefficients, and degrees of reaction can be studied in the ranges of 0.4-1.0, 0.3-0.5, and 0.5-0.9, respectively. Varying only one coefficient at a time and keeping all others equal to their nominal values, the individual effects of each duty coefficient can be isolated. The machine dimensions using the minimum and maximum of each range are shown in Table 3.20, with the weight estimation of these same cases shown in Table 3.21. Cross-sections are included in Appendix C.2.1.2.

Table 3.20: Outer dimensions of CFM56 HPC model for various combinations of duty coefficients.

Category	**Parameter**	**Units**	**Case**					
			ϕ^1_{min}	ϕ^1_{max}	ψ^1_{min}	ψ^1_{max}	R^1_{min}	R^1_{max}
Duty Coefficients	Flow Coefficient, ϕ	-	0.4	1.0	*0.495*	*0.495*	*0.495*	*0.495*
	Work Coefficient, ψ	-	*0.333*	*0.333*	0.3	0.5	*0.333*	*0.333*
	Degree of Reaction, R	-	*0.598*	*0.598*	*0.598*	*0.598*	0.5	0.9
Dimensions	(Max) Outer Radius	m	(0.316)	(0.300)	(0.315)	(0.284)	(0.308)	(0.305)
	Length[1]	m	(0.586)	(0.314)	(0.448)	(0.655)	(0.503)	(0.464)

[1] [2]Total length excluding guide vane.

As seen in Table 3.20, increasing the flow coefficient results in a reduction of both outer radius and total length. This makes sense since ϕ is proportional to meridional velocity (Equation 2.1), thus a higher axial velocity will require a smaller channel height for the same mass flow rate, and a smaller channel/blade height with fixed aspect ratios will also therefore yield a shorter overall length. Thus, a higher flow coefficient also produces a reduction in weight, a claim which is supported by the results shown in Table 3.21.

Increasing the work coefficient, as the specific work is taken constant, reduces the outer radius, but increases the length. Overall, the smaller outer radius is eclipsed by the larger length with regard to impact on

Table 3.21: Comparison of weight estimation results of CFM56 HPC model for various combinations of duty coefficients.

Component	**Weight [kg]**					
	ϕ^1_{min}	ϕ^1_{max}	ψ^1_{min}	ψ^1_{max}	R^1_{min}	R^1_{max}
Total	**201.4**	**67.8**	**129.9**	**212.9**	**140.8**	**121.9**
Rotors + Disks	122.2	51.8	92.1	121.1	94.1	85.6
Rotor Blades	17.0	1.48	6.86	35.2	9.97	7.65
Disks	105.2	50.3	85.2	85.8	84.2	77.9
Stator Vanes	37.9	3.60	12.5	53.1	18.2	9.17
Casing	31.9	6.83	17.4	29.9	20.2	19.4
Connecting Hardware	9.35	5.67	7.83	8.90	8.28	7.71

[1] Duty coefficient.

machine weight, meaning that a higher work coefficient increases the weight of the compressor.

The degree of reaction produces a similar trend as the flow coefficient, although the sensitivity of the design to this parameter is noticeably less. Both the dimensions and weight of the compressor do not vary much compared to the nominal design, despite a wide range of degrees of reaction studied.

Using the nominal values as reference points, the influence of a 1% change in any of the duty coefficients on compressor weight can be quantified. These results are shown in Table 3.22. As is clear from this table, the weight estimation is most sensitive to changes in work coefficient, followed next by flow coefficient, and lastly by degree of reaction, for which the sensitivity is rather low. While weight is more sensitive to work coefficient, the range of typical flow coefficients is much larger (0.4-1.0 for ϕ compared to only 0.3-0.5 for ψ), thus the potential to influence compressor design and weight with flow coefficient is still quite high. Note that these sensitivities apply only to the formulation of the present methodology; other engine design programs may exhibit different behaviour.

Table 3.22: Comparison of average change in weight estimation results of CFM56 HPC model for a ±1% change in duty coefficients.

Parameter	**Rel. Weight [-]** $\pm 1\%$[1]
Flow Coefficient, ϕ	$\mp 0.81\%$
Work Coefficient, ψ	$\pm 1.03\%$
Degree of Reaction, R	$\mp 0.21\%$

[1] Variation in parameter of interest.

3.3.5. DISK

As seen in the various results sets – for example, Table 3.10 – disks are typically the heaviest component type in axial compressors. Thus, changes in disk design can have a large impact on the weight of the machine, so analyzing the sensitivity with regard to possible design choices is important. The influence of disk type is discussed in Section 3.3.5.1 and that of inner radius in Section 3.3.5.2.

3.3.5.1. TYPE

Three disk formulations were presented in Section 3.1.2: the web, hyperbolic, and ring disk. While different disk types are typically used in different applications (e.g., web in HPCs, hyperbolic in HPTs, and ring in LPCs), it is still beneficial to observe the effect of disk type selection on compressor weight, perhaps as a means of justifying the conventional design choices. Figure 3.21 shows the differences in designs for the three disk types when applied to the CFM56 HPC. Table 3.23 shows the weight estimation results for the both the CFM56 low- and high-pressure compressors for each of the three disk types.

As is evident in this table, ring disks offer the lightest-weight solution for LPCs. Here, the rotational speed is low, which results in lower centrifugal forces and therefore reduced stresses, meaning that even the minimum-sized web and hyperbolic disks are oversized according to the present formulations. The use of ring disks in LPCs is consistent with real engine designs, reinforcing the validity of the results.

Web disks, on the other hand, are most advantageous in the case of HPCs according to Table 3.23 as they offer the lowest-weight, which is also consistent with expectations. Hyperbolic disks are well-suited for high-temperature, high-stress environments with stricter geometrical constraints, thus these will be more

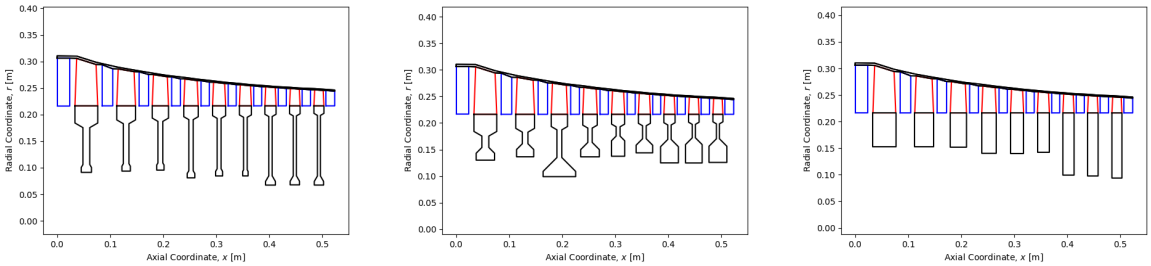

Figure 3.21: Design results of CFM56 HPC for web (left), hyperbolic (middle), and ring (right) disk types.

Table 3.23: Comparison of weight estimation results of CFM56 LPC and HPC models for various disk types.

Component	**Weight [kg]**		
	Web[1]	Hyperbolic[1]	Ring[1]
LPC (Total)	**165.8**	**224.1**	**83.7**[2]
Rotors + Disks	123.7	182.0	41.1
Rotor Blades	(4.20)	(4.20)	(4.20)
Disks	119.5	177.8	36.9
Stator Vanes	(7.01)	(7.01)	(7.01)
Casing	(23.9)	(23.9)	(23.9)
Connecting Hardware	11.2	11.2	11.7
HPC (Total)	**134.6**[2]	**157.9**	**178.1**
Rotors + Disks	91.0	113.8	133.9
Rotor Blades	(9.19)	(9.19)	(9.19)
Disks	81.8	104.6	124.7
Stator Vanes	(16.1)	(16.1)	(16.1)
Casing	(19.4)	(19.4)	(19.4)
Connecting Hardware	8.07	8.57	8.63

[1]Disk type. [2]Nominal.

prevalent in the case of axial turbines as presented in Chapter 4. While the ring disks shown in Figure 3.21 do satisfy the stress criteria, they require more material to do so compared to the other disk types since they feature only a single design variable – the inner radius. In higher-temperature (turbine) applications, even the largest ring disks will typically be incapable of satisfying the stress criteria. Thus, web disks remain the disk type of choice in high-pressure compressor applications.

Table 3.24 shows representative execution times of the WEST program when designing the compressors according to various disk types. Note that these results are for a particular machine, on a particular day, and for a particular build of the program. Thus, results may vary, and so the times listed in Table 3.24 should be used for reference only.

Table 3.24: Comparison of execution time of CFM56 LPC and HPC models for various disk types.

Component	**Time**[1] **[s]**		
	Web[2]	Hyperbolic[2]	Ring[2]
LPC	162.3	147.4	14.2[3]
HPC	315.4[3]	751.7	45.1

[1]Results may vary. [2]Disk type. [3]Nominal.

That said, the ring disk is clearly the most computationally-efficient disk type, which makes sense since it employs iteration, not optimization, in its design. Web and hyperbolic disks take around the same amount of time to design in the case of the CFM56 LPC; however, the discrepancy is much more noticeable for the HPC. This increase in computational time for hyperbolic disks is likely due to the added geometrical constraint expressed by Equation 3.43. The higher computational cost was not as pronounced with the LPC likely due to the fact that the minimum disk size imposed in the optimization is already satisfying the stress criteria.

3.3.5.2. INNER RADIUS

The disk optimization procedure is one of the slowest parts of the WEST preliminary engine design program. Not only is optimization computationally expensive, but this procedure must be repeated for every rotor row in a multi-stage turbomachine, for engines with multiple compressors and turbines. Thus, improvements in algorithm efficiency and/or further reduction of the size of the design vector could result in significant reduction of execution times of the overall program.

Figure 3.22 [64] and Figure 3.23 [65] show cross-sections of the CFM56 and PW2037 turbofan engines, respectively. Visual inspection of the high-pressure compressors show a nearly-constant inner radius of the disks at what appears to be close to the minimum inner radius. Thus, if it is assumed that r_1 of the disk is fixed at its minimum value, then this removes one of the disk design variables, leaving a three-parameter design vector (r_2, t_2, and t_4). Figure 3.24 compares the PW2037 HPC design results when r_1 is either variable or fixed. Table 3.25 compares the weight estimation results for the HPCs of both the CFM56 and PW2037.

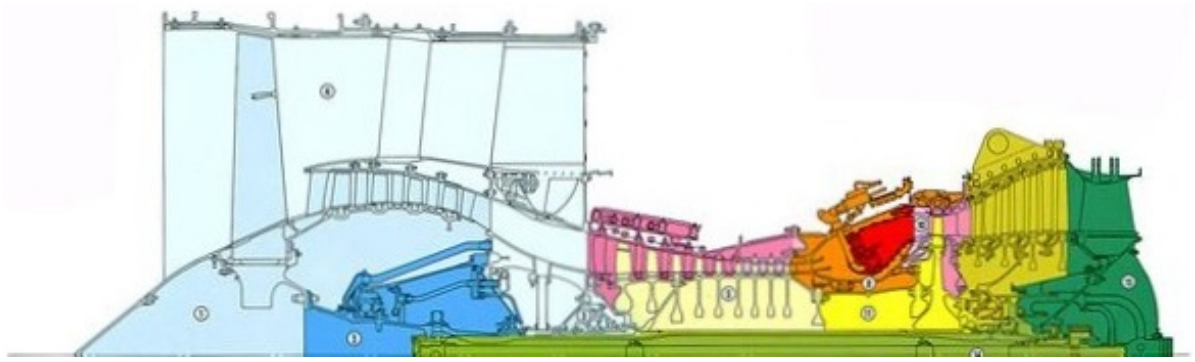

Figure 3.22: Cross-sectional view of the upper half of the CFM56-5B engine [64].

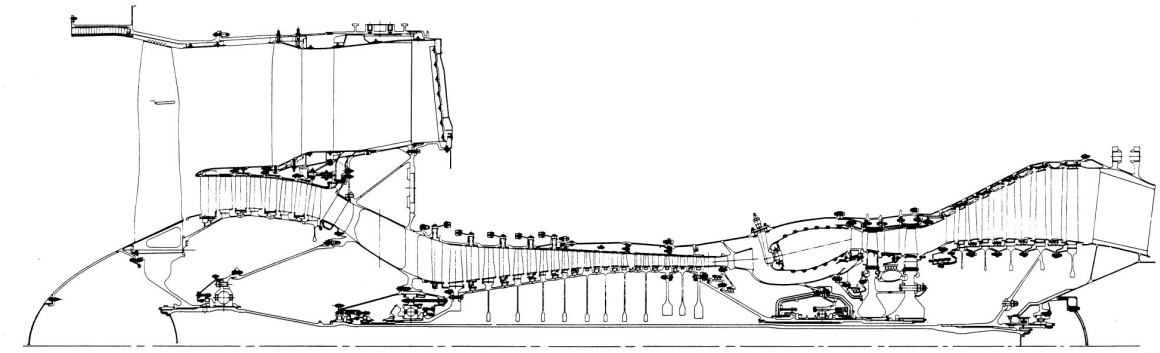

Figure 3.23: Cross-sectional view of the upper half of the PW2000 engine [65].

As seen in Table 3.25, the compressor weight estimation does not vary significantly with the application of this simplifying assumption. In fact, the weight actually grows slightly in both cases, which actually yields more accurate results since, as seen in Table 3.10, the results previously tended towards underprediction of weight. Additionally, the program run time is reduced substantially by fixing the inner radius as seen in Table 3.26. Thus, it may be beneficial from both an accuracy and efficiency perspective to fix the inner radius of the web disk to its minimum value in the case of HPCs, assuming the real engine shows a similar design. Note of course that this should not be done for the ring disks of LPCs since the low stresses mean low weight, thus fixing the inner radius to its minimum value would result in entirely unrealistic and oversized designs.

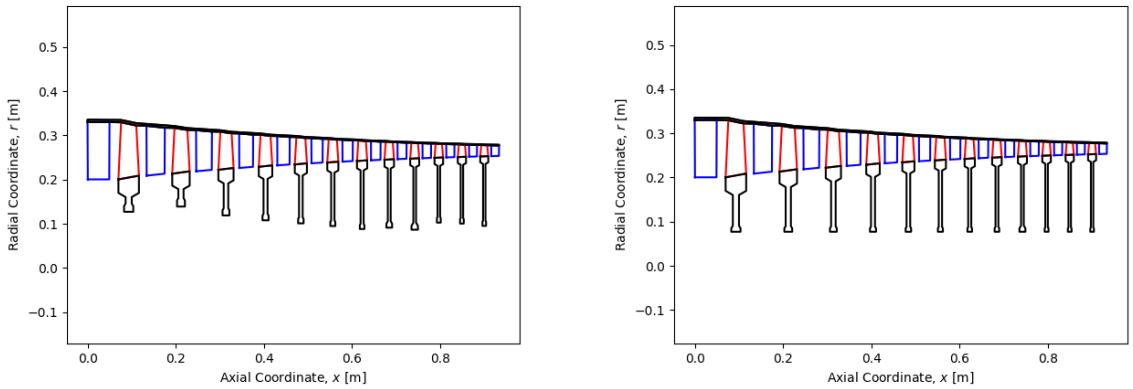

Figure 3.24: Design results of PW2037 HPC for variable (left) and fixed (right) inner radius.

Table 3.25: Comparison of weight estimation results of CFM56 and PW2037 HPC models for various disk inner radius types.

Engine	Component	Weight [kg] Variable[1,2]	Weight [kg] Fixed[1]
CFM56	**HPC (Total)**	**134.6**	**137.0**
	Rotors + Disks	91.0	93.6
	Rotor Blades	(9.19)	(9.19)
	Disks	81.8	84.3
	Stator Vanes	(16.1)	(16.1)
	Casing	(19.4)	(19.4)
	Connecting Hardware	8.07	7.86
PW2037	**HPC (Total)**	**267.6**	**279.9**
	Rotors + Disks	180.7	193.6
	Rotor Blades	(14.3)	(14.3)
	Disks	166.3	179.2
	Stator Vanes	(29.0)	(29.0)
	Casing	(41.6)	(41.6)
	Connecting Hardware	16.2	15.6

[1]Type of inner radius r_1. [2]Nominal.

Table 3.26: Comparison of execution time of CFM56 and PW2037 HPC models for various disk inner radius types.

Engine	Test	Time[1] [s] Variable[2,3]	Time[1] [s] Fixed[2]
CFM56	1	214.8	151.9
	2	212.6	150.5
PW2037	1	689.3	96.3

[1]Results may vary. [2]Type of inner radius r_1.
[3]Nominal.

3.3.6. MATERIAL SELECTION

As discussed in Section 3.2, many assumptions were made with regard to material selection, especially in the case of the PW2037. A largely steel-based design was assumed for this engine, but it is also useful to evaluate the effects of other material types. Table C.8 (Appendix C.2.1.3) shows the material selection for two cases: the first being the nominal steel-based design, and the second including a much larger quantity of titanium, which is an alternative and quite possible material choice of the actual engine. Figure 3.25 shows the differences in design results for the HPC when the two material sets are applied, and Table 3.27 features the weight estimation results.

As could be expected, the titanium-based material selection (Case 2) produces a much lighter-weight de-

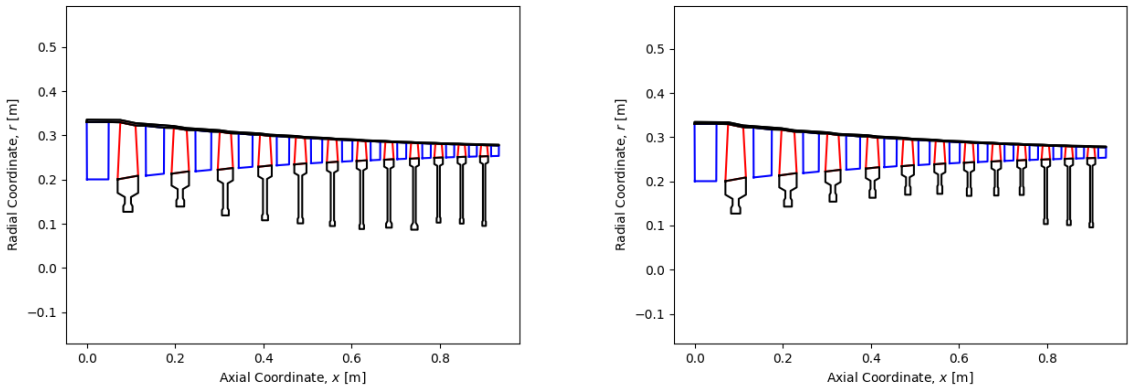

Figure 3.25: Design results of PW2037 HPC for material combinations Case 1 (left) and Case 2 (right).

Table 3.27: Comparison of weight estimation results of PW2037 LPC and HPC models for various material combinations.

Component	**Weight [kg]**	
	Case 1[1]	Case 2
LPC (Total)	**168.4**	**111.6**
Rotors + Disks	98.5	58.7
Rotor Blades	11.5	6.83
Disks	87.1	51.9
Stator Vanes	21.8	13.0
Casing	35.3	27.1
Connecting Hardware	12.8	12.8
HPC (Total)	**267.6**	**192.3**
Rotors + Disks	180.7	110.5
Rotor Blades	14.3	11.3
Disks	166.3	99.2
Stator Vanes	29.0	29.0
Casing	41.6	35.7
Connecting Hardware	16.2	17.1

[1] Nominal.

sign for the two axial compressors studied, showing that the results are *highly-sensitive* to choice of material. The differences in appearance of the two cases (Figure 3.25) reinforces this claim. If Case 2 is assumed to be the correct material choice, then the WEST weight estimation results are significantly less accurate when compared to the WATE++ data shown in Table 3.10 than previously expected. However, the steel-based design (Case 1) not only produces heavier (and apparently more accurate) weight results, but the visual appearance of the disks also appear to more closely match the HPC cross-section of the real engine shown in Figure 3.23. This may therefore imply that the original assumption was not entirely far off.

The high degree of sensitivity to material selection is somewhat problematic since so little is known of the material breakdown of real engines in most cases. This means that the potential usefulness of an engine preliminary design tool such as WEST is somewhat jeopardized by the validity of the starting assumptions, at least in the study of existing engines and validation efforts. This is less problematic in the design of novel engines, however, since the user determines the materials, resulting in fewer unknowns.

3.3.7. SETTINGS

While the design methodology described in Section 3.1 deals with scientific and engineering design methods for various components of axial compressors, little was said about the practical, software implementation. A great deal of development effort was placed into transforming the methodology into an open-source, Python-based, object-oriented program capable of engine preliminary design, weight estimation, and visualization. In this regard, it is beneficial to evaluate the sensitivity of the weight estimations with regard to specific set-

tings of the program, namely the number of finite elements used in the disk discretization for stress analysis (Section 3.3.7.1) and the step size of the finite difference method used during Newton-Raphson iteration (Section 3.3.7.2).

3.3.7.1. DISK FINITE ELEMENT COUNT

As discussed in Section 3.1.2.3 and visualized in Figure B.4, the disk is discretized into discrete, finite elements during the stress analysis procedure. As with any finite element analysis (FEA), the size of the elements is important; this can affect both the accuracy of the results and computational cost. It is imperative that convergence is obtained such that the results are independent of further grid refinement, without causing the code execution to become unnecessarily time-consuming. Thus, the number of elements used to discretize the disk in the radial direction was varied between 10 and 2000. All elements have a *uniform* thickness in the radial direction. The design results are shown in Figure 3.26, the weight estimation results in Table 3.28, and representative execution times in Table 3.29.

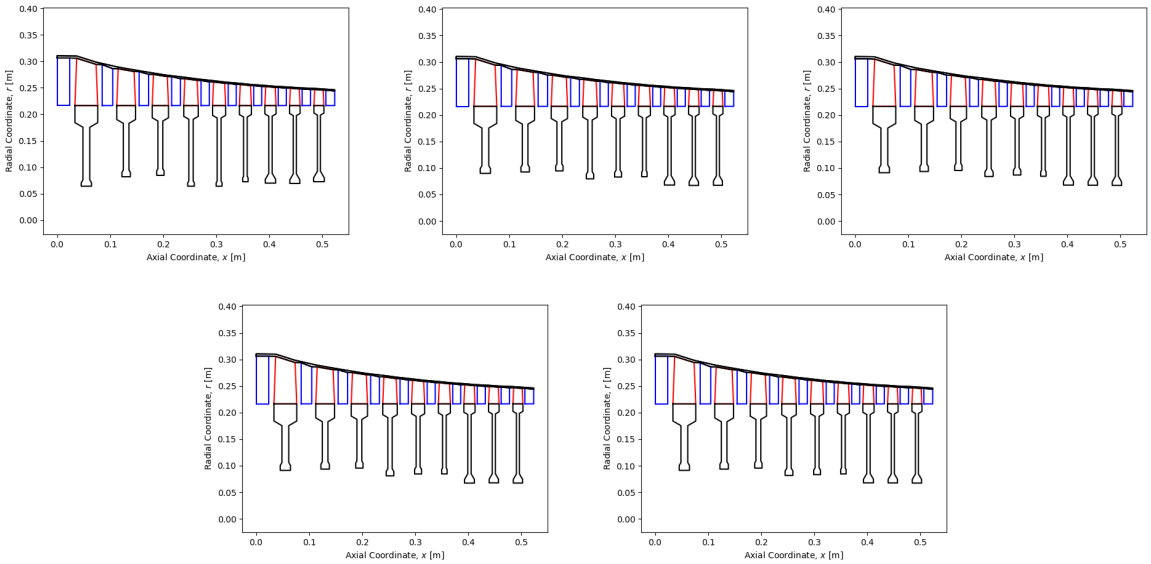

Figure 3.26: Design results of CFM56 HPC using 10 (top left), 100 (top middle), 500 (top right), 1000 (bottom left), and 2000 (bottom right) finite elements.

Table 3.28: Comparison of weight estimation results of CFM56 HPC model for various number of discrete finite disk elements.

Component	**Weight [kg]**				
	10^1	100^1	500^1	$1000^{1,2}$	2000^1
Total	**134.6**	**134.9**	**134.6**	**134.6**	**134.6**
Rotors + Disks	91.1	91.3	91.0	91.0	91.0
Rotor Blades	(9.19)	(9.19)	(9.19)	(9.19)	(9.19)
Disks	81.9	82.1	81.8	81.8	81.8
Stator Vanes	(16.1)	(16.1)	(16.1)	(16.1)	(16.1)
Casing	(19.4)	(19.4)	(19.4)	(19.4)	(19.4)
Connecting Hardware	7.95	8.06	8.07	8.07	8.07

[1] Number of discrete finite disk elements. [2] Nominal.

As can be seen in Table 3.28, the CFM56 HPC weight estimation is nearly independent of element size, even when only 10 elements, which is rather course, was used. This shows that the nominal use of 1000 elements is likely too fine for the present (axial compressor) application as it results in additional, and unnecessary, computational cost. Closer observation of the design results in Figure 3.26 shows more noticeable variation, however, with greater consistency occurring for designs using 100 elements or more. It is therefore recommended to reduce the number of elements used in disk discretization in order to lessen the computational cost of the disk design procedure without any significant effect on the accuracy of the results. The

Table 3.29: Comparison of execution time of CFM56 HPC model for various number of discrete finite disk elements.

Test	**Time**[1] **[s]**				
	10^2	100^2	500^2	$1000^{2,3}$	2000^2
1	14.1	89.0	119.1	228.7	732.6

[1]Results may vary. [2]Number of discrete finite disk elements. [3]Nominal.

sensitivity of weight estimation to number of disk elements will be reevaluated for turbines in the next chapter, since the temperature gradients present in turbine disks alter the stress distribution, meaning that these findings may only hold in the case of compressor disks.

3.3.7.2. FINITE DIFFERENCE STEP SIZE

Lastly, the sensitivity of the results was evaluated with regard to the step size used in the finite difference method. As mentioned throughout Section 3.1, iteration (specifically the Newton-Raphson method) is used to solve for several unknown variables during the axial compressor design procedure. The formulation is presented in Appendix B.1. Since the analytical derivatives of functions/procedures are often unknown, a forward finite difference method is used to approximate the derivatives used in the Newton-Raphson method. Varying the non-dimensional step size parameter h (Appendix B.1) between 1% of the iteration variable and 0.0001% yields a total weight estimation of 134.6 kg in all cases, i.e., the same as the nominal. The computation cost does vary, however, as shown in Table 3.30, thus attention should be paid such that the step size corresponding to the shortest execution times is selected, since doing so does not affect the quality of the obtained results within the range studied.

Table 3.30: Comparison of execution time of CFM56 LPC and HPC models for various finite difference steps sizes.

Test	**Time**[1] **[s]**		
	$h = 1 \times 10^{-2}$	[2]$h = 1 \times 10^{-4}$	$h = 1 \times 10^{-6}$
1	279.7	212.5	414.6
2	393.6	228.7	446.2

[1]Results may vary. [2]Nominal.

3.4. SUMMARY

- The meanline analysis and design results of the gas path, blades, disks, and casing of axial compressors (Section 3.2.2) all appear physically-sound and realistic. There are no major causes for concern in this regard.
- General underprediction of axial compressor weight is observed (Table 3.10), which is consistent with expectations (Section 1.2). However, the results do lie well within the expected range of +10%/-40%. Overall, the results appear quite viable, showing that the newly-developed WEST methodology can be used to predict the weight of axial compressors to a reasonable degree of accuracy given the established knowledge limitations.
- The estimated weight of rotor blades is low when compared to WATE++ results (Table 3.10), and the weight of disks are (generally) higher. This makes sense since the weight of the blade root is included in the weight estimation of the disks, not the rotor blades, an approach described by Lolis [21] and adopted here. Thus, only the combined weight of the two components should match the WATE++ results (see Section 3.1.2.1).
- Stator vane weight estimations are rather low, which may be due to the fact that only the vane airfoils and inner shrouds (Section 3.1.2.1) are modelled, not the roots.
- Casing weight is generally underpredicted (Table 3.10). This is likely due to the fact that a variety of casing attributes are not accounted for, such variable stator vane hardware, bleed flow extraction equipment, connecting hardware, etc. (Section 3.1.3).
- For the same length and outer radius, a compressor design with a constant hub radius has the lowest weight (Table 3.13). For the same duty coefficients (i.e., equivalent performance), a compressor with a constant mean radius has the lowest weight (Table 3.15).
- The length of the compressor has a larger influence on weight than the outer radius.
- Reducing the number of stages reduces the weight of a turbomachine, as is somewhat obvious. However, there are practical limits (e.g., single-stage pressure ratio, off-design performance) to how much the number of stages can or should be reduced (see Section 3.3.2).
- Among the main engine process parameters, the mass flow rate has the largest effect on the weight of the machine, followed by pressure ratio and then by rotational speed (Section 3.3.3). A 1% change in mass flow rate results in a 1.41% change in machine weight, on average, for the particular case study investigated (i.e., the CFM56 HPC).
- Of the three duty coefficients, the work coefficient has the largest effect on machine weight and dimensions, with a 1% change in work coefficient corresponding to a 1.03% change in machine weight, on average (see Section 3.3.4). This is followed by the flow coefficient, which follows an inverse trend, yielding a $\mp$0.81% change in compressor weight for a $\pm$1% change in value (on average, with respect to the nominal, for a particular reference case). The degree of reaction has a much lower influence on weight and dimensions than the other two duty coefficients ($\mp$0.21% change in weight for a $\pm$1% change in value). It follows an inverse trend, just like the flow coefficient.
- Disk design and optimization is the most computationally-expensive part of the WEST methodology. This accounts for the majority of the execution time, so reductions in computational cost of these methods have the potential to significantly influence the computational efficiency of the entire program (see, for example, Table 3.24). Disks cannot be simply overlooked since they constitute such a large share of total engine weight (see Table 1.3).
- Ring disks are the least computationally-expensive disk type to design, since they have only one design variable – the inner radius – and therefore require iteration only, not optimization (Table 3.24). Web and hyperbolic disks are comparable, with web disks being somewhat more computationally-efficient.
- Ring disks are most suitable and yield the lowest-weight results in the case of low-pressure compressors (Table 3.23). Web disks are most suitable and yield the lowest-weight results in the case of high-pressure compressors. It is not necessary to evaluate each of the three disk types for these applications. Using ring disks for LPCs and web disks for HPCs is sufficient and should produce the best results.

- Fixing the inner radius of the disk to its minimum value in the case of HPCs produces disk designs which appear quite consistent with the visual appearance of the real engines (Section 3.24). This is also a means of reducing the size of the optimization design vector, which can be used as a strategy to lower the computational cost of the optimization by a considerable margin (Table 3.26) without significant influence on the actual design and weight estimation results (Table 3.25).
- Material selection (Section 3.3.6) has a significant influence on compressor design and weight estimation. This is also one of the areas with the largest amount of uncertainty since the materials/alloys used in real engines, such as the CFM56 and PW2037 validation cases, are primarily unknown.
- Reducing the number of elements used to discretize the disk for stress analysis has little effect on compressor weight estimation (Table 3.28), meaning the number of elements used can be reduced in order to shorten the execution times of the program (Table 3.29). See Section 3.3.7.1.
- The step size used in the finite difference approximation – which is used to approximate the local derivative for use in the Newton-Raphson iteration method – does have some level of influence on the speed of the program, but no effect on the final results (within the range studied). For the particular case of axial compressor design, it was found that a step size of 0.01% of the nominal value produced the best (fastest) results (see Section 3.3.7.2).

4

AXIAL TURBINES

Operating at higher pressure ratios increases the efficiency of the Brayton thermodynamic cycle, and the introduction of fans in turbofan engines improves the propulsive efficiency of the engine. It is axial turbines which generate the massive amounts of power consumed by the compressors and fan, making these performance improvements possible. In turboshafts, the free power turbine (FPT) provides the necessary power required by whatever external application is being addressed, for example, a helicopter rotor or electric generator. This chapter follows a similar format as Chapter 3, presenting the design methodology (Section 4.1), validation (Sec. 4.2), and sensitivity analysis (Sec. 4.3) of the WEST program with regard to the preliminary design and weight estimation of axial turbines.

4.1. DESIGN METHODOLOGY

The design methodology of axial turbines follows largely the same structure as that of axial compressors. For this reason, only the *differences* in methods, nomenclature, equations, etc. will be described here. The reader is referred to Chapter 3 for the complete structure of the procedure. This section follows a similar sequence as Section 3.1, addressing the design of the gas path (Section 4.1.1), blades (Sec. 4.1.2), disks (Sec. 4.1.3), and casing (Sec. 4.1.4). The design methodologies of the inner shrouds and connecting hardware remain unchanged with respect to the compressor case. There is one additional component type in turbines, namely, the *frame*, which is described in Section 4.1.5.

4.1.1. GAS PATH

Two of the most notable differences between the gas path designs of axial turbines compared to axial compressors are as follows: first, the channel diverges, i.e., the channel height increases along the flow path, and second, stator rows come before rotor rows in any individual stage. The channel diverges due to the fact that the static pressure of the working fluid is dropping over each row, and since the mass flow must remain constant, the channel height must increase to accommodate this. Stator rows appear first in a stage, since these turn the fluid and increase its velocity, setting up the rotor rows for the subsequent extraction of energy/work.

4.1.1.1. REQUIRED INPUTS

Table 4.1 shows the difference in input parameters required for the definition of axial turbines. All other required inputs are the same as those listed in Table 2.1. As is evident from this table, power capacity, $\dot{W}$, is used to define turbines in place of pressure ratio, PR. The overall pressure ratio of the engine is an important design and performance parameter, hence the use of pressure ratio in analyzing the compressors, while turbines are often designed to supply a particular power demand, whether that be for a compressor attached to the same spool or other application, hence the use of power in defining turbines.

Table 4.1: Required inputs for meanline analysis and gas path design of axial turbines.

Category	#	Input Parameter	Symbol	Unit
Performance	~~2~~	~~Pressure Ratio~~	~~PR~~	~~-~~
	2	Power	$\dot{W}$	W

Table 4.2 lists typical range of duty coefficients for the design of axial turbines, as well as working fluid properties assuming calorically-perfect post-combustion gases (i.e., the working fluid downstream of the combustor) [40, 66, 67]. These values replace those listed in Table 2.2.

Table 4.2: Typical ranges/values for axial turbine duty coefficients and (post-combustion gases) working fluid properties [40, 66, 67].

Parameter	Units	Range/Value
ϕ	-	0.4 - 1.2
ψ	-	1.0 - 3.0
R	-	0.5
R_g	J/kg·K	287
c_p	J/kg·K	1150
γ	-	(1.33)

4.1.1.2. OVERALL PERFORMANCE

Figure 4.1 shows a Smith chart for axial turbines, which is used in place of those in Figure 2.3 when estimating the polytropic efficiency of an axial turbine stage; this chart was originally proposed by Zelesky et al. and reproduced by Turner et al. [67, 68]. Unlike in the case of compressors, only one Smith chart is presented here and is available for a degree of reaction of 0.5. This is because the expected range of degrees of reaction is much lower for turbines than compressors when used in aircraft engine applications, and since this value tends to stay around 0.5, one Smith chart is sufficient.

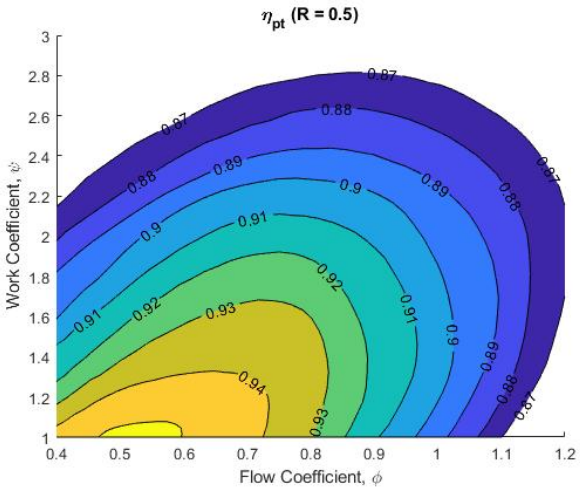

Figure 4.1: Smith chart for axial turbines at 0.5 degree of reaction [67, 68].

Because power is used as an input parameter for turbines instead of pressure ratio, the procedure for calculating overall performance is different. To begin, the total specific work and total temperature at the turbine outlet can be calculated using Equations 4.1 and 4.2, respectively.

$$w_{t,total} = \frac{\dot{W}}{\dot{m}} \tag{4.1}$$

$$T_{t,out} = T_{t,in} - \frac{w_{t,total}}{c_p} \tag{4.2}$$

Working backwards, the pressure ratio can then be calculated using Equation 4.3, followed by the total pressure at the outlet using Equation 4.4.

$$PR = \left(\frac{T_{t,in}}{T_{t,out}}\right)^{\frac{\gamma}{(\gamma-1)\eta_{pt}}} \tag{4.3}$$

$$p_{t,out} = \frac{p_{t,in}}{PR} \tag{4.4}$$

The relation for total-to-total isentropic efficiency is represented by Equation 4.5:

$$\eta_{tt} = \frac{1 - PR^{\frac{(\gamma-1)\eta_{pt}}{\gamma}}}{1 - PR^{\frac{\gamma-1}{\gamma}}} \tag{4.5}$$

Finally, the number of stages can be determined if not already specified by the user. Here, a maximum single-stage pressure ratio of 4.0 is used, and the result of Equation 4.6 is always rounded *up* (instead of to the nearest integer as was done with Equation 2.10 for axial compressors) since 4.0 represents a reasonable upper limit for the pressure ratio of a single axial turbine stage [42, 69].

$$n_{stg} \approx \log_{4.0}(PR) \tag{4.6}$$

4.1.1.3. STAGE-BY-STAGE DESIGN

The main difference in the stage-by-stage design procedure is the fact that work is extracted from the working fluid, not added, and that the rotors now represent the second row of a particular stage.

Nomenclature Figure 4.2 shows the station numbering and nomenclature for a single stage of an axial turbine at a fixed radial coordinate. The inlet to the rotor is still considered Station 1 and the rotor outlet Station 2, just as with compressors as shown in Figure 2.4. The third station in the case of turbines is denoted as Station 0 and occurs at the stator inlet, which is now in front of the rotor.

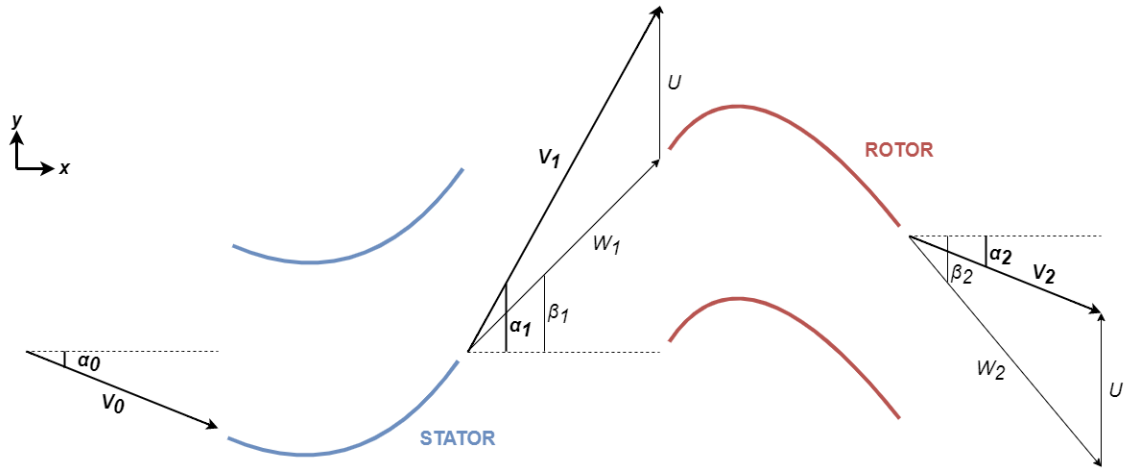

Figure 4.2: Station numbering and nomenclature of a single axial turbine stage.

Angles The equations for the flow angle α_1 and blade angle β_2 in the case of axial turbines feature a slight modification compared to what was presented in the previous chapter. Thus, Equations 4.7 and 4.9 replace Equations 2.11 and 2.13, respectively. The equations for β_1 (Equation 4.8) and α_2 (Equation 4.10) remain the same. For repeated stages, the relationship shown in Equation 4.11 is also true.

$$\alpha_1 = \tan^{-1}\left(\frac{1 + \frac{\psi}{2} - R}{\phi}\right) \tag{4.7}$$

$$\beta_1 = \tan^{-1}\left(\tan(\alpha_1) - \frac{1}{\phi}\right) \tag{4.8}$$

$$\beta_2 = \tan^{-1}\left(\frac{\phi \cdot \tan(\alpha_1) - \psi - 1}{\phi}\right) \tag{4.9}$$

$$\alpha_2 = \tan^{-1}\left(\tan(\beta_2) + \frac{1}{\phi}\right) \tag{4.10}$$

$$\alpha_0 = \alpha_2 \tag{4.11}$$

Total Properties Equation 4.12 can be used to determine the tangential velocity of the stage. This is the same as Equation 2.16, only it is calculated at the stator inlet, Station 0, since this now represents in the inlet of a given stage according to the turbine nomenclature (Figure 4.2.

$$U_{stg} = \omega \cdot r_{m,0} \tag{4.12}$$

The calculation procedure for V_m, V_1, and V_2 described in Equations 2.17 through 2.19 is still valid. For repeated stages with the assumption of constant mean radius, Equation 4.13 replaces Equation 2.20.

$$V_0 = V_2 \tag{4.13}$$

The total specific enthalpy at the stator inlet is calculated using Equation 4.14 assuming the total temperature is already known at this location and using a reference temperature of zero kelvin:

$$h_{t,0} = c_p \cdot \left(T_{t,0} - T_{ref}\right) \tag{4.14}$$

Since total enthalpy stays constant across stator rows, $h_{t,1}$ can be calculated using Equation 4.15:

$$h_{t,1} = h_{t,0} \tag{4.15}$$

The change in total enthalpy across the rotor is equal to the specific work of that stage, $w_{t,stg}$, calculated using the imposed duty coefficients according to Equation 2.22. In the case of turbines, work is extracted from the working fluid, thus the total enthalpy at the rotor/stage outlet can be calculated using Equation 4.16:

$$h_{t,2} = h_{t,1} - w_{t,stg} \tag{4.16}$$

Finally, the total temperature and pressure at any row and/or stage outlet can be calculated using Equations 4.17 and 4.18, respectively. In these equations, the subscript n denotes any arbitrary station number (e.g., 1 or 2) in the single-stage nomenclature convention (Figure 4.2), and $n-1$ the station preceding the current one (e.g., 0 or 1).

$$T_{t,n} = \frac{h_{t,n}}{c_p} + T_{ref} \tag{4.17}$$

$$p_{t,n} = p_{t,n-1} \cdot \left(\frac{T_{t,n}}{T_{t,n-1}}\right)^{\frac{\gamma}{(\gamma-1)\eta_{pt}}} \tag{4.18}$$

4.1.1.4. BLOCKAGE FACTORS

No blockage factors are applied in the case of turbines. The boundary layer grows slower due to the presence of a favourable pressure gradient, meaning the perceived effects of boundary layer on channel height are not as noticeable. Thus, $K_B = 1$ for all axial turbine stages.

4.1.2. BLADES

Turbine blades undergo massive loads at extremely high temperatures. In high-pressure turbine applications, they are often formed of a single metallic crystal, with numerous cooling passages to lower the blade temperature, thus reducing the severity of the operating conditions and extending the blade life. The same steps are taken in the design of turbine blades as compressor blades; however, the final result is quite different. The primary differences relate to the blade airfoil design, with additional deviations in methodology occurring for the way in which the number of blades in a row (Section 4.1.2.3) and operating temperature (Section 4.1.2.4) are determined. Table 4.3 lists the additional inputs required for the detailed design of turbine blades, besides those stated in Table 2.3. The cooling air temperature affects the temperatures and temperature distribution in the disks, as well as the blade bulk temperature if the blades are cooled. The Zweifel coefficient is used in determining the number of blades in a row.

Table 4.3: Additional inputs required for detailed blade design of axial turbines.

Category	#	Input Parameter	Symbol	Units
Quantity	18	Zweifel Coefficient	Z	-
Cooling	19	Cooled Blades		True/False
	20	Cooling Air Temperature	$T_{cooling}$	K

4.1.2.1. AIRFOILS

Unlike compressor blades, turbine blades are not simply represented by circular arc camber lines and NACA-series airfoils. They have much larger camber angles and thicknesses, as shown in Figure 4.3, and the design procedure typically involves experimentation and/or industry experience and (proprietary) design tools.

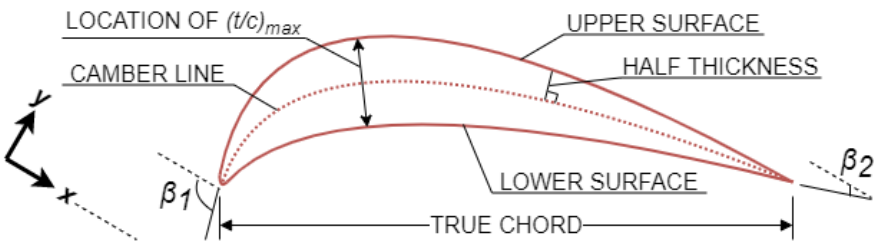

Figure 4.3: Composition of a turbine blade local airfoil section.

Fortunately, the work of Dunham provides an excellent starting point with regard to turbine blade design, offering mathematical formulations for both the highly-cambered camber lines and thickness distributions [70]. This study uses a great deal of existing experience to suggest default values and design steps to achieve profiles which are suitable from both an aerodynamic and structural perspective. For the purposes of this present study, profile tuning for the best fluid-dynamic performance can simply be skipped since the primary goal is weight estimation, which requires essentially representative turbine blade profiles at a low computational cost.

Maximum Thickness-to-Chord Ratio The default (minimum) maximum thickness-to-chord ratios are shown in Table 4.4 [70]. These replace those values listed in Table 3.2 in the case of axial turbines and are noticeably larger. These entries correspond to the mid-span values shown in an exemplary design presented by Dunham [70]. The thickness distribution methodology for turbine blades, which will be discussed shortly, is from this same paper, and these values were therefore taken as appropriate, representative defaults.

Table 4.4: Default thickness-to-chord ratios for different row types of an axial turbine [70].

Row Type	Minimum $(t/c)_{max}$ [%]
Stator	22.5
Rotor	20.0

Thickness Distribution The procedure for calculating the base profile, or thickness distribution, is described by Dunham [70] and is repeated in Appendix B.7.1. Dunham [70] also offers a methodology for the design of the mean camber line. However, the implementation of this procedure showed infeasible results. Considerable efforts were spent in solving this issue, but to no avail. It was therefore opted to develop an alternative methodology for the modelling of turbine blade camber lines.

Camber Line Turbine blades feature much larger camber angles than compressor blades, making circular arc camber lines insufficient for the purposes of turbine blade design. Thus, a *class-function/shape-function transformation* (CST) that is nothing else than a parameterization technique can be applied to efficiently model the camber lines. The CST method was originally developed by Kulfan and Bussoletti [71]. The procedure used as part of the WEST methodology is described in full in Appendix B.7.3.

Upper/Lower Surfaces and Dimensionalization Once both the camber line y_c/l and thickness distribution y_t/l of the turbine blade are defined, these two quantities can be combined to derive the coordinates of the upper and lower surfaces of the airfoil, as shown in Figure 4.3. This is done in the same way as with compressor blades, using Equations 3.3 through 3.7. The same procedure as compressor blades can also then be followed for rotating and scaling the normalized profile to its actual dimension (e.g., Figure 3.5).

4.1.2.2. WEIGHT

For cooled turbine blades, hollow regions exist for the transport of cooling air, thus the net profile area is smaller than the gross profile area, as shown in Figure 4.4.

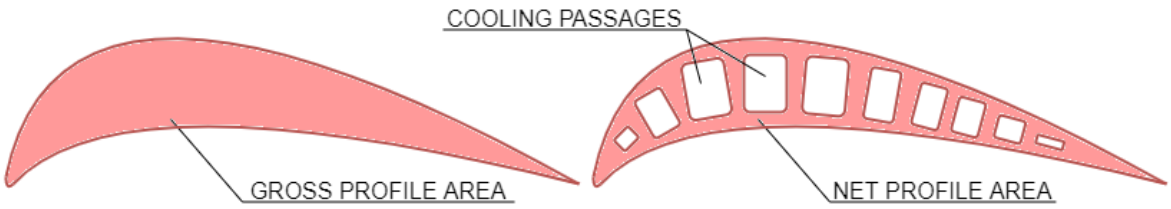

Figure 4.4: Gross vs. net profile area of a cooled turbine blade.

According to Grieb, the net area is always larger or equal to half of the gross area [42]. As shown in Table 4.3, the designer must specify if the turbine blades are cooled, and if they are, a solid-volume fraction must also be specified. Uncooled blades with no cooling passages (e.g., typical LPT blades) have a solid-volume fraction of unity, since their entire interior volume is filled with material, thus the weight estimation procedure remains unchanged compared to that of axial compressor blades. If dealing with cooled turbine blades, then the cross-sectional area of each of the three sections used to reconstruct the 3D blade profile can be modified according to the solid-volume fraction of the particular blade design. Since the lower limit of this value is 0.5 [42] and the upper limit 1.0, a default (median) value of **0.75** will be assumed; however, the user is free to modify this at any time. Thus, Equation 4.19 can be applied when calculating the area of a blade section (e.g., A_i and A_o in Equation 3.9), thus reducing the effective area compared to the original airfoil. The effect on blade weight will then the apparent in subsequent calculations (i.e., Equations 3.9 through 3.13).

$$A_{bl,seg} = 0.75 \cdot A_{airfoil} \tag{4.19}$$

4.1.2.3. NUMBER OF BLADES IN ROW

The method for determining the number of blades in a turbine row is somewhat simpler than that of axial compressors, requiring only one step, as shown in Equation 4.20 [20]:

$$n_{bl} = 4\pi r_m \frac{1}{c_{ax} \cdot Z} |\tan\beta_1 - \tan\beta_2| \cos^2\beta_2 \tag{4.20}$$

In the equation above, β_1 and β_2 represent the leading- and trailing-edge blade angles, respectively. Thus, in the case of stator vanes, these actually represent α_0 and α_1, respectively. The radius and axial chord of the row are evaluated according to their mean (or mid-span) values, r_m and c_{ax}. Finally, the variable Z represents the Zweifel coefficient (Table 4.3), which is a measure of actual blade loading compared to the maximum. The Zweifel coefficient is typically applied in the range of 0.8 to 1.1, with **1.1** being a representative value for low-pressure turbines [66]. Just as with Equation 3.21, the result of Equation 4.20 can be rounded up to the nearest integer to determine the final number of blades in that row.

4.1.2.4. OPERATING TEMPERATURE

For uncooled turbine blades, the operating temperature can be determined in the same way as that of compressor blades, i.e., equal to the adiabatic wall temperature with a specified recovery factor (Equation 3.27). For cooled turbine blades, the blade bulk temperature, T_{bl}, depends on the temperature of the cooling air, $T_{cooling}$ (an input according to Table 4.3), and the cooling effectiveness, e, as shown in Equation 4.21 [42]:

$$T_{bl} = T_{t,avg} - e\left(T_{t,avg} - T_{cooling}\right) \tag{4.21}$$

In this equation, the average total temperature is calculated in the absolute frame of reference for stator vanes and relative frame of reference for rotor blades, just as was done in the procedure for determining compressor blade operating temperatures (Section 3.1.1.7). The cooling effectiveness typically varies between 0.4 and 0.6 [42], thus a median default value of **0.5** will be assumed.

4.1.3. DISKS

Turbine disks are subject to higher blade loads and very high temperatures and temperature gradients, meaning that designing turbine disks which satisfy the stress criteria can be challenging. Fatigue and creep are critical; however, with the selection of appropriate materials (e.g., high-temperature super-alloys), very little changes in the way of disk design and formulation in the present methodology when compared to the one presented for axial compressor disks. The main difference between these and the disks of axial compressors is the presence of a temperature gradient throughout the disk, with the addition of one relaxed geometrical constraint in the case of single-stage high-pressure turbines.

4.1.3.1. GEOMETRY

In the case of single-stage turbomachines (usually HPTs), the rotor disks are not constrained by the presence of disks in adjacent rows, thus the constraint shown in Equation 3.39 can be replaced by Equation 4.22. For definition of these variables, see, for example, Figure 4.5.

$$1.5 \cdot t_4 \leq t_2 \leq 4 \cdot t_6 \tag{4.22}$$

The value of $4 \cdot t_6$ in this equation was determined based on digitization of the single-stage HPT disk of the CFM56-5B engine [64]. Thus, slightly more design freedom can be applied in the case of single stage turbines, which is beneficial since the stresses in these disks are typically very high, so increasing the thickness of the inner rim can aid in stress reduction.

4.1.3.2. OPERATING TEMPERATURE AND TEMPERATURE PROFILE

For turbines, the disk platform temperature for rows with uncooled (uc) blades, $T_{plt,uc}$, can be defined according to Equation 4.23 [24]:

$$T_{plt,uc} = T_{t,avg} \cdot (1 - RTDF) \tag{4.23}$$

In this equation, $T_{t,avg}$ is calculated in the relative frame of reference since disks are rotating, so no further correction factors need to be applied to account for this. The radial temperature distribution factor, $RTDF$, is defined by Grieb in Equation 4.24 [42]. In this equation, T_3 is assumed to be the temperature of the cooling airflow and T_4 the gas temperature, meaning that Grieb is defining $RTDF$ in the context of a cooled HPT. This factor is typically less than or equal to 0.08 to 0.10 [42], so a representative default of **0.08** for the RTDF will be assumed, thus Equation 4.24 is included for reference only.

$$RTDF = \frac{T_{4,max}(r) - \bar{T}_4}{\bar{T}_4 - T_3} \tag{4.24}$$

For rows with cooled blades, an additional temperature correction will be applied. This involves a cooling effectiveness factor, e (equal to 0.5), in the same way as done when determining the operating temperature of cooled turbine blades in Section 4.1.2.4. The final disk platform temperature for rows with cooled blades, $T_{plt,cooled}$, can therefore be calculated using Equation 4.25:

$$T_{plt,cooled} = T_{plt,uc} - e\left(T_{plt,uc} - T_{cooling}\right) \tag{4.25}$$

Like Grieb, the present methodology assumes that the temperature of the cooling air flow, $T_{cooling}$, for HPTs is equal to the gas temperature at the HPC outlet station, as shown in Equation 4.26. The cooling air for LPTs has a temperature somewhere between $T_{t,25}$ and $T_{t,3}$, thus the relationship shown in Equation 4.27 will be assumed.

$$T_{cooling,HPT} = T_{t,3} \tag{4.26}$$

$$T_{cooling,LPT} = T_{t,25} + 0.75 \cdot \left(T_{t,3} - T_{t,25}\right) \tag{4.27}$$

In addition to the modified procedure for calculating the disk platform temperature, i.e., the temperature at the blade root / disk hub, a temperature gradient also now exists throughout the (turbine) disk. An example of such a profile is shown in Figure 4.5 [42]. According to the stress analysis procedure described in Section 3.1.2.3, temperature gradients in the will induce additional stresses in the disk.

The platform temperature, T_{plt}, whether cooled or uncooled, is the temperature at the disk platform, which is synonymous with the outer radius (r_6) and/or hub (r_{hub}) according to the convention shown in

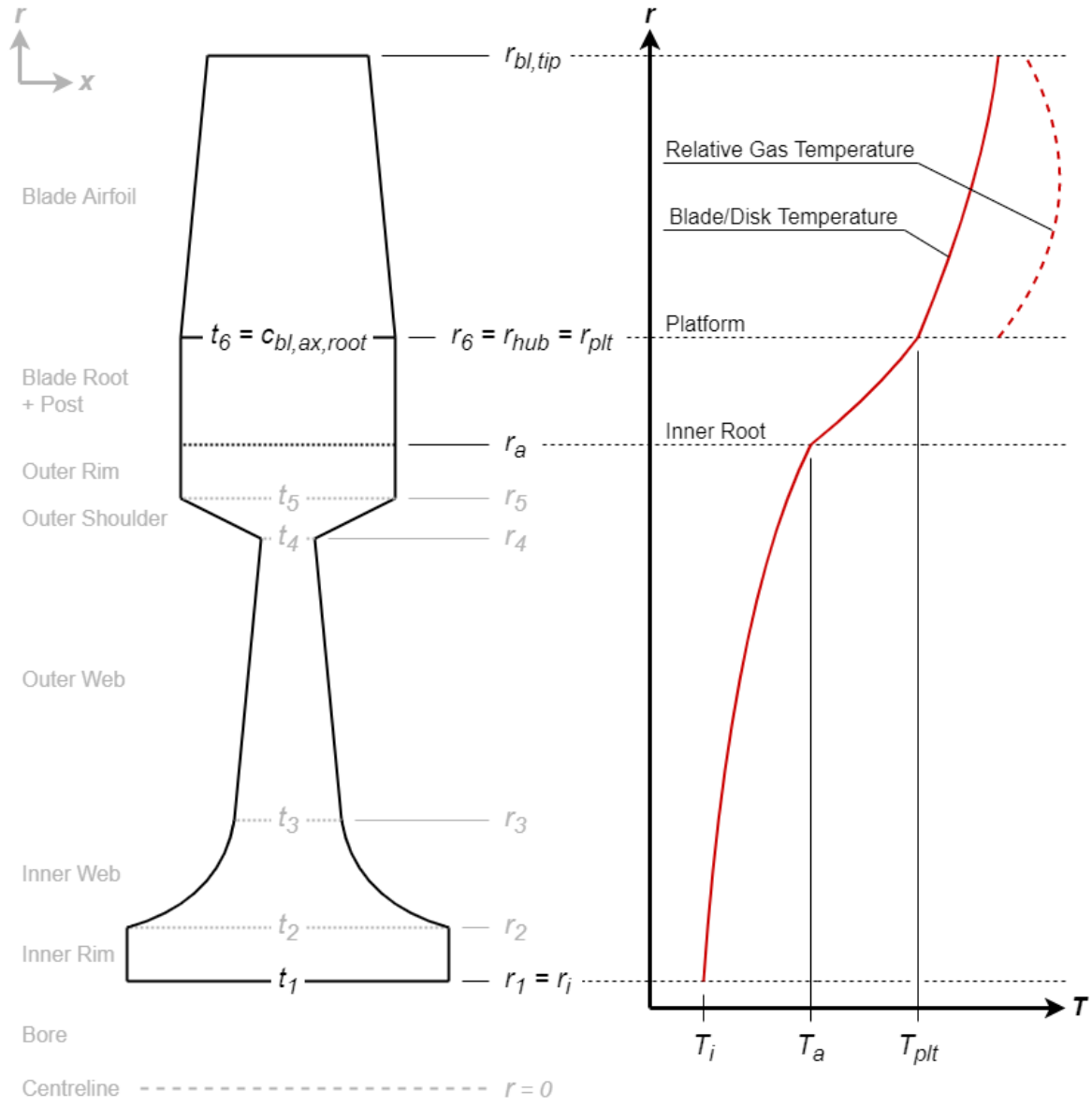

Figure 4.5: Temperature profile of a cooled hyperbolic disk [42].

Figure 4.5. The temperature at the inner radius ($r_i = r_1$) of the disk, T_i, is assumed equal to the temperature of the cooling air, $T_{cooling}$, as shown in Equation 4.28 [42]. This also applies for uncooled stages since, whether the blade is cooled or not, all turbine disks are assumed to be cooled.

$$T_i = T_{cooling} \tag{4.28}$$

The inner radius of the blade root is denoted as r_a in Figure 4.5 (and r_6 in Figure 3.8 and Figure 3.9). This radial coordinate can be approximated by Equation 4.29. The temperature at the inner radius of the blade root, T_a, can be calculated according to Equation 4.30 [42].

$$r_a = r_5 + 0.33 \cdot (r_{hub} - r_5) \tag{4.29}$$

$$T_a = T_i + \alpha \cdot \left(T_{plt} - T_i\right) \tag{4.30}$$

In Equation 4.30, the factor α is typically within the range of 0.4 to 0.6 [42], so a median default value of **0.5** will be assumed. With T_{plt}, T_a, and T_i all determined, the temperature distribution along the entire disk

can now be determined. A linear profile is assumed across the blade root, and a quadratic profile throughout the rest of the disk, as expressed in Equation 4.31 (and illustrated in Figure 4.5) [42]:

$$T(r) = \begin{cases} T_i + (T_a - T_i) \cdot \left(\frac{r-r_i}{r_a-r_i}\right)^2, & r_i \leq r \leq r_a \\ T_a + \left(T_{plt} - T_a\right) \cdot \left(\frac{r-r_a}{r_{hub}-r_a}\right), & r_a \leq r \leq r_{hub} \end{cases} \tag{4.31}$$

4.1.4. CASING

The only difference between the design methodologies for axial turbine and compressor casings is the operating temperature. For high-pressure turbines, cooled blades and disks are necessary in order to mitigate the high temperatures and increase the survivability of the components. The same is true for the casing. The application of cooling reduces the material temperature, thus increasing its yield strength and reducing the amount of material required for blade containment, resulting in a more lightweight component. The equation for local casing temperature is shown in Equation 4.32:

$$T_{cas} = T_{t,avg} - e\left(T_{t,avg} - T_{cooling}\right) \tag{4.32}$$

This equation can be repeated for each rotor row to determine the local thickness required for blade containment. The cooling effectiveness, e, has the same value of 0.5 as discussed in Sections 4.1.2.4 and 4.1.3.2. Note that $T_{t,avg}$ must be calculated in the absolute frame of reference since the casing is non-rotating.

For uncooled casings, the temperature which can be used in determining the material properties is the adiabatic wall temperature, calculated in the same ways as for axial compressors (Section 3.1.3.2).

4.1.5. FRAME

The last component type requiring weight estimation in axial turbines is the frame. Since no preliminary design methodologies exist for frames, the weight will be estimated using empirical correlations based on the average outer radius of the turbine. Such correlations are shown in Figure 4.6 [17] for four frame types.

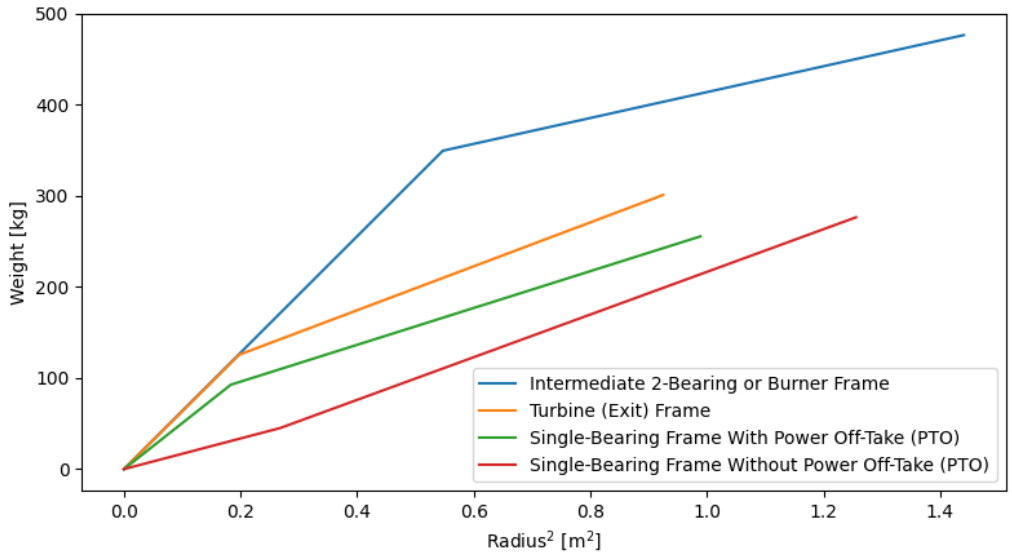

Figure 4.6: Empirical correlations for the weight estimation of frames [17].

Intermediate 2-bearing frames will be applied in the case of HPTs, since these occur between the HPT and LPT. Turbine exit frames will be used in the case of LPTs. The 2-bearing (or burner) frame type will also be applied to combustors, as will be seen in the next chapter. The remaining two frame types shown in Figure 4.6 are of relevance when designing turboshaft engines with a free power turbine. Thus, the weight of turbine and combustor frames can be estimated using only the average outer radius of the component.

4.2. VERIFICATION AND VALIDATION

This section follows a similar format as Section 3.2, with the objective of describing validation efforts in the case of the axial turbine model developed as part of the WEST preliminary engine design and weight estimation methodology. The inputs are listed in Section 4.2.1 so that the results in Section 4.2.2 can be reproduced. Section 4.2.3 closes with a discussion of the validation efforts.

4.2.1. INPUTS

Table 4.5 shows the meanline thermodynamic inputs for the four axial turbine validation cases being studied. A turbine inlet temperature (TIT) of 1522 K for the CFM56 was taken from Kurzke's model of the same engine [24][1], and a TIT of 1666.7 K corresponds to the one used by Greitzer et al. in developing the WATE++ results of the PW2037 [22][2]. These values are equal to $T_{t,4}$ in the full-engine nomenclature system and apply to the inlet of the HPTs. The temperature of the cooling air, $T_{cooling}$, for an HPT is equal to $T_{t,3}$ of the same engine, i.e., the temperature at the outlet of the HPC.

Table 4.5: Thermodynamic input parameters for turbines of CFM56 and PW2037 [22, 24].

		CFM56		PW2037	
Parameter	**Units**	**HPT**	**(LPT)**	**HPT**	**(LPT)**
$\dot{m}$	kg/s	59.6	59.6	82.7	82.7
$\dot{W}$	MW	26.16	24.40	35.91	33.00
N	RPM	15183	5380	12250	4575
$P_{t,in}$	bar	26.5	7.37	25.14	8.23
$T_{t,in}$	K	1522.0	1140.1	1666.7	1289.0
$T_{cooling}$	K	855.6	744.9	842.7	732.8

The mass flow rate of the fuel can then be solved using Equation 4.33, where the factor a is defined in Equation 4.34. The adiabatic efficiency of the combustion chamber, η_{cc}, can be assumed equal to **0.99** [40], and the lower heating value (LHV) of Jet A-1 kerosene fuel equal to **43.39** MJ per kilogram of fuel [72]. The specific heat, c_p, corresponds to that of post-combustion gases (Table 4.2). Once the mass flow rate of the fuel is solved for, this can be combined with the air flow rate $\dot{m}_{21}$ used in the compressor models to obtain the total mass flow rate through the turbines.

$$\dot{m}_f = \frac{a \cdot \dot{m}_{21}}{1-a} \tag{4.33}$$

$$a = \frac{c_p \cdot \left(T_{t,4} - T_{t,3}\right)}{\eta_{cc} \cdot LHV} \tag{4.34}$$

The power which must be supplied by the high- and low-pressure turbines can be calculated using the power consumed by the compressors and fan assuming a mechanical efficiency, η_{mech}, of **0.99** in all cases [40]. The power consumed by the compressors can be obtained by running their respective models, and the power consumed by the fan was approximated with simple calculations as shown in Section 3.2.1.

The pressure at the inlet of the HPTs, $P_{t,4}$, can be obtained using the pressure at the outlet of the HPCs, $P_{t,3}$, and assuming a combustor relative pressure drop of **0.06** [20].

Finally, as discussed in Section 4.1.3.2, the temperature of the cooling air flow can be calculated using the compressor model data according to Equations 4.26 and 4.27. In these equations, $T_{t,25}$ is the total temperature at the inlet of the HPC and $T_{t,3}$ the total temperature at its outlet.

Next, the inputs of the mechanical design inputs of the axial turbines are shown in Table 4.6. Just as with axial compressors, the outer dimensions of the turbines, aspect ratios, gaps, taper ratios, and shaft radii were obtained through digitization of cross-sections of the CFM56-5B and PW2037 available through Jane's AeroEngines [64, 65]. The duty coefficients were obtained by optimizing these three parameters to obtain the specified outer dimensions, with all other inputs as listed in Table 4.6. The number of stages, annulus type, absence of outlet guide vanes, and disk types can all be determined by means of the same cross-sections. The materials were selected based on operating temperature and the procedure outlined in Section 3.1.1.6.

[1] Kurzke actually reports this value as 1577 K [24], thus a small error exists with the present results.

[2] Greitzer et al. uses a TIT of 1666.7 K for all engines studied, including the CFM56 [22]. However, because Kurzke's TIT is case-specific, it was used instead since it is assumed more accurate than the generic TIT employed by the Greitzer et al. study.

The choice of NIMONIC 105 and INCONEL 718 alloys is consistent with that of Greitzer et al. in the WATE++ models [22].

Table 4.6: Mechanical design input parameters for turbines of CFM56 and PW2037.

			CFM56		PW2037	
Category	**Parameter**	**Units**	**HPT**	**LPT**	**HPT**	**LPT**
Dimensions	Outer Radius	m	(0.373)	(0.502)	(0.385)	(0.581)
	Length[1]	m	(0.074)	(0.303)	(0.215)	(0.434)
Duty Coefficients[2]	Flow Coefficient, ϕ	-	0.411	1.011	0.408	0.807
	Work Coefficient, ψ	-	1.472	2.505	1.188	1.983
	Degree of Reaction, R	-	0.477	0.450	0.477	0.455
General Design	Working Fluid		Gas[3]	Gas[3]	Gas[3]	Gas[3]
	Number of Stages, n_{stg}	-	1	4	2	5
	Fixed Diameter[4]		Mid	Hub	Mid	Hub
	Outlet Guide Vane		No	No	No	No
	Zweifel Coefficient, Z	-	0.8	1.1	0.8	1.1
	Cooled Blades		Yes	No	Yes	No
Aspect Ratios, AR	First Stage Stator	-	0.90	1.60	1.661	3.259
	Last Stage Stator	-	N/A	5.85	1.530	6.391
	First Stage Rotor	-	1.73	4.58	1.710	4.427
	Last Stage Rotor	-	N/A	5.36	2.195	6.211
Gaps, g	Row	-	0.567	0.33	0.444	0.489
	Stage	-	N/A	0.49	0.710	0.526
Taper Ratios, λ	Stator	-	1.0	0.97	1.022	0.884
	Rotor	-	1.0	0.91	0.754	0.840
Disk Design	Disk Type		Web	Web	Hyp.	Web
	Max. Shaft Radius	m	0.058	0.215	0.066	0.076
Materials	Stator Vane Material 1		NI 105[5]	NI 105[5]	NI 105[5]	NI 105[5]
	→ Stages	-	1	1-3	All	All
	Stator Vane Material 2			IN 718[6]		
	→ Stages	-		4		
	Rotor Blade Material 1		NI 105	NI 105	NI 105	NI 105
	→ Stages	-	1	1-2	All	All
	Rotor Blade Material 2			IN 718		
	→ Stages	-		3-4		
	Disk Material 1		NI 105	NI 105	NI 105	NI 105
	→ Stages	-	1	1-2	All	1-4
	Disk Material 2			IN 718		IN 718
	→ Stages	-		3-4		5
	Casing Material		NI 105	NI 105	NI 105	NI 105

[1]Total length excluding guide vane. [2]Obtained by optimizing for the prescribed bounding dimensions using the other inputs as listed below. [3]Post-combustion gases. [4]I.e., annulus type. [5]NIMONIC 105. [6]INCONEL 718.

4.2.2. RESULTS

Figure 4.7 shows the meanline and mechanical design results of the CFM56 LPT. Similar plots are provided in Appendices C.1.2.1 through C.1.2.3 for the other axial turbines being studied. Examples of axial turbine blade profiles are included in Figure 4.8; these are for the single stage of the CFM56 HPT. Examples of disk stress distributions are included in Figure 4.9 and Figure 4.10 for the CFM56 HPT and LPT, respectively. Table 4.7 compares the WEST weight estimation results with the WATE++ data provided by Greitzer et al. [22]. It is important to point out at this stage that, in many cases (e.g., CFM56 and PW2037 HPTs, first two stages of the PW2037 LPT), the disk stress criteria are not satisfied. Lastly, Figure 4.11 shows real CFM56 HPT nozzle guide vanes and stage 4 stator vanes, with Table 4.8 offering a comparison between the properties of these stators and the design results generated by WEST.

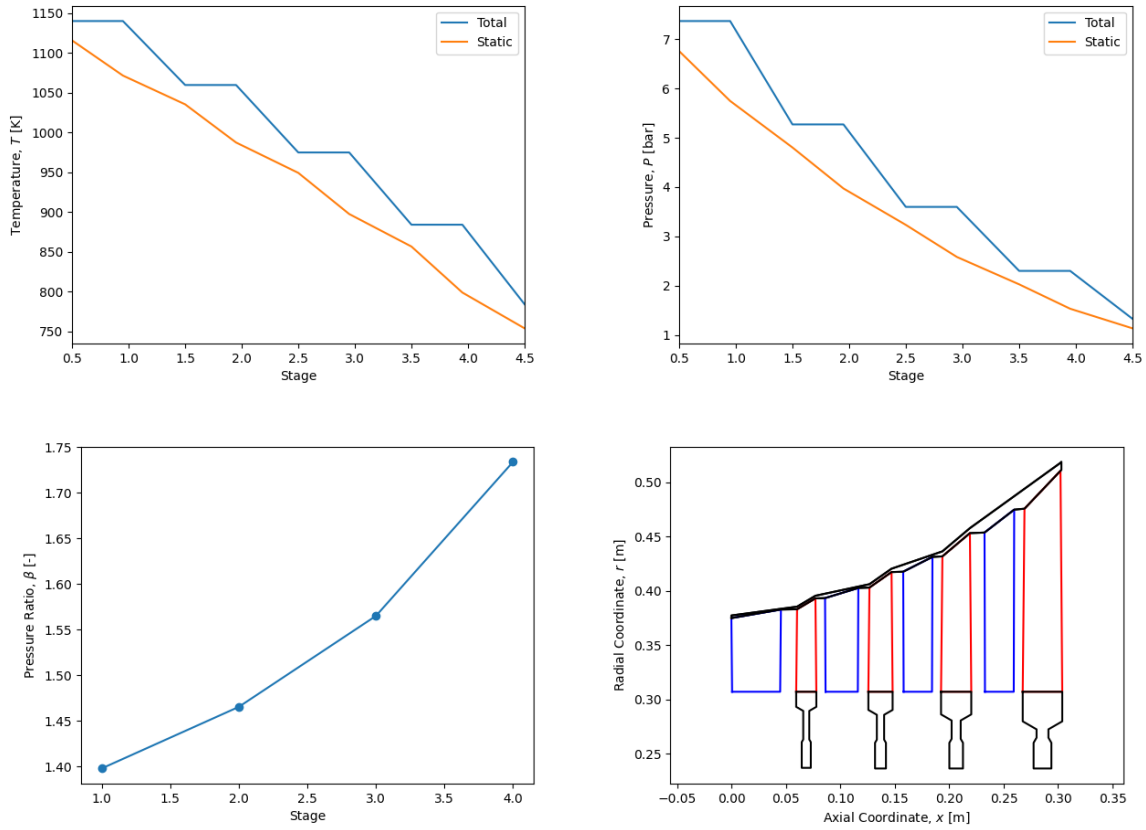

Figure 4.7: Meanline performance and mechanical design results of CFM56 LPT.

4.2.3. DISCUSSION

As evident in Figure 4.7, the meanline results continue to be consistent with expectations, so there are no surprises in this regard. The pressure ratio of the single-stage HPT (Figure C.4) is less than but in the order of 4.0, and the pressure ratios across each stage of the two-stage HPT (Figure C.5) are less than but of the order of 2.0, which are all consistent with typical trends [42]. The very large aspect ratios of the LPT blades were measured based on engine cross-sections [64, 65], so the final results are visually quite similar to the turbines shown in Figure 3.22 and Figure 3.23, as are the large disks present in the HPT stages.

The turbine blades shown in Figure 4.8 have greater thickness and more camber than the compressor blades seen in Figure 3.14, and the profiles appear consistent with general turbine blade shapes. The geometry is also quite smooth, showing that the camber line design methodology developed for WEST is compatible with the thickness distribution method proposed by Dunham [70]. The pointed leading edges (i.e., noses) of the blade profiles are due to an approximation in the procedure, something which is not expected to influence the weight estimation results.

Just as was discussed in the previous chapter, the duty coefficients – which are optimized in order to obtain the specified outer machine dimensions – can be checked against typical values for axial turbines to validate if the meanline and gas path design procedure produces realistic results. Table 4.2 shows ranges of duty coefficients which may be expected, and Table 4.6 the determined duty coefficients. As is evident from these tables, the flow coefficients of all four machines lie within the expected range of 0.4 to 1.2, all four work coefficients lie within the range of 1.0 to 3.0, and three of the four degrees of reaction lie within the range of 0.45 to 0.55. The value of R for the CFM56 LPT is 0.45 because this was the lower bound specified in the optimization procedure; however, relaxing this bound and rerunning the program results in a degree of reaction of 0.448, so still close to the representative value of 0.5. The reason R is limited to 0.45 is to maintain applicability of the Smith chart (Figure 4.1) in estimating polytropic efficiency. Reducing this further varies the value to 0.448, which is still extremely close, however the flow coefficient then reaches its upper limit of 1.2, so some tradeoff is required. Thus, all but one of the duty coefficients lie within the range of expected

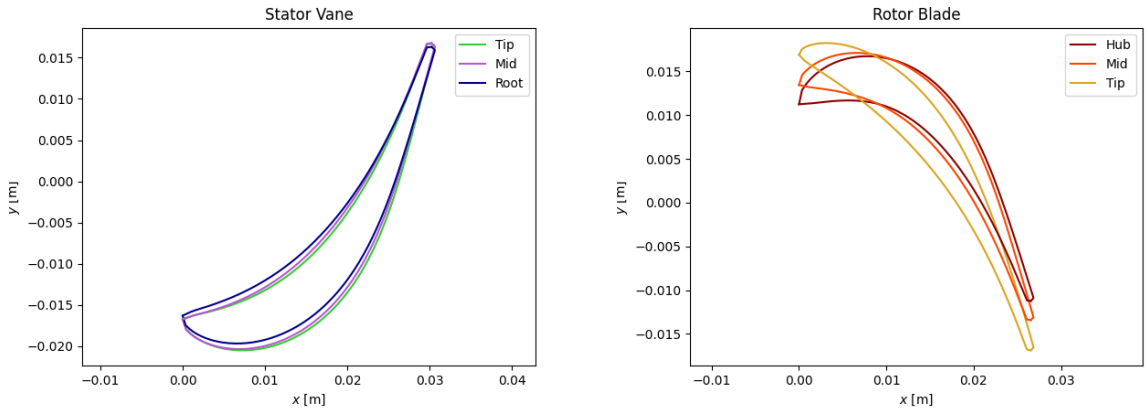

Figure 4.8: Spanwise blade profiles of CFM56 HPT (single stage), i.e., the nozzle guide vane (NGV) (left) and rotor blade (right).

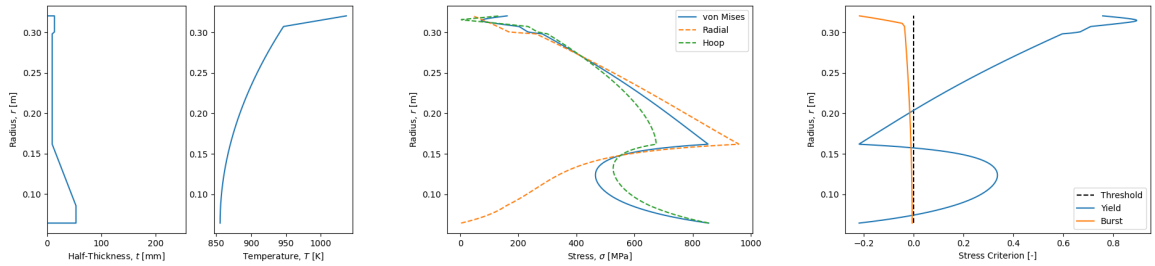

Figure 4.9: Stress distributions of CFM56 HPT (single stage) disk. Regions for which one or more of the stress criteria fall below the threshold of zero indicate that the structural requirements are not satisfied.

values, supporting to some degree the validity of the gas path design procedure.

Figure 4.9 and Figure 4.10 show the disk design, temperature distribution, and stress distributions along the radius of the CFM56 HPT single stage disk and LPT first stage disk, respectively. As previously mentioned, the CFM56 HPT disk, among others, does not satisfy the stress criteria. This is due mainly to two factors: first, the operating temperatures are significantly higher, thus the material yield strengths are lower, resulting in reduced factors of safety; and second, the temperature gradients which exist in the disks due to cooling induce additional stresses, which increase the critical stress conditions and reduce the factors of safety. The weight of the blades per row is also more, thus the radial stresses at the disk hub will be higher compared to compressors; however, this is not expected to have as much of an impact as the other two factors: as seen in Figure 4.9 and Figure 4.10, the radial stresses at the outer disk radius are not overly high when compared to the hoop stresses. Thus, while it is recommended to continue investigating solutions to lessen the stresses (such as, for example, using rounder geometry in the hyperbolic disk formulation instead of simplified linear profiles), this does not mean that the results are not usable. Each disk design represents the design with maximum factor of safety for that particular application, thus there is still physical meaning to the selected geometries compared to any other. In other words, the disk designs are not arbitrary, they simply cannot satisfy all stress criteria using the present formulation and the simplified methodology. Thus, it is an application-specific problem, not an issue with the methodology.

As seen in Figure 4.9, the HPT disk has a stress peak at the location where the inner shroud and the web meet; the sudden change in geometry at this location causes a stress concentration, so the peaks are to be expected. This disk and the one in Figure 4.10 display spikes in the stresses near the outer radius. This is likely due to the steep temperature gradient at this location, since temperature gradients induce additional stresses.

Table 4.7 shows the weight estimation results. As with axial compressors, the total weight of any given turbine matches fairly closely the WATE++ results, with relative errors varying from -4.3% to -19.4%. The weights of individual components types vary much more heavily, however, with values ranging from -97.3% (CFM56 HPT stator vanes) to +167.1% (CFM56 LPT frame). Frames are based solely on empirical correlations,

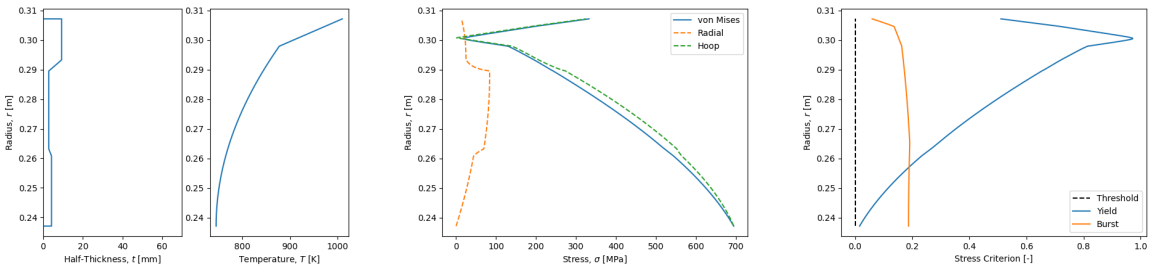

Figure 4.10: Stress distributions of CFM56 LPT first stage disk. Regions for which one or more of the stress criteria fall below the threshold of zero indicate that the structural requirements are not satisfied.

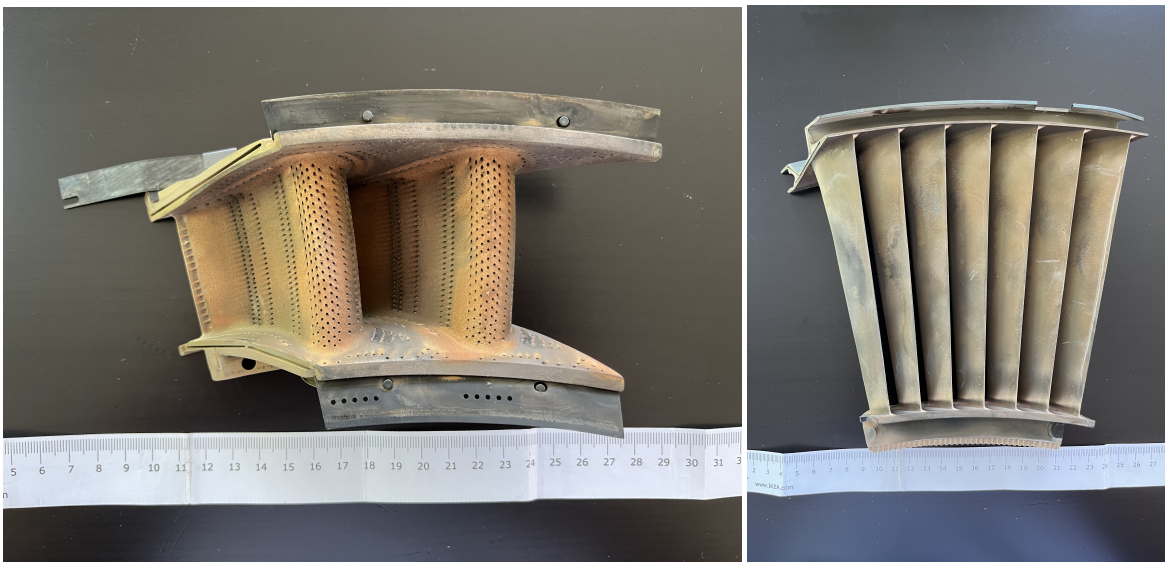

Figure 4.11: CFM56-5C nozzle guide vanes (left) and stage 4 LPT stator vanes (right).

not preliminary designs, so reduced accuracy for this component type is to be expected. As discussed in the last chapter, underestimation of stator weight can be attributed to the fact that the attachment methods are not accounted for, only the weight of the blade airfoil and inner shroud. In the case of low-pressure turbines, however, the weight of stator vanes is overpredicted, not underpredicted, as are rotor blades in the same machines. The reasons for this are not entirely apparent, but the ultra-high aspect ratios produce rather large blades, so a proportionally higher weight estimation should be expected. Another possible explanation of this is the fact that it is unknown if LPT blades are cooled. If they are, then the weight would be between 50% and 100% of the weights currently listed in Table 4.7 (see Equation 4.19), which would bring the estimations into the expected range of underprediction. For now though, LPT blades are assumed uncooled. The trends for casings vary, but they remain within the right order of magnitude. Disks are for the most part overpredicted, which is expected since the blade roots are included in these weight estimations.

Overall, the results again appear quite usable, though the apparent 'accuracy' of the weight estimates may be the results of the compensation of various errors. In the case of turbines, the weight is overpredicted for more components than was the case with axial compressors (e.g., some frames, rotor blades, stator vanes, disks, and casings). These cancel out with the underpredicted component weights to produce a total turbine-level weight estimation that is very close to the WATE++ results in most cases. So, on some level, the results are very promising, and on another level there could be room for improvement of the weight estimation method. All things considered, the axial turbine model developed as part of the WEST program does appear to have the capability to design and estimate turbines to a reasonable degree of usefulness, overall producing results which are believable and physically meaningful.

Finally, comparing the WEST results to real CFM56-5C engine components (Table 4.8), it is apparent that the weight of the nozzle guide vanes is significantly underpredicted. As seen in Figure 4.11, the weight of both the HPT and LPT stators includes a lot of mass in addition to the airfoils themselves. The platforms above

and below the NGVs are rather thick, accounting for a large share of the weight discrepancy. The weight of LPT stage 4 stator vanes are slightly overpredicted, even more so when considering the fact that the weight estimation does not include the platforms or seal.

The number of blades for each of these cases was approximated by measuring the arc width and arc height of the real engine components, and then using these to estimate the machine radius at that location. This could then be used to determine the circumference and estimate the number of components (and thus the number of blades) that fit around that circumference. These approximate results are compared to the WEST predictions in Table 4.8. As is evident from this table, WEST estimates a higher number of NGVs and lower number of LPT stage 4 vanes.

Table 4.7: Comparison of weight estimation results for CFM56 and PW2037 axial turbines [22].

Engine	Component	WATE++ [kg]	WEST [kg]	Rel. Error [-]
CFM56	**HPT (Total)**	**220.0**	**177.4**	**-19.4%**
	Rotors + Disks	60.3	76.4	26.7%
	Rotor Blades	12.7	2.57	
	Disks	47.6	73.9	
	Stator Vanes	30.8	3.93	-87.3%
	Casing	21.8	12.6	-42.4%
	Frame	59.4	84.5	42.2%
	Connecting Hardware		0.00	
	Other	47.6		
CFM56	**LPT (Total)**	**353.3**	**320.2**	**-9.4%**
	Rotors + Disks	116.1	105.3	-9.3%
	Rotor Blades	34.9	42.9	
	Disks	81.2	62.4	
	Stator Vanes	35.8	45.3	26.4%
	Casing	54.4	38.9	-28.5%
	Frame	46.7	124.8	167.1%
	Connecting Hardware		5.92	
	Other	100.2		
PW2037	**HPT (Total)**	**371.9**	**350.0**	**-5.9%**
	Rotors + Disks	122.0	190.3	56.0%
	Rotor Blades	18.6	11.3	
	Disks	103.4	179.0	
	Stator Vanes	44.9	16.3	-63.6%
	Casing	29.9	52.7	75.9%
	Frame	107.5	87.7	-18.4%
	Connecting Hardware		3.04	
	Other	67.6		
PW2037	**LPT (Total)**	**574.7**	**549.9**	**-4.3%**
	Rotors + Disks	195.5	236.2	20.8%
	Rotor Blades	61.7	74.5	
	Disks	133.8	161.7	
	Stator Vanes	64.0	78.8	23.2%
	Casing	85.3	83.2	-2.4%
	Frame	70.3	141.4	101.2%
	Connecting Hardware		10.3	
	Other	159.7		

Table 4.8: Comparison of WEST design and weight estimation results with real engine components.

Category	Parameter	Units	WEST[1]	CFM56[2,3]
HPT Nozzle Guide Vanes	Blade Weight, m_{bl}	g	32.9	306
	Number of Blades, n_{bl}	-	60	48
LPT Stage 4 Stator Row	Blade Weight, m_{bl}	g	176.2	164.9
	Number of Blades, n_{bl}	-	78	133

[1] CFM56-5B. [2] CFM56-5C. [3] Approximate (based on measurements of real components).

4.3. SENSITIVITY ANALYSIS

Analyzing the sensitivity of the design and its weight estimation to key parameters of interest can again be performed in the case of axial turbines. Since the design methodologies of axial compressors and turbines are largely the same, not all parameters will be revisited. Instead, the main focus of this chapter will be on analyzing the sensitivity to factors which may not have been present with axial compressors, namely the disk temperatures and temperature distribution. It is likely safe to assume that the weight estimation will indeed be fairly sensitive to annulus type, number of stages, thermodynamic inputs, duty coefficients, disk type, material selection, etc., without going into much detail. Section 4.3.1 investigates the sensitivity of the disk design, stresses, and weight to the temperature profile (and resulting temperature gradients), while Section 4.3.2 studies the sensitivity of the results to the numerical settings of the software implementation.

4.3.1. DISK TEMPERATURE PROFILE

Four temperature profiles will be studied. The nominal profile – which was proposed by Grieb [42] and will therefore be subsequently referred to as the *Grieb* temperature profile – is described in Section 4.1.3.2. Here, the temperature varies between T_{hub} at the hub and $T_{cooling}$ at the disk inner radius. The same profile will be studied in both its nominal case and with a reduced cooling temperature. Besides these, the case of constant disk temperature (i.e., $T = T_{hub}$ throughout the disk) will be studied, as well as an entirely linear profile varying between T_{hub} at the hub and $T_{cooling}$ at the inner radius.

4.3.1.1. SAME DISK

By designing/optimizing a particular disk to the nominal case and then changing the temperature profile, the sensitivity of the stresses can be examined, without any changes to the disk design and/or weight estimation. Figure 4.10 and Figure 4.12 show examples of the distribution of stresses (and stress criteria) for two of the profiles studied, i.e., the nominal and linear profiles, respectively, for the same disk. The full result set is included in Appendix C.2.2.1, while a direct comparison of the yield and burst criteria for all profile types is included in Figure 4.13. The maximum von Mises stress and worst stress criterion of all profiles are summarized in Table 4.9 for the CFM56 LPT first stage disk and Table 4.10 for the CFM56 HPT disk.

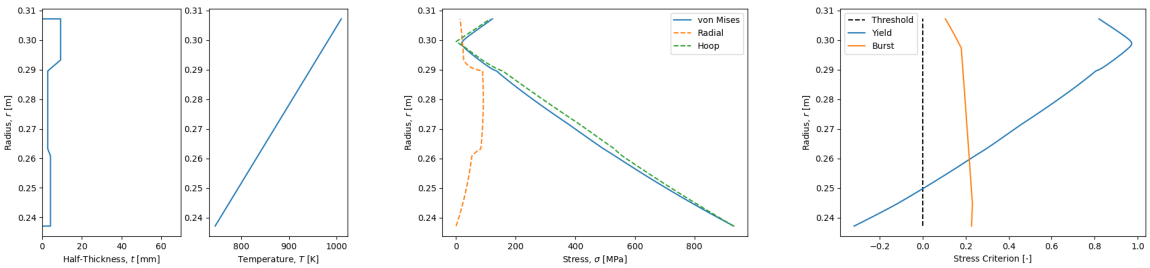

Figure 4.12: Stress distributions of CFM56 LPT first stage disk (linear temperature profile). Regions for which one or more of the stress criteria fall below the threshold of zero indicate that the structural requirements are not satisfied.

Table 4.9: Comparison of stress results of CFM56 LPT model first stage disk for various temperature profiles.

		Temperature Profile			
Parameter	**Units**	**Grieb (Case 1)**[1]	**Grieb (Case 2)**[2]	**Linear**	**Constant**
Max. von Mises Stress[3], $\sigma_{e,max}$	MPa	695.0	1082.8	932.2	372.4
Worst Stress Criterion	-	0.0156	-0.5164	-0.3202	0.3053

[1] Nominal. $T_{cooling} = T_{t,25} + 0.75 \cdot (T_{t,3} - T_{t,25})$. [2] $T_{cooling} = T_{t,25}$.

As is clear from Table 4.9 and Table 4.10, reducing the temperature of the cooling air actually results in a worse minimum stress criterion. In principle, reducing the material temperature increases its yield strength, thus the factor of safety is expected to rise. However, in the case of disk design, the lower cooling temperature results in steeper temperature gradients (assuming the temperature at the hub is fixed), which induces additional stresses. The net effect of this is actually a lower factor of safety overall. Application of a linear profile but with the same inner and outer temperatures as the nominal case also increases the stresses. While the temperature gradient is less steep at the hub, it is higher at the inner radius, and since the inner radius

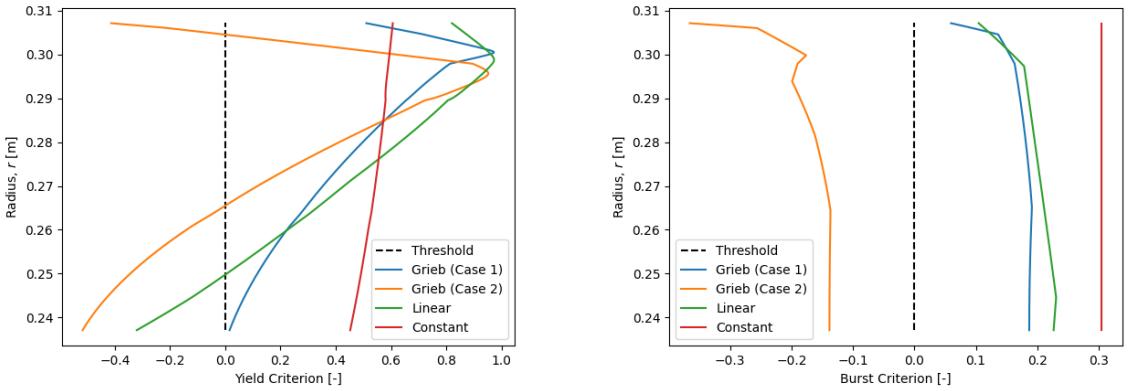

Figure 4.13: Stress criteria of CFM56 LPT first stage disk for various temperature profiles. Regions for which one or more of the stress criteria fall below the threshold of zero indicate that the structural requirements are not satisfied.

Table 4.10: Comparison of stress results of CFM56 HPT model (single stage) disk for various temperature profiles.

		Temperature Profile			
Parameter	**Units**	**Grieb (Case 1)**[1]	**Grieb (Case 2)**[2]	**Linear**	**Constant**
Max. von Mises Stress[3], $\sigma_{e,max}$	MPa	855.2	1098.4	981.3	793.2
Worst Stress Criterion	-	-0.2196	-0.6440	-0.3996	-0.2981

[1] Nominal. $T_{cooling} = T_{t,3}$. [2] $T_{cooling} = T_{t,25}$.

is often the critical region, the larger gradient here means higher stresses and a reduced minimum factor of safety. In the case of the CFM56 LPT, application of a linear profile actually means the difference between a mechanically viable disk and one that is not.

Keeping the temperature constant throughout the disk, i.e., an uncooled disk like what is applied in the case of compressors, results in lower stresses due to the absence of temperature-induced stresses. In the case of the CFM56 HPT first stage disk, this actually results in a higher factor of safety despite the lower material yield strength which comes as a result of the higher operating temperature. While it may therefore seem beneficial to not cool the turbine blades, this is not practical. Without cooling, the temperatures would continue to rise, thus it is necessary to keep the material operating temperature within reason. However, it is clear that a balance must be sought between the magnitude of the temperatures and the temperature gradients. This can be controlled with the temperature and mass flow rate of the cooling air. Thus, the selected temperature distribution has a significant effect on the disk stresses.

4.3.1.2. DIFFERENT (OPTIMIZED) DISKS

Next, the effect of different temperature profiles on disk weight will be investigated. For this, disks will be designed and optimized according to the prescribed methodology, with only the temperature profile changing. This will give insight into the sensitivity of disk design and weight to the assumption of the type of profile. Even the method proposed by Grieb [42] is an approximation, so it is beneficial to evaluate how dependent the results are on such approximations and assumptions. The design results are presented in Figure 4.14, followed by the weight estimations in Table 4.11. The worst stress criterion and representative execution times are included in Table 4.12.

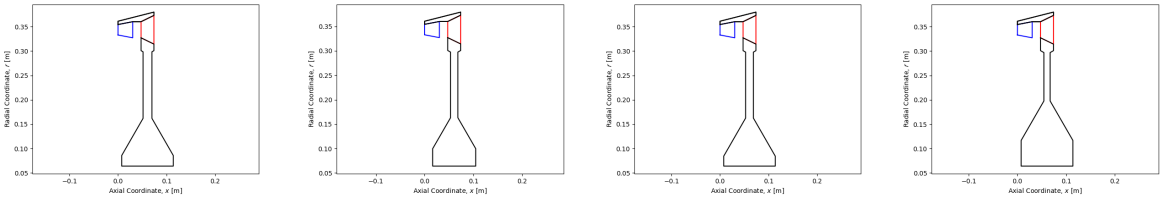

Figure 4.14: Design results of CFM56 HPT for various temperature profiles. Left to right: Grieb (Case 1), Grieb (Case 2), Linear, Constant.

Table 4.11: Comparison of weight estimation results of CFM56 HPT model for various disk temperature profiles.

Component	**Weight [kg]**			
	Grieb (Case 1)[1,2]	Grieb (Case 2)[1,3]	Linear[1]	Constant[1]
HPT (Total)	**177.4**	**169.8**	**173.3**	**189.6**
Rotors + Disks	76.4	70.4	72.3	88.6
Rotor Blades	(2.57)	2.64	(2.57)	(2.57)
Disks	73.9	67.8	69.7	86.1
Stator Vanes	(3.93)	2.95	(3.93)	(3.93)
Casing	(12.6)	11.9	(12.6)	(12.6)
Frame	(84.5)	(84.5)	(84.5)	(84.5)
Connecting Hardware	(0.00)	(0.00)	(0.00)	(0.00)

[1]Temperature profile. [2]Nominal. [3]Reduced $T_{cooling}$.

Table 4.12: Comparison of stress results and execution time of CFM56 HPT model for various disk temperature profiles when the disks are designed/optimized for their respective profiles.

		Temperature Profile			
Parameter	**Units**	**Grieb (Case 1)[1]**	**Grieb (Case 2)[2]**	**Linear**	**Constant**
Worst Stress Criterion	-	-0.2196	5.362e-08	-0.3433	-0.1548
Execution Time[3]	s	445.5	89.2	468.3	288.2

[1]Nominal. [2]Reduced $T_{cooling}$. [3]Results may vary.

As seen in Table 4.11, the weights of the disks vary when designed with different temperature distributions, but not excessively (+6.9%/-4.3% from the nominal case). This limited variation in weight estimation is good since the temperature distributions used in the WEST methodology are assumptions, so the lower the sensitivity of the results to such unknown factors, the better. The appearance does change, however, as seen in the various disks designs shown in Figure 4.14, thus there is some clear sensitivity to the assumed profile.

When the four temperature profiles were assigned to the same disk design, the case with the worst stresses was the one for which the temperature of the cooling air was reduced substantially, which resulted in steeper gradients and higher induced stresses. However, when the design of the disk is optimized for the specified temperature profile, then it is actually the one with the most cooling that yields the lowest weight result (Table 4.11) and the only one which satisfies the stress criteria. This is due partially to the fact that the blade and platform temperatures are reduced as well as a result of the lower cooling temperature: reducing the platform temperature mitigates some of the temperature-induced stresses since it decreases the slope of the gradient, and reducing the blade bulk temperature results in lighter blades, meaning the disk has to carry a smaller radial load at its hub. Additionally, it does this at the lowest computational cost (Table 4.12) since an optimal result is found, so the program does not need to continue until its iteration limit.

4.3.2. SETTINGS

Next, the sensitivity of the design and weight estimation results of WEST's axial turbine model can be analyzed with regard to numerical settings of the program. Ideally, the designs should be as physically-based as possible, not dependent on the practical software implementation of the methodology.

4.3.2.1. DISK FINITE ELEMENT COUNT

The number of finite elements used to discretize the disks for their elementwise stress analysis and weight estimation was a software setting already investigated for axial compressors (see Section 3.3.7.1). Here it was shown that the results were nearly independent of the number of elements used in the discretization. However, axial turbine disks feature temperature gradients and temperature-induced stresses, so it is beneficial to re-evaluate this sensitivity for the present turbomachinery model. Figure 4.15 shows the design results of six settings: when 10, 100, 500, 1000, 2000, and 4000 elements are used to discretize the disk. Table 4.13 shows the weight estimation results of these designs, and Table 4.14 the execution time required for these weight estimations.

Assuming that the highest level of refinement produces the most realistic weight estimation results, the use of 4000 elements comes at a huge computational cost, without much change compared to the nominal case. The case using 2000 elements has over three times the execution time compared to the nominal case

for only a 0.53% difference in weight estimation, although the design does change. Thus, the use of 500 or 1000 elements may be sufficient. Further reduction in the number of elements changes (increases) the weight by 0.95-2.78% with respect to the nominal. The more error that is considered acceptable, the more the computational cost can be reduced, so in some cases it may be acceptable to reduce the number of elements to 100. Thus, the axial turbine disk design is more sensitive to finite element count than was the case with axial compressors, but even still the reduction in execution time may be worth the slightly lower accuracy of the results.

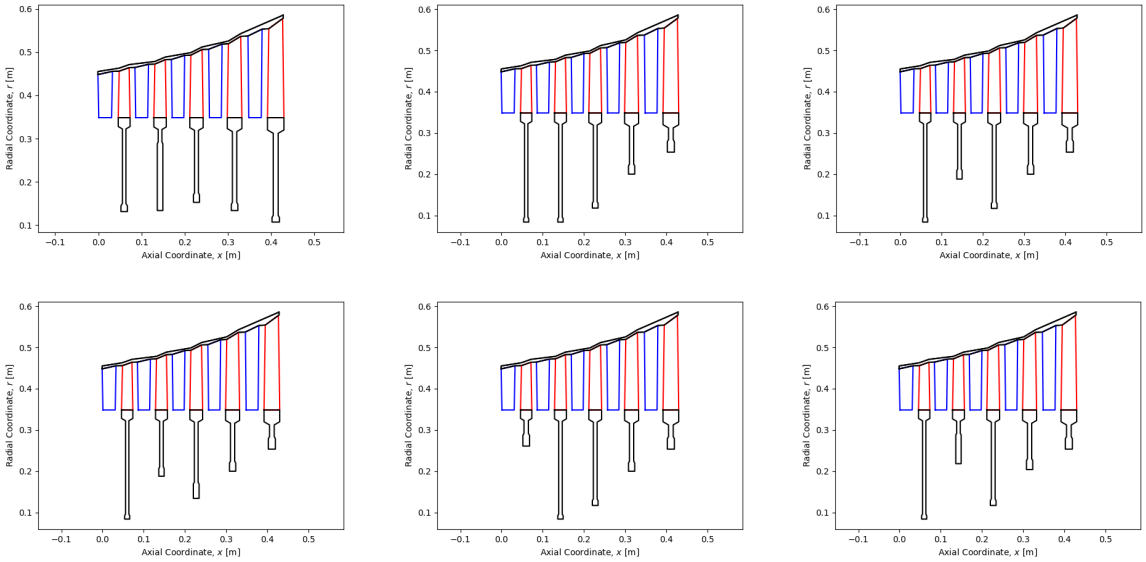

Figure 4.15: Design results of PW2037 LPT using 10 (top left), 100 (top middle), 500 (top right), 1000 (bottom left), 2000 (bottom middle), and 4000 (bottom right) finite elements.

Table 4.13: Comparison of weight estimation results of PW2037 LPT model for various number of discrete finite disk elements.

Component	**Weight [kg]**					
	10[1]	100[1]	500[1]	1000[1,2]	2000[1]	4000[1]
Total	**565.2**	**555.1**	**550.0**	**549.9**	**547.0**	**550.3**
Rotors + Disks	251.8	241.6	236.3	236.2	233.3	236.5
Rotor Blades	(74.5)	(74.5)	(74.5)	(74.5)	(74.5)	(74.5)
Disks	177.3	167.1	161.8	161.7	158.8	162.0
Stator Vanes	(78.8)	(78.8)	(78.8)	(78.8)	(78.8)	(78.8)
Casing	(83.2)	(83.2)	(83.2)	(83.2)	(83.2)	(83.2)
Frame	(141.4)	(141.4)	(141.4)	(141.4)	(141.4)	(141.4)
Connecting Hardware	10.0	10.1	10.3	10.3	10.3	10.4

[1]Number of discrete finite disk elements. [2]Nominal.

Table 4.14: Comparison of execution time of PW2037 LPT model for various number of discrete finite disk elements.

Test	**Time[1] [s]**					
	10[2]	100[2]	500[2]	1000[2,3]	2000[2]	4000[2]
1	30.1	69.1	221.0	346.6	1153.1	3154.4

[1]Results may vary. [2]Number of discrete finite disk elements.
[3]Nominal.

As is evident from the results shown in Figure 4.15, the design/appearance of the disks varies more noticeably than the weight estimations. The disks of the first two rows of the PW2037 LPT do not satisfy the stress criteria, and it is these same two disks for which no apparent trend exists between the designs of the

difference cases. Thus, the number of elements used significantly affects the optimized design result when the stress criteria are not satisfied. Even for cases using a large number of elements, the results do not appear to converge, which is problematic. The designer should therefore take this into consideration when selecting the number of finite elements to use, since a tradeoff exists between the computational cost and the convergence of the design results.

4.4. SUMMARY

- The meanline analysis and design of the gas path, blades, disks, and casing of axial turbines follows largely the same approach as that of axial compressors. Some differences do exist, such as the use of power instead of pressure ratio in defining the machine (Section 4.1.1.1), the shape of the airfoils used in blade design (Section 4.1.2.1), and the ways in which the operating temperatures of various components are calculated and/or distributed (e.g., Section 4.1.3.2).
- The design method for turbine blade camber lines (Section 4.1.2.1), which was developed as part of the WEST methodology, collaborates well with the thickness distributions obtained using the method proposed by Dunham [70], producing realistic turbine blade airfoils (Figure 4.8).
- Due to cooling, turbine disks feature temperature gradients, unlike compressor disks which were assumed to have a uniform temperature. The temperature gradients present in the disks induce additional stresses (Section 3.1.2.3).
- The weight estimations of axial turbines (Table 4.7) appears to match more closely the WATE++ results compared to axial compressors (Table 3.10). Underprediction is still observed, which is consistent with expectations. This 'improved accuracy' may not be accuracy at all, but rather a cancellation of errors, since some of the components in the turbine subassemblies are more consistently overpredicted.
- Rotor blades and stator vanes continue to be underpredicted in the case of high-pressure turbines, but are actually much heavier than the WATE++ results in the case of low-pressure turbines (Table 3.10).
- The higher turbine inlet temperature assumed for the PW2037 validation case compared to the CFM56 (Table 4.5) causes the operating temperature of turbine components to be higher, which reduces the yield strength of the materials and causes component weights to be higher (see, for example, the weights of the PW2037 turbine casings in Table 3.10).
- The empirical correlation used to estimate the weight of turbine frames (Figure 4.6 [17]) overpredicts the turbine weight, in most cases, when compared to the WATE++ predictions (Table 3.10).
- The temperature gradient and profile significantly affect the stresses in the disk (Section 4.6), since temperature gradients induce additional stresses. Higher gradients (i.e., more cooling) can in some cases increase the factor of safety and reduce the weight of the disk, if it is designed/optimized for that case. Otherwise, additional cooling can increase stresses (and reduce the factor of safety) if not applied properly.
- The selection of realistic temperatures and temperature profiles is therefore essential in achieving realistic weight estimations. Since temperatures and their gradients affect the yield strength and stress distributions, respectively, these heavily influence the final design and therefore the weight of the components.
- The number of finite elements used to discretize turbine disks has a larger influence on the design and weight estimation results compared to when the same study was performed for axial compressor disks (compare Table 4.13 to Table 3.28). This is likely due to the presence of a temperature gradient and the stresses this induces, meaning more elements are required to correctly resolve all stresses. Nevertheless, reducing the number of elements has the potential to substantially reduce the computational cost (Table 4.14), so doing so is advisable in applications where slight reductions in accuracy are acceptable.

5

GAS TURBINE ENGINES

The objective of this chapter is to describe the methodology (Section 5.1), validation (Sec. 5.2), and sensitivity analysis (Sec. 5.3) of the preliminary gas turbine engine design and weight estimation tool *WEST*, which was developed as part of this study. Compressors and turbines represents an important part of any gas turbine, and these were already addressed in Chapters 3 and 4, respectively; the design methodology described in Section 5.1 will therefore discuss the engine-level assembly, as well as all less significant (but no less important) component types such as shafts and combustors. The results presented in this chapter (Sec. 5.2) will either make or break WEST, since it is the full-engine weight estimation which is so important in the design and optimization studies of future engine and aircraft architectures.

5.1. DESIGN METHODOLOGY

This section addresses the design methodology of a complete (two-spool) *gas generator*, or engine *core*, as would be used in a turbofan engine, as well as the methodologies for component types which do not fall under the category of turbomachinery. The full engine is mainly an assembly of the various components and subassemblies. The design methodology of ducts, combustors, and shafts are described in Sections 5.1.1, 5.1.2, and 5.1.3, respectively, with the weight estimation of engine accessories discussed in Section 5.1.4. This section closes with the two-spool gas generator in Section 5.1.5.

The design of ducts, combustors, and shafts have in common that they can only be finalized once the full engine structure begins to take shape. For example, the mean radius and height of the gas path channel at the inlets and outlets of compressors and turbines determines the mean radii and channel heights of ducts and combustors, while the combustor length and width depends on the mass flow rate of the core. Next, when the ducts and combustor designs are finalized, their dimensions can be extracted and then combined with the lengths of the turbomachinery to determine the necessary lengths of the shafts which connect all rotating components. The radii of shafts also depends on the power and torque transmitted between turbines and compressors, thus they too must wait until the full engine comes together. Lastly, the weight of accessories are often proportional to the weight of the otherwise complete engine.

Thus, since the performance of the compressors and turbines is critical for the overall performance of the engine (e.g., power output, specific fuel consumption, etc.), these are designed first. The other components can then be designed using the turbomachinery design output data.

5.1.1. DUCTS

Ducts are flow passages which form part of the gas path. They are used to connect the channels of the low- and high-pressure compressors or high- and low-pressure turbines. Since the mean radius and/or channel height at the outlet of one turbomachine may not match the inlet geometry of the next, ducts are used in a sense to 'bridge' these gaps. This is better than designing the compressors/turbines to have matching inlet/outlet geometry since the radii and channel heights have a large effect on machine performance, and everything should be done to keep the performance as optimal as possible. Thus, ducts are introduced to accommodate the differences in geometry with minimal friction/separation losses, factors which will not be accounted for in the present methodology.

5.1.1.1. REQUIRED INPUTS

A great deal of overlap exists between the design methodology of ducts and the discussion of stator vane inner shrouds described in Section 3.1.4.1. However, for the sake of completion, the necessary steps and equations will be repeated here. Table 5.1 lists the inputs required for a complete duct design.

Table 5.1: Required inputs for duct design.

Category	#	Input Parameter	Symbol	Units
Geometry	1	Mean Radius (Inlet)	$r_{m,in}$	m
	2	Mean Radius (Outlet)	$r_{m,out}$	m
	3	Channel Height (Inlet)	b_{in}	m
	4	Channel Height (Outlet)	b_{out}	m
Gas Properties	5	Operating Temperature	T_{aw}	K
	6	Static Pressure	p_s	Pa
Design	7	Length[1]	l	m
	8	Maximum Flare Angle	$\theta_{fl,max}$	deg
	9	Minimum Wall Thickness	t_{min}	m
	10	Safety Factor	SF	-
	11	Material		

[1] Optional.

In this table, the mean radii and channel heights at the inlet and outlet are determined by the turbomachinery at either end; these values are fixed in order to maintain compatibility with the surrounding components, and are therefore not necessarily free design variables. The same goes for the operating temperature and pressure, T_{aw} and p_s, since these are properties of the gas and are therefore equal to the outlet properties of the upstream turbomachine; they are not specified by the user. The operating temperature is assumed equal to the (static) adiabatic wall temperature calculated using the gas properties according to Equation 5.1. The same recovery factor, f_R, of 0.892 can be used in this equation as discussed earlier in Section 3.1.1.7. The user is free, however, to specify the length, maximum flare angle, minimum wall thickness, factor of safety, and material.

$$T_{aw} = T_s + f_R\,(T_t - T_s) \tag{5.1}$$

Default Values A default maximum flare angle, $\theta_{fl,max}$, of **30 degrees** is built in to curb losses due to separation. The default minimum wall thickness, t_{min}, of **1 millimetre** (mm), which was, instead, defined based on manufacturing considerations. A default minimum factor of safety, SF, of **1.1** will be applied, unless specified otherwise by the user. This is the value recommended by Tong et al. [18] for the disk yield criterion, and since no other more suitable value was found for ducts, this will be used. The default material is **17-4PH** alloy steel. The length, l, is optional since, if no length is specified, it will be calculated such that the maximum flare angle is not exceeded. This can be done using Equation 5.2 if the mean radius decreases downstream (i.e., $r_{m,in} > r_{m,out}$) or Equation 5.3 if it increases downstream. The inner and outer radii at any location, r_i and r_o, are defined in Equations 5.4 and 5.5, respectively.

$$l = \frac{r_{i,in} - r_{i,out}}{\tan\left(\theta_{fl,max}\right)} \tag{5.2}$$

$$l = \frac{r_{o,out} - r_{o,in}}{\tan\left(\theta_{fl,max}\right)} \tag{5.3}$$

$$r_i = r_m - \frac{b}{2} \tag{5.4}$$

$$r_o = r_m + \frac{b}{2} \tag{5.5}$$

5.1.1.2. WALL THICKNESSES

The required wall thickness can then be calculated using Equation 5.6 [21]. This ensures the duct is strong enough to contain the pressure of the working fluid. This operation is repeated for each of the four 'corner' locations (when viewed as a 2D cross-section) of a duct, i.e., the inner and outer channel radius at both the inlet and the outlet of the duct. The material yield strength, σ_y, depends on the material selected by the user and the static operating temperature. A safety factor, SF, is added to the calculation, as shown in Equation 5.6.

$$t = SF \cdot \frac{p_s \cdot r}{\sigma_y} \tag{5.6}$$

The two thicknesses for the inner wall, one for the inlet and one for the outlet, can then be combined and the maximum of the two taken so that the inner wall has a uniform thickness, denoted as t_i, thus improving the manufacturability of this component. This concept is shown in Equation 5.7. The same can be done for the outer wall (Equation 5.8).

$$t_i = \max\left(t_{i,in}, \quad t_{i,out}\right) \tag{5.7}$$

$$t_o = \max\left(t_{o,in}, \quad t_{o,out}\right) \tag{5.8}$$

Finally, the estimated values can be rounded *up* to the nearest sheet/plate metal thickness; see the standard values listed in Table 3.6.

As an example, if the minimum thickness of the outer wall was calculated to be 1.97 mm at the inlet and 2.13 mm at the outlet using Equation 5.6, then combining these yields 2.13 mm according to Equation 5.8. The values of 2.13 mm lies in the range of 2 to 3mm, so it should be rounded up to the nearest multiple of 0.50 mm according to Table 3.6, resulting in an outer wall thickness of 2.50 mm.

5.1.1.3. WEIGHT

Lastly, the weight of the duct can be calculated. The volume of the inner and outer walls can be calculated using Equations 5.9 and 5.10, respectively, followed by the weight using Equation 5.11.

$$V_i = \frac{\pi \cdot l}{3}\left[\left[r_{i,in}^2 + \left(r_{i,in} \cdot r_{i,out}\right) + r_{i,out}^2\right] - \left[\left(r_{i,in} - t_i\right)^2 + \left(\left(r_{i,in} - t_i\right) \cdot \left(r_{i,out} - t_i\right)\right) + \left(r_{i,out} - t_i\right)^2\right]\right] \tag{5.9}$$

$$V_o = \frac{\pi \cdot l}{3}\left[\left[\left(r_{o,in} + t_o\right)^2 + \left(\left(r_{o,in} + t_o\right) \cdot \left(r_{o,out} + t_o\right)\right) + \left(r_{o,out} + t_o\right)^2\right] - \left[r_{o,in}^2 + \left(r_{o,in} \cdot r_{o,out}\right) + r_{o,out}^2\right]\right] \tag{5.10}$$

$$m_{duct} = \rho \cdot \left(V_i + V_o\right) \tag{5.11}$$

5.1.2. COMBUSTOR

The *combustor*, also known as the burner or combustion chamber, is the component whereby the chemical energy of the fuel is transferred to the working fluid. The detailed design of combustors involve complex, multi-phyiscal aspects and must account for fluid-dynamic, thermal, chemical, and mechanical considerations. This is also the component which experiences the largest pressures and temperatures, thus the design of the combustor is by no means trivial.

However, since the primary objective of the WEST program is weight estimation, a simplified combustor model was developed in order to reduce the development time and computational cost. The present methodology takes inspiration from the work of Onat and Klees [17] and Becker et al. [20], as will be discussed shortly. Despite the simplified design method, it was shown that the combustor weight estimations matched very closely to the WATE++ results of the CFM56 and PW2037 engines provided by Greitzer et al. [22], as will be shown in Section 5.2. Thus, while the combustor design module can be significantly improved in the future through higher-fidelity analysis and a wider range of considerations, further refinement of the methodology was not considered necessary at this time.

5.1.2.1. REQUIRED INPUTS

Table 5.2 shows the inputs required for the simplified design of the combustor. The first eight input parameters all correspond to results of the meanline analysis and gas path design, and are therefore not free design variables. In this case, Station 3 is the outlet of the high-pressure compressor and inlet of the combustor (e.g., $\dot{m}_3 = \dot{m}_{in}$), while Station 4 is the outlet of the combustor and inlet of the high-pressure turbine. The mean radii and channel heights can be used to calculate the inner and outer radii at the inlet and outlet using Equations 5.4 and 5.5, as was done during the duct design procedure.

Table 5.2: Required inputs for combustor design.

Category	#	Input Parameter	Symbol	Units
Geometry	1	Mean Radius (Inlet)	$r_{m,in}$	m
	2	Mean Radius (Outlet)	$r_{m,out}$	m
	3	Channel Height (Inlet)	b_{in}	m
	4	Channel Height (Outlet)	b_{out}	m
Performance	5	Air Mass Flow Rate	$\dot{m}_3$	kg/s
	6	Inlet Total Pressure	$p_{t,3}$	Pa
	7	Inlet Total Temperature	$T_{t,3}$	K
	8	Inlet Static Temperature	$T_{s,3}$	K
Design	9	Turbine Inlet Temperature	$T_{t,4}$	K
	10	Reference Velocity[1]	V_{ref}	m/s
	11	Residence Time	τ_R	ms
	12	Pressure Ratio	PR_{cc}	-
	13	Adiabatic Efficiency	η_{cc}	-

[1] Optional.

The first 'free' design variable is the turbine inlet temperature (TIT), or $T_{t,4}$ (although this must already be known when the HPT is designed). This represents one of the key engine-level design parameters and has the potential to significantly affect the engine performance and efficiency, as well as the lifetime of combustor and turbine components.

Default Values The reference velocity is optional since, if none is specified by the user, a value will automatically be calculated using Equation 5.12 [20]. In this and all subsequent equations in this section, the working fluid properties (such as the gas constant R_g used in Equation 5.12) correspond to those of post-combustion gases, i.e., the values listed in Table 4.2.

$$V_{ref} = \sqrt{0.006 \cdot R_g \cdot T_{s,3}} \tag{5.12}$$

For the residence time, pressure ratio, and adiabatic efficiency, default values will be assumed if none is specified by the user. For these, a residence time of 5 ms [73], pressure ratio of 0.94 [20], and adiabatic efficiency of 0.99 [40] are used.

5.1.2.2. CHANNEL LENGTH AND HEIGHT

As discussed in Section 4.2.1, the outlet pressure, $p_{t,4}$, and fuel mass flow rate, $\dot{m}_f$, of the combustor can be calculated using Equations 5.13 and 5.14, respectively, where Equation 5.14 is solved iteratively using a lower heating value, LHV, of Jet A-1 kerosene fuel equal to 43.39 MJ/kg$_f$ [72].

$$p_{t,4} = p_{t,3} \cdot PR_{cc} \tag{5.13}$$

$$\dot{m}_f = \frac{\left(\dot{m}_3 + \dot{m}_f\right) \cdot c_p \cdot \left(T_{t,4} - T_{t,3}\right)}{\eta_{cc} \cdot LHV} \tag{5.14}$$

The total mass flow rate through the combustor, $\dot{m}_4$, can therefore be calculated using Equation 5.15:

$$\dot{m}_4 = \dot{m}_3 + \dot{m}_f \tag{5.15}$$

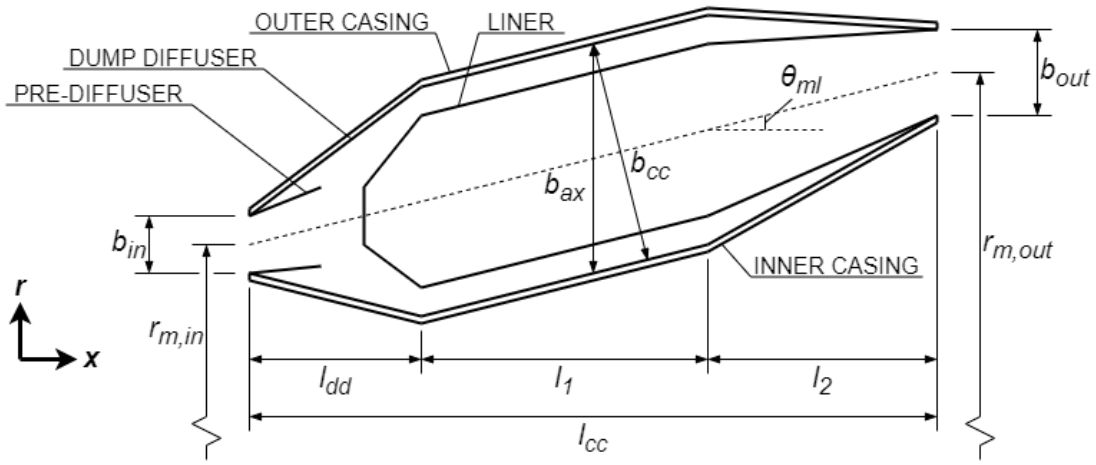

Figure 5.1: Simplified visualization of gas turbine combustor.

Figure 5.1 shows a simplified representation of a gas turbine combustor as used in the present methodology. The total axial length of the combustor, l_{cc}, can be determined according to Equation 5.16 (where τ_R is expressed in units of seconds, not milliseconds):

$$l_{cc} = V_{ref} \cdot \tau_R \tag{5.16}$$

If the user would like to prescribe a specific length, then this can be done indirectly through selection of a suitable set of V_{ref} and τ_R which produce the desired result. A combustor with a high reference velocity and low residence time may have the same length as a combustor with a low reference velocity and a long residence time: the difference comes in the width (or channel/passage height), b. In the case of the high V_{ref}, low τ_R design, the passage height will be much lower than the latter case, giving it a 'thinner' appearance.

The meanline angle, θ_{ml}, i.e., the angle between the combustor mean axis and the axial direction, can be calculated using Equation 5.17:

$$\theta_{ml} = \tan^{-1}\left(\frac{|r_{out} - r_{in}|}{l_{cc}}\right) \tag{5.17}$$

The total specific enthalpy of the flow, h_t, and (average) total pressure, p_t, can then be calculated using Equations 5.18 and 5.19.

$$h_t = c_p \cdot T_{t,4} \tag{5.18}$$

$$p_t = \frac{p_{t,3} + p_{t,4}}{2} \tag{5.19}$$

These two values can then be used to determine the required channel cross-sectional area, A_{cc}, using the calculations described in Equations 2.27 through 2.33. For these calculations, the combustor reference velocity V_{ref} can be used in place of V and V_m. The properties of calorically-perfect post-combustion gases (Table 4.2) are used in these equations, as well as the total combustor mass flow rate, $\dot{m}_4$, in Equation 2.33.

With the required cross-sectional area now known, this can be followed up by calculation of the average combustor channel height, b_{cc}, using Equation 5.20.

$$b_{cc} = \frac{A_{cc}}{2 \cdot \pi \cdot r_m} \tag{5.20}$$

Finally, the channel height can be converted into a height which is perpendicular to the axial direction (and parallel to the inlet and outlet channel heights specified as input parameters). This value can be denoted as b_{ax} and calculated using Equation 5.21. The difference between b_{cc} and b_{ax} is illustrated in Figure 5.1.

$$b_{ax} = \frac{b_{cc}}{\cos(\theta_{ml})} \tag{5.21}$$

While the value of b_{ax} is calculated using the mean radius and mean thermodynamic properties, it is assumed to be sufficiently representative, meaning the calculations will not be repeated for different locations in the combustor and different mean radii. Instead, the combustor casing design can now commence.

5.1.2.3. CASING AND LINER

The inner and outer casing thicknesses (t_i and t_o, respectively, which are assumed constant across the inner/outer casing walls) can be determined using the duct design procedure described in Section 5.1.1. For this procedure, $r_{m,in}$ and $r_{m,out}$ are the same as the combustor. The inlet and outlet channel heights are assumed equal to b_{ax} in both cases, i.e., $b_{in} = b_{out} = b_{ax}$. For combustor design, the material is assumed to be **steel**, and a yield strength of σ_y = 70,000 pounds per square inch, or 482.6 MPa, is appropriate [17]. The value of p_s in Equation 5.6 is the value of static pressure calculated using Equation 2.31 as one of the steps in determining the cross-sectional area of the combustor (as done in the preceding section).

The combustor length can then be split into three sections of length l_{dd}, l_1, and l_2, as shown in Figure 5.1. The length of the dump diffuser, $l_d d$, is assumed equal to one quarter of the total length (Equation 5.22) in the present, simplified methodology, while the length of the tapered region, l_2, is assumed equal to one third of the total length (Equation 5.23).

$$l_{dd} = \frac{1}{4} \cdot l_{cc} \tag{5.22}$$

$$l_2 = \frac{1}{3} \cdot l_{cc} \tag{5.23}$$

The channel inlet height of the dump diffuser section is set equal to the channel height of the combustor, b_{in}, while the channel outlet height of the tapered region is set to match the outlet height b_{out} in a similar fashion. This ensures continuity in the gas path and compatibility with the upstream compressor and downstream turbine.

The liners are assumed to have a thickness of 0.055 inches [17], which is rounded to **1.5 mm**. The liner walls are located at 20% of the passage height from either the inner or outer casings. Thus:

$$b_{liner} = 0.60 \cdot b_{ax} \tag{5.24}$$

5.1.2.4. WEIGHT

To determine the weight of the combustor, WEST begins by creating duct components to model each section of the casing and liner. The weight of each of these can then be calculated according to the methodology described in Section 5.1.1.3 and then added together for the full casing and liner weight. The weight of the pre-diffuser and of the liner section lying in the region of l_{dd} (as shown in Figure 5.1) are not included, since these portions are not modelled.

Primary combustors are also assumed to have a frame. The weight of the frame can be approximated using the frame weight estimation methodology described in Section 4.1.5. Here, a *burner* frame type is used, and a radius equal to the maximum of either $r_{o,in}$ or $r_{o,out}$.

Finally, the weight of the burner dome, fuel manifold and nozzles, and all remaining components can be estimated using Equation 5.25 [17]:

$$WT_{dome} = 0.0106 \cdot \left(r_o^2 - r_i^2\right) \tag{5.25}$$

In this equation, the radii r_o and r_i are expressed in units of inches, and the weight, WT_{dome}, in units of pounds. Thus, this must be converted to the metric weight of kilograms, yielding m_{dome}, before being added to the weight of the combustor casing, liner, and frame in order to obtain the full combustor weight estimation.

5.1.3. SHAFTS

The shafts in gas turbine engines are used to transmit mechanical power between compressors and turbines. In the case of the low-pressure spool, the shaft can span a large portion of the engine's length, and its weight can represent several percentage points of the total engine weight, meaning that shaft design is an important consideration in gas turbine weight estimation.

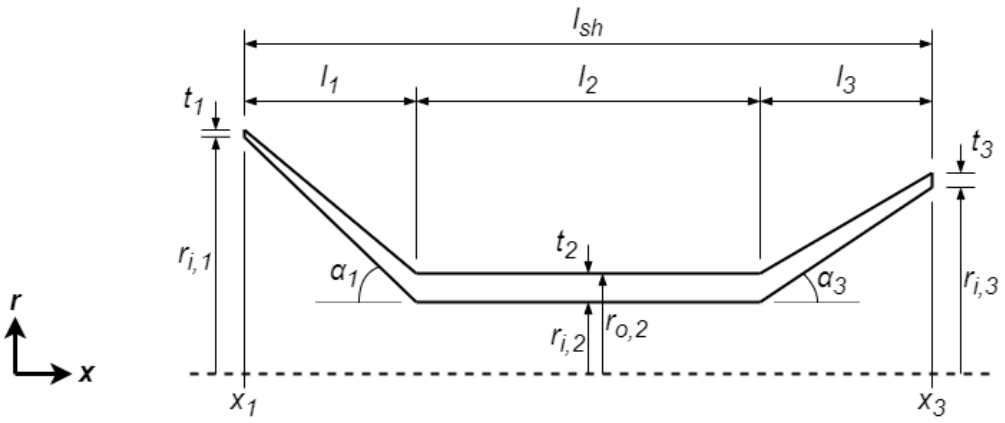

Figure 5.2: Simplified visualization of gas turbine shaft [20].

Table 5.3: Required inputs for combustor design.

Category	#	Input Parameter	Symbol	Units
Geometry	1	Inner Radius 1	$r_{i,1}$	m
	2	Inner Radius 2	$r_{i,2}$	m
	3	Inner Radius 3	$r_{i,3}$	m
	4	Axial Location Start	x_1	m
	5	Axial Location End	x_3	m
	6	Shaft Angle Segment 1	α_1	deg
	7	Shaft Angle Segment 3	α_3	deg
Performance	8	Angular Velocity	ω	rad/s
	9	Power	$\dot{W}$	W
	10	Axial Force	F_{ax}	N
	11	Material Temperature Segment 1	$T_{s,1}$	K
	12	Material Temperature Segment 3	$T_{s,3}$	K
Design	13	Mechanical Efficiency	η_{mech}	-
	14	Minimum Shaft Thickness	t_{min}	m
	15	Safety Factor	SF	-
	16	Material		

5.1.3.1. REQUIRED INPUTS

Figure 5.2 shows a representation of the shaft model geometry. This figure, along with the shaft design methodology, is based largely on the work of Becker et al. [20]. The required inputs are listed in Table 5.2.

The first three input parameters in Table 5.3 concern the radii of various shaft sections. Shafts typically connect to one of the last few rows of the compressor and one of the first few rows of the turbine. In the present methodology, it will be assumed that the shafts connect to the last compressor disk and the first turbine disk, and the radial coordinate of this connection point is 75% of the distance between r_1 and r_6 of the *disk*. This is shown in Equations 5.26 and 5.27, which are adaptations of Equation 3.60. This is consistent with the mounting location of the connecting hardware as described in Section 3.1.4.2. Thus, r_1 and r_3 of the *shaft* can be determined using the disks of the connected compressor and turbine.

$$\left(r_{i,1}\right)_{sh} = \left[r_1 + 0.75 \cdot (r_6 - r_1)\right]_{disk,cmp,last} \tag{5.26}$$

$$\left(r_{i,3}\right)_{sh} = \left[r_1 + 0.75 \cdot (r_6 - r_1)\right]_{disk,trb,first} \tag{5.27}$$

For inner shafts (such as low-pressure spools), the central part of the shaft is not hollow. For outer shafts (such as high-pressure spools), the inner radius can be assumed to be the outer radius of the inner shaft, multiplied by a factor of 1.1 to provide clearance (Equation 5.29).

$$\left(r_{i,2}\right)_{sh,inner} = 0 \tag{5.28}$$

$$\left(r_{i,2}\right)_{sh,outer} \geq 1.1 \cdot \left(r_{i,2} + t_2\right)_{sh,inner} \tag{5.29}$$

The shaft length, l_{sh}, depends on the location of the first turbine disk and last compressor disk. It can be evaluated using Equation 5.30. The axial positions x_1 and x_3 are available once the design of all compressors, turbines, ducts, and the combustor have been completed.

$$l_{sh} = x_3 - x_1 \tag{5.30}$$

The angles of the first and third shaft segments, α_1 and α_3, respectively, can be selected in order to avoid interference with other components in the engine. Default values of 60° can be used otherwise.

The angular velocity, ω, and compressor power, $\dot{W}_{cmp}$, both come from the meanline analysis. The power which must be supplied to the compressor (or external power demand) should be corrected using the mechanical efficiency of the shaft, η_{mech}. The mechanical efficiency can be taken as **0.99** [40].

The axial force in the shaft is a summation of the axial forces acting on every row of the adjoining compressor and turbine, calculated using Equation B.42 during the blade design procedure. The total axial force of all rows can be added to determine the axial force in the shaft, as shown in Equation 5.31. Note that this is a tensile force.

$$(F_{ax})_{sh} = \sum \left(F_{ax,row}\right)_{cmp} + \sum \left(F_{ax,row}\right)_{trb} \tag{5.31}$$

The temperatures at either end of the shaft, $T_{s,1}$ and $T_{s,3}$, can be calculated using the disk temperatures as shown in Equations 5.32 and 5.33, respectively. The disk platform and inner temperatures are those temperatures calculated during the disk design procedure (Sections 3.1.2.5, 4.1.3.2).

$$\left(T_{s,1}\right)_{sh} = \left(T_{plt}\right)_{disk,cmp,last} \tag{5.32}$$

$$\left(T_{s,3}\right)_{sh} = \left(T_i + 0.5 \cdot \left(T_{plt} - T_i\right)\right)_{disk,trb,firsrt} \tag{5.33}$$

The temperature of the middle shaft segment can therefore be approximated using Equation 5.34:

$$T_{s,2} = \frac{T_{s,1} + T_{s,3}}{2} \tag{5.34}$$

Finally, a minimum shaft thickness of **2 mm** can be used based on manufacturing considerations, followed by a minimum factor of safety with a default value of **1.1**, this default being selected for the same reason as in the case of ducts (Section 5.1.1.1). The default material is **17-4PH** alloy steel. Thus, the majority of the shaft inputs are determined based on the design results of previous components. The user mainly controls the angles of the various shaft segments, and, as previously stated, these should be selected such that the shaft does not interfere with other components.

5.1.3.2. STRESS ANALYSIS

The stress analysis procedure can begin by applying the minimum thickness to each of the three primary segments of the shaft. Depending on the results of the stress analysis, the thickness may need to be iterated, as described in the next section.

Firstly, the outer radius, r_o, at the start (1), middle (2), or end (3) of the shaft can be calculated rather simply using Equation 5.35:

$$r_o = r_i + t \tag{5.35}$$

Three stresses will then be analyzed. In each shaft, there is an axial stress caused by the axial forces induced by the compressor and turbine, there is a tangential stress caused by the centrifugal forces, and there is a shear stress due to torsion, according to the procedure described by Becker et al. [20]. In this methodology, critical speeds, longitudinal stiffness, and other potentially-limiting design criteria are not considered [20]. The axial (σ_{ax}), (maximum) tangential ($\sigma_{tg,max}$), and shear (τ) stresses can be calculated using Equations 5.36, 5.37, and 5.38, respectively [20].

$$\sigma_{ax} = \frac{F_{ax}}{\pi \cdot \left(r_o^2 - r_i^2\right)} \tag{5.36}$$

$$\sigma_{tg,max} = 0.825 \cdot \rho \cdot \omega^2 \cdot r_o^2 \cdot \left(1 + 0.212 \cdot \frac{r_i^2}{r_o^2}\right) \tag{5.37}$$

$$\tau = \frac{2 \cdot r_o \cdot T}{\pi \cdot \left(r_o^4 - r_i^4\right)} \tag{5.38}$$

These stresses can then be combined to calculate the maximum von Mises stress, $\sigma_{e,max}$, using Equation 5.39 [20]:

$$\sigma_{e.max} = \sqrt{\sigma_{ax}^2 - \left(\sigma_{ax} \cdot \sigma_{tg,max}\right) + \sigma_{tg,max}^2 + 3 \cdot \tau^2} \tag{5.39}$$

The safety factor, SF, with regard to the yield criterion can then be calculated using Equation 5.40. In this equation, σ_y is the material yield strength at the local operating temperature.

$$SF = \frac{\sigma_y}{\sigma_{e,max}} \tag{5.40}$$

5.1.3.3. LOCAL THICKNESSES

If the yield stress criterion is satisfied, i.e., if the calculated factor of safety is equal to or greater than the user-prescribed minimum factor of safety, then the design can proceed. If not, then the local thickness can be iterated using the Newton-Raphson iteration method (Appendix B.1) in order to obtain a thickness which satisfies the yield criterion and the required factor of safety. The stress analysis and thickness iteration procedure can be repeated for each of the three shaft sections in order to determine the local thicknesses, which can then be used to finalize the shaft geometry and estimate the weight.

5.1.3.4. WEIGHT

Calculation of the shaft weight is relatively straightforward. This component can be divided into its three segments, and the weight estimated using an outer (solid) frustum and an inner (hollow) frustum, in a similar manner to what done for duct weight calculation in Section 5.1.1.3. Thus, the volume of the three segments can be calculated using Equations 5.41 through 5.43. The lengths of the three segments are defined in Equations 5.44 through 5.46.

$$V_1 = \frac{\pi \cdot l_1}{3}\left[\left[\left(r_{i,1} + t_1\right)^2 + \left(\left(r_{i,1} + t_1\right) \cdot \left(r_{i,2} + t_2\right)\right) + \left(r_{i,2} + t_2\right)^2\right] - \left[r_{i,1}^2 + \left(r_{i,1} \cdot r_{i,2}\right) + r_{i,2}^2\right]\right] \tag{5.41}$$

$$V_2 = \pi \cdot l_2 \cdot \left[\left(r_{i,2} + t_2\right)^2 - r_{i,2}^2\right] \tag{5.42}$$

$$V_3 = \frac{\pi \cdot l_3}{3}\left[\left[\left(r_{i,2} + t_2\right)^2 + \left(\left(r_{i,2} + t_2\right) \cdot \left(r_{i,3} + t_3\right)\right) + \left(r_{i,3} + t_3\right)^2\right] - \left[r_{i,2}^2 + \left(r_{i,2} \cdot r_{i,3}\right) + r_{i,3}^2\right]\right] \tag{5.43}$$

$$l_1 = \frac{r_{i,1} - r_{i,2}}{\tan\left(\alpha_1\right)} \tag{5.44}$$

$$l_3 = \frac{r_{i,3} - r_{i,2}}{\tan\left(\alpha_3\right)} \tag{5.45}$$

$$l_2 = l_{sh} - l_1 - l_3 \tag{5.46}$$

Finally, the weight can be calculated using the total shaft volume and density of the selected material, as shown in Equation 5.47:

$$m_{sh} = \rho \cdot \left(V_1 + V_2 + V_3\right) \tag{5.47}$$

5.1.4. ACCESSORIES

For small engines, the WATE-2 methodology developed by Onat and Klees [17] estimates that accessories typically account for about 17% of the total engine weight, excluding accessories. Lolis estimates that accessories account for only 10% of the total engine weight [21]. However, as will be seen in the validation efforts in Section 5.2, the weight of accessories is already generally underpredicted in the current methodology, thus Onat and Klees' estimate of 17% is retained. Thus, to estimate the weight of accessories in the present methodology, the weight of all engine components will be added up, yielding a preliminary total weight. **17%** of this value will then be taken and added to the preliminary total in order to reach the final total weight estimation. With this, the WEST weight estimation methodology is complete.

5.1.5. TWO-SPOOL GAS GENERATOR

The last and highest-level model in the WEST program is that of the engine itself. This does not present new component designs or weight estimation methodologies, but is rather used to link the various components in an engine. For example, using the engine-level thermodynamic inputs (i.e., the first nine entries of Table 5.4 below), the engine model can assign the necessary values to, for example, the LPC in the case of a two-spool gas generator. It can then extract the thermodynamic parameters at the outlet of this compressor and assign them as inputs for the HPC, continuing downstream and repeating this procedure for the combustor, HPT, and LPT. This avoids the user providing these input values manually.

Table 5.4: Required inputs for two-spool gas generator design.

Category	#	Input Parameter	Symbol	Units
Performance	1	Air Mass Flow Rate	$\dot{m}_{21}$	kg/s
	2	Overall Pressure Ratio	OPR	-
	3	HPC Pressure Ratio	CPR	-
	4	Power Supplied Externally	$\dot{W}$	W
	5	Rotational Speed (Spool 1)	N_1	RPM
	6	Rotational Speed (Spool 2)	N_2	RPM
	7	Inlet Total Pressure	$P_{t,in}$	bar
	8	Inlet Total Temperature	$T_{t,in}$	K
	9	Turbine Inlet Temperature	$TIT = T_{t,4}$	K
Pre-Configured Component Models	10	Low-Pressure Compressor (LPC)		
	11	Inter-Compressor Duct		
	12	High-Pressure Compressor (HPC)		
	13	Combustor		
	14	High-Pressure Turbine (HPT)		
	15	Inter-Turbine Duct		
	16	Low-Pressure Turbine (LPT)		
	17	High-Pressure Shaft		
	18	Low-Pressure Shaft		

The second set of inputs required in the full-engine model are the list of mechanical design inputs (as seen in Table 3.9 and Table 4.6, for example) for each component based on the engine configuration. These should be specified, either by creating a component model and then assigning it to the engine model, or by editing the engine subcomponent at runtime. Many default values exist for the various component types as well, meaning only the most necessary must be selected by the user, with further design freedom always possible. Values such as shaft length are determined by the engine model based on the design results of the turbomachinery and the resulting axial lengths of all components. Thus, through the engine model, much of the design process is automated, and the interrelated design variables are shared between components automatically.

5.2. VERIFICATION AND VALIDATION

The objective of this section is to describe the results of the validation exercise performed for the CFM56 and PW2037 gas generators. The gas generators – or engine cores – were selected since no fan module is yet implemented in the WEST methodology, as this is aimed at weight estimation of turboshaft engines. Section 5.2.1 lists the remaining inputs required to complete engine designs and obtain the results described in Section 5.2.2. This is followed by a discussion of the results in Section 5.2.3.

5.2.1. INPUTS

Table 5.5 lists the mechanical design inputs for the ducts, combustors, and shafts of the CFM56 and PW2037 engine cores. Only those values which are different from the default values described in Section 5.1 are listed in this table. The thermodynamic and mechanical design input parameters of the turbomachinery are the same as those listed in the previous chapters, i.e., Section 3.2 for axial compressors and Section 4.2 for axial turbines. Thus Table 5.5 represents only the remaining input parameters necessary in completing the engine design. The selection of NIMONIC 105 as the material for some shafts was based on the temperature-dependent material selection procedure described in Section 3.1.1.6 and the maximum shaft temperature. The residence times of the combustor model were selected to get the desired length, given the value of the reference velocity, according to Equation 5.16.

Table 5.5: Mechanical design input parameters for ducts, combustor, and shafts of CFM56 and PW2037.

Category	Parameter	Units	CFM56	PW2037
Inter-Compressor Duct	Length, l	m	0.35	0.29
Combustor	Residence Time, τ_R	ms	6.2	9.0
	Reference Velocity, V_{ref}	m/s	(50.72)	48.67
Inter-Turbine Duct	Length, l	m	0.0360	0.0945
High-Pressure Shaft	Shaft Angle Segment 1, α_1	deg	(60)	30
	Inner Radius 2, $r_{i,2}$	m	0.1635	
	Shaft Angle Segment 3, α_1	deg	(60)	50
	Material		NI 105[1]	NI 105[1]
Low-Pressure Shaft	Shaft Angle Segment 3, α_3	deg	80	70
	Material		(17-4PH)	NI 105

[1] NIMONIC 105.

5.2.2. RESULTS

In this section, results are presented for the gas generators of two turbofan engines: the CFM56 (Section 5.2.2.1) and the PW2037 (Section 5.2.2.1). Note that many variants of the CFM56 exist. In this case, the thermodynamic inputs are those presented by Greitzer et al. for the CFM56-7B27 in Table 3.7 [22], whereas the mechanical design inputs (Table 3.9, Table 4.6, Table 5.5) are based on digitization of the CFM56-5B cross-section (Figure 3.22) available in Jane's Aero Engines database [64].

5.2.2.1. CFM56

Figure 5.3 presents the temperature-entropy (T-s) diagram, i.e., the thermodynamic cycle, of the CFM56 gas generator. This focuses on the core airflow, ignoring the bypass flow and properties of the engine inlet and exhaust. Figure 5.4 features the cross-section of the CFM56 gas generator, complete with blades, disks, casings, ducts, the combustor, and shafts. This excludes connecting hardware, stator vane inner shrouds, and turbine/burner frames, which are based more on weight estimation correlations. Figure 5.5 [64] shows an overlay of the CFM56-5B will the gas generator as designed by WEST, which is shown in red. Finally, the weight estimation results of the complete engine core are shown in Table 5.6 and compared to the WATE++ results presented by Greitzer et al. [22] and converted to SI units. For the compressors and turbines, only the total of each of these assemblies is presented in Table 5.6 for the sake of brevity, since the full breakdowns are presented in their respective chapters and validation sections (Table 3.10 for axial compressors and Table 4.7 for axial turbines).

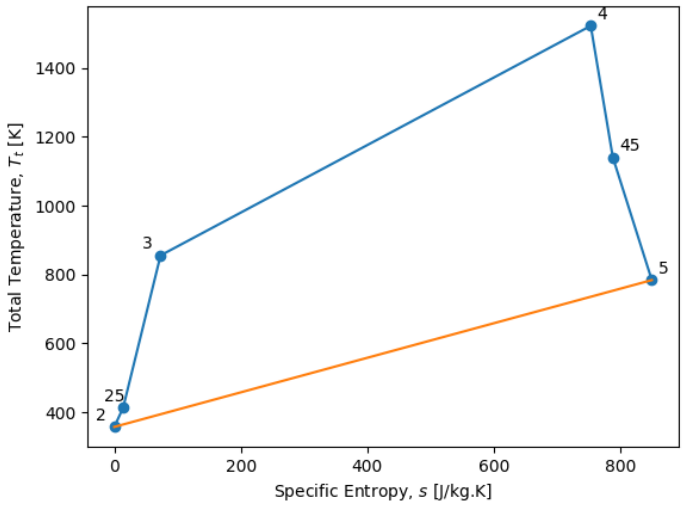

Figure 5.3: Temperature-entropy diagram (meanline performance results) of CFM56 gas generator.

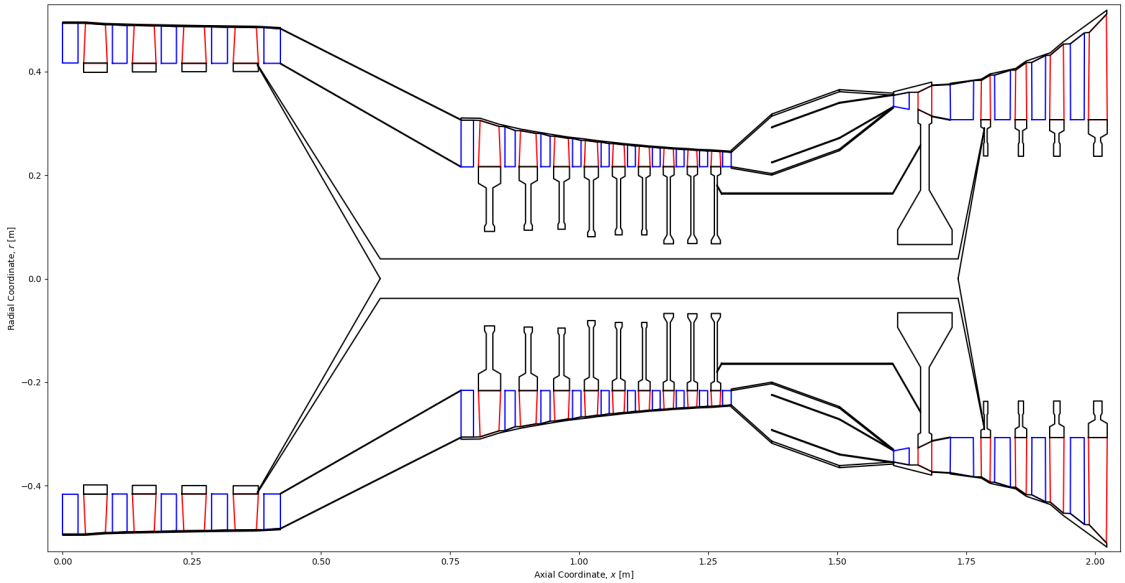

Figure 5.4: Mechanical design results of CFM56 gas generator.

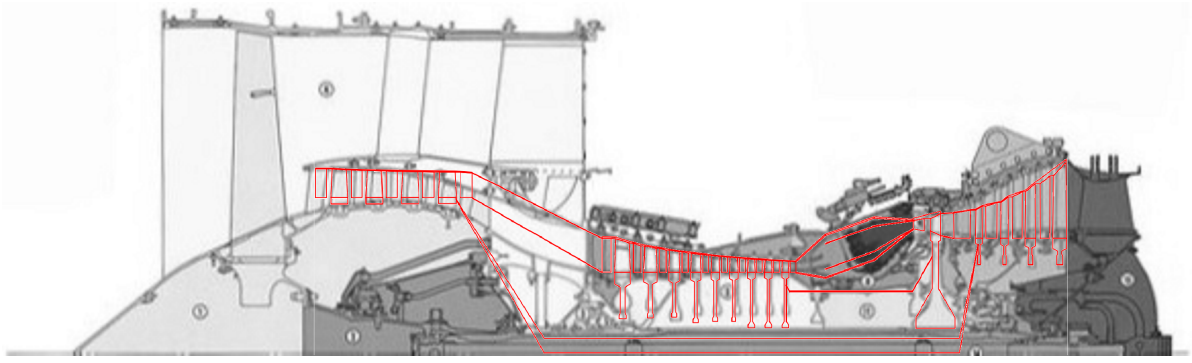

Figure 5.5: Overlay of CFM56 actual and WEST cross-sections [64].

Table 5.6: Comparison of weight estimation results for CFM56 gas generator [22].

Component	**WATE++ [kg]**	**WEST [kg]**	**Rel. Error [-]**
LPC	97.1	83.7	-13.8%
Duct	5.90	12.2	106.7%
HPC	184.2	134.6	-26.9%
Combustor (Total)	107.0	122.7	14.7%
Casing + Liner		42.1	
Frame		80.2	
Other		0.45	
HPT	220.0	178.7	-18.8%
Duct	18.6	1.21	-93.5%
LPT	353.3	320.2	-9.4%
High-Pressure Shaft	10.9	6.79	-37.6%
Low-Pressure Shaft	67.1	82.4	22.7%
Accessories	317.1	160.2	-49.5%
Other	39.9	0.0	-100.0%
Total	**1421.1**	**1102.7**	**-22.4%**

5.2.2.2. PW2037

This section presents similar result sets to those of the CFM56. For the PW2037, the T-s diagram, cross-section of WEST design results, and overlay with the real engine are shown in Figure 5.6, Figure 5.7, and Figure 5.8 [65], respectively. Table 5.7 shows the weight estimation results.

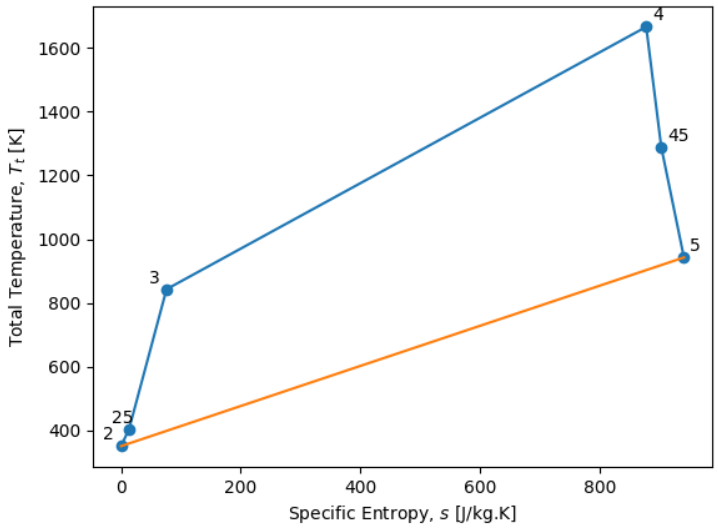

Figure 5.6: Temperature-entropy diagram (meanline performance results) of PW2037 gas generator.

5.2.3. DISCUSSION

The temperature-entropy diagrams of the CFM56 and PW2037 core air flows – Figure 5.3 and Figure 5.6 – are consistent with the form of the real Brayton cycle. The lines connecting Stations 3 and 4 are, for example, straight, when in reality shey should be curved. This is simply due to the fact that only two data points are taken, one at each of the stations, and not anywhere in between, so the line connecting them is linear.

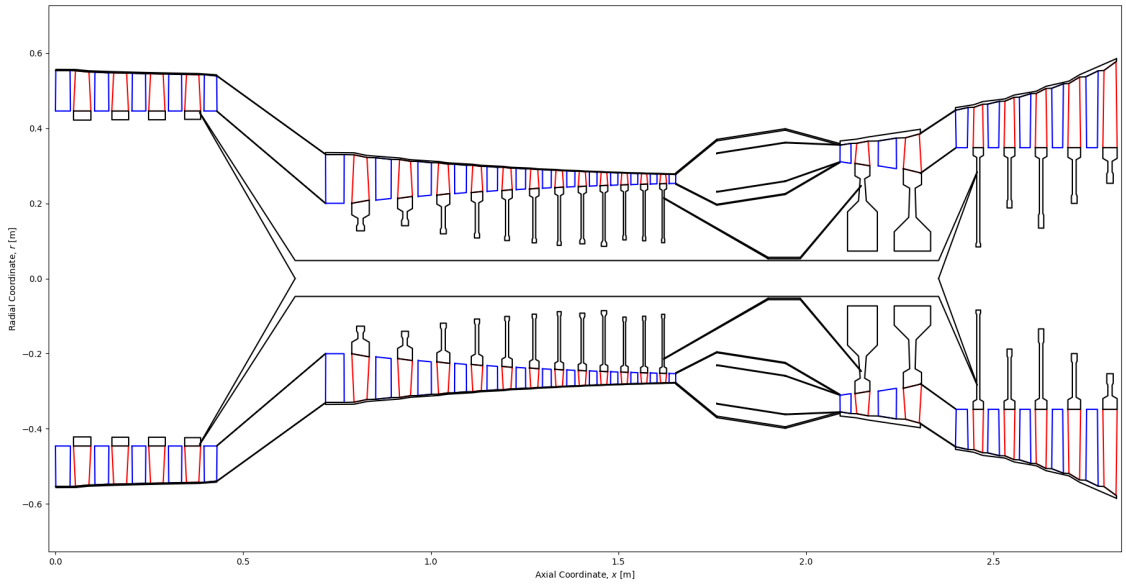

Figure 5.7: Mechanical design results of PW2037 gas generator.

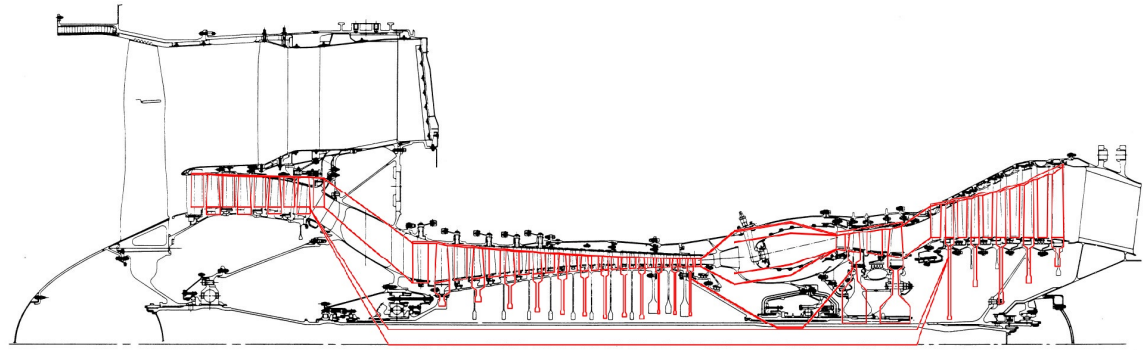

Figure 5.8: Overlay of PW2037 actual and WEST cross-sections [65].

The engine cross-sections shown in Figure 5.4 and Figure 5.7 are rather impressive, showing the complete core gas path and the mechanical design of the surrounding components. These demonstrate the relevance and physical-meaningfulness of the obtained weight estimation results, compared to, for example, a historically-based single-equation model, which estimates the weight based solely on an empirical correlation. With the WEST component-based design method, weight estimations are based on the mechanical design of actual components, together accounting for a large portion of the actual engine.

The top half of the cross-sections which are overlaid on top of the real engines, as shown in Figure 5.5 and Figure 5.8, show the relationships between the simplified methodology in this report and the complexity of actual mechanical engine design. The gas path channels are much simpler/straighter, noting especially the LPCs. Real engine shafts and connecting hardware also feature a great deal more complexity and smaller components, as do casings and combustors. Overall, however, the overlays show relatively good agreement, especially considering WEST is only a preliminary design tool.

Last of all are the weight estimation results. The results for the CFM56 included in Table 5.6 show that duct weight estimation is rather inaccurate, although the actual magnitude of the weight of ducts are so low that this has little effect on the total engine weight. The same is true for the PW2037 turbine duct, as shown in Table 5.7. For both engines, the simplified combustor design module produced very realistic results, within 15% of the WATE++ data in both cases. The weight of the dome, fuel manifold, fuel nozzles, and other combustor components are estimated using Equation 5.25, as described in Section 5.1.2. The weight estimation of all these components, which are shown in the category of 'other' combustor subcomponent in the tables

Table 5.7: Comparison of weight estimation results for PW2037 gas generator [22].

Component	**WATE++ [kg]**	**WEST [kg]**	**Rel. Error [-]**
LPC	189.6	168.4	-11.2%
Duct	9.07	10.8	18.8%
HPC	352.9	267.6	-24.2%
Combustor (Total)	152.4	140.2	-8.0%
Casing + Liner		58.8	
Frame		80.6	
Other		0.74	
HPT	371.9	350.3	-5.8%
Duct	30.4	4.36	-85.7%
LPT	574.7	549.9	-4.3%
High-Pressure Shaft	16.3	9.42	-42.3%
Low-Pressure Shaft	122.9	167.2	36.0%
Accessories	502.6	283.6	-43.6%
Other	63.0	0.0	-100.0%
Total	**2385.9**	**1951.6**	**-18.2%**

mentioned, is extremely low, implying that there may be problems associated with this equation, which was suggested by Onat and Klees [17].

The weight estimation of the shafts also show a considerable degree of variance compared to the WATE++ results. Both high-pressure shafts are underpredicted, while both low-pressure shafts are overpredicted. As previously stated, shafts feature additional components and overall have much more complicated geometry than what is modelled in WEST, as shown in Figure 5.2, so inaccuracies for this component type are expected. The weight estimation of engine accessories is also rather low. This is simply 17% of the engine weight excluding accessories, as described in Section 5.1.4. Note that these values would be higher if a fan design module was included in the WEST methodology, since 17% of the fan weight would also be added to the weight estimation of the accessories. What is modelled by the 'other' category in WATE++ is not made clear, nor is any methodology provided, so this is left entirely unmodelled in the present approach, accounting for some of the underprediction in total gas generator weight.

Overall, however, the weight estimations achieved by WEST show relatively good agreement with those of WATE++, the benchmark component-based preliminary design tool. The CFM56 is 22.4% lower than the WATE++ results, and the PW2037 only 18.2% lower. This is fairly consistent, and reasonably close, considering that around 80% of the WATE++ weight has been accounted for. Some of this perceived 'accuracy' is due to the cancellation of errors, as discussed in previous chapters, in which the overprediction of some components mitigated the underprediction of others. However, these are still quite good results, and do validate the WEST methodology and its practical implementation to a considerable degree. All in all, it appears that the WEST program is indeed suitable for the weight estimation of aeronautical gas turbine engines.

As discussed in Section **??**, it is expected that the results of the methodology could lie within +10%/-40% of the actual engine weight. The weight comparison tables shown thus far have all been with regard to WATE++ data provided by Greitzer et al. [22], not the actual engine. This is because this source offer a breakdown of weight by component type, information which is not made publically-available by the manufacturers of aircraft engines. Nevertheless, the expected accuracy was not intended to be compared to WATE++ results, but rather the real engines, so it is beneficial at this stage to perform such a comparison.

However, since no fan design module has yet been developed in WEST, it is difficult to make a straightforward comparison of total engine weight for the two turbofan validation cases, since only the gas generator can be modelled at present. To make such a comparison, though, the fan weight estimation results of WATE++ will be added to the gas generator weights obtained using WEST.

In the WATE++ studies, the total weight of the fan module is 538.9 kg for the CFM56 and 873.2 kg for the PW2037 [22]. Assuming that WEST could predict this weight on its own, then this can be added to the

running total of 1102.7 kg and 1951.6 kg for the two engines, as shown in Table 5.6 and Table 5.7, respectively. If this were the case, then an additional 17% of the fan weight would be added to WEST's estimation of the weight of the accessories, resulting in a 91.6 kg and 148.4 kg increase in accessories weight for the CFM56 and PW2037, respectively. Combining all of these, the results are shown in Table 5.8, along with the weight of the real engines [64, 65] and the relative error with regard to this.

Table 5.8: Comparison of full-engine weight estimation results for CFM56 and PW2037 with real/actual engine weights [22, 64, 65].

Engine	**Actual [kg]**	**WEST[1] [kg]**	**Rel. Error [-]**
CFM56	2405	1733.2	-27.9%
PW2037	3311	2973.2	-10.2%

[1] With correction for fan module and additional accessories.

As seen in Table 5.8, the weight estimation of the full engines (for which the fan weight estimation was not achieved by WEST), vary compared to the gas-generator-only results. The PW2037 improves to be within 10.2% of the real engine weight, whereas the CFM56 is now -27.9%. Overall, however, both of these lie comfortably within the expected range of +10%/-40% showing once again the viability of the present methodology in producing reasonable, physically-based gas turbine designs and weight estimations.

The ATLAS program developed by Lolis claims a weight estimation for the CFM56 within 5% of the actual engine, and a breakdown by component as shown in Table 5.9 [21]. WEST results are included in this table as well, using the fan weight from Greitzer et al. [22] and the total engine weight of 1733.2 kg from Table 5.8 as the reference weight. As is evident in this table, the breakdown of weight results shown very good agreement with the breakdown generated by ATLAS, which serves as further validation for the WEST tool. The only exception is shafts, for which the WEST prediction is over twice the relative weight as the shafts predicted by ATLAS.

Table 5.9: Comparison of full-engine weight estimation results for CFM56 with ATLAS [21, 22].

Component	**ATLAS**	**WEST[1]**
Fan	30.8%	31.1%[1]
I/LPC	7.5%	4.83%
HPC	9.8%	7.77%
Combustor	2.4%	2.45%[2]
HPT	4.6%	5.44%[2]
LPT	11.3%	11.3%[2]
Ducts	0.9%	0.77%
Shafts	2.4%	5.15%
Frames	20.2%	16.7%
Accessories	10.0%	14.5%[3]
Total	100.0%	100.0%

[1] Weight from WATE++ [22].
[2] Excluding frame. [3] Corrected.

As a final note, it is interesting that Lolis [21] does not provide any breakdown by component type within the turbomachinery subassemblies, for example, by showing the weight of rotor blades, stator vanes, disks, and the casings individually, as was done repeatedly throughout this report. Instead, only the weight percentage of each assembly compared to the total engine weight is provided. Nor is any information given with regard to the inputs necessary in achieving the published results. Thus, it is difficult to make conclusions, but the absence of such information could imply that Lolis' results and apparent accuracy were also a result of the cancellation of errors, as is sometimes the case with the results presented in this report.

5.3. SENSITIVITY ANALYSIS

One of the key strengths of the WEST program and component-based weight estimation methods in general is their ability to capture trends in engine weight for variations in input parameters and/or design choices. Thus, the possibilities for sensitivity analysis are vast, and it is these trends which will be studied and captured by the yet-to-be-developed regression equations used in hybrid weight estimation models which will provide a key functionality within the ARENA project and other aircraft-level design and optimization research projects. At present, however, the sensitivity analysis for the full engine model will be kept brief, focusing on only one parameter at present: the mass flow rate.

5.3.1. MASS FLOW RATE

The power capacity of the engine is, as shown in Equation 2.8, proportional to the mass flow rate. Thus, variations in mass flow rate are, in essence, variations in the engine's power or thrust. It is therefore beneficial to study the engine's weight trends with respect to its power capacity. Additionally, of the three process parameters of the engine system model (i.e., pressure ratio, mass flow rate, and rotational speed) studied during the sensitivity analysis of the axial compressor model (Section 3.3.3), it was the mass flow rate that the compressor weight was most sensitive to.

To perform this study for the complete engine core, the mass flow rate of the CFM56 was varied by ±25% of its nominal value. Note that this was done for the mass flow at Station 2, $\dot{m}_2$, thus both the core and bypass flows are varied, which will also yield a change in the power required by the fan, $\dot{W}_{fan}$, as calculated in Equation 3.66. The nominal value of $\dot{m}_2$ for the CFM56 is 351.1 kg/s at sea level static conditions according to Greitzer et al. [22]. Table 5.10 shows the mass flow rates studied, when varied to ±25% of the nominal value. The differences in the outer dimensions – i.e., the outer radius and length – of the engine are also included in this table, followed by engine cross-sections in Figure 5.9. The complete engine weight and breakdown is shown in Table 5.11.

Table 5.10: Outer dimensions and consumed power of CFM56 HPC model for various mass flow rates.

Category	Parameter	Units	Case 1	Case 2[1]	Case 3
Performance	Mass Flow Rate, $\dot{m}_2$	kg/s	263.3	351.1	438.9
Dimensions	(Max) Outer Radius	m	0.483	0.519	0.552
	Length	m	1.698	2.023	2.346

[1] Nominal.

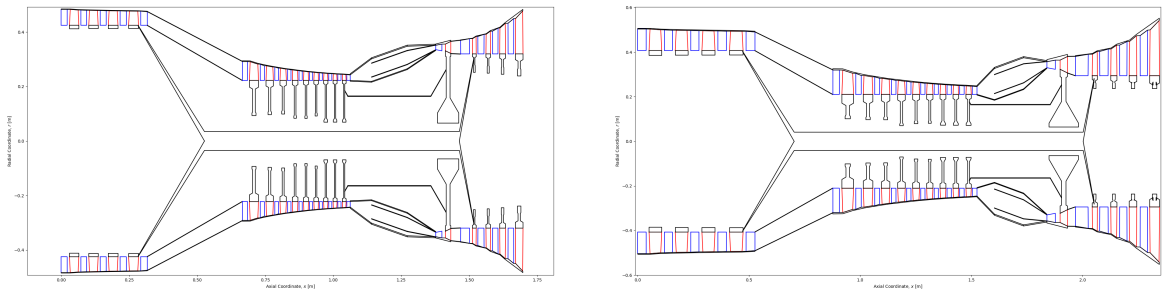

Figure 5.9: Design results of CFM56 gas generator for 0.75x (left) and 1.25x (right) nominal mass flow rate.

As is clear from Table 5.10 and Figure 5.9, the size of the engine changes considerably, with a ±25% change in mass flow rate (or power) yielding a +16.0%/-16.1% change in engine length and a +6.36%/-6.94% change in outer radius. The weight estimation also changes substantially, as shown in Table 5.11. Overall, a ±1% change in mass flow rate produces, on average, a 0.92% change in weight. This is a noticeable effect, and shows the strong correlation between engine weight and power capacity.

Table 5.11: Comparison of weight estimation results of CFM56 gas generator model for various mass flow rates.

Component	**Weight [kg]**		
	263.3[1]	351.1[1,2]	438.9[1]
LPC (Total)	48.8	83.7	128.5
Rotors + Disks	23.7	41.1	62.5
Rotor Blades	2.37	4.20	6.38
Disks	21.3	36.9	56.1
Stator Vanes	4.45	7.01	10.1
Casing	11.6	23.9	41.7
Connecting Hardware	8.99	11.7	14.3
Duct	12.1	12.2	12.2
HPC (Total)	91.0	134.6	185.3
Rotors + Disks	65.0	91.0	118.9
Rotor Blades	5.72	9.19	13.1
Disks	59.3	81.8	105.8
Stator Vanes	10.0	16.1	23.2
Casing	9.66	19.4	33.4
Connecting Hardware	6.29	8.07	9.75
Combustor (Total)	121.4	122.7	129.4
Casing + Liner	42.1	42.1	47.4
Frame	79.0	80.2	81.4
Other	0.33	0.45	0.56
HPT (Total)	151.5	178.7	209.3
Rotors + Disks	60.4	77.7	95.6
Rotor Blades	1.49	2.57	4.05
Disks	58.9	75.2	91.5
Stator Vanes	2.60	3.93	5.44
Casing	6.36	12.6	21.5
Frame	82.2	84.5	86.8
Connecting Hardware	0.0	0.0	0.0
Duct	1.21	1.21	1.20
LPT (Total)	238.2	320.2	400.7
Rotors + Disks	72.2	105.3	132.5
Rotor Blades	25.9	42.9	61.7
Disks	46.3	62.4	70.8
Stator Vanes	27.3	45.3	66.1
Casing	19.8	38.9	65.8
Frame	114.2	124.8	129.3
Connecting Hardware	4.67	5.92	7.10
High-Pressure Shaft	6.47	6.79	7.11
Low-Pressure Shaft	68.2	82.4	97.3
Accessories	125.6	160.2	199.1
Total	**864.7**	**1102.7**	**1370.2**

[1]Mass flow rate, $\dot{m}_2$ [kg/s]. [2]Nominal.

5.4. SUMMARY

- The design of ducts, combustors, and shafts require the completed design of the surrounding turbomachinery. The performance of the turbomachinery has a large influence on total engine performance and efficiency, so these components are designed first. Their designs then influence the inlet/outlet locations of the ducts and combustor, as well as the total length and attachment points of the shafts.
- The weight estimation results of the CFM56 and PW2037 gas generator validation cases (Section 5.2.2) show very good agreement with the WATE++ results, accounting for about 80% of the weight modelled by WATE++.
- The weight of ducts is not predicted accurately; however, these contribute such a small share to total engine weight that the effects are not very noticeable.
- The simplified combustor design methodology (Section 5.1.2) produces very reasonable results, within 15% of the WATE++ results (Section 5.2.2).
- High-pressure shafts are consistently underpredicted, while low-pressure shafts are consistently overpredicted by the WEST program (see Section 5.2.2).
- Applying a correction to account for the fan module, the CFM56 full-engine weight estimation (not just that of the gas generator) is -27.9% of that of the real engine, while the PW2037 is -10.2% of its counterpart (Table 5.8). These values fall well within the range of +10%/-40% as was initially expected (see Section 1.2). The WEST program is therefore able to reliably predict engine weight overall, which to some degree validates the tool and makes it useful for the weight prediction of current and novel gas turbine engines, as shown by the program's acceptable weight estimations of the CFM56 and the PW2037 gas generators.
- The breakdown by component/assembly type shows very close agreement to the results generated by ATLAS (Table 5.8) [21].
- A 1% change in engine mass flow rate (i.e., a 1% change in power/thrust) corresponds to a 0.92% change in engine weight, on average, for the CFM56 gas generator reference case. This also produces considerable changes in engine dimensions (see Section 5.3.1).

6

CONCLUSIONS

The objective of this chapter is to list all the relevant, high-level conclusions of this thesis. Summaries of each individual chapter have already been included at the end of their respective chapters.

1. It is possible to develop a reliable, component-based weight estimation tool that offers improved accuracy over existing, available methods. This can be done using design procedures described in literature and without significant proprietary knowledge of one or more existing engine designs.

    - WEST was able to capture between 70 and 90% of actual engine weight, exceeding initial accuracy expectations and offering better results than the other publically/commercially-available methods. This was possible in part due to the availability of robust theoretical design frameworks for blades and disks, components which represent a large share of total engine weight. The development of such a tool – and the fulfillment of the initial research aim – therefore proved to be feasible.
    - The apparent 'accuracy' of the methodology may not be entirely due to accurate weight estimations, but rather a cancellation of errors, since some components types are consistently overpredicted while others are underpredicted. This leads to a net result closer to the intended target than what is observable on an individual-component basis.

2. Weight estimation methodologies such as WEST can be improved through the acquisition of the design data and weights of real engines and their components.

    - Knowledge that constitutes a limit to the accuracy of weight estimation methods relates to accessories and other (uncategorized) components, which can account for over one third of the weight of the engine, but for which weight estimation and/or design methods do not exist, leading to underprediction of engine weight.
    - The development of improved design methods and weight estimation models is hindered by the lack of available information regarding existing engine designs. Knowledge such as a breakdown of engine components by their weight would at least allow the weight of some component types to be estimated based on (or validated against) historical trends, even if no simplified design methods exist.
    - Improvements in the design methods of individual components should lead to more reliable engine-level weight estimations, since the engine weight is simply a sum of the weight of all components.

3. WEST fulfills an important need within the ARENA project, providing weight estimation of the main power unit. These weight estimations will be used in collaboration with other research findings and simulation results to evaluate the plausibility of combined-cycle engines and similar architectures. Such technologies have the potential to increase aircraft engine thermal efficiencies by up to 20%, which could therefore significantly improve the sustainability of aviation in the future.

4. The work of this thesis and the development of the WEST methodology/tool has significant potential to impact ongoing research within the larger (aeronautical) scientific community. The weight estimation of engines – turboshafts in particular – is necessary to obtain quantitative, meaningful results in a wide range of projects involving current aircraft/engine design trends. Making WEST open-source could provide many researchers with access to reliable weight estimations, which are necessary for further development.

5. Using duty coefficients instead of geometry as input allows WEST to overcome the challenge of evaluating the weight of novel gas turbine engine architectures, whose performance is known to a deeper extent than its final geometry/profile/dimensions.

6. The types of available weight estimation methodologies represent a trade-off between accuracy, computational cost, and applicability to novel engines. Hybrid, single-equation models (which are based on the results of component-based models) constitute a midpoint that can be effectively used in aircraft-level performance and design/optimization studies.

    - Several component types, namely disks, require optimization for every design case. This accounts for the majority of the computational cost of component-based design methods. A variety of strategies can be employed to improve the computational efficiency of component-based methods; however, they will never be as efficient as single-equation models.
    - A component-based preliminary design tool is a necessary intermediate step for developing hybrid single-equation models. Thus, WEST provides the necessary foundation for such equations to be developed in the future.

7. For the CFM56 reference case studied, a 1% change in mass flow rate (i.e., power or thrust) results in a 0.92% change in gas generator weight, on average. Combining this with sensitivity to other design inputs means that WEST can be used to quantify the weight trends of gas turbine engines with respect to key parameters of interest, providing a new level of insight to engine designers pertaining to the impact of various design choices.

8. Under the present methodology, the weight of an axial compressor is proportional to the mass flow rate and work coefficient, and is inversely proportional to the pressure ratio, rotational speed, flow coefficient, and degree of reaction. The sensitivity is highest for the mass flow rate, work coefficient, and flow coefficient (in that order). The length of the compressor has a larger influence on weight than the outer radius.

9. The selection of realistic temperatures and temperature profiles in disks is essential in achieving realistic weight estimations. The magnitude of the temperature gradient and the selection of the type of profile affect the final design of the disk, and therefore its weight and internal stresses.

    - Temperature gradients induce additional stresses. Higher gradients (i.e., more cooling) can in some cases increase the factor of safety (by lowering the temperature and therefore raising the yield and ultimate tensile strengths) and therefore reduce the weight of the disk. This applies if the disk is designed/optimized for that case. Otherwise, additional cooling can reduce the factor of safety by increasing the thermally-induced stresses, if not applied properly.

10. Adopting industry-standard design practices – for example, by fixing the inner radius of HPC disks to their minimum value – can reduce the computational cost of the methodology and improve the accuracy of the results. Additionally, the coarseness of the discretization of the disk for stress analysis has little effect on compressor weight estimation, thus it is feasible to minimize the number of discretization elements to reduce execution times at a low cost in accuracy.

7

RECOMMENDATIONS

The objective of this chapter is to list relevant recommendations for the future use and development of the WEST preliminary engine design methodology and weight estimation program. These recommendations fall into four main categories: improvements to the current methodology (Section 7.1), expansions to the current methodology (Sec. 7.2), methods of reducing the computational cost of the program (Sec. 7.3), and the next steps needed to use the WEST tool as part of the larger ARENA project (Sec. 7.4).

7.1. METHODOLOGY IMPROVEMENTS

To improve the methodology described in this report, it is recommended to:

- Update the meanline analysis and gas path design aspects of the program to work with a gas model for which the specific heat capacity at constant pressure, c_p, of the working fluid is temperature-dependent, as discussed in Section 2.1.1.1, or a model for which all fluid properties are a function of temperature. The added computational cost can be compared with the improvements in accuracy, to determine if such a fluid model is beneficial overall.
- Improve the Smith charts (Figure 4.1) and equivalent Smith charts (Figure 2.3) by applying smoothing. The original contour plots were digitized; however, the values between contour lines do not vary smoothly, but instead feature discontinuous steps in values next to each line. An improved interpolation method is required in developing these charts so that the value of polytropic efficiency varies smoothly, and so that the gradients are continuous, which is important when using this as part of a larger optimization study.
- Improve the engine model by accounting for the extraction of cooling air bleed flows from the compressors and their reintroduction in the turbines. Account for turbine cooling by how this affects the mass flow rates, enthalpies of the meanline gas, and component operating temperatures.
- Improve the means by which the fluid properties surrounding inlet and outlet guide vanes are estimated. IGVs and OGVs currently feature a simplified design procedure, one where the inlet/outlet conditions are considered the same, meaning the channel height stays constant across their chord. This is not typically the case with real engines.
- Implement the forced vortex, constant reaction, exponential vortex, and general vortex design methods [44] as alternatives to the Free Vortex method when determining the twist and blade angles in axial turbomachinery blades (Section 3.1.1.1).
- Use a computer aided design (CAD) 3D-modelling kernel that is compatible with Python to model the blades. The volume can then be extracted from this model and multiplied by the material density to obtain the weight. This is a more accurate way of determining blade volume and weight than what is described in Section 3.1.1.3.
- Reduce the minimum thickness-to-chord ratio for compressor rotor blades. Real CFM56 HPC blades (Table 3.11) appeared to have much lower $(t/c)_{max}$ values at the tip than the default value of 7.5%

(Table 3.2), thus the methodology may be improved by matching this value more closely to the design trends of real engines.

- Update the method of determining the number of blades in a compressor row (Section 3.1.1.4) to use true chord, not axial chord, when determining the maximum pitch (Equation 3.20), since this is the intention of the original equation. Additionally, investigate alternative methods and/or tuning of the diffusion factor and DeHaller number (Equations 3.16 and 3.17) since the estimated number of blades adds to much less than that of the real engine (Table 3.11).
- Account for the fact that the cross-sectional (airfoil) area of cooled HPT blades are not solid when performing stress analysis, which is due to the presence of cooling passages (Section 4.1.2.2). This affects (reduces) the root area and the calculation of the second moment of area (Section 3.1.1.5), and will therefore lead to higher maximum stresses, which should be considered in the blade design procedure.
- Compare the blade stress analysis procedure described in this report (which was developed as part of this methodology) with methodologies from other sources. The calculation of moments and stresses at the blade root do not account for variation in the root radius and are based mainly on general mechanics of deformable solids and simplified analysis techniques. The current method also does not account for thermal stresses in the blade, something which should be considered. Thus, it is recommended to research alternative approaches to see if a higher-fidelity blade stress analysis method is available.
- Modify the blade and disk design methods to include the root of the blade with the blade, not the disk. This will affect the component weights and stresses in the disk. This can be done by implementing the procedure described by Tong et al. [18], not the simplified method recommended by Lolis [21].
- Add curvature to the geometry formulation of hyperbolic disks (Section 3.1.2.1). In its current state, the curved sections of hyperbolic disks are approximated using two linear sections, thus more realistic designs (and lower stresses) can be obtained by using curvature as is seen in real disks.
- Reduce the minimum web thickness of web disks (Figure 3.8, Equation 3.40) such that it is based on manufacturing considerations, not the axial chord of the blade root. This will ensure that disk webs can be thinner, which may result in more uniformity between the disks of adjoining rows, something which seems to be present in real engines (Figure 3.22 [64], Figure 3.23 [65]).
- Perform additional verification of the disk stress analysis procedure (Section 3.1.2.3) by comparing the results to those obtained using a higher-fidelity tool, such as T-Axi [74, 75]. Visual inspection of the stress distributions in axial compressors matched fairly closely with examples provided by Kurzke and Halliwell (Section 3.2.3, Figure 3.18 [24]), and the weight predictions seemed consistent with WATE++ results (Sections 3.2.2 and 4.2.2); nevertheless, it is advisable to check this more closely with an alternative, validated tool.
- Account for high- and low-cycle fatigue, as well as creep, in the disk stress analysis and material selection procedures (Section 3.1.2.3). In its current state, WEST only accounts for the yield strength and burst criteria of the disk (Equations 3.48 and 3.49). Gas turbine disks are subject to a large number of cycles, so it is recommended to account for fatigue when designing the disks. Turbine disks are also subject to very high temperatures, so accounting for creep is also advisable. This can be done using the Larson-Miller parameter, for example, which will require some additional material data and changes to the material class. Alternatively, Tong et al. [18] includes a methodology for disk life estimation.
- Replace the disk optimization algorithm [76, 77] with something that is able to reach a solution without violation of constraints. This would allow the objective function (Section 3.1.2.6) to be based on weight only, without the need for a stress-violation penalty factor.
- Improve the combustor model (Section 5.1.2) such that it accounts for more of the physical phenomena and design practices typically associated with combustor design. This will improve the physical meaningfulness of the combustor design results.
- Account for more of the complex aspects of component geometries, such as the presence of small disks when connecting the various segments of a single shaft (Section 5.1.3). Other possibilities include the weight estimation of variable stator vane hardware and bleed offtake hardware in compressor casings, stator vane roots, the presence of inlet diffusers and exhaust ducts in the engine, gearboxes (in the case of turboshafts and geared turbofans), etc.

7.2. METHODOLOGY EXPANSIONS

To expand the WEST methodology, it is recommended to:

- Develop and implement a radial compressors model to expand the flexibility of WEST to model a wider range of turboshaft engines, since radial compressors are common in turboshafts. This may be done by linking WEST and a TU Delft in-house radial compressor design code called *TurboSim*.
- Develop and implement a reverse-flow combustor model to expand the flexibility of WEST to model a wider range of turboshaft engines, since reverse-flow combustors are common in turboshafts.
- Develop and implement a fan model to expand the flexibility of WEST to model full turbofan engines, not just their cores / gas-generators.
- Expand the number of materials available in the WEST material database (Section 3.1.1.6), including temperature-dependent properties. Possible materials which may be good to add can be found in the databases of WATE++ [18, 22] and GTlab [20].
- Implement a meanline loss model to predict losses, deviation angles, etc. and get a more advanced estimation of polytropic efficiency.
- Ensure that the aforementioned loss model includes sensitivity to design factors such as blade aspect ratios, row and stage gaps, etc. Then, modify the program such that aspect ratios and other such design variables are selected/optimized automatically based on a specified set of criteria (e.g., maximum efficiency, minimum weight, reduced blade stresses) instead of needing to be manually input by the user. This reduced set of inputs will improve the methodology's applicability to the design of novel engines. It could also be used to ensure a better tradeoff between fluid-dynamic performance (shorter blades) and blade stresses (wider blades with larger root area).

7.3. REDUCTIONS IN COMPUTATIONAL COST

To reduce the computational cost of the WEST program, it is recommended to:

- Replace the Smith charts (Figure 4.1) and equivalent Smith charts (Figure 2.3) with either an equation-based method of estimating polytropic efficiency, or with Smith charts which have a lower resolution. The charts used in WEST have an unnecessarily high number of data points given the resolution of the original plots, and loading this data slows down the meanline analysis and gas path design procedure. In fact, it is the slowest part of this procedure, so execution times can be reduced by replacing the method of estimating polytropic efficiency with something faster.
- Investigate the possibility of formulating and using analytical derivatives wherever the Newton-Raphson iteration method is applied instead of the use of finite differences in approximating these derivatives (Appendix B.1). The use of a first order forward finite difference means that the procedure must be executed twice for every iteration, which increases the computational cost.
- Improve the method of guessing the tangential stress at the inner rim of the disk (Section 3.1.2.3). This provides the starting point for the stress analysis procedure, and must be iterated until the imposed radial stress at the hub is obtained. Selecting the value of the first guess in a more informed manner may result in reduction of computation cost, since the iteration procedure will not have to iterate as many times.
- Fix the inner disk radius to its minimum value in the case of high-pressure compressors. This produces results which are quite comparable to the designs of actual engine HPCs, so if the particular case being studied features such geometry, then fixing this radius reduces the size of the optimization design vector and therefore decreases the computational cost substantially.
- Reduce the number of finite elements used to discretize the disk to improve computational efficiency of the stress analysis. This has a large impact on the execution time of WEST as a whole, since disk optimization is the most computationally-expensive part of the program. For the particular validation cases investigated in this report, the number of elements can be reduced from 1000 to 100 in the case of axial compressor disks (Section 3.3.7.1) and 1000 to 500 in the case of axial turbine disks (Section

4.3.2.1) with little influence on the results, but a significant reduction in execution times. In instances where computational efficiency is imperative, further reduction of execution time with limited effect on weight (although considerably more effect on the appearance of the design) can be obtained by reducing the number of elements to 10 in the case of compressor disks and 100 in the case of turbine disks. The appropriate number of elements should be reevaluated for different investigations in case these suggested figures do not apply generally to all axial compressors and turbines.

- Explore the possibility of discretization optimization, i.e., choosing the size of local disk elements strategically, as opposed to them all having a uniform height. This could allow for a reduction in the number of elements used to discretize each disk (and therefore improve the computational efficiency) without much effect on the actual results, since the elements could be more numerous in regions where there is more to resolve, and more coarse in regions without, for example, steep temperature gradients or sharp changes in geometry.

- Investigate alternative disk optimization algorithms. Disk design and optimization is the slowest part of the WEST methodology, and it currently uses the *scipy.optimize.minimize* function [76] with the SLSQP algorithm [77]. However, GTlab uses the COBYLA and ISRES algorithms for fast local optimization and longer global searches, respectively [20], so it may be beneficial to investigate these methods for use in WEST as well to see if improved results or reduced execution times can be obtained.

7.4. NEXT STEPS

To take the WEST program – which satisfies the thesis-level research aim – and employ it as part of the larger ARENA project, as well as to enlarge its impact in the wider scientific community, it is recommended to:

1. Create a model of a two-spool turboshaft engine with a free-power turbine (FPT) (or a novel engine architecture). An FPT will be similar to the two-spool gas generator, but with some modifications, such as the removal of the LPC.

2. Create a design function which designs the engine for a fixed (user-specified) power output given other high-level input parameters. For example, the function could involve an iteration scheme which calculates the mass flow rate necessary to obtain the specified power requirement for variations in OPR (assuming a fixed exhaust pressure ratio). This can then be used to study the effect of OPR on turboshaft weight for a particular application / power requirement. Note that this iteration should include gas path design only, not detailed mechanical design. Only once a thermodynamic solution is reached should mechanical design commence. This ensures lower computational cost of the method.

3. Use the engine model and design function to create a large set of possible turboshaft engine designs, all with variations in high-level input parameters such as mass flow rate, power output, OPR, TIT, turbomachinery configuration, etc.

4. Use statistical regression to develop single-equation surrogate models to approximate the results of the component-based designs so that they can be incorporated into aircraft-level design and optimization studies with low computational cost. Make sure to account for – i.e., include sensitivity to – the key parameters of interest.

5. Publish these equations in the case of free-power turbines for use by the larger scientific community. This ensures that anyone has access to turboshaft weight estimation equations which are reasonably accurate, computationally efficient, sensitive to various design choices, and maintain physical meaningfulness.

A

Appendix: Motivation

A.1. Modelon JPL JT9D Weight Estimation Results

Firstly, evaluating only the data published in 2019 shows several aspects which do not build confidence in the results generated by this program [13]. The total HPT weight, for example, is 57% lower than the benchmark WATE++ value. The disks of the HPT are 88% lower, while the disks of the LPC are 80% higher.

Moreover, the results presented in the validation paper discuss only turbomachinery while omitting all other component types such as the combustor, ducts, shafts, controls and accessories, etc. [13]. This makes the true potential of the Modelon JPL for full-engine weight estimation (or lack thereof) unclear. However, this data is several years old, and development efforts since the time of publishing may have improved the program's accuracy, which is why practical simulations were run, the results of which are included on the right of Table A.1.

Unfortunately, these results show even worse performance, with nearly every component weight estimation being worse than the value for the same component published in the validation paper [13]. (This is indicated by the 'Is Worse' column on the right of Table A.1, which is used to highlight those fields for which the results are more further from the WATE++ results compared to the 2019 publishings.) In some cases, the latest estimates are significantly worse, such as the rotor blades, stator vanes, and disks of the high-pressure turbine, all of which show around 100% error. The total HPT weight is actually an improvement over its former value, but observation of the individual component breakdown shows that every single HPT component is worse, meaning that the improved total is actually just a compounding of errors, not a genuine improvement in results. Something similar is likely the case for the LPC, where the total weight has only 9% error, but four out of five subcomponents show worse results than the original paper. Overall, the total weight of all components listed (which, as previously stated, excludes all components not related to turbomachinery) is 2050 kg, 1644 kg, and 1466 kg according to WATE++, WATE-2 (Modelon JPL in 2019), and Modelon JPL 2.2, respectively.

Since these results were obtained using Modelon's own JT9D engine model, it is clear that the weight estimation accuracy of the JPL is not suitable for the purposes of this investigation and others in the ARENA project. The WATE-2 methodology, originally published in 1979 [17], was valuable for its time, but clearly does hold up to the standards required by today's design tools, at least not in this Modelica-based version of its implementation. This, compounded with the other disadvantages of the Modelon JPL previously discussed, means it is advisable to look elsewhere for an engine preliminary design and weight estimation tool.

Table A.1: Weight estimation results for JT9D engine according to Modelon JPL 2.2 [13].

Data From Article [13]					Modelon JPL 2.2		
Group	**Component**	**WATE++ [kg]**	**WATE-2 (JPL) [kg]**	**Rel. Error [-]**	**Weight [kg]**	**Rel. Error [-]**	**Is Worse**
LPC	**Total**	**196**	**225**	**15%**	**177.63**	**-9%**	
	Rotor Blades	18	18	0%	16.53	-8%	X
	Stator Vanes	58	35	-40%	32.35	-44%	X
	Disks	66	119	80%	78.61	19%	
	Casing	38	38	0%	35.41	-7%	X
	Nuts and Bolts	15	15	0%	14.73	-2%	X
HPC	**Total**	**564**	**498**	**-12%**	**319.14**	**-43%**	X
	Rotor Blades	114	114	0%	74.11	-35%	X
	Stator Vanes	143	124	-13%	79.68	-44%	X
	Disks	188	141	-25%	75.50	-60%	X
	Casing	99	99	0%	74.46	-25%	X
	Nuts and Bolts	20	20	0%	15.39	-23%	X
HPT	**Total**	**688**	**295**	**-57%**	**515.79**	**-25%**	
	Rotor Blades	141	55	-61%	5.80	-96%	X
	Stator Vanes	204	56	-73%	5.84	-97%	X
	Disks	172	20	-88%	346.60	102%	X
	Casing	32	27	-16%	9.02	-72%	X
	Nuts and Bolts	6	5	-17%	2.12	-65%	X
	Frame	134	132	-1%	146.40	9%	X
LPT	**Total**	**602**	**626**	**4%**	**452.99**	**-25%**	X
	Rotor Blades	138	130	-6%	64.76	-53%	X
	Stator Vanes	99	172	74%	82.77	-16%	
	Disks	144	83	-42%	83.68	-42%	
	Casing	67	58	-13%	39.34	-41%	X
	Nuts and Bolts	12	10	-17%	7.84	-35%	X
	Frame	141	151	7%	174.60	24%	X

A.2. TURBOSHAFT ENGINES USED IN HISTORICAL DATA

Table A.2 includes a list of the relevant engine models and variants which were used to compile a database of historical turboshaft engine weight data. This data is used in Figure A.2 (Appendix A.3) for comparison with GasTurb 14 results. Note that, for the most part, only one variant was included per engine family for the sake of brevity. All data was compiled from Jane's Aero-Engines [14].

Table A.2: Turboshaft engine models and variants used in historical data compilation [14].

Manufacturer	**Model / Variant**	**Power**[1] [kW]	**Power**[2] [kW]	**Mass** [kg]
General Electric	CT58-110	1007	932	143
	T58-GE-16A	1394	1320	201
	T700-700	1210	987	198
Honeywell	HTS900	761.9	676.1	142.9
Ivchenko-Progress	AI-450C	346.7	223.7	115
Mitsubishi Heavy Industries	TS1-M-10	700		151.5
	MG5-10	653		154.2
MTU Turbomeca Rolls-Royce	MTR390-2C	958	873	169
Omsk	MKB GTD-3F	671	357	141
Pratt & Whitney	PZL-10W	671	574	141
	PZL GTD-350	294	236	139.5
Pratt & Whitney Canada	PT6B-36	732	649	169
	PW206A	463	423	107.5
Rolls-Royce	Gem 42	746	664	183
	Gnome H.1200	1007	783	142
	Gnome H.1400-1	1238	932	148
	RR300	223.7	179	97.5
Rolls-Royce Turbomeca	RTM322-Mk250	1694	1491	256
Safran	Aneto-1K	1839	914	260
	Ardiden 1	1053	880	180
	Arrano 1A	851	738	175.1
	Arriel 1B	478	440	120
	Arrius 1A	357	303	101
	Artouste IIC	395	358	115
	Makila 1A1[3]	1357	1185	174
	Makila 1A1[4]	1357	1185	241
Safran (Turbomeca)	TM 333 2B2	801	711	167
Turbomeca	Astazou III	441	390	147

[1]Take-off. [2]Maximum continuous. [3]Basic. [4]Equipped.

A.3. GASTURB 14 GENERIC TURBOSHAFT WEIGHT ESTIMATION RESULTS

Figure A.1 presents the cross-section of the nominal generic turboshaft GasTurb 14 engine model used to develop the results shown in Figure A.2. The historical data used in Figure A.2 is as listed in Table A.2.

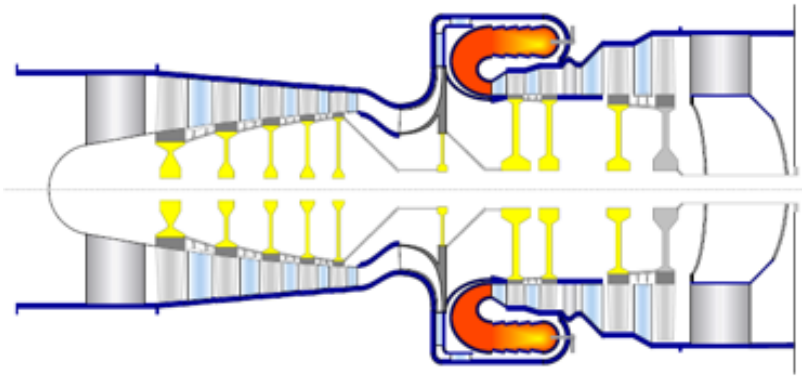

Figure A.1: GasTurb 14 generic two-spool 1210kW turboshaft engine.

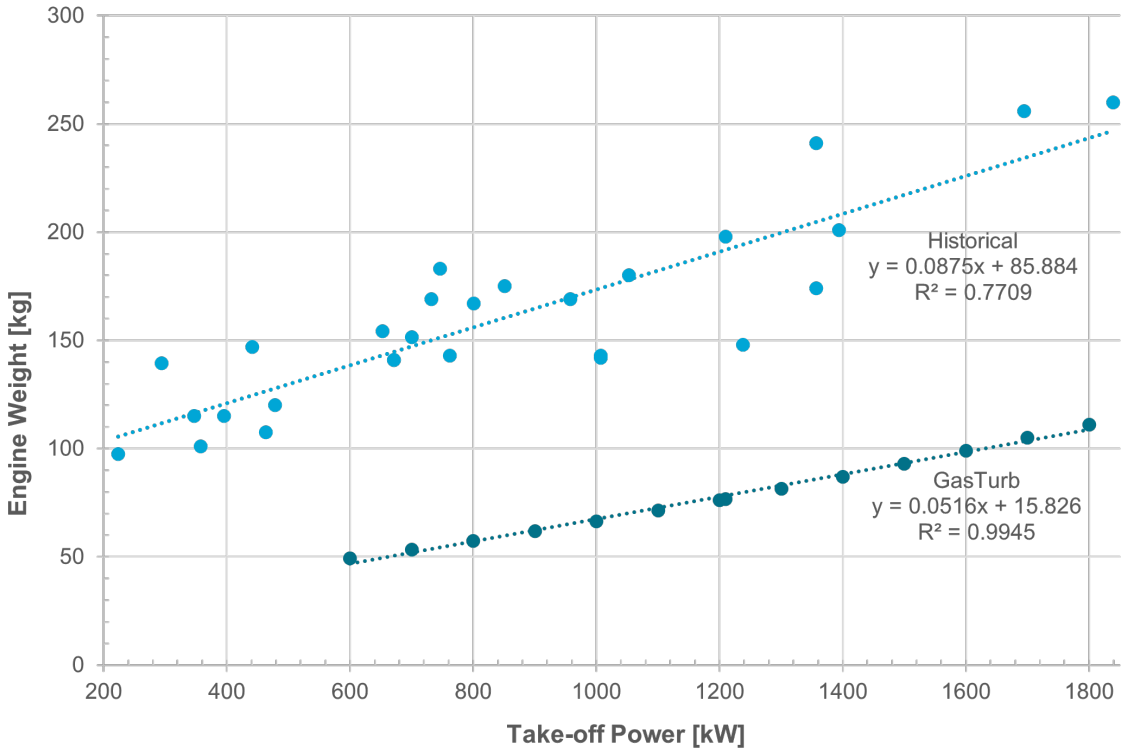

Figure A.2: GasTurb 14 weight estimation results for generic 2-spool turboshaft engine configuration.

B

APPENDIX: DESIGN METHODOLOGY

B.1. NEWTON-RAPHSON ITERATION METHOD

Iteration is required at several points throughout the axial compressor design procedure. Examples include:

- Determining the fixed radial coordinate (and/or first stage work) of the machine during the meanline analysis and preliminary gas path design for machines with fixed hub or tip radii (Section 2.1.1.5).
- Determining the maximum thickness-to-chord ratio of a blade at its root such that it satisfies the blade yield-stress criterion (Section 3.1.1.5).
- Determining the tangential stress of the disk at its bore when analyzing disk stresses (Section 3.1.2.3).
- Determining the inner radius of a ring disk which results in minimum component weight while still adhering to all stress criteria (Section 3.1.2.1).

For these instances, the Newton-Raphson iteration method can be employed to reduce calculation times. The formulation of this method – as implemented in the WEST program – will be presented here.

B.1.1. FORMULATION

Let f represent an arbitrary function. Let x represent the (unknown) root of that function and the iteration variable. If x is the root of f, then it follows that:

$$f(x) = 0 \tag{B.1}$$

Let x_0 represent the first guess of the root. An improved guess for the root, x_1, can therefore be estimated using the Newton-Raphson method as follows:

$$x_1 = x_0 - \frac{f(x_0)}{f'(x_0)} \tag{B.2}$$

Here, f' denotes the derivative of function f. Subsequent guesses for the root (x_2, x_3,..., x_{m-1}, x_m, etc.) can be obtained by repeating Equation B.3 as many times as required until sufficient convergence is obtained.

$$x_{n+1} = x_n - \frac{f(x_n)}{f'(x_n)} \tag{B.3}$$

Since the analytical derivative of the function f may not be known or readily available in many cases, this can be approximated using a forward finite difference method:

$$f'(x_n) \approx \frac{f(x_n + dx_n) - f(x_n)}{dx_n} \tag{B.4}$$

The finite difference (step size), dx_n, can be determined by selecting a (small) value for h according to the following equation:

$$dx_n = x_n \cdot h \tag{B.5}$$

Since $f(x) = 0$, convergence is obtained when the residual, $f(x_n)$, is within a specified tolerance:

$$\left|f(x_n)\right| \leq tolerance \approx 0 \tag{B.6}$$

Possible values for h and $tolerance$ are 1×10^{-4} and 1×10^{-6}, respectively.

B.1.2. EXAMPLE

As discussed in Section 2.1.1.5, the total specific work done by the designed axial compressor, $\left(w_{t,total}\right)_{des}$, calculated using Equation 2.45 must match the required value of total specific work, $w_{t,total}$, calculated using Equation 2.7. Thus, it is necessary that:

$$\left(w_{t,total}\right)_{des} \approx w_{t,total} \tag{B.7}$$

Since neither of these values are or should be equal to zero, a function must be defined for which the first stage work, $\left(w_{t,stg}\right)_1$ – in this case the iteration variable x – is the root. An example of such a function is shown in Equation B.8:

$$f(x) = \frac{\left(w_{t,total}\right)_{des}}{w_{t,total}} - 1 \tag{B.8}$$

Here, the required work value which is fixed, $w_{t,total}$, is in the denominator. If the formulation were to change such that $\left(w_{t,total}\right)_{des}$ (which can vary) was in the denominator, then there is the risk of division by zero, which could cause the entire method to fail. Instead, $\left(w_{t,total}\right)_{des}$ is kept in the numerator, and the value of 1 is subtracted from the fraction such that, when the two values of total specific work are equal (as is desired), the function $f(x)$ will be equal to zero, thus $\left(w_{t,stg}\right)_1$ is correctly defined as the root of the function.

B.2. BLOCKAGE FACTORS

It is common to apply empirical blockage factors in the meanline design of compressors: such factors aim to reduce the effective cross-sectional area in order to account for the boundary layer, something which is especially prevalent in compressors since the boundary layer thickness grows faster due to the adverse pressure gradient [78]. For turbines, no factor is applied, thus $K_B = 1$ in Equation 2.34. Table B.1 shows the average *work-done factors*, Λ_{avg}, for axial compressors with different total number of stages; these factors were originally proposed by Howell and Bonham [79] and reproduced (and digitized) by Korpela [80]. Work-done factors are meant to account for local variation of stagnation temperature in adiabatic flow (even though the average is assumed constant) through modification of the Euler equation, as shown in Equation B.9 [80]:

$$w_{t,stg} = h_{t,3} - h_{t,1} = \Lambda \cdot U \cdot \left(V_{t,2} - V_{t,1}\right) \tag{B.9}$$

Table B.1: Average work-done factors for axial compressors with different number of stages [79, 80].

n_{stg}	1	2	3	4	5	6	7	8	9
Λ_{avg}	0.982	0.952	0.929	0.910	0.895	0.883	0.875	0.868	0.863
n_{stg}	10	11	12	13	14	15	16	17	18
Λ_{avg}	0.860	0.857	0.855	0.853	0.851	0.850	0.849	0.848	0.847

These work-done factors were used and applied directly as compressor blockage factors by Tiemstra [44], an approach that produces results in good agreement with the blockage factors used by Lolis [21]. However, the original source states clearly that these are *mean* values for the entire machine, not local factors applying to the specified stage number [79]. Thus, a slightly modified approach is taken in the present methodology; the values will indeed be used as blockage factors, but are treated as the average values which they are.

Variation is still expected between stages, however, since the boundary layer grows as the flow progresses. A linear distribution of the blockage factors is assumed for simplicity, with the value at the first stage being the same as for a single-staged machine (i.e., the first entry in Table B.1). For example, a compressor with three stages has an average work-done factor – or blockage factor in this case – of 0.929 according to Table B.1. If this is to be the average, and if the first stage blockage factor is taken as 0.982 according to the first entry in Table B.1, then the last stage must be 0.876 according to the steps shown in Equations B.10 and B.11:

$$(K_B)_{stg,avg} = \frac{(K_B)_{stg,1} + (K_B)_{stg,3}}{2} = \frac{0.982 + (K_B)_{stg,3}}{2} = 0.929 \tag{B.10}$$

$$(K_B)_{stg,3} = (2 \cdot 0.929) - 0.982 = 0.876 \tag{B.11}$$

If the first value is applied to the inlet of the first stage, and the second value to the outlet of the last stage, then the values between every other row in the machine can be determined based on their relative position and linear interpolation between the first and last blockage factors.

B.3. FREE VORTEX METHOD

The principle of the Free Vortex design method is described in Equations 3.1 and 3.2. The first step in using this method is to fully-define the velocity triangles at mid-span, i.e., the mean radius. The blade angles here are already known, or can be determined once again, using Equations 2.11 through 2.14.The tangential velocity can be calculated using Equation B.12 and the meridional velocity using Equation B.13.

$$U_{mid} = \omega \cdot r_{mid} \tag{B.12}$$

$$V_m = \phi \cdot U_{mid} \tag{B.13}$$

The absolute and relative velocities can then be calculated using Equations B.14 through B.17.

$$V_1 = \frac{V_m}{\cos \alpha_1} \tag{B.14}$$

$$V_2 = \frac{V_m}{\cos \alpha_2} \tag{B.15}$$

$$W_1 = \frac{V_m}{\cos \beta_1} \tag{B.16}$$

$$W_2 = \frac{V_m}{\cos \beta_2} \tag{B.17}$$

The tangential components of the velocities, denoted with the subscript t, can be calculated using Equations B.18 through B.21.

$$V_{1,t} = V_1 \cdot \sin \alpha_1 \tag{B.18}$$

$$V_{2,t} = V_2 \cdot \sin \alpha_2 \tag{B.19}$$

$$W_{1,t} = W_1 \cdot \sin \beta_1 \tag{B.20}$$

$$W_{2,t} = W_2 \cdot \sin \beta_2 \tag{B.21}$$

For compressors with repeated stages and constant mean radius, the following relations are also true:

$$\alpha_3 = \alpha_1, \quad V_3 = V_1, \quad V_{3,t} = V_{1,t} \tag{B.22}$$

The blade may be divided into discrete spanwise locations; for example, the root, mid, and tip. With the velocities at the mid-radius now defined, the velocity triangles and blade angles at the other two locations (or any location in between) can begin, starting with the local tangential velocity shown in Equation B.23:

$$U_{loc} = \omega \cdot r_{loc} \tag{B.23}$$

According to Equation 3.1 of the Free Vortex method, which implies that the meridional velocity is not a function of radius (i.e., it is independent of spanwise location), it follows that:

$$V_{m,loc} = V_{m,mid} \tag{B.24}$$

The tangential component of the absolute velocity at Station 1 can be calculated through the application of Equation 3.2 as follows:

$$\left(V_{1,t}\right)_{mid} \cdot r_{mid} = const. = \left(V_{1,t}\right)_{loc} \cdot r_{loc} \tag{B.25}$$

$$\left(V_{1,t}\right)_{loc} = \frac{\left(V_{1,t}\right)_{mid} \cdot r_{mid}}{r_{loc}} \tag{B.26}$$

The total absolute velocity and flow angle at the local spanwise location can then be calculated using Equations B.27 and B.28, respectively.

$$V_{1,loc} = \sqrt{(V_m)^2 + \left(V_{1,t}\right)^2_{loc}} \tag{B.27}$$

$$\alpha_{1,loc} = \tan^{-1}\left(\frac{\left(V_{1,t}\right)_{loc}}{V_m}\right) \tag{B.28}$$

The relative velocity at the local spanwise location can be determined using Equations B.29 through B.31.

$$\left(W_{1,t}\right)_{loc} = \left(V_{1,t}\right)_{loc} - U_{loc} \tag{B.29}$$

$$W_{1,loc} = \sqrt{(V_m)^2 + \left(W_{1,t}\right)^2_{loc}} \tag{B.30}$$

$$\beta_{1,loc} = \tan^{-1}\left(\frac{\left(W_{1,t}\right)_{loc}}{V_m}\right) \tag{B.31}$$

The procedure outlined in Equations B.23 through B.31 can then be repeated for Station 2, namely, at the blade outlet, instead of Station 1. The relations described in Equation B.22 also hold for any local spanwise location, just as they were applied at the mid-span, allowing the stator vane blade angles (α_2 and α_3) to be fully-defined as well. Thus, using the Free Vortex design methodology, the blade angles at any spanwise location can be calculated using the meanline design as a starting point.

B.4. COMPRESSOR BLADE AIRFOIL DESIGN

B.4.1. CIRCULAR ARC MEAN CAMBER LINE

An illustration of a circular arc camber line is shown in Figure B.1.

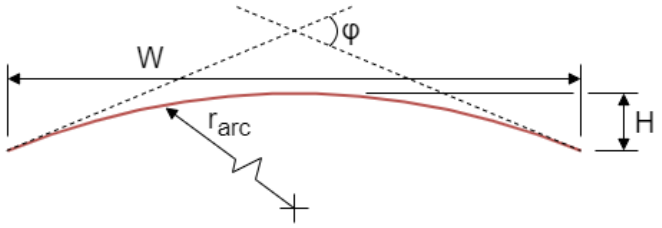

Figure B.1: Composition of a compressor blade circular arc mean camber line.

The geometric profile camber angle, φ, is defined as the angle between the lines tangent to the camber line at both the leading and trailing edges, and can be calculated using Equation B.32 for rotor blades and Equation B.33 for stators [45].

$$\varphi_{rotor} = |\beta_1 - \beta_2| \tag{B.32}$$

$$\varphi_{stator} = |\alpha_2 - \alpha_3| \tag{B.33}$$

The theoretical lift coefficient, c_{fL}, of an inviscid airfoil can then be calculated using Equation B.34 [45]:

$$c_{fL} = \frac{2\pi}{\ln 2} \cdot \tan\left(\frac{\varphi}{4}\right) \tag{B.34}$$

The normalized *skeleton line* – defined by Carolus – can then be calculated using Equation B.35 [45]:

$$\frac{y_{sk}}{l} = -\frac{c_{fL}}{4\pi}\left[\left(1-\frac{x}{l}\right)\cdot\ln\left(1-\frac{x}{l}\right)+\left(\frac{x}{l}\right)\cdot\ln\left(\frac{x}{l}\right)\right] \tag{B.35}$$

The only information used from the skeleton line is the maximum arc height, not the profile itself. This is then used to define the actual mean camber line, which follows a circular arc profile with the same maximum arc height. Assuming leading and trailing edges at points (0,0) and (1,0), respectively, for a normalized profile in the (x, y) coordinate system, the maximum arc height can be denoted as H and found using the skeleton line coordinates as shown in Equation B.36. The normalized width can be denoted as W and, as shown in Equation B.37, is simply equal to unity since l represents the true chord length of the blade (also sometimes denoted with symbol c), and this is a normalized profile.

$$H = \left(\frac{y_{sk}}{l}\right)_{max} \tag{B.36}$$

$$W = \frac{l}{l} = 1 \tag{B.37}$$

The radius of the circular arc, r_{arc}, can then be calculated using Equation B.38 [81]:

$$r_{arc} = \frac{H}{2} + \frac{W^2}{8H} \tag{B.38}$$

The coordinates of the arc's origin, $(x_o/l, y_o/l)$, can therefore be calculated using Equations B.39 and B.40.

$$\frac{x_o}{l} = \frac{W}{2} \tag{B.39}$$

$$\frac{y_o}{l} = H - r_{arc} \tag{B.40}$$

For values of x/l between 0 and 1, the (normalized) y-coordinates of the circular arc mean camber line (denoted with subscript c) can therefore be calculated using Equation B.41 [82]:

$$\frac{y_c}{l} = \sqrt{(r_{arc})^2 - \left(\frac{x}{l} - \frac{x_o}{l}\right)^2} + \frac{y_o}{l} \tag{B.41}$$

B.4.2. THICKNESS DISTRIBUTIONS (OF SOME SYMMETRIC NACA 65-SERIES AIRFOILS)

Table B.2: Thickness distributions of some symmetric NACA 65-series airfoils [45].

	NACA 65				
	-006	-008	-010	-012	-015
x/l [-]	y_t/l [%]	y_t/l [%]	y_t/l [%]	y_t/l [%]	y_t/l [%]
0	0	0	0	0	0
0.0050	0.476	0.627	0.772	0.923	1.124
0.0075	0.574	0.756	0.932	1.109	1.356
0.0125	0.717	0.945	1.169	1.387	1.702
0.025	0.956	1.267	1.574	1.875	2.324
0.050	1.310	1.745	2.177	2.606	3.245
0.075	1.589	2.118	2.647	3.172	3.959
0.10	1.824	2.432	3.040	3.647	4.555
0.15	2.197	2.931	3.666	4.402	5.504
0.20	2.482	3.312	4.143	4.975	6.223
0.25	2.697	3.599	4.503	5.406	6.764
0.30	2.852	3.805	4.760	5.716	7.152
0.35	2.952	3.938	4.924	5.912	7.396
0.40	2.998	3.998	4.996	5.997	7.498
0.45	2.983	3.974	4.963	5.949	7.427
0.50	2.900	3.857	4.812	5.757	7.168
0.55	2.741	3.638	4.530	5.412	6.720
0.60	2.518	3.337	4.146	4.943	6.118
0.65	2.246	2.791	3.682	4.381	5.403
0.70	1.935	2.553	3.156	3.743	4.600
0.75	1.594	2.096	2.584	3.059	3.744
0.80	1.233	1.617	1.987	2.345	2.858
0.85	0.865	1.131	1.385	1.630	1.977
0.90	0.510	0.664	0.810	0.947	1.144
0.95	0.195	0.252	0.306	0.356	0.428
1	0	0	0	0	0

B.5. BLADE STRESS ANALYSIS

B.5.1. FORCES

Figure B.2 shows the forces acting on an axial compressor rotor blade, as will be discussed and calculated in this section. Figure B.3 shows the resultant reaction forces acting at the root/base of the same blade.

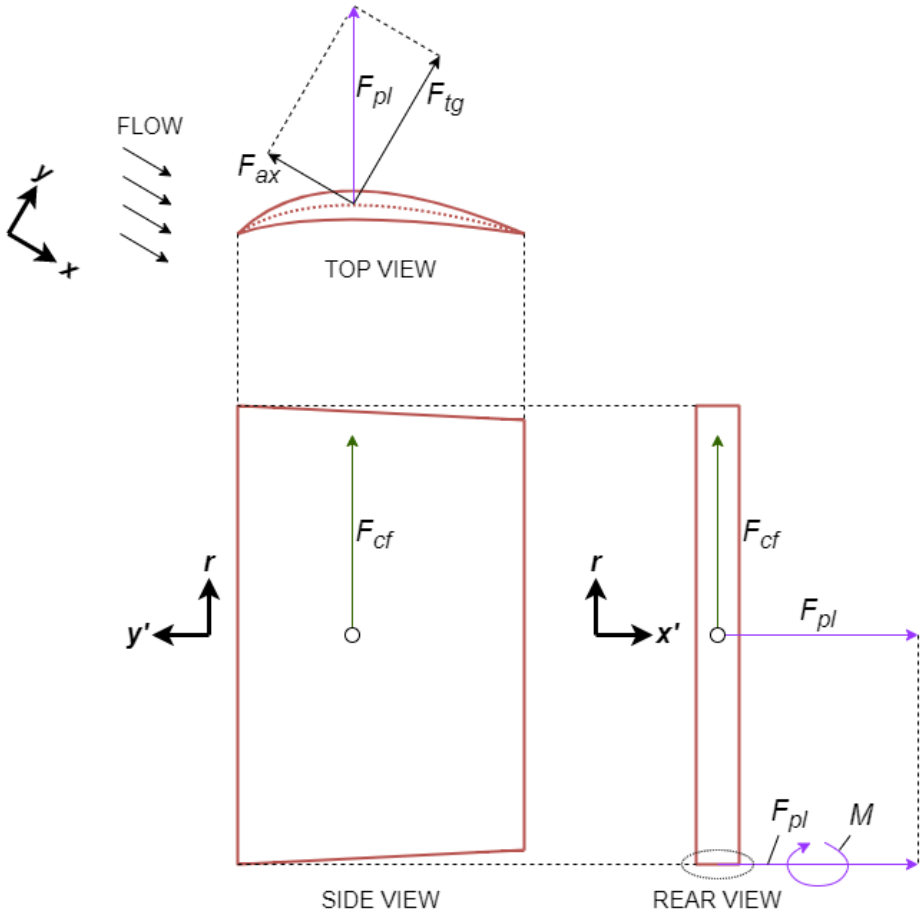

Figure B.2: Forces acting on an axial compressor rotor blade.

The total axial force acting on a blade row, $F_{ax,row}$, can be calculated using Equation B.42 [83]. This equation omits the axial force due to change in the flow momentum since it is assumed that the axial/meridional velocity, V_m, is constant across the stage.

$$F_{ax,row} = \left(p_{s,n} \cdot A_n\right) - \left(p_{s,n+1} \cdot A_{n+1}\right) \tag{B.42}$$

It follows then that the axial force acting on a single blade can be expressed as:

$$F_{ax,bl} = \frac{F_{ax,row}}{n_{bl}} \tag{B.43}$$

In Equation B.42, subscripts n and $n+1$ refer to arbitrary station numbers denoting the inlet and outlet of the specific row, respectively (this can also be understood as the leading and trailing edge locations). Thus, $n = 1$ for rotor rows and $n = 2$ for stator rows in the single-stage numbering system (e.g., Figure 2.4). The static pressure at that station is represented by p_s, and A represents the cross-sectional area of the gas path, as calculated previously using Equation 2.34, or alternatively with Equation B.44:

$$A = \pi\left[(r_{cas})^2 - (r_{hub})^2\right] = \pi\left[\left(r_m + \frac{b}{2}\right)^2 - \left(r_m - \frac{b}{2}\right)^2\right] \tag{B.44}$$

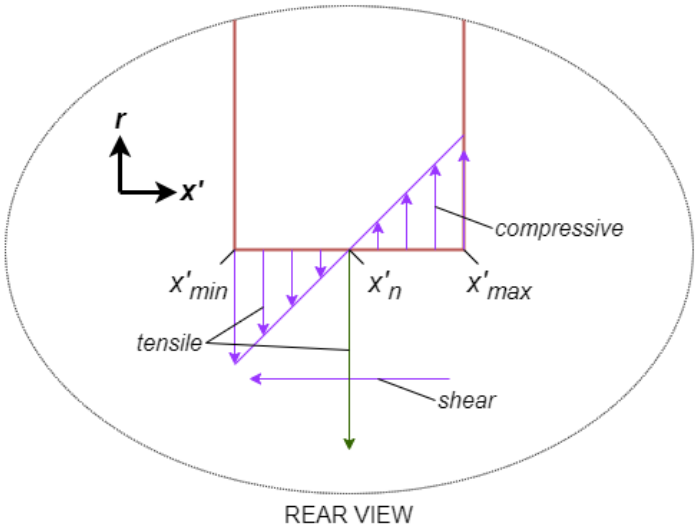

Figure B.3: Reaction forces acting on the base of an axial compressor rotor blade.

In this equation, the subscript cas denotes the casing of the machine, i.e., the outer radius, and hub the inner radius. For rotor blades, the casing is synonymous with the blade tip, thus cas and hub refer to the tip and root radii, respectively. The opposite is true for stator vanes.

Something important to note regarding the axial forces calculated in Equations B.42 and B.43 is the sign convention. With the downstream component being subtracted from the upstream component, this will produce axial force values which are negative for compressors (where the static pressure is increasing along the flow path) and positive for turbines (where the static pressure is decreasing along the flow path). With this accounted for, Equation B.42 can be applied for the cases of both compressors and turbines.

The total tangential force acting on a blade row, $F_{tg,row}$, can be calculated using Equation B.45 for rotors and Equation B.46 for stators [83]. The tangential force acting on a single blade, $F_{tg,bl}$, can then be calculated using Equation B.47.

$$\left(F_{tg,row}\right)_{rotor} = \dot{m} \cdot |W_{1,t} - W_{2,t}| \tag{B.45}$$

$$\left(F_{tg,row}\right)_{stator} = \dot{m} \cdot |V_{2,t} - V_{3,t}| \tag{B.46}$$

$$F_{tg,bl} = \frac{F_{tg,row}}{n_{bl}} \tag{B.47}$$

As shown in Equation B.45, calculations for rotor rows use the tangential components of the relative velocities, whereas calculations for stator rows (Equation B.46) use the tangential components of the absolute velocities. In these equations, the order of subtraction does not matter since the absolute value is taken: this is because the tangential force is assumed positive, and always will be, according to the way in which blades are designed and forces are applied in the present stress analysis methodology.

If the blade is subject to rotation, i.e., it is a rotor blade, then a centrifugal force will also be present. This can be calculated using Equation B.48:

$$F_{cf,bl} = m_{bl} \cdot r_{G,bl} \cdot \omega^2 \tag{B.48}$$

Since the axial and tangential forces act on the same plane, these can be combined into one planar force, F_{pl}, using Equation B.49, and the angle of this force with respect to the axial direction using Equation B.50.

$$F_{pl} = \sqrt{\left(F_{ax,bl}\right)^2 + \left(F_{tg,bl}\right)^2} \tag{B.49}$$

$$\theta_{F_{pl}} = \tan^{-1}\left(\frac{F_{tg,bl}}{F_{ax,bl}}\right) \tag{B.50}$$

B.5.2. STRESSES

The tensile normal stress due to centrifugal forces acting on the (rotor) blade root/hub can be calculated using Equation B.51:

$$\sigma_{cf} = \frac{F_{cf,bl}}{A_{root}} \tag{B.51}$$

In this equation, the area A_{root} is the airfoil cross-sectional area of the blade root profile, i.e., the area with which the blade is connected to the disk hub.

For the planar force, it is assumed that this can be applied as a point force centred and at the average mid-radius, thus not inciting any torque or twist in the blade. Nevertheless, application of this force at the mid-span results in a bending moment at the root, as shown in Figure B.2, which in turn yields both a normal stress due to bending and a shear stress due to transverse shear. The bending moment, M, can be calculated using Equation B.52:

$$M = F_{pl} \cdot \frac{b_{avg}}{2} = F_{pl} \cdot \frac{r_{avg,tip} - r_{avg,root}}{2} \tag{B.52}$$

To proceed, a new, transformed coordinate system, denoted with x' and y', can be temporarily defined to simplify the notation in some of the following equations. Within this system, the x'-axis is aligned with the planar force and planar angle, such that the entire planar force lies on the x'-axis. It is positive in the direction in which the force is pointing. The y'-axis is perpendicular to this, but on the same plane as the original two forces. The radial r-axis remains unchanged and is 'out of the page', i.e., normal to the 2D airfoil.

The location of the *neutral axis*, x'_n, and the second-area moment about the y'-axis, $I_{y'y'}$, can be calculated using Equations B.53 and B.54, respectively [84]:

$$x'_n = \frac{\int_A x' dA}{A} \tag{B.53}$$

$$I_{y'y'} = \int_A \left(x'\right)^2 dA \tag{B.54}$$

Once the location of the neutral axis is calculated, this becomes the new origin, such that $x' = 0$ at x'_n. The maximum and minimum x' coordinates of the root profile can then be denoted x'_{max} and x'_{min}, respectively.

The normal stress due to bending, σ_{bn}, can then be calculated using Equation B.55 where x' represents the x'-coordinate measured relative to the neutral axis x'_n [84]:

$$\sigma_{bn} = -\frac{M \cdot x'}{I_{y'y'}} \tag{B.55}$$

The transverse shear stress, τ, at the same location can be calculated using Equation B.56 [84]:

$$\tau = \begin{cases} \frac{3 \cdot F_{pl}}{2 \cdot A_{root}} \left(1 - \frac{(x')^2}{(x'_{max})^2}\right), & x' \geq 0 \\ \frac{3 \cdot F_{pl}}{2 \cdot A_{root}} \left(1 - \frac{(x')^2}{\left(x'_{min}\right)^2}\right), & x' < 0 \end{cases} \tag{B.56}$$

For negative values of x', the normal stress due to bending will be tensile, not compressive. This tensile stress will add to the tensile stress due to centrifugal forces already calculated in Equation B.51. Thus, the region of the blade root behind the neutral axis (i.e., for negative values of x') is the critical stress region. The total tensile stress in the r-axis (i.e., radial direction) can therefore be calculated using Equation B.57:

$$\sigma_r = \sigma_{cf} + \sigma_{bn} \tag{B.57}$$

The von Mises stress, σ_e, can be calculated using Equation B.58 [84]:

$$\sigma_e = \sqrt{(\sigma_r)^2 + 3\,(\tau)^2} \tag{B.58}$$

The tensile stress is maximum at the location x'_{min}, whereas the transverse shear stress is maximum at the neutral axis, x'_n. Therefore, the maximum von Mises stress does not always occur right at x'_{min}. Instead, the calculation of the von Mises stress (Equations B.55 through B.58) can be repeated for several discrete locations within the range $x'_{min} \leq x' \leq x'_n$ where $x'_n = 0$, and the maximum value for all locations can be taken as the maximum von Mises stress present in the blade, $\sigma_{e,max}$.

B.6. DISK STRESS ANALYSIS

B.6.1. ELEMENT-BY-ELEMENT STRESS CALCULATIONS

If two adjoining infinitesimal ring elements are denoted as A and B, with A being the inner element and B the outer, then the stresses at the outer radius of A and inner radius of B can be calculated assuming that the stresses at the inner radius of A are already known. Figure B.4 shows an exaggerated representation of such elements. In the equations presented in this section, σ refers to stress, with subscripts h and r distinguishing between hoop and radial stresses, respectively, i and o between inner and outer locations of the element, respectively, and A and B between two adjoining elements.

For the very first element in the disk, the inner tangential/hoop stress $\sigma_{h,i,A}$ is equal to $\sigma_{h,1}$, which was a guessed value, and the inner radial stress, $\sigma_{r,i,A}$, is equal to zero since there are no centrifugal loads here [21]. For all other cases, the calculation procedure can be performed on an element-by-element basis, moving from the inner radius to outer radius of the disk. Once the values of $\sigma_{h,o,A}$, $\sigma_{r,o,A}$, $\sigma_{h,i,B}$, and $\sigma_{r,i,B}$ have been determined for a particular set of adjoining elements, element B can be renamed A and the procedure restarted with the next element set.

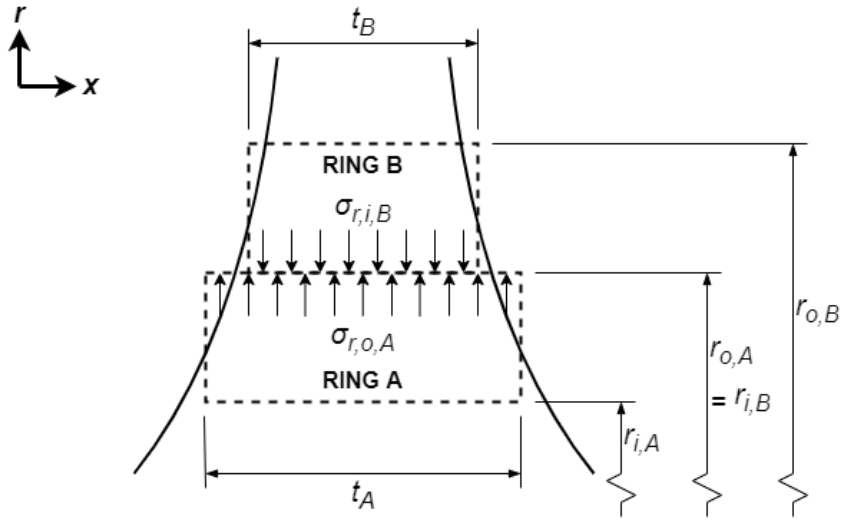

Figure B.4: Adjoining infinitesimal ring elements of discretized disk [21].

There are no axial or shear stresses in the disk, making this a case of planar stress. A sum (S) and difference (D) method can therefore be used; these stresses can be calculated for the inner radius of element A using Equations B.59 and B.60, respectively.

$$S_{i,A} = \sigma_{h,i,A} + \sigma_{r,i,A} \tag{B.59}$$

$$D_{i,A} = \sigma_{h,i,A} - \sigma_{r,i,A} \tag{B.60}$$

The sum and difference method stresses at the outer radius of element A can be calculated using Equations B.61 and B.62, respectively [21].

$$S_{o,A} = S_{i,A} - \frac{1+\nu}{2} \cdot \rho \cdot \omega^2 \cdot \left(r_{o,A}^2 - r_{i,A}^2\right) \tag{B.61}$$

$$D_{o,A} = D_{i,A} \cdot \left(\frac{r_{i,A}^2}{r_{o,A}^2}\right) - \frac{(1-\nu) \cdot \rho \cdot \omega^2}{4} \cdot \left(\frac{r_{i,A}^4}{r_{o,A}^2} - r_{o,A}^2\right) \tag{B.62}$$

Note that the Poisson's Ratio, ν, used in Equations B.61 and B.62, as well as the elastic moduli, E, and coefficients of thermal expansion, α, used in later equations, are temperature-dependent material properties. Thus, the temperature of the local infinitesimal element must be calculated. Determining the temperature distribution throughout the disk is the subject of Section 3.1.2.5, so for here it will be assumed that the temperature, material, and temperature-dependent material properties for each ring element are all known.

Next, the tangential and radial stresses at the outer radius of element A can be calculated using Equations B.63 and B.64, respectively [21].

$$\sigma_{h,o,A} = \frac{S_{o,A} + D_{o,A}}{2} \tag{B.63}$$

$$\sigma_{r,o,A} = \frac{S_{o,A} - D_{o,A}}{2} \tag{B.64}$$

Each adjoining infinitesimal element is assumed small enough such that the assumption of constant thickness, t, and constant temperature, T, are valid for that single element. Thus, changes in disk thickness are achieved through a large number of incremental changes over many elements, as visualized in Figure B.4. Equations B.65 and B.66 can be used to determine the change in radial and tangential stresses, respectively, over the interface between two adjoining elements, while also accounting for the stresses induced by the temperature gradient [21].

$$\delta\sigma_r = \sigma_{r,o,A} \cdot \left(\frac{t_A}{t_B} - 1\right) \tag{B.65}$$

$$\delta\sigma_h = \left(\sigma_{h,o,A} - \nu \cdot \sigma_{r,o,A}\right) \cdot \left(\frac{E_B}{E_A} - 1\right) + E_B \cdot (\alpha_A \cdot T_A - \alpha_B \cdot T_B) + \nu \cdot \delta\sigma_r \tag{B.66}$$

Thus, the radial and tangential stresses at the inner radius of element B can be calculated using Equations B.67 and B.68, respectively.

$$\sigma_{r,i,B} = \sigma_{r,o,A} + \delta\sigma_r \tag{B.67}$$

$$\sigma_{h,i,B} = \sigma_{h,o,A} + \delta\sigma_h \tag{B.68}$$

Repeating this procedure for all elements means that the distribution of radial and tangential stresses can be determined along the entire disk. Once the radial stress at the hub, $\sigma_{r,hub}$, is known (i.e., the $\sigma_{r,o,B}$ value of the very last element set), it can be compared to the rim stress calculated earlier. If these values are the same, then the initial guess of the inner tangential stress was correct. Otherwise, the value of $\sigma_{h,1}$ can be iterated using the Newton-Raphson method (Appendix B.1) until convergence between the calculated outer radial stress and the rim stress is obtained.

The radial and tangential stress distributions can now be combined to determine the maximum *von Mises stress*, σ_e, at every radial location in the disk. The von Mises stress can be calculated using Equation B.69 [85], where the axial stress, σ_{ax}, and shear stress, τ, are both zero.

$$\sigma_e = \sqrt{\frac{(\sigma_{ax} - \sigma_r)^2 + (\sigma_r - \sigma_h)^2 + (\sigma_h - \sigma_{ax})^2}{2} + 3\tau^2} \tag{B.69}$$

$$\sigma_{ax} = 0 \tag{B.70}$$

$$\tau = 0 \tag{B.71}$$

B.7. TURBINE BLADE AIRFOIL DESIGN

B.7.1. THICKNESS DISTRIBUTION

First, a scaling parameter, S, for the x-coordinates is defined in Equation B.72:

$$S = 1 + \left(TER \cdot (t/c)_{max} \cdot 10^{-4}\right) \tag{B.72}$$

Here, TER refers to the trailing-edge radius and is expressed as a percentage of maximum thickness-to-chord ratio. Also, both the TER and $(t/c)_{max}$ are expressed as the magnitude of their percentages, thus a value of 25%, or 0.25, for example, is applied as 25 in the above equation, hence the 10^{-4} correction factor[1].

The normalized blade thickness distribution, δ/l, can be calculated according to Equation B.73 [70], where XT is the position of maximum blade thickness. The coefficients A through H are described in Appendix B.7.2. Note that the term $H(1-x)^4$ was mistakenly written as $H(1-x^4)$ in the original work of Dunham [70].

$$\frac{\delta}{l} = \begin{cases} 0.1 \cdot (t/c)_{max} \cdot \left(Ax^{0.5} + Bx + Cx^2 + Dx^3\right), & x < 0.01 \cdot XT \cdot S \\ 0.1 \cdot (t/c)_{max} \cdot \left(E + F(1-x) + G(1-x)^3 + H(1-x)^4\right), & x > 0.01 \cdot XT \cdot S \end{cases} \tag{B.73}$$

Since δ/l represents the full blade thickness, the half-thickness, y_t/l, can be calculated using Equation B.74. While the thickness distribution is assumed symmetric, the application of a camber line means that the actual blade is not symmetric.

$$\frac{y_t}{l} = \frac{\delta}{2l} \tag{B.74}$$

In the aforementioned calculations, values for various parameters must be specified. Default values are taken in order to produce a generally-representative turbine blade base profile with minimal user input/effort; however, the user is able to modify these at any time if they have specific requirements and/or improved insight regarding the particular application being studied. Dunham suggests that the best position of maximum thickness, which depends on the maximum thickness-to-chord ratio, can be determined according to Equation B.75 [70]. To reiterate, values of XT and $(t/c)_{max}$ are here expressed in the magnitude of their percentage values.

$$XT = 13.7 + 0.588 \cdot (t/c)_{max} \tag{B.75}$$

A reasonable trailing edge wedge angle can be calculated using Equation B.76 [70]:

$$WA = 2 \cdot \tan^{-1}\left(\frac{(t/c)_{max}}{300}\right) \tag{B.76}$$

A typical trailing-edge thickness, which is expressed as a percentage of $(t/c)_{max}$, is **7.5%** according to the exemplary case presented by Dunham [70].

The procedure for determining a suitable leading-edge radius is slightly more complicated. First, the leading and trailing edge flow angles must be considered. These are based on relative velocities, so they are α_0 and α_1 for stator vanes and β_1 and β_2 for rotor blades. However, the actual blade angles of the designed turbine blade may vary from these due to the presence of an incidence angle at the leading edge and a deviation angle at the trailing edge. The actual blade angles, i.e., the angles of a line tangent to the camber line at the leading and trailing edges, will be denoted as $\beta_{1,i}$ and $\beta_{2,d}$, respectively, where the subscripts i and d indicate correction for incidence and deviation angles, respectively. An appropriate leading-edge blade angle can then be calculated using Equation B.77 [70]:

$$\beta_{1,i} = \beta_1 - 7.3 - 0.262 \cdot \left(\beta_1 + \beta_2\right) \tag{B.77}$$

Next, the parameter $\left(\beta_{1,i} - \beta_2\right)$ can be calculated, which this is then used to determine the leading-edge radius. According to Dunham, a LER value of 15 is suitable for $\left(\beta_{1,i} - \beta_2\right)$ below 70°. At higher camber angles, other values are proposed, as shown in Equation B.78 [70]. For values between 70 and 110 degrees, linear interpolation can be used between the provided values.

[1] The variables throughout the procedure given by Dunham, such as the position of maximum thickness, XT, and leading-edge radius, LER, are all percentage values applied as the magnitude of their percentage (i.e., as the fractional decimal value multiplied by 10^2). Also worth noting is that angles, such as the trailing edge wedge angle, WA, are expressed in units of degrees for the remaining equations in this section.

$$LER = \begin{cases} 15, & (\beta_{1,i} - \beta_2) \leq 70^\circ \\ 13, & (\beta_{1,i} - \beta_2) = 90^\circ \\ 10, & (\beta_{1,i} - \beta_2) = 100^\circ \\ 4, & (\beta_{1,i} - \beta_2) = 110^\circ \end{cases} \tag{B.78}$$

B.7.2. COEFFICIENTS USED IN TURBINE BLADE THICKNESS DISTRIBUTION EQUATION

The following coefficients, A through H, are used in Equation B.73 when defining the thickness distribution for turbine blade airfoils. These are defined in Equations B.79 through B.86, respectively [70]. Additional factors r and q are used in these equations and are defined in Equations B.87 and B.88, respectively [70].

$$A = \left(0.08 \cdot \frac{LER}{(t/c)_{max} \cdot S}\right)^{0.5} \tag{B.79}$$

$$B = \frac{0.3 - \frac{15r}{8} + q}{0.01 \cdot XT \cdot S} \tag{B.80}$$

$$C = \frac{-0.3 + \frac{5r}{4} - 2q}{(0.01 \cdot XT \cdot S)^2} \tag{B.81}$$

$$D = \frac{0.1 - \frac{3r}{8} + q}{(0.01 \cdot XT \cdot S)^3} \tag{B.82}$$

$$E = 0.002 \cdot TER \tag{B.83}$$

$$F = \frac{20 \cdot \tan\left(\frac{WA}{2}\right)}{(t/c)_{max} \cdot S} \tag{B.84}$$

$$G = \left[0.4 - 0.008 \cdot TER - \frac{60 \cdot \tan\left(\frac{WA}{2}\right)}{(t/c)_{max} \cdot S}(1 - 0.01 \cdot XT \cdot S)\right](1 - 0.01 \cdot XT \cdot S)^{-3} \tag{B.85}$$

$$H = -\left[0.3 - 0.006 \cdot TER - \frac{40 \cdot \tan\left(\frac{WA}{2}\right)}{(t/c)_{max} \cdot S}(1 - 0.01 \cdot XT \cdot S)\right](1 - 0.01 \cdot XT \cdot S)^{-4} \tag{B.86}$$

$$r = \left(\frac{0.0008 \cdot LER \cdot XT}{(t/c)_{max}}\right)^{0.5} \tag{B.87}$$

$$q = \left[-0.6 + 0.012 \cdot TER + \frac{60 \cdot \tan\left(\frac{WA}{2}\right)}{(t/c)_{max} \cdot S}(1 - 0.01 \cdot XT \cdot S)\right]\left(\frac{0.01 \cdot XT \cdot S}{1 - 0.01 \cdot XT \cdot S}\right)^2 \tag{B.88}$$

B.7.3. MEAN CAMBER LINE

For $0 \leq x/l \leq 1$, the class function, C, is represented by Equation B.89:

$$C = \left(\frac{x}{l}\right)^{N1} \left(1 - \frac{x}{l}\right)^{N2} \tag{B.89}$$

The exponents of the class function, $N1$ and $N2$, are used to define the blade shape type. For example, if $N1 = N2 = 0.5$, an elliptical shape is obtained, one with rounded nose and rounded tail; for $N1 = N2 = 1.0$, a pointed nose and pointed tail; and for $N1 = 0.5$ and $N2 = 1.0$, an almost airfoil-like shape with a rounded nose and a pointed tail [71]. Thus, for the CST parameterization of the outer surfaces of airfoils, the combination of $N1 = 0.5$ and $N2 = 1.0$ is commonly used.

However, since the objective in this case is to model camber lines, not external airfoils, the curvature should not be as heavily concentrated towards the leading edge. Slightly higher values of $N1$ are used (with $N2$ always fixed at 1.0).In the present methodology, $N1$ is initially set to 0.6 and then increased incrementally until a curve is obtained such that the camber angle is satisfied, and such that the entire curve is concave, i.e., there is no inflection point where the *direction* of curvature changes directions.

The shape function, S, can then be used to morph the initial characteristic shape obtained from the class function into a more specific geometry[2]. The shape function is defined according to Equation B.90 [71]:

$$S = \sum_{r=0}^{n} b_{r,n} \cdot A_r \tag{B.90}$$

In this equation, $b_{r,n}$ is a Bernstein basis polynomial and is defined according to Equation B.91 [71]:

$$b_{r,n} = \frac{n!}{r!\,(n-r)!} \left(\frac{x}{l}\right)^{r} \left(1 - \frac{x}{l}\right)^{n-r} \tag{B.91}$$

The term A_r in Equation B.90 represents a scaling factor, or Bernstein coefficient. The user can choose any number of Bernstein coefficients, and the order of a Bernstein polynomial is n when there are $n+1$ coefficients specified. The more terms used, the more complex of a shape can be achieved.

Both the class and shape functions are combined in Equation B.92 to obtain the final CST-method function, where C and S are functions of the normalized x-coordinate x/l:

$$\frac{y_c}{l} = C \cdot S \tag{B.92}$$

Once the class function exponents, $N1$ and $N2$, are fixed, the main design freedom comes through the Bernstein coefficients, A_r, and the number of the adopted coefficients, n. In this present study, one continuous, fairly simple camber line is desired, so only two coefficients are used, A_0 and A_1, resulting in a first-order Bernstein polynomial (i.e., $n = 1$). These coefficients are determined using a quickly-executing optimization scheme which matches the camber angle of the curve to the desired camber angle ($\beta_2 - \beta_1$) with minimum error. As previously stated, this optimization procedure is repeated for varying values of $N1$ until the smallest value of $N1$ is obtained such that the camber angle is achieved, and such that the curve is concave over its entire domain (i.e., no inflection points are present). Lower and upper bounds of zero and unity are used, respectively, for both A_0 and A_1.

Note that, with the camber line equation design method shown here, nothing is done to account for the incidence or deviations angles of the blade. Instead, it is assumed that the flow simply enters and leaves tangent to the camber line, an assumption which is not accurate for fluid dynamic performance but which is likely to make only a negligible difference with respect to weight estimation.

[2] This is different from the variable S defined in Equation B.72.

C

Appendix: Results

C.1. Validation

C.1.1. Axial Compressors

C.1.1.1. CFM56 LPC

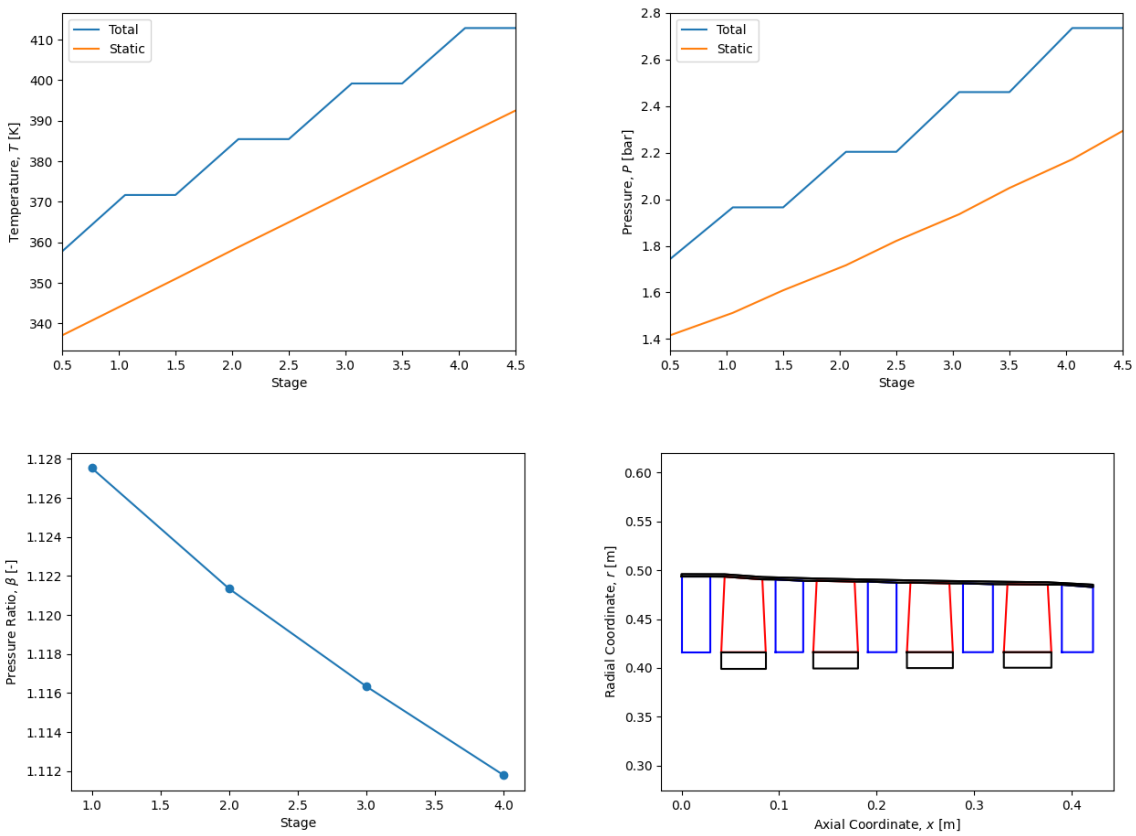

Figure C.1: Meanline performance and mechanical design results of CFM56 LPC.

C.1.1.2. PW2037 LPC

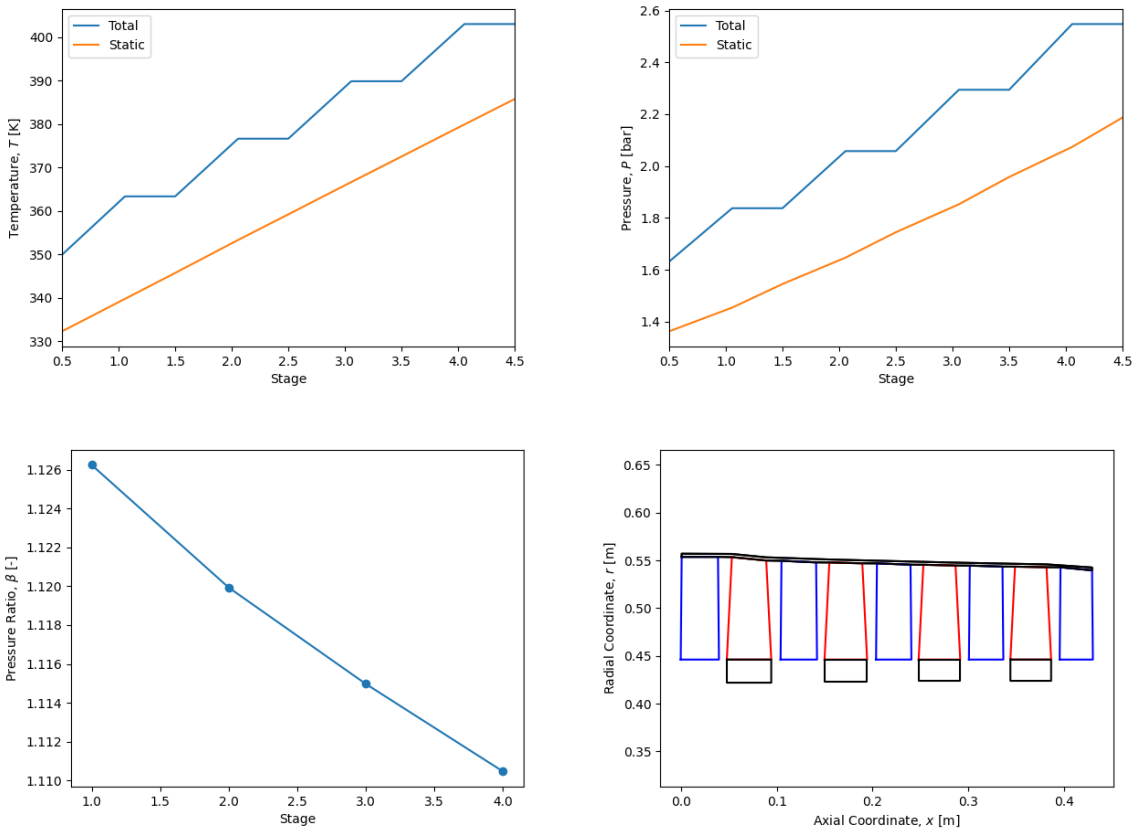

Figure C.2: Meanline performance and mechanical design results of PW2037 LPC.

C.1.1.3. PW2037 HPC

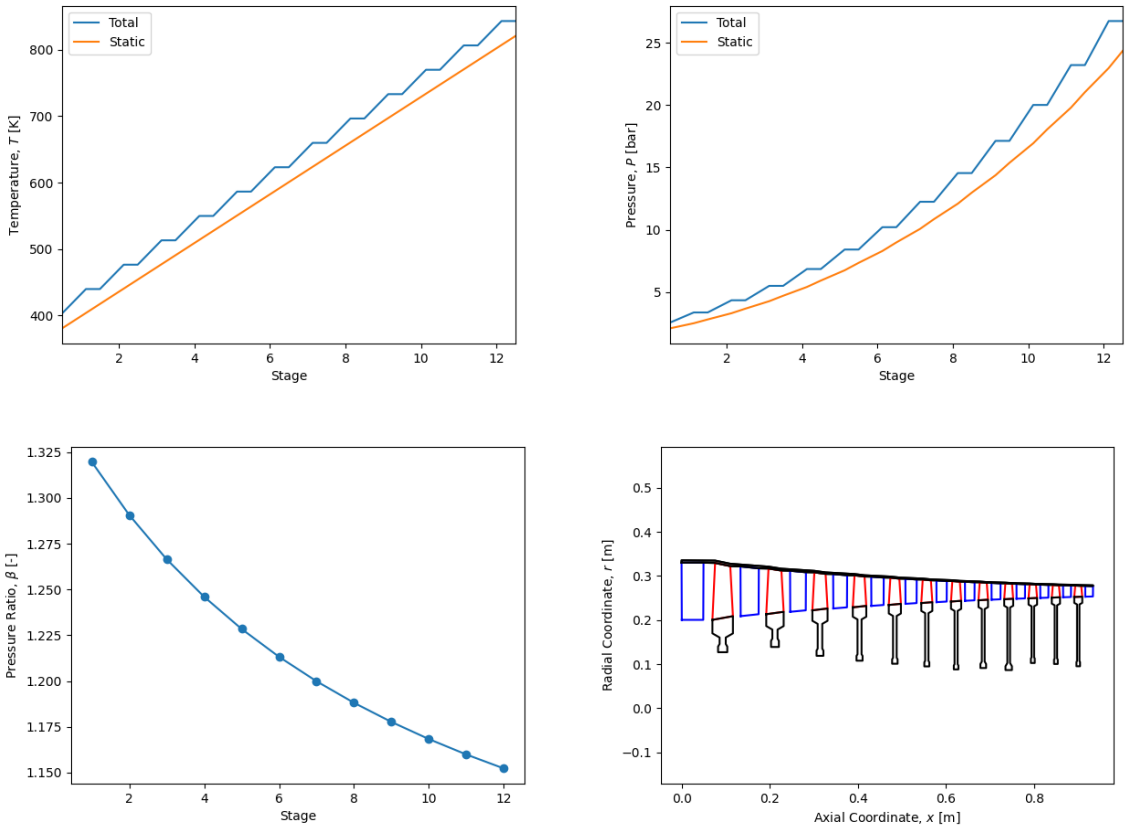

Figure C.3: Meanline performance and mechanical design results of PW2037 HPC.

C.1.2. AXIAL TURBINES

C.1.2.1. CFM56 HPT

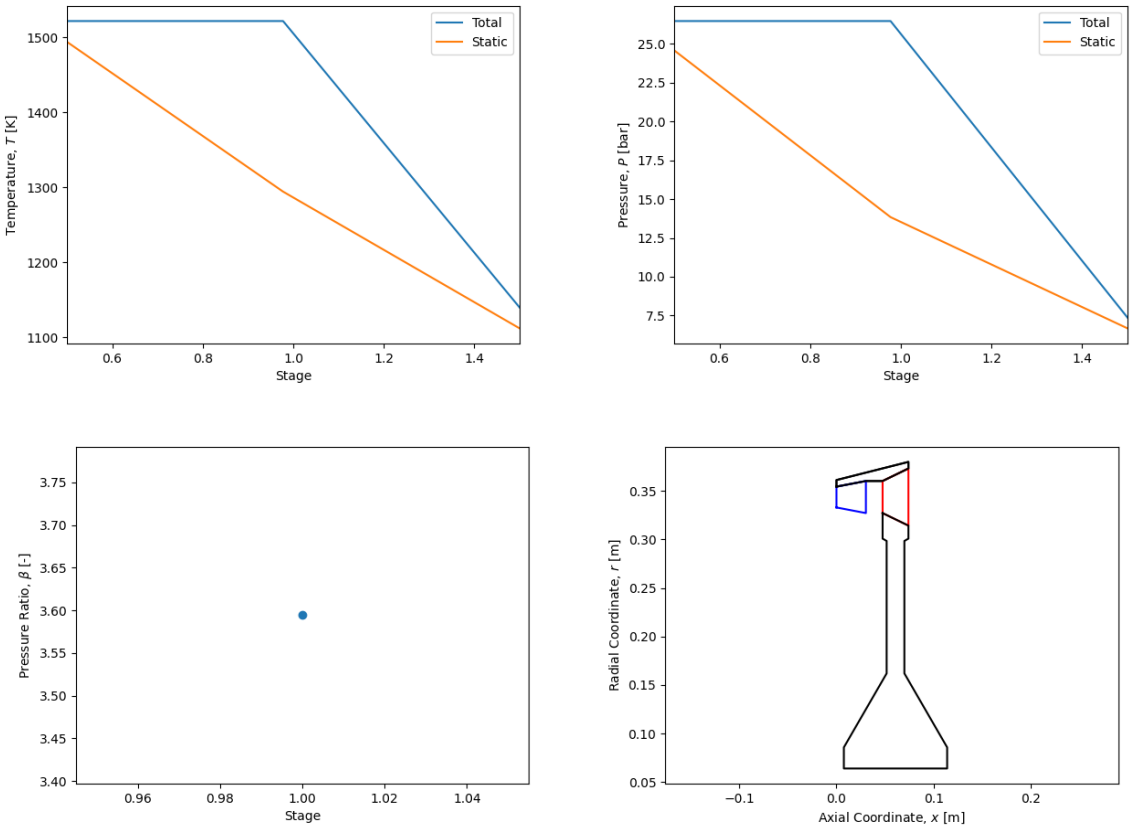

Figure C.4: Meanline performance and mechanical design results of CFM56 HPT.

C.1.2.2. PW2037 HPT

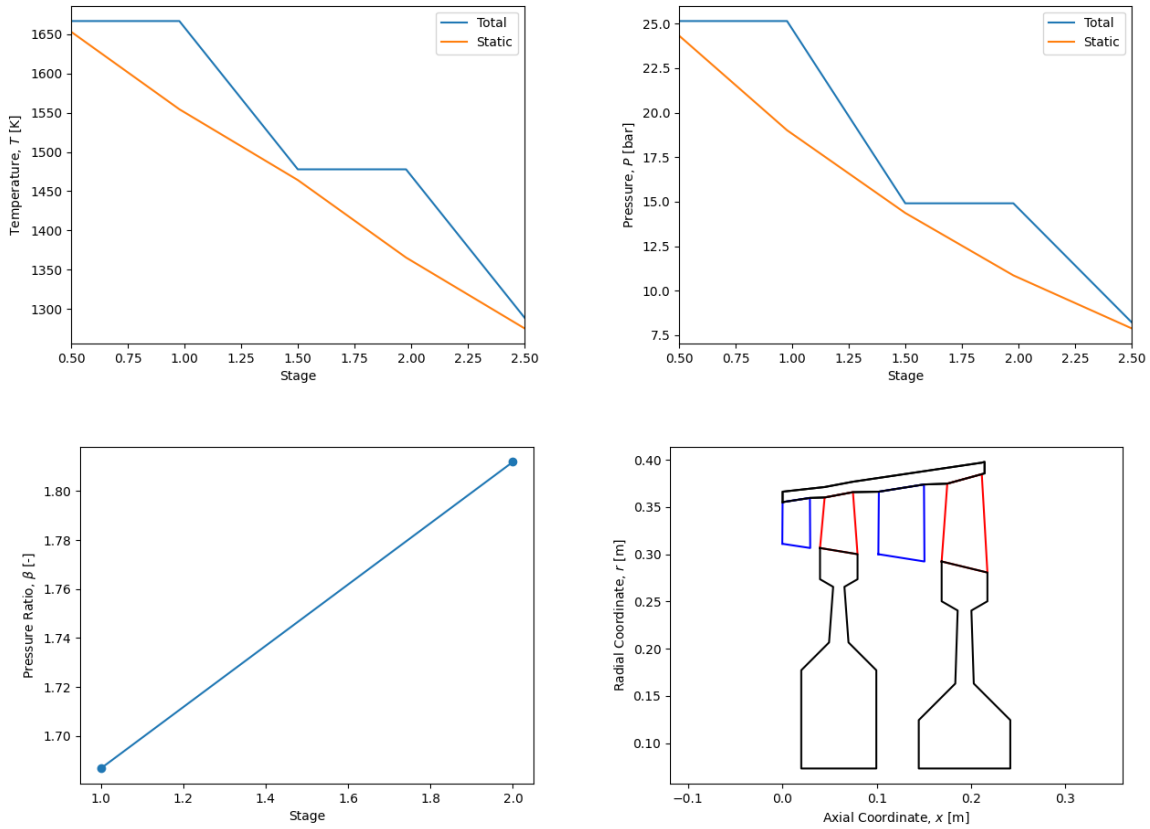

Figure C.5: Meanline performance and mechanical design results of PW2037 HPT.

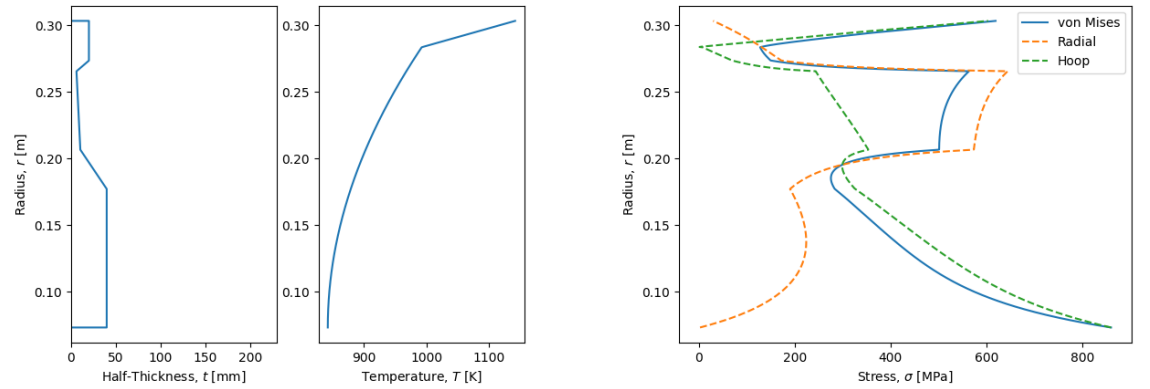

Figure C.6: Stress distributions of PW2037 HPT first stage disk.

C.1.2.3. PW2037 LPT

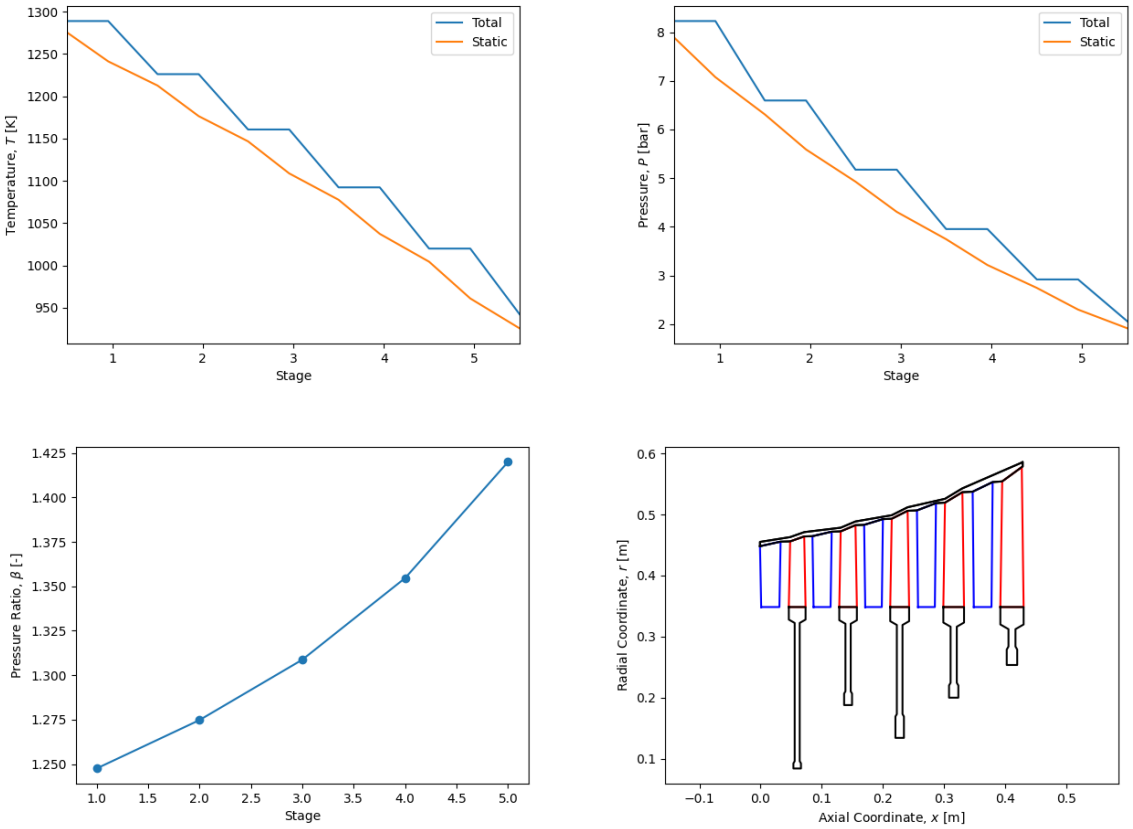

Figure C.7: Meanline performance and mechanical design results of PW2037 LPT.

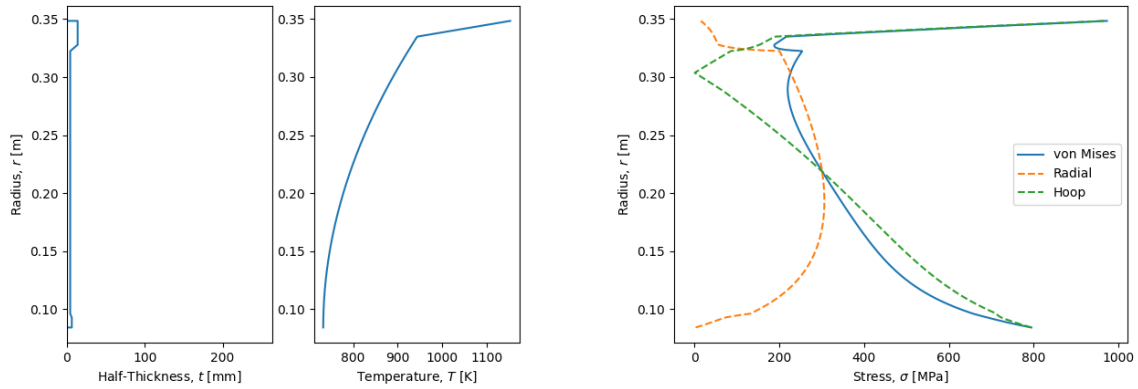

Figure C.8: Stress distributions of PW2037 LPT first stage disk.

C.2. SENSITIVITY ANALYSIS

C.2.1. AXIAL COMPRESSORS

C.2.1.1. MAIN PARAMETERS OF THE ENGINE SYSTEM MODEL

Pressure Ratio

Table C.1: Outer dimensions and consumed power of CFM56 HPC model for various pressure ratios.

Category	Parameter	Units	Case 1	Case 2[1]	Case 3
Performance	Pressure Ratio, PR	-	7.725	10.3	12.875
	Power, $\dot{W}$	MW	(21.6)	(25.9)	(29.5)
Dimensions	Outer Radius	m	(0.292)	(0.306)	(0.318)
	Length[2]	m	(0.646)	(0.488)	(0.398)

[1]Nominal. [2]Total length excluding guide vane.

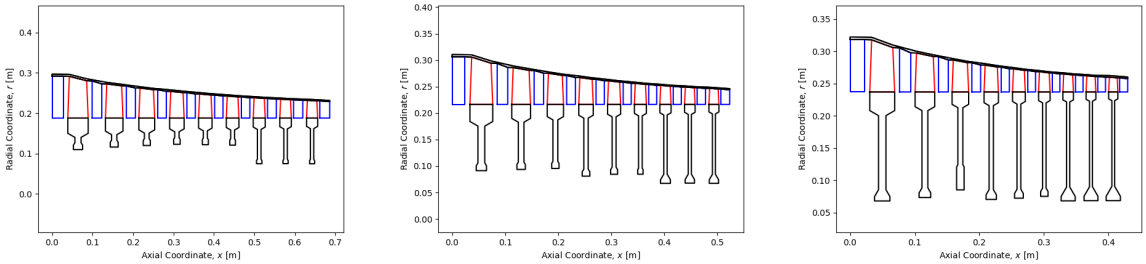

Figure C.9: Design results of CFM56 HPC for 7.725 (left), 10.3 (middle), and 12.875 (right) compressor pressure ratios.

Table C.2: Comparison of weight estimation results of CFM56 HPC model for various pressure ratios.

Component	Weight [kg]		
	7.725[1]	10.3[1,2]	12.875[1]
Total	**159.2**	**134.6**	**120.8**
Rotors + Disks	97.5	91.0	85.8
Rotor Blades	12.7	9.19	7.21
Disks	84.7	81.8	78.6
Stator Vanes	22.1	16.1	13.1
Casing	29.9	19.4	14.8
Connecting Hardware	9.69	8.07	7.08

[1]Compressor pressure ratio. [2]Nominal.

Table C.3: Comparison of single-stage pressure ratio of CFM56 HPC model for various compressor pressure ratios.

Type	PR_{stg} [-]		
	7.725[1]	10.3[1,2]	12.875[1]
Maximum	1.427	1.518	1.595
Average	1.258	1.300	1.334

[1]Compressor pressure ratio [-]. [2]Nominal.

Mass Flow Rate

Table C.4: Outer dimensions and consumed power of CFM56 HPC model for various mass flow rates.

Category	Parameter	Units	Case 1	Case 2[1]	Case 3
Performance	Mass Flow Rate, $\dot{m}$	kg/s	43.9	58.5	73.1
	Power, $\dot{W}$	MW	(19.4)	(25.9)	(32.4)
Dimensions	Outer Radius	m	(0.292)	(0.306)	(0.320)
	Length[2]	m	(0.369)	(0.488)	(0.606)

[1]Nominal. [2]Total length excluding guide vane.

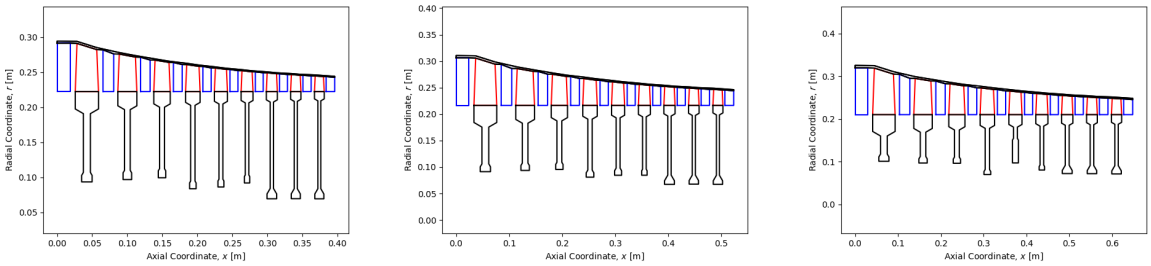

Figure C.10: Design results of CFM56 HPC for 0.75x (left), 1.0x (middle), and 1.25x (right) nominal mass flow rate.

Table C.5: Comparison of weight estimation results of CFM56 HPC model for various mass flow rates.

Component	Weight [kg]		
	43.9[1]	58.5[1,2]	73.1[1]
Total	**91.0**	**134.6**	**185.7**
Rotors + Disks	65.0	91.0	119.2
Rotor Blades	5.72	9.19	13.1
Disks	59.3	81.8	106.1
Stator Vanes	10.0	16.1	23.2
Casing	9.66	19.4	33.4
Connecting Hardware	6.29	8.07	9.78

[1]Mass flow rate [kg/s]. [2]Nominal.

Rotational Speed

Table C.6: Outer dimensions and consumed power of CFM56 HPC model for various rotational speeds.

Category	Parameter	Units	Case 1	Case 2[1]	Case 3
Performance	Rotational Speed, N	RPM	11387	15183	18979
Dimensions	Outer Radius	m	(0.374)	(0.306)	(0.269)
	Length[2]	m	(0.372)	(0.488)	(0.601)

[1]Nominal. [2]Total length excluding guide vane.

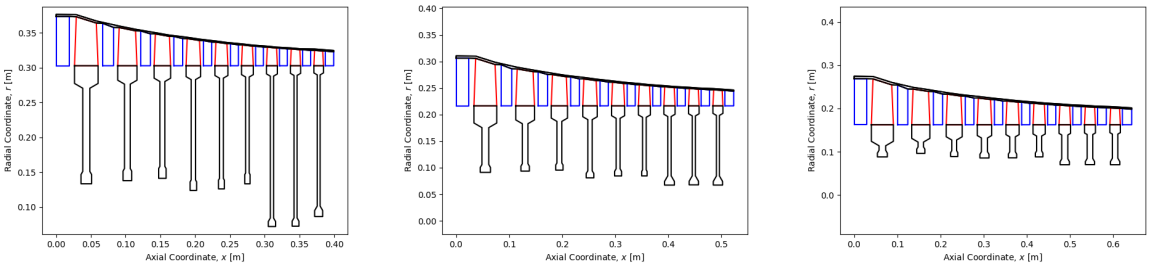

Figure C.11: Design results of CFM56 HPC for 11387 RPM (left), 15183 RPM (middle), and 18979 RPM (right) rotational speeds.

Table C.7: Comparison of weight estimation results of CFM56 HPC model for various rotational speeds.

Component	Weight [kg]		
	11387[1]	15183[1,2]	18979[1]
Total	**145.8**	**134.6**	**133.2**
Rotors + Disks	109.7	91.0	81.0
Rotor Blades	8.32	9.19	9.42
Disks	101.4	81.8	71.6
Stator Vanes	14.2	16.1	17.6
Casing	13.2	19.4	26.9
Connecting Hardware	8.65	8.07	7.72

[1]Rotational speed [RPM]. [2]Nominal.

C.2.1.2. DUTY COEFFICIENTS

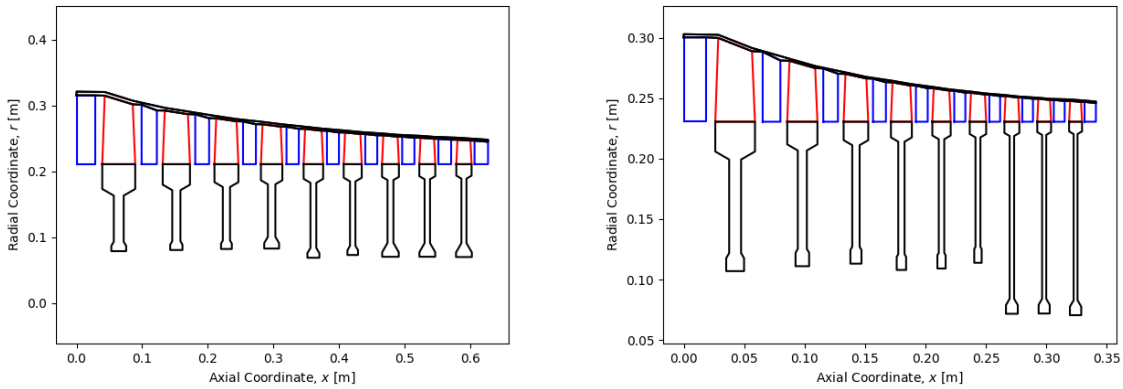

Figure C.12: Design results of CFM56 HPC for minimum (left) and maximum (right) flow coefficients.

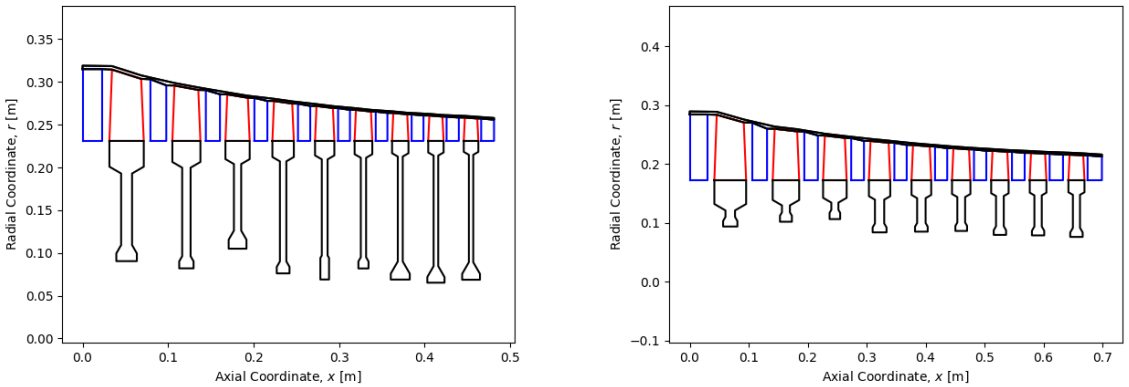

Figure C.13: Design results of CFM56 HPC for minimum (left) and maximum (right) work coefficients.

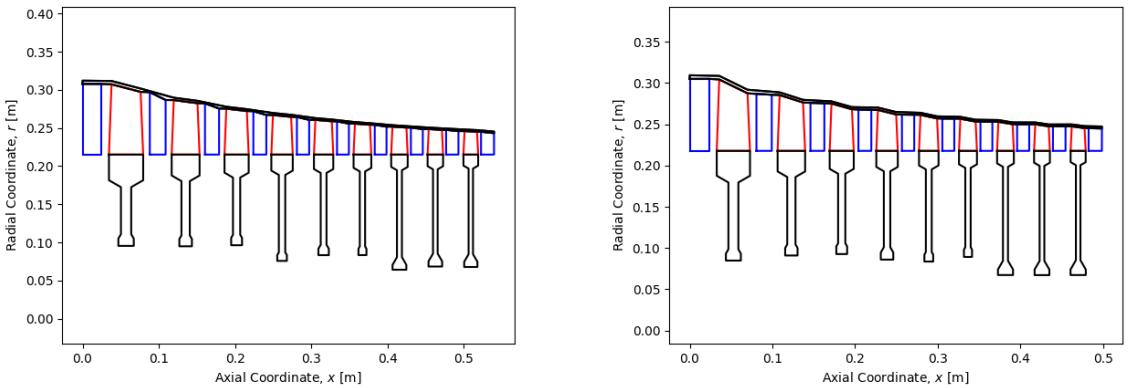

Figure C.14: Design results of CFM56 HPC for minimum (left) and maximum (right) degrees of reaction.

C.2.1.3. MATERIAL SELECTION

Table C.8: Various possible material combinations of PW2037 LPC and HPC models.

		Case 1[1]		Case 2	
Category	**Parameter**	**LPC**	**HPC**	**LPC**	**HPC**
Materials	Rotor Blade Material 1	17-4PH	17-4PH	Ti-17	Ti-17
	→ Stages	All	1-9	All	1-3
	Rotor Blade Material 2		IN 718[2]		17-4PH
	→ Stages		10-12		4-12
	Stator Vane Material 1	17-4PH	17-4PH	Ti-17	17-4PH
	→ Stages	All	All	All	All
	Stator Vane Material 2				
	→ Stages				
	Disk Material 1	17-4PH	17-4PH	Ti-17	Ti-17
	→ Stages	All	1-9	All	1-9
	Disk Material 2		IN 718		IN 718[2]
	→ Stages		10-12		10-12
	Casing Material	17-4PH	17-4PH	17-4PH	17-4PH

[1] Nominal. [2] INCONEL 718.

C.2.2. AXIAL TURBINES

C.2.2.1. DISK TEMPERATURE PROFILE (SAME DISK)

CFM56 LPT

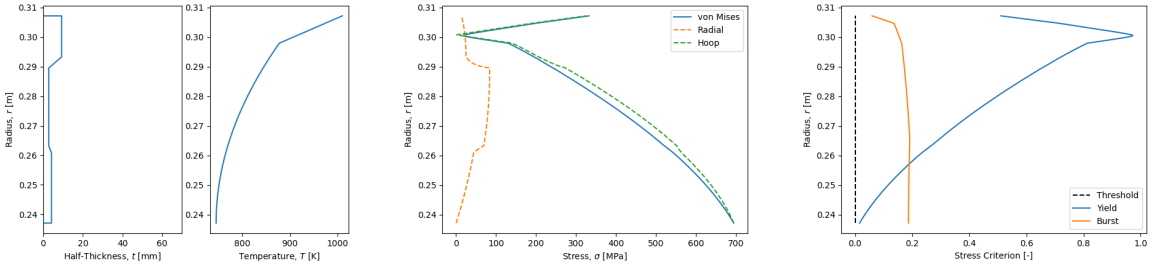

Figure C.15: Stress distributions of CFM56 LPT first stage disk (nominal temperature profile).

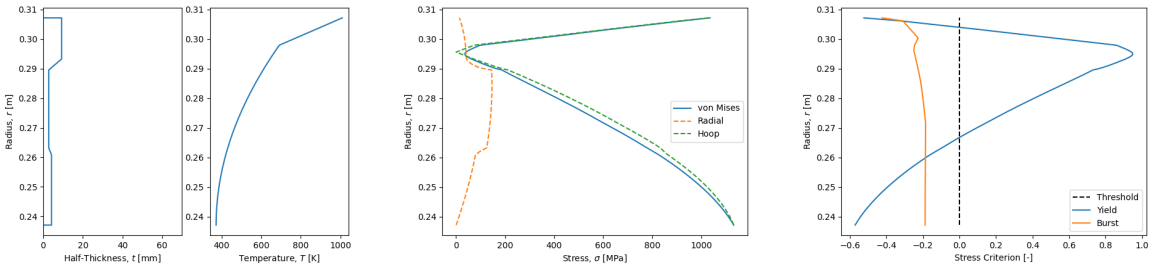

Figure C.16: Stress distributions of CFM56 LPT first stage disk (nominal temperature profile, reduced cooling temperature).

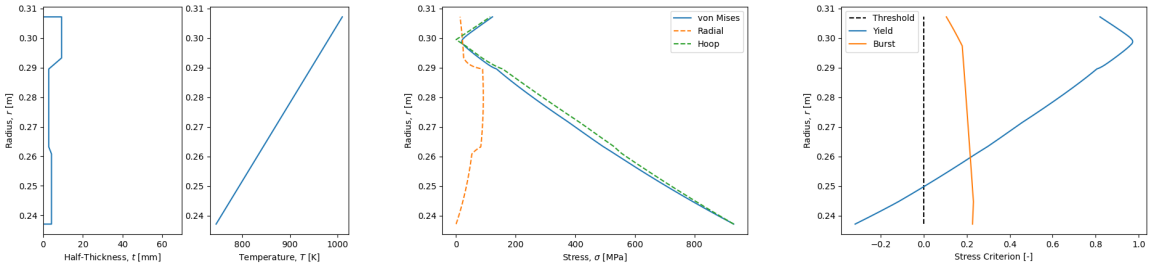

Figure C.17: Stress distributions of CFM56 LPT first stage disk (linear temperature profile).

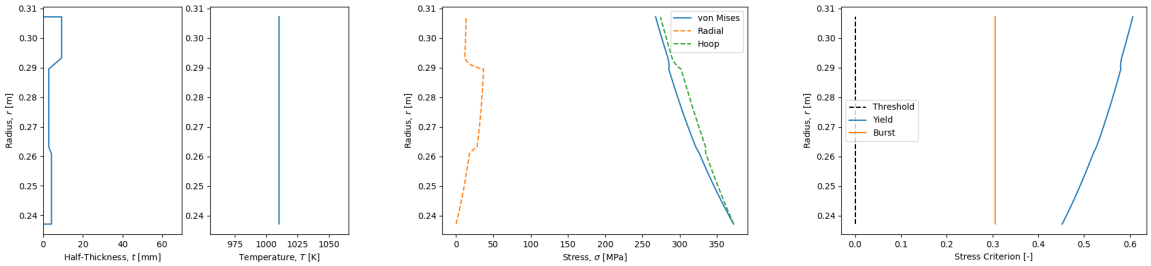

Figure C.18: Stress distributions of CFM56 LPT first stage disk (constant temperature profile).

CFM56 HPT

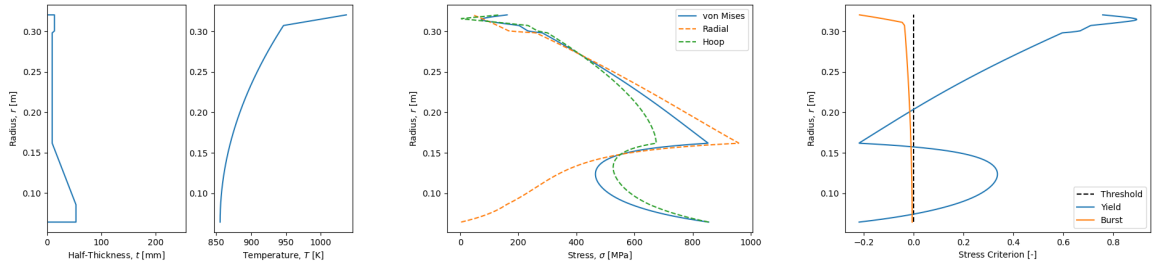

Figure C.19: Stress distributions of CFM56 HPT single stage disk (nominal temperature profile).

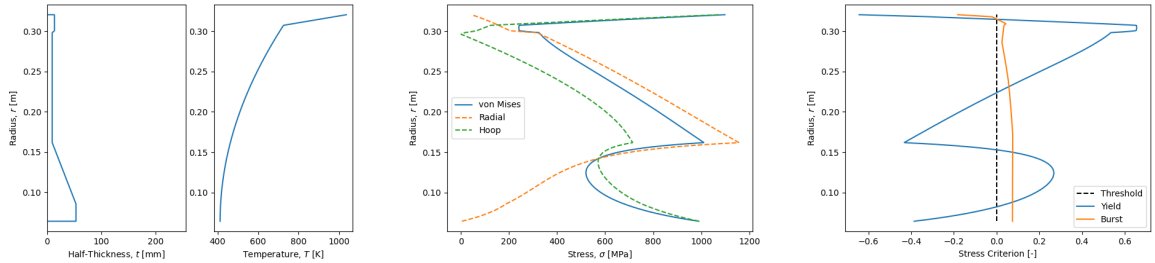

Figure C.20: Stress distributions of CFM56 HPT single stage disk (nominal temperature profile, reduced cooling temperature).

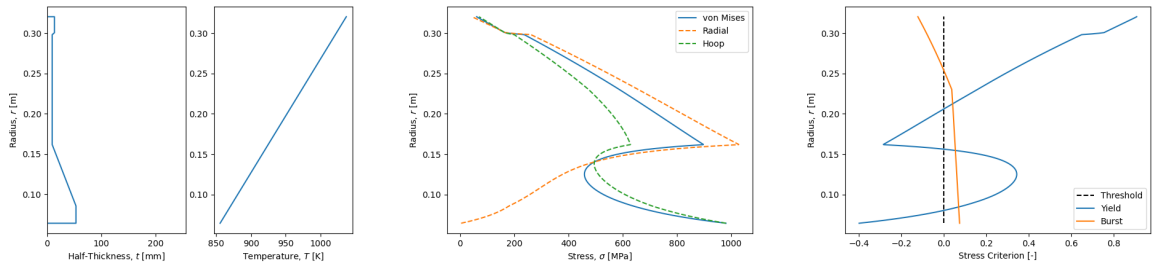

Figure C.21: Stress distributions of CFM56 HPT single stage disk (linear temperature profile).

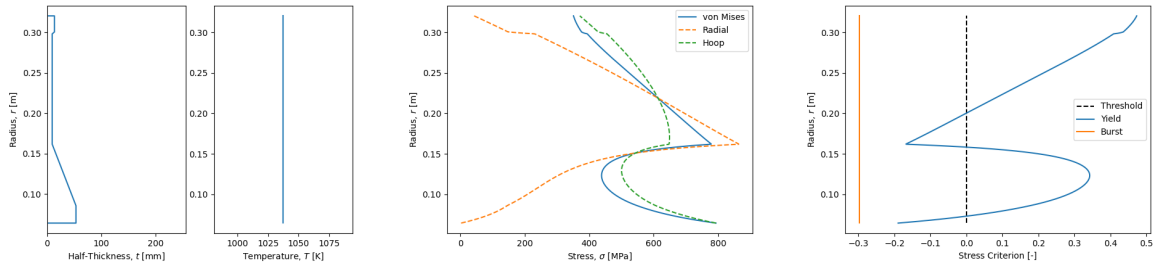

Figure C.22: Stress distributions of CFM56 HPT single stage disk (constant temperature profile).

BIBLIOGRAPHY

[1] H. Ritchie, "Climate change and flying: what share of global CO2 emissions come from aviation." *Our World in Data*. 22 Oct. 2022. https://ourworldindata.org/co2-emissions-from-aviation.

[2] A. C. for Aviation Research and I. in Europe (ACARE), "Strategic Research and Innovation Agenda : 2017 Update : Volume 1." *ACARE*. 2017. https://www.dlr.de/dlr/Portaldata/1/Resources/documents/2017/acare-strategic-research-innovation-volume-1-v2.7-interactive.pdf.

[3] M. Sielemann, A. Pitchaikani, N. Selvan, and M. Sammak, (), "The Jet Propulsion Library: Modeling and simulation of aircraft engines." *Proceedings of the 12th International Modelica Conference, Session 11D: Aerospace*. Prague, Czech Republic. 15-17 May 2017. pp. 909-920. https://doi.org/10.3384/ecp17132909.

[4] D.-G. f. M. European Commission, D.-G. f. R. Transport, and Innovation, "Flightpath 2050 : Europe's vision for aviation : maintaining global leadership and serving society's needs." *Publications Office*. 2011. https://data.europa.eu/doi/10.2777/50266.

[5] "Airborne Energy Harvesting for Aircraft (ARENA)." *Knowledge Centre Organic Rankine Cycle (KCORC) : R&D Projects*. Accessed 7 Sept. 2021. https://www.kcorc.org/en/rd-projects/arena/.

[6] P. Colonna, M. Pini, and R. Vos, "Waste Heat Recovery Systems for More Electric Aircraft." *NWO Domain : Applied and Engineering Sciences (TTW) : Open Technology Program*. 16 July 2019. [Research Proposal].

[7] C. de Servi, L. Azzini, M. Pini, A. G. Rao, and P. Colonna, "Exploratory assessment of a combined-cycle engine concept for aircraft propulsion." *Proceedings of the 1st Global Power and Propulsion Forum*. Zurich, Switzerland. 16-18 January 2017. [GPPF-2017-78]. https://repository.tudelft.nl/islandora/object/uuid%3A9150dd0e-b2ef-46dd-8b1d-9bd59831e234.

[8] "13.3 Aircraft Range: the Breguet Range Equation." *Massachusetts Institute of Technology*. Accessed 18 May 2022. https://web.mit.edu/16.unified/www/FALL/thermodynamics/notes/node98.html.

[9] "Specific Impulse." *National Aeronautics and Space Administration*. Accessed 18 May 2022. https://www.grc.nasa.gov/www/k-12/airplane/specimp.html.

[10] E. S. Hendricks and J. S. Gray, "pyCycle: A Tool for Efficient Optimization of Gas Turbine Engine Cycles." *Aerospace*. 2019; 6(8):87. https://doi.org/10.3390/aerospace6080087.

[11] "Design And Integration Tools: Weight Analysis of Turbine Engine - an Object-Oriented Version (WATE) (LEW-19687-1)." *NASA Technology Transfer Program*. Accessed 13 Sept. 2021. https://software.nasa.gov/software/LEW-19687-1.

[12] G. A. C. I. of Propulsion Technology, Engine, *"gtlab." German Aerospace Center: Institute of Propulsion Technology : Engine. accessed 13 sept. 2021. https://www.dlr.de/at/en/desktopdefault.aspx/tabid-9029/*. .

[13] M. Sielemann, M. Thorade, J. Claesson, A. Nguyen, X. Zhao, S. Sahoo, and K. Kyprianidis, (), "Modelica and Functional Mock-Up Interface: Open Standards for Gas Turbine Simulation." *Proceedings of the ASME Turbo Expo 2019: Turbomachinery Technical Conference and Exposition. Volume 3: Coal, Biomass, Hydrogen, and Alternative Fuels; Cycle Innovations; Electric Power; Industrial and Cogeneration; Organic Rankine Cycle Power Systems*. Phoenix, Arizona, USA. 17-21 June 2019. https://doi.org/10.1115/GT2019-91597.

[14] Jane's, *Jane's Aero-Engines*. Accessed Nov. 2021. https://customer.janes.com/janes/search?f=PUBSECTION(Aero-Engines).

[15] P. Lolis, P. Giannakakis, V. Sethi, A. Jackson, and P. Pilidis, "Evaluation of aero gas turbine preliminary weight estimation methods." *The Aeronautical Journal,* 118:1204. June 2014. pp. 625-641. https://doi.org/10.1017/S0001924000009404.

[16] E. Torenbeek, *Synthesis of Subsonic Airplane Design.* Martinus Nijhoff. The Hague, The Netherlands. 1975. pp. 129-130.

[17] E. A. Onat and G. W. Klees, "A Method to Estimate Weight and Dimensions of Large and Small Gas Turbine Engines." *National Aeronautics and Space Administration.* Jan. 1979. NASA-CR-159481 [Technical Report]. https://ntrs.nasa.gov/citations/19790006875.

[18] M. Tong, I. Halliwell, and L. Ghosn, "A Computer Code for Gas Turbine Engine Weight and Disk Life Estimation." *ASME. J. Eng. Gas Turbines Power*, Vol. 126, No. 2. April 2004. pp. 265-270. https://doi.org/10.1115/1.1691980.

[19] M. T. Tong and B. A. Naylor, "An Object-Oriented Computer Code for Aircraft Engine Weight Estimation." *Proceedings of the ASME Turbo Expo 2008: Power for Land, Sea, and Air. Volume 1: Aircraft Engine; Ceramics; Coal, Biomass and Alternative Fuels; Manufacturing, Materials and Metallurgy; Microturbines and Small Turbomachinery.* Berlin, Germany. 9-13 June 2008. pp. 1-7. https://doi.org/10.1115/GT2008-50062.

[20] R. Becker, S. Reitenbach, C. Klein, T. Otten, M. Nauroz, and M. Siggel, "An Integrated Method for Propulsion System Conceptual Design." *Proceedings of the ASME Turbo Expo 2015: Turbine Technical Conference and Exposition. Volume 1: Aircraft Engine; Fans and Blowers; Marine.* Montreal, Quebec, Canada. 15–19 June 2015. V001T01A021. ASME. https://doi.org/10.1115/GT2015-43251.

[21] P. Lolis, "Development of a Preliminary Weight Estimation Method for Advanced Turbofan Engines," Department of Power and Propulsion, School of Engineering, Cranfield University. Cranfield, England. July 2014. [PhD Thesis]. http://dspace.lib.cranfield.ac.uk/handle/1826/9244.

[22] E. M. Greitzer, et al., "N+3 Aircraft Concept Designs and Trade Studies, Final Report. Volume 2: Appendices - Design Methodologies for Aerodynamics, Structures, Weight, and Thermodynamic Cycles," *NASA Technical Reports Server.* Dec. 2010. NASA/CR—2010-216794/VOL2 [Technical Report]. pp. 133-146. https://ntrs.nasa.gov/citations/20100042398.

[23] C. A. Snyder and M. T. Tong, "Modeling Turboshaft Engines for the Revolutionary Vertical Lift Technology Project." *Vertical Flight Society's 75th Annual Forum Technology Display.* Philadelphia, PA, USA. 13-16 May 2019. https://ntrs.nasa.gov/citations/20190026450.

[24] J. Kurzke and I. Halliwell, "Propulsion and Power: An Exploration of Gas Turbine Performance Modeling." *Springer International Publishing AG.* 2018. pp. 119, 429, 434, 435. https://doi.org/10.1007/978-3-319-75979-1.

[25] R. de Vries, M. F. M. Hoogreef, and R. Vos, "Aeropropulsive Efficiency Requirements for Turboelectric Transport Aircraft." *Proceedings of the AIAA SciTech Forum.* Orlando, Florida, USA. 6-10 January 2020. https://doi.org/10.2514/6.2020-0502.

[26] R. H. Jansen, C. Bowman, A. Jankovsky, R. Dyson, and J. Felder, "Overview of NASA Electrified Aircraft Propulsion Research for Large Subsonic Transports." *Proceedings of the AIAA Propulsion and Energy Forum.* Atlanta, Georgia, USA. 10-12 July 2017. https://ntrs.nasa.gov/citations/20170006235.

[27] C. L. Bowman, J. L. Felder, and T. V. Marien, "Turbo- and Hybrid-Electrified Aircraft Propulsion Concepts for Commercial Transport." *Proceedings of the AIAA/IEEE Electric Aircraft Technologies Symposium.* Cincinnati, Ohio, USA. 9-11 July 2018. https://ntrs.nasa.gov/citations/20180005437.

[28] J. L. Felder, G. V. Brown, H. D. Kim, and J. Chu, "Turboelectric Distributed Propulsion in a Hybrid Wing Body Aircraft." *Proceedings of the 20th International Society for Airbreathing Engines.* Gothenburg, Sweden. 12-16 September 2011. https://ntrs.nasa.gov/citations/20120000856.

[29] B. T. Schiltgen, J. L. Freeman, and D. W. Hall, "Aeropropulsive Interaction and Thermal System Integration within the ECO-150: A Turboelectric Distributed Propulsion Airliner with Conventional Electric Machines." *Proceedings of the 16th AIAA Aviation Technology, Integration, and Operations Conference.* Washington, D.C., USA. 13-17 June 2016. https://doi.org/10.2514/6.2016-4064.

[30] P. Schmollgruber, D. Donjat, M. Ridel, I. Cafarelli, O. Atinault, C. François, and B. Paluch, "Multidisciplinary design and performance of the ONERA Hybrid Electric Distributed Propulsion concept (DRAGON)." *Proceedings of the AIAA SciTech Forum.* Orlando, Florida, USA. 6-10 January 2020. https://doi.org/10.2514/6.2020-0501.

[31] T. Sinnige, N. van Arnhem, T. C. A. Stokkermans, G. Eitelberg, and L. L. M. Veldhuis, "Wingtip-Mounted Propellers: Aerodynamic Analysis of Interaction Effects and Comparison with Conventional Layout." *Journal of Aircraft.* 2019; 56:1. pp. 295-312. https://doi.org/10.2514/1.C034978.

[32] A. Seitz, A. L. Habermann, F. Peter, F. Troeltsch, A. C. Pardo, B. D. Corte, M. van Sluis, Z. Goraj, M. Kowalski, X. Zhao, T. Grönstedt, J. Bijewitz, , and G. Wortmann, "Proof of Concept Study for Fuselage Boundary Layer Ingesting Propulsion." *Aerospace.* 2021; 8:1. p. 16. https://doi.org/10.3390/aerospace8010016.

[33] "Single-aisle Turboelectric Aircraft with Aft Boundary-Layer Propulsion." *National Aeronautics and Space Administration.* Accessed 24 May 2022. https://sacd.larc.nasa.gov/asab/asab-projects-2/starc-abl/.

[34] C. A. Snyder, "Exploring advanced technology gas turbine engine design and performance for the Large Civil Tiltrotor (LCTR)." *AIAA Propulsion and Energy Forum. Cleveland, Ohio, USA. 28-30 July 2014. https://doi.org/10.2514/6.2014-3442.*,.

[35] C. Silva, W. Johnson, K. Antcliff, and M. Patterson, "VTOL Urban Air Mobility Concept Vehicles for Technology Development." *AIAA Aviation Forum, 2018 Aviation Technology, Integration, and Operations Conference.* Atlanta, Georgia, USA. 25-29 June 2018. https://doi.org/10.2514/6.2018-3847.

[36] J. W. Chapman, "Multi-point Design and Optimization of a Turboshaft Engine for a Tiltwing Turboelectric VTOL Air Taxi." *AIAA SciTech Forum.* San Diego, California, USA. 7-11 January 2019. https://doi.org/10.2514/6.2019-1948.

[37] S. Reitenbach, M. Vieweg, R. Becker, C. Hollmann, F. Wolters, J. Schmeink, T. Otten, and M. Siggel, "Collaborative Aircraft Engine Preliminary Design using a Virtual Engine Platform, Part A: Architecture and Methodology," *AIAA Scitech 2020 Forum.* Orlando, Florida, USA. 6-10 January 2020. https://doi.org/10.2514/6.2020-0867.

[38] M. Pini, (2021), "Lecture 7 – Axial Compressors," *AE4206 Turbomachinery*, Department of Flight Performance and Propulsion, Faculty of Aerospace Engineering, Delft University of Technology. Delft, The Netherlands. March 2021. p. 6. [Lecture Content].

[39] M. V. Casey, "A mean line prediction method for estimating the performance characteristics of an axial compressor stage," *Proceedings of the Institution of Mechanical Engineers International Conference on Turbomachinery – Efficiency Prediction and Improvement.* Cambridge, United Kingdom. 1-3 September 1987. Paper C 264/87.

[40] F. Yin, "Tutorial: Engine Cycle Calculations," *AE4238 Aero Engine Technology*, Department of Flight Performance and Propulsion, Faculty of Aerospace Engineering, Delft University of Technology. Delft, The Netherlands. September 2020. p. 8. [Lecture Content].

[41] R. I. Lewis, *Turbomachinery Performance Analysis.* Elsevier Science & Technology Books. May 1996. ISBN: 0340631910. p. 90.

[42] H. Grieb, "Projektierung von Turboflugtriebwerken." *Springer Basel AG.* 2004. ISBN: 978-3-0348-9627-6. pp. 192, 201, 247, 260, 265, 271-273, 277. https://doi.org/10.1007/978-3-0348-7938-5.

[43] J. D. Denton, "Multall – An Open Source, Computational Fluid Dynamics Based, Turbomachinery Design System," *ASME Journal of Turbomachinery*, Vol. 139, No. 12: 121001. Dec. 2017. https://doi.org/10.1115/1.4037819.

[44] J. C. Tiemstra, "On the Conceptual Engine Design and Sizing Tool," Department of Aerodynamics, Wind Energy Propulsion, Faculty of Aerospace Engineering, Delft University of Technology. Delft, The Netherlands. 3 February 2017. [MSc Thesis]. http://resolver.tudelft.nl/uuid:09567825-56cf-4a9d-8898-deb5999e23a6.

[45] T. Carolus, *Ventilatoren: Aerodynamischer Entwurf, Schallvorhersage, Konstruktion*. B. G. Teubner / GWV Fachverlage GmbH, Wiesbaden, Deutschland. 2003. ISBN: 978-3-519-00433-2. https://doi.org/10.1007/978-3-322-94864-9. pp. 52-53, 146.

[46] P. Marzocca, "The NACA airfoil series," *Clarkson University*. Accessed 20 Apr. 2022. https://lin-web.clarkson.edu/~pmarzocc/AE429/The%20NACA%20airfoil%20series.pdf.

[47] H. I. H. Saravanamuttoo, G. F. C. Rogers, H. Cohen, P. V. Straznicky, and A. C. Nix, *Gas Turbine Theory Seventh Edition*. Pearson Education Limited. 2017. ISBN: 9781-292-09309-3. p. 431.

[48] Mechanical Properties Data Center. *Aerospace Structural Metals Handbook. Volume I*. Belfour Stulen Inc., Traverse City, Michigan, USA. 1972. [Technical Report]. https://ntrl.ntis.gov/NTRL/dashboard/searchResults/titleDetail/AD737970.xhtml.

[49] *AISI 4340 Alloy Steel (UNS G43400)*. AZo Materials. 13 Sept. 2012. https://www.azom.com/article.aspx?ArticleID=6772.

[50] R. Boyer, G. Welsch, and E. W. Collings, *Materials Properties Handbook — Titanium Alloys*. ASM International, Materials Park, OH, USA. 1994. ISBN: 978-0-87170-481-8. pp. 337-362, 453-463, 483-636 (Sections III and IV). https://app.knovel.com/kn/resources/kpMPHTA002/toc.

[51] *Grade Ti 5Al 2Sn 2Zr 4Mo 4Cr Alloy (UNS R58650)*. AZo Materials. 30 July 2013. https://www.azom.com/article.aspx?ArticleID=9393.

[52] *HASTELLOY S alloy*. Haynes International. Accessed: 31 Mar. 2022. https://www.haynesintl.com/alloys/alloy-portfolio_/High-temperature-Alloys/hastelloy-s-alloy/principal-features.

[53] *INCONEL Alloy 600*. Special Metals. Accessed: 28 Jan. 2022. https://www.specialmetals.com/documents/technical-bulletins/inconel/inconel-alloy-600.pdf.

[54] *INCONEL Alloy 718*. Special Metals. Accessed: 26 Jan. 2022. https://www.specialmetals.com/documents/technical-bulletins/inconel/inconel-alloy-718.pdf.

[55] *Special Metals INCONEL Alloy 718*. Aerospace Specification Metals Inc. Accessed: 26 Jan. 2022. http://asm.matweb.com/search/SpecificMaterial.asp?bassnum=NINC34.

[56] *NIMONIC Alloy 105*. Special Metals. Accessed: 27 Jan. 2022. https://www.specialmetals.com/documents/technical-bulletins/nimonic-alloy-105.pdf.

[57] *Super Alloys Nimonic 105, DIN 2.4634*. Metal Ministry Inc. Accessed: 27 Jan. 2022. http://www.steelsalesonline.com/nimonic-105-chemical-properties.html.

[58] P. P. Walsh and P. Fletcher, "Gas Turbine Performance Second Edition." *Blackwell Science*. 2004. ISBN 0-632-06434-X. pp. 530, 555.

[59] V. A. Kurganov, "Adiabatic wall temperature," *Thermopedia*. Accessed: 8 June 2022. https://doi.org/10.1615/AtoZ.a.adiabatic_wall_temperature.

[60] "Air - Prandtl Number," *The Engineering Toolbox*. Accessed: 16 June 2022. https://www.engineeringtoolbox.com/air-prandtl-number-viscosity-heat-capacity-thermal-conductivity-d_2009.html.

[61] S. Bretschneider, F. Rothe, M. G. Rose, and S. Staudacher, "Compressor Casing Preliminary Design Based on Features." *Proceedings of ASME Turbo Expo 2008: Power for Land, Sea and Air. Volume 5: Structures and Dynamics, Parts A and B*. Berlin, Germany. 9-13 June 2008. ASME. https://doi.org/10.1115/GT2008-50102.

[62] "Steel sheets." *MCB*. Accessed 20 June 2022. https://www.mcb.eu/en/steel/steel-sheets/c/0010030009?q=%3Arelevance.

[63] "Steel Plates - Size & Weight." *The Engineering Toolbox*. Accessed 20 June 2022. https://www.engineeringtoolbox.com/steel-plates-weight-d_1561.html.

[64] Jane's, "CFM International CFM56." *Jane's Aero-Engines*. 7 Sept. 2020. https://customer.janes.com/Janes/Display/JAE_0631-JAE_.

[65] Jane's, "Pratt Whitney PW2000." *Jane's Aero-Engines*. 6 Jan. 2021. https://customer.janes.com/Janes/Display/JAE_0749-JAE_.

[66] M. Pini, (2021), "Lecture 5 – Axial Turbines," *AE4206 Turbomachinery*, Department of Flight Performance and Propulsion, Faculty of Aerospace Engineering, Delft University of Technology. Delft, The Netherlands. February 2021. p. 5. [Lecture Content].

[67] M. F. Zelesky, N. C. Baines, H. Moustapha, and D. Japikse, *Axial and Radial Turbines*, Concepts ETI, Inc., 2003. ISBN: 0-933283-12-1.

[68] M. G. Turner, A. Merchant, and D. Bruna, "Applications of a Turbomachinery Design Tool for Compressors and Turbines." *Proceedings of the 43rd AIAA/ASME/SAE/ASEE Joint Propulsion Conference & Exhibit*. Cincinnati, OH, USA. 8-11 July 2007. https://doi.org/10.2514/6.2007-5152.

[69] "GasTurb 14: Design and Off-Design Performance of Gas Turbines." *GasTurb GmbH*. 2022. p. 13. https://www.gasturb.de/Downloads/Manuals/GasTurb14.pdf.

[70] J. Dunham, "A Parametric Method of Turbine Blade Profile Design." *Proceedings of the ASME 1974 International Gas Turbine Conference and Products Show. Volume 1B: General*. Zurich, Switzerland. 30 Mar. - 4 Apr. 1974. V01BT02A037. ASME. https://doi.org/10.1115/74-GT-119.

[71] B. M. Kulfan and J. E. Bussoletti, "'Fundamental' Parametric Geometry Representation for Aircraft Component Shapes." *Proceedings of the 11th AIAA/ISSMO Multidisciplinary Analysis and Optimization Conference*. Portsmouth, Virginia, USA. 6-8 Sept. 2006. https://arc.aiaa.org/doi/abs/10.2514/6.2006-6948.

[72] "Technical Q&A Fuels." *International Association for Stability, Handling and Use of Liquid Fuels*. Accessed: 28 June 2022. https://iashulf.memberclicks.net/technical-q-a-fuels.

[73] M. Huth and A. Heilos, "14 - Fuel flexibility in gas turbine systems: impact on burner design and performance." *In Woodhead Publishing Series in Energy, Modern Gas Turbine Systems: High Efficiency, Low Emission, Fuel Flexible Power Generation*. Woodhead Publishing, 2013. ISBN 9781845697280. p. 669. https://doi.org/10.1533/9780857096067.3.635.

[74] D. P. Gutzwiller and M. G. Turner, "Rapid low fidelity turbomachinery disk optimization." *Advances in Engineering Software*. 2010; 41:5. pp. 779-791. https://zbmath.org/?q=an:05693330.

[75] D. P. Gutzwiller, "T-Axi Disk V2.2 User's Guide and Tutorial." *Penn State University*. 26 May 2009. http://citeseerx.ist.psu.edu/viewdoc/download?doi=10.1.1.457.1606&rep=rep1&type=pdf.

[76] "scipy.optimize.minimize." *The SciPy community*. Accessed 7 July 2022. https://docs.scipy.org/doc/scipy/reference/generated/scipy.optimize.minimize.html.

[77] "minimize(method='SLSQP')." *The SciPy community*. Accessed 7 July 2022. https://docs.scipy.org/doc/scipy/reference/optimize.minimize-slsqp.html#optimize-minimize-slsqp.

[78] H. I. H. Saravanamuttoo, G. F. C. Rogers, and H. Cohen, *Gas Turbine Theory, 5th Edition*. Pearson Education. 2001. ISBN: 978-81-7758-902-3. p. 195.

[79] A. R. Howell and R. P. Bonham, "Overall and Stage Characteristics of Axial-Flow Compressors," *Proceedings of the Institution of Mechanical Engineers*. Vol. 163, Issue 1. 1 June 1950. p. 239.

[80] S. A. Korpela, *Principles of Turbomachinery, 1st Edition*. John Wiley & Sons, Inc., Hoboken, New Jersey, USA. 2011. ISBN: 978-0-470-53672-8. p. 261.

[81] *Radius of an Arc or Segment*. Math Open Reference. 2011. Accessed 20 Apr. 2022. https://www.mathopenref.com/arcradius.html.

[82] *Equation of a Circle, Standard Form (Center Anywhere)*. Math Open Reference. 2011. Accessed 20 Apr. 2022. https://www.mathopenref.com/coordgeneralcircle.html.

[83] M. Pini, (2021), "Lecture 1 – Turbomachinery Fundamentals," *AE4206 Turbomachinery*, Department of Flight Performance and Propulsion, Faculty of Aerospace Engineering, Delft University of Technology. Delft, The Netherlands. February 2021. pp. 11, 14. [Lecture Content].

[84] R. G. Budynas and J. K. Nisbett, *Shigley's Mechanical Engineering Design Tenth Edition*. McGraw-Hill Education, New York, NY, USA. 2015. ISBN: 978-0-07-339820-4. pp. 104, 110, 263.

[85] "Burst and Collapse - Pressure Vessel Design," *EngrApps.com*. Accessed: 13 June 2022. http://engrapps.com/mechanical-systems-and-materials/mechanical-components/pressure-vessels/burst-collapse-analysis.php.